hhu.

Clinical Implications of Silicon Photomultiplier-based Positron Emission Tomography for Different Radionuclides

Inaugural-Dissertation

vorgelegt von

David Manuel Kersting

geboren am 17. Juni 1989 in Essen

Düsseldorf, Februar 2023

aus der Klinik für Nuklearmedizin des Universitätsklinikums Essen, Medizinische Fakultät der Universität Duisburg-Essen

Gedruckt mit der Genehmigung der
Mathematisch-Naturwissenschaftlichen Fakultät der
Heinrich-Heine-Universität Düsseldorf

Berichterstatter

1. Prof. Dr. Dr. Walter JENTZEN

2. Prof. Dr. Thomas HEINZEL

Tag der mündlichen Prüfung: 01. August 2023

Abstract

Positron emission tomography (PET) is a medical imaging modality which plays an important role in daily clinical practice. It primarily serves as a tool for whole-body staging in oncology, utilizing various radioactively labelled tracers for distinct tumour entities. Since its introduction, PET imaging has benefited from continuous technical developments, including both new hardware components and advanced image reconstruction software. Most recently, the introduction of silicon photomultiplier-based (SiPM-based) PET detectors has led to major advancements. These exhibit, inter alia, an increased effective sensitivity and time-of-flight resolution. On the one hand, this can result in improved image quality and higher detectability. On the other hand, the PET acquisition time could be reduced while maintaining diagnostic performance. Shorter acquisition times can enhance patient comfort. Alternatively, lower levels of activity could be administered, potentially leading to substantial improvements in radiation safety for both patients and medical personnel. The aim of this thesis is to investigate the clinical implications of SiPM-based PET with a special focus on tumour lesion detectability and reductions in acquisition time for three PET tracers labelled with different radionuclides.

In the first experiments, we examined the effects of a reduced acquisition time on clinical SiPM-based PET imaging for the standard tracers ^{18}F-FDG and ^{68}Ga-PSMA. For ^{18}F-FDG PET, in 20 lymphoma patients a reduction by a factor of 2.8 compared to the clinical standard was feasible without negative effects on region-based lesion detection rates and PET-based clinical scores. For ^{68}Ga-PSMA, in 20 prostate cancer patients a reduction by a factor of 3.7 was associated with missed detection of two small lymph node metastases with low tracer uptake in two different patients. In one case, this would have resulted in under-assessment of the stage using standard clinical scoring methods, potentially affecting patient management. For both ^{18}F-FDG and ^{68}Ga-PSMA, image noise - as an indicator of image quality - was only slightly increased for the reduced acquisition time and image-based lesion quantification was comparable. These results indicate that the limit for reductions in acquisition time to maintain diagnostic quality for ^{18}F and ^{68}Ga is about 3. However, potential under-diagnosis of small and low-uptake

lesions requires careful patient selection for reduced protocols. For patients with a high tumour load, a shortened acquisition time may be appropriate for follow-up scans where diagnosis does not rely on the characterisation of individual lesions. However, for primary staging evaluations or suspected recurrence cases, a standard acquisition protocol should be employed. In these clinical experiments, no direct comparison to previous-generation PET scanners were performed, as - because of the short half-lives of ^{18}F and ^{68}Ga (109.77 min and 67.71 min, respectively) - detectability and image quality in subsequent PET scans after single tracer administration would be influenced by decay and biological metabolism. However, this does not hold true for tracers with long half-life and slow metabolism.

Therefore, we focused our next experiments on the non-standard radionuclide ^{124}I. It is typically used for imaging of differentiated thyroid cancer but exhibits more challenging PET properties (for example, a low positron branching ratio). With a half-life of 4.2 d, ^{124}I enables a direct comparison of different PET systems after single tracer administration. In an evaluation of 10 patients with differentiated thyroid cancer, the SiPM-based system outperformed two PET systems with detectors from previous generations (photomultiplier tubes and avalanche photodiodes) in lesion detectability and visual image quality. It almost reached the detectability results of scan with fivefold-prolonged duration on the avalanche photodiode-based system which was used as reference. Additionally detected lesions were of small sizes and low tracer uptake values indicating pronounced benefits of SiPM-based PET for metastases with these properties. To quantify these results, we performed a phantom investigation to compare the minimum detectable activity across a SiPM- and a photomultiplier tube-based PET system under defined conditions.

The phantom was designed to resemble clinical differentiated thyroid cancer metastases at the lower ends of typical size and ^{124}I activity concentration ranges. Overall, the minimum detectable activity was improved by a factor of 0.5 with pronounced benefits for small lesions. Moreover, the minimum detectable activity correlated linearly with the acquisition time. We, therefore, suggest a prolonged acquisition time for body regions which are typically affected by metastases - like the neck region in thyroid cancer patients. Finally, we investigated the impact of improved detectability on radioiodine therapy planning. In thyroid cancer patients, ^{124}I PET can be used for pre-therapeutic dosimetry to predict response to ^{131}I therapy. In a dosimetry model, we showed that lesions with predicted therapy response ≥4.5 mm in diameter are detectable on both systems at a standard acquisition

time. Smaller lesions, however, were only detectable on the SiPM-based system. As they yet were predicted to show response to radioiodine therapy, SiPM-based PET can have beneficial effects on clinical patient and therapy management.

Eidesstattliche Versicherung

Ich versichere an Eides Statt, dass die Dissertation von mir selbständig und ohne unzulässige fremde Hilfe unter Beachtung der „Grundsätze zur Sicherung guter wissenschaftlicher Praxis an der Heinrich-Heine-Universität Düsseldorf" erstellt worden ist.

Düsseldorf, den 03. Februar 2023

This thesis is based on four publications that resulted from the performed experiments:

1. *Evaluation of ^{18}F-FDG PET/CT images acquired with a reduced scan time duration in lymphoma patients using the digital biograph vision*, M. Weber, W. Jentzen, R. Hofferber, K. Herrmann, W. P. Fendler, C. Rischpler, L. Umutlu, M. Conti, P. Fragoso Costa, M. Sraieb and D. Kersting, BMC Cancer **21**, 62 (2021)

2. *Evaluation of $[^{68Ga}]$Ga-PSMA PET/CT images acquired with a reduced scan time duration in prostate cancer patients using the digital biograph vision*, M. Weber, W. Jentzen, R. Hofferber, K. Herrmann, W. P. Fendler, M. Conti, A. Wetter, D. Kersting, C. Rischpler and P. Fragoso Costa, EJNMMI Research **11**, 21 (2021)

3. *Comparing lesion detection efficacy and image quality across different PET system generations to optimize the iodine-124 PET protocol for recurrent thyroid cancer*, D. Kersting, W. Jentzen, M. Sraieb, P. Fragoso Costa, M. Conti, L. Umutlu, G. Antoch, M. Nader, K. Herrmann, W. P. Fendler, C. Rischpler and M. Weber, EJNMMI Physics **8**, 14 (2021)

4. *Silicon-photomultiplier-based PET/CT reduces the minimum detectable activity of iodine-124*, D. Kersting, W. Jentzen, P. Fragoso Costa, M. Sraieb, P. Sandach, L. Umutlu, M. Conti, F. Zarrad, C. Rischpler, W. P. Fendler, K. Herrmann, and M. Weber, Scientific Reports **11**, 17477 (2021)

Contents

Introduction

Positron emission tomography (PET) is a widely used clinical molecular imaging modality whose importance is steadily increasing. In PET imaging, biological processes are visualised by *in vivo* administration of radioactively labelled tracers which interact with a distinct target structure [1]. Today, PET is almost exclusively performed in hybrid imaging technique in combination with computed tomography (CT) or magnetic resonance (MR) imaging (PET/CT or PET/MR) [2]. The superior characteristics of hybrid imaging in comparison to stand-alone CT or MR imaging, for example, in tumour lesion detectability lead to an increasing demand for oncological PET imaging [3]. The majority of clinical PET examinations is performed for staging or re-staging of tumour patients [4]. Moreover, it is used for planning of systemic radionuclide therapies [5]. However, PET imaging is not limited to tumour imaging. Other fields of application include imaging of infectious diseases [6] and dedicated heart [7] or brain scans [8] for cardiological or neurological assessments.

The most common molecular targets are glucose transporters (GLUTs) to visualise cellular glucose metabolism after administration of the radioactively labelled glucose analogue ^{18}F-FDG [9]. Most tumour tissues exhibit increased glycolysis and can, therefore, be detected in ^{18}F-FDG PET [10]. For example, ^{18}F-FDG PET/CT is recommended in lymphoma patients for interim analysis and at the end of chemotherapy to evaluate the therapy response [11]. It can be used to identify patients with lymphomas who require intensified treatment regimens [12] and to prognosticate event-free survival and overall survival after immunochemotherapy [13]. Moreover, ^{18}F-FDG PET is well established for imaging of lung cancer patients [14]. More specific oncological targets include somatostatin receptors (SSTRs) [15], prostate specific membrane antigen (PSMA) [16], and sodium/iodide symporter (NIS) [17].

With the approval of ^{177}Lu-based SSTR- and PSMA-targeting radionuclide therapies for neuroendocrine tumours [18] and metastasised prostate cancers [19], PET imaging is becoming more and more important to validate the individual expression of the respective molecular target [20, 21]. The field of radionuclide therapies also includes ^{131}I-based radioiodine therapy in differentiated thyroid

cancer patients [22], for whom pre-therapeutic dosimetry can be performed by ^{124}I PET. It is used to estimate the optimal amount of administered ^{131}I activity in an individualised theranostic approach [23]. In this context, theranostic refers to an application of a radionuclide/tracer pair (here, ^{124}I and ^{131}I) which allows both diagnostic (^{124}I) and therapy (^{124}I) using the same element. Over the past decades, new developments have expanded the applicability of PET imaging. However, they also present new challenges, for example, an increasing number of examinations and imaging of critically ill patients. The relatively long acquisition time of a PET scan can be a particular burden for patients patients experiencing chronic pain.

Since its introduction in the 1950s, PET imaging has steadily been subject to various technical improvements affecting both hardware components like PET detectors [24–26] and software components like image reconstruction algorithms [27–29]. Recently, silicon photomultiplier-based (SiPM-based) PET/CT systems were introduced which show a higher detector sensitivity, smaller detector elements, and improved timing resolutions. Compared to previous-generation systems, this leads to improvements in, inter alia, spatial resolution and time-of-flight (TOF) reconstructions [30–32]. These characteristics translate into clinical benefits like improved image quality and higher detectability in oncological PET imaging [33–35].

Since detectability in PET imaging depends on the acquisition time [36], different practical consequences may be drawn from the improved characteristics of SiPM-based PET. For example, the improved detectability can be used to reduce the acquisition time or the administered amount of activity (as these values are, in a rough approximation, in linear correlation [37]) while maintaining diagnostic quality. A reduced acquisition time could help to meet the increasing demand for examinations and enhance patient comfort. A lower amount of administered activity may also contribute to an increase in the number of possible investigations, if the available amount of radionuclide is limited, for example, by ^{68}Ge/^{68}Ga-generator yield for ^{68}Ga-based PET tracers [38]. Moreover, it can reduce radiation exposure for both patients and medical staff. If the acquisition time/administered activity is not reduced, the increased detectability can have a clinical benefit on patient management. This is particularly relevant for non-standard radionuclides like ^{124}I which show lower image quality and higher image noise. For example, there is an unmet clinical need for improved diagnostics in differentiated thyroid cancer patients with rising serum tumour markers, in whom no tumour tissue

can be identified in standard imaging. In these patients, the application of a „blind" radioiodine therapy is a controversial option [39]. As a limited PET scanner sensitivity may be a reason for ^{124}I-negative differentiated thyroid cancer lesions which are ^{131}I-positive in subsequent radioiodine therapy [40–42], the problem might be addressable by SiPM-based PET.

In this thesis, we investigate two main topics. First, the possible reduction in acquisition time (or administered activity) by SiPM-based PET is examined for the standard PET tracers ^{18}F-FDG (in lymphoma patients) and ^{68}Ga-PSMA (in prostate cancer patients). Second, the improved detectability for the non-standard radionuclide ^{124}I is evaluated and compared to previous-generation PET systems. Moreover, the limits of detectability regarding lesion size and accumulated ^{124}I activity concentration are determined to assess the impact of SiPM-based PET on patient management and radioiodine therapy planning in differentiated thyroid cancer patients in challenging conditions. The thesis follows the structure which is outlined below. A synopsis of the thesis is presented in Figure 1.

Chapter 1 explains the fundamentals of PET imaging in the context of current clinical applications. First, principles of PET acquisition are described. Next, different detector technologies currently used in clinical routine, fundamentals of PET image reconstruction, and the three PET tracers that are applied in this thesis are introduced. The chapter ends with a characterisation of the different tumour entities that are investigated in the clinical part of the thesis.

Chapter 2 explains the experimental techniques which were applied for the studies. First, the characteristics of the investigated PET/CT and PET/MR systems are introduced in chapter 2.1. For the evaluated patient groups and phantoms, different PET acquisition protocols and image reconstruction parameters were employed. These are presented in chapter 2.2. For analysis of patient and phantom PET images, different detectability metrics, standardised PET image reporting scores, uptake metrics, visual image quality scoring systems, image noise evaluations, and the minimum detectable activity were used. To relate the minimum detectable activity with predicted success of clinical radioiodine therapy, the ^{124}I activity concentrations were projected to absorbed ^{131}I radiation doses in a dosimetry model. These techniques are described in chapter 2.3 (for patient images) and chapter 2.4 (for phantom images).

Chapter 3 contains the four publications resulting from this work. The first and the second publication investigate a 2.8-fold reduced acquisition time in 20 lymphoma
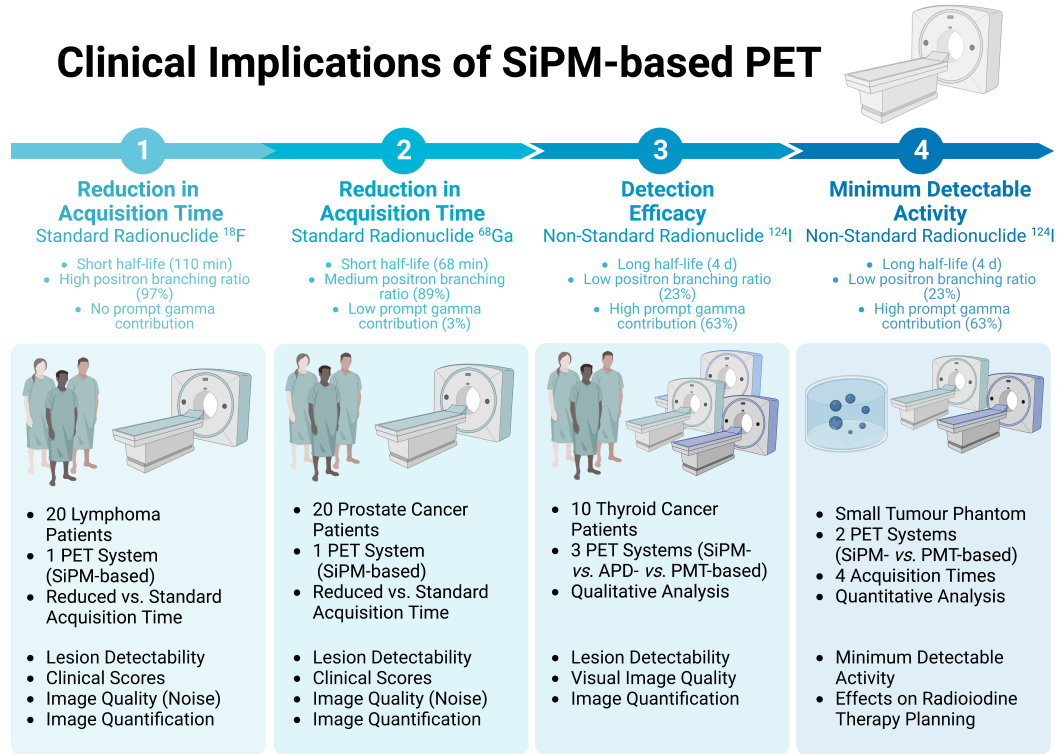
Figure 1: Synopsis of the thesis. In paper 1 [43] and paper 2 [44], a reduced clinical acquisition acquisition time in SiPM-based PET is investigated for the standard radionuclides ^{18}F and ^{68}Ga. In paper 3 [45], three PET systems that use detectors from different generations are compared in a clinical investigation for the non-standard radionuclide ^{124}I (APD: avalanche photodiode, PMT: photomultiplier tube). In paper 4 [46], the minimum detectable ^{124}I activity is determined for two PET systems and different acquisition times in a phantom study; moreover, implications on radioiodine therapy planning are investigated. Created with BioRender.com

patients and a 3.7-fold reduced acquisition time in 20 prostate cancer patients who underwent ^{18}F-FDG or ^{68}Ga-PSMA PET imaging, respectively, on a SiPM-based PET/CT system. These examinations were chosen as examples of typical PET imaging performed on clinical indication, using two PET tracers labelled with the standard radionuclides ^{18}F and ^{68}Ga. The two radionuclides show differences in their physical properties such as positron branching ratio, emission of prompt gamma quanta that possibly fall into the PET scanners' energy windows, and positron energy. These properties lead to different imaging characteristics, for example, regarding image quality and resolution. However, both radionuclides are well established for clinical PET imaging. In both publications, different reconstruction algorithms were compared. To evaluate the clinical impact of

a reduced acquisition time, region-based tumour lesion detectability, different standardised clinical scores, quantification accuracy, and image noise - as an indicator of image quality - were examined. As the short half-lives of ^{18}F and ^{68}Ga (109.77 min and 67.71 min, respectively) would bias results from subsequent PET imaging on different PET systems after single tracer administration, no direct comparison between PET scanners equipped with different detectors was performed.

The third publication compares lesion detectability and visual image quality in ^{124}I PET of 10 differentiated thyroid cancer patients across three PET/CT and PET/MR scanners equipped with different types of PET detectors. The physical half-life of ^{124}I is 4.2 d and its effective half-live was reported in a range of 59-116 h [47–50]. At a typical imaging time of 1 d after ^{124}I administration, steady state is expected and decay and biological metabolism do not substantially influence the comparability of images acquired subsequently within a short time interval. PET imaging of ^{124}I is challenging, as this non-standard radionuclide exhibits a low positron branching ratio and a high fraction of prompt gamma quanta. Moreover, typically low activities are administered. To optimise the clinical PET protocol, different acquisition times and image reconstruction algorithms were probed. The fourth publication quantifies the minimum detectable ^{124}I activity under challenging but clinically realistic imaging conditions in a phantom study, comparing a SiPM-based to a photomultiplier tube-based (PMT-based) PET/CT system. Moreover, the ^{124}I activity concentration is correlated with predicted response to high-activity ^{131}I radioiodine therapy to investigate the clinical impact of SiPM-based PET in challenging differentiated thyroid cancer patients regarding both diagnosis and therapy planning.

The closing chapter 4 contains the conclusion of the thesis and an outlook on possible future developments as well as clinical and scientific applications of SiPM-based PET imaging.

1 Fundamentals

In this chapter, the fundamentals of PET data acquisition and image reconstruction, the investigated PET tracers, and the examined tumour entities are discussed. The chapter starts with a description of the fundamentals of PET and of hybrid imaging in PET/CT or PET/MR techniques. Next, basic principles of PET detector technologies with an emphasis on the differences between devices from different generations are explained followed by a brief introduction into PET image reconstruction. Thereafter, the PET tracers ^{18}F-FDG, ^{68}Ga-PSMA, ^{124}I and differences between the respective radionuclides are discussed. Finally, lymphoma, prostate cancer, and differentiated thyroid cancer and the clinical indications for performing PET examinations in patients with these diseases are introduced.

1.1 Positron emission tomography (PET)

„*Molecular imaging*" comprises PET and other nuclear medicine imaging techniques which are applied for *in vivo* visualisation of cellular and sub-cellular biological processes. These are metabolic pathways and other physiological and pathological parameters including deposition of specific proteins (for example, amyloid [51]) or perfusion of specific organs (for example, the heart [52]). According to the tracer principle, for the establishment of which George de Hevesy was awarded the Nobel Prize in Chemistry in 1943, small amounts of radioactively labelled substances are (predominantly intravenously) applied to the patients [53]. The amount is, on the one hand, sufficient to visualise the respective (molecular) biological process, but, on the other hand, does not evoke biological effects [54]. Typically, molecular imaging tracers consist of a radionuclide that is bound to a molecule interacting with a target structure inside the human body (for example, cellular surface receptors) or is distributed without direct binding to a target (for example, perfusion tracers). In principal, the radionuclide is crucial for imaging, while the molecule bound to it targets a specific biomarker [55].

Typical molecular imaging techniques that are used in clinical routine are two-dimensional planar scintigraphy, three-dimensional single photon emission computed tomography (SPECT), and three-dimensional PET [56]. For both planar

scintigraphy and SPECT, γ-emitting radionuclides (predominantly ^{99m}Tc) are applied and detected by γ-cameras that use the set-up of an Anger camera for signal detection and processing [57]. For SPECT imaging, multiple γ-camera elements are combined to construct detector heads which are rotated around the patient body [58].

In contrast to planar scintigraphy and SPECT, PET imaging uses positron-emitting radionuclides [59]. The technique exploits the fact that positrons, after a short free mean path in biological tissue, collide with their antiparticles, electrons. Two annihilation photons with an energy of 511 keV are produced and emitted at an angle of about 180° [9]. In tomographic PET imaging, these strike opposite detector elements of multi-headed γ-camera systems (PET systems). For image generation, only coincidence events of two photons arriving within a small time window (coincidence time) at opposing elements of the detector ring are used. True coincidence events belong to an annihilation having occurred along the line-of-response between the two detector elements; in the image reconstruction process data from thousands of lines-of-response are processed to determine the exact place of the annihilation event [60]. Thus, the contribution of random detections (for example, belonging to natural background radiation) is reduced. This leads, in comparison to SPECT imaging, to lower image noise and higher image quality. Basic principles of PET signal generation and detection are shown in Figure 1.1. Details on PET detectors and signal processing are outlined in section 1.2.
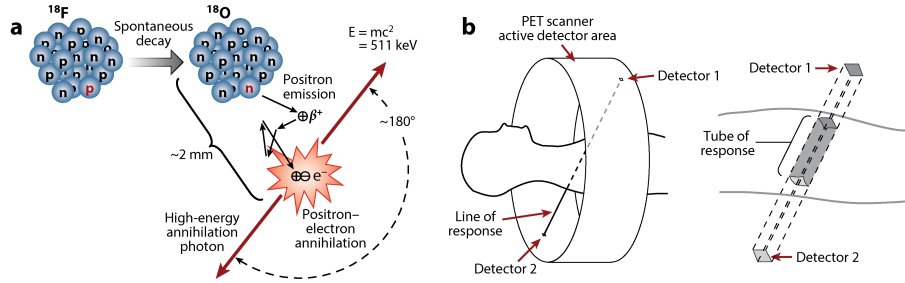
Figure 1.1: Basic principles of PET acquisition. (a) Annihilation event with emission of two 511-keV photons at an angle of about 180°. (b) Coincidence detection at two opposing detector elements of a PET detector ring. Figure reproduced from [61] with permission from Annual Reviews, Inc.

First clinical applications of positron-radiation-based imaging of brain tumours were published in December 1951 by the physicist Gordon L. Brownell and the neurologist William Sweet from Massachusetts General Hospital in Boston [62].

For these first approaches, coincidence recording was performed using two opposite detector plates [63]. First developments of positron-radiation-based imaging in tomography technique were described in the early 1970s [1]. These first tomographic systems already showed elements which are still used in today's PET systems like a set-up of combined detector elements in a multi-line and ring-shaped arrangement. First applications of the technique were presented in 1975 by the medical physicists and „fathers of PET imaging" Michel Ter-Pogossian and Michael E. Phelps [64]. Both scientists were also involved in the introduction of the first commercial PET system (ECAT I) at the *University of California Los Angeles* in 1976 [1].

Since then, PET imaging has more and more been integrated into clinical routine. In addition, the technique has benefited from many software and hardware improvements. These include, for example, improved detector technologies and reconstruction algorithms, which will be introduced in the following chapters, as well as the possibility of PET data acquisition in continuous-bed-motion mode. Using this technique, the patient is continuously moved through the detector ring, comparable to a helical CT scan. Compared to PET acquisition in conventional step-and-shoot mode, in which the patient is moved sequentially through the scanner and overlapping trans-axial images are acquired at fixed positions along the longitudinal axis, this leads to a more homogeneous effective axial sensitivity [65].

Today, the majority of clinical PET examinations is performed as part of diagnostic work-up of patients with oncological diseases [66]. These examinations are predominantly performed as whole-body imaging and allow the characterization and identification of primary tumours and metastases. Molecular target structures to interact with PET tracers are, for example, indicators of metabolic pathways like GLUT transporters (for imaging of glucose metabolism) or NIS (for imaging of iodine metabolism), of receptor status (like expression of SSTRs), or of surface antigen status (like expression of PSMA). GLUT transporters can be targeted by ^{18}F-FDG for imaging of various tumours [4], NIS by ^{124}I for imaging of differentiated thyroid cancer [67], SSTRs by ^{68}Ga-DOTATOC/DOTATATE for imaging of neuroendocrine tumors [68], and PSMA by ^{68}Ga-PSMA for imaging of prostate cancer [69]. Some of these target structures can also be used in theranostic oncological concepts: For example, ^{68}Ga-DOTATOC/DOTATATE, ^{68}Ga-PSMA, or ^{124}I PET imaging can be performed in preparation for radionuclide therapies which target the same structures but use α- or β$^-$- emitting radionuclides [70]. Another field of application is the precise determination of the target volume for

radiotherapy of tumour diseases [71].

Moreover, PET imaging can be performed on non-oncological clinical indications. Examples are imaging of inflammation [72] (typically whole-body examinations to identify an infectious focus), imaging of brain glucose consumption and cerebral amyloid deposits in dementia diagnostics [73], and examinations of cardiac inflammation [74] or myocardial viability [75] (partial-body examinations). In addition, a variety of other PET tracers are available for the investigation of different molecular targets, which are used in specific clinical or scientific investigations and are labelled with different radionuclides. Examples include tracers that bind to fibroblast activation protein (FAP) [76, 77], which is expressed in the tumour micro-environment of solid tumours, or radioactively labelled monoclonal antibodies that specifically bind to various target structures [78].

Examples for typical positron emitters that are used to label tracers for diagnostic PET imaging are ^{18}F, ^{68}Ga, ^{124}I, ^{11}C, ^{15}O, ^{13}N, ^{64}Cu, ^{89}Zr, or ^{86}Y [54]. These radionuclides show different characteristics, for example, regarding the probability of positron emission per decay or half-life. Details for the radionuclides ^{18}F, ^{68}Ga, and ^{124}I that are used in this thesis are given in section 1.4. In addition to diagnostic imaging, the clinical application of PET comprises the field of intra-therapeutic imaging in radionuclide therapy for visualisation of tracer bio-distribution, therapy monitoring, and quality control, if radionuclides like ^{90}Y which exhibit positron emission or internal photon pair production are used [79].

Positron emission tomography - Computed tomograpy

Today, clinical PET images are almost exclusively acquired in PET/CT or PET/MR hybrid imaging technique. Advantages are, on the one hand, benefits for clinical image interpretation, since CT or MR images allow exact anatomical localisation of abnormal structures and provide complementary morphological and structural information [80]. On the other hand, they are used for attenuation correction of the PET images. When passing through human tissue, the 511-keV annihilation photons experience an attenuation mainly evoked by Compton scattering and photoelectric effect. Their proportions depend on the photon energy but also on the tissue type [81]. By attenuation correction, PET image quality can be improved and accurate image quantification can be achieved.

To use CT data for attenuation correction, the attenuation coefficients for the 511-keV photons are determined from the polychromatic X-ray radiation of CT imaging. Typical methods use bilinear functions for the denomination of PET

attenuation maps (μ-maps) from CT data [82]. These use two different linear correlation coefficients for 2 ranges of Hounsfield units.

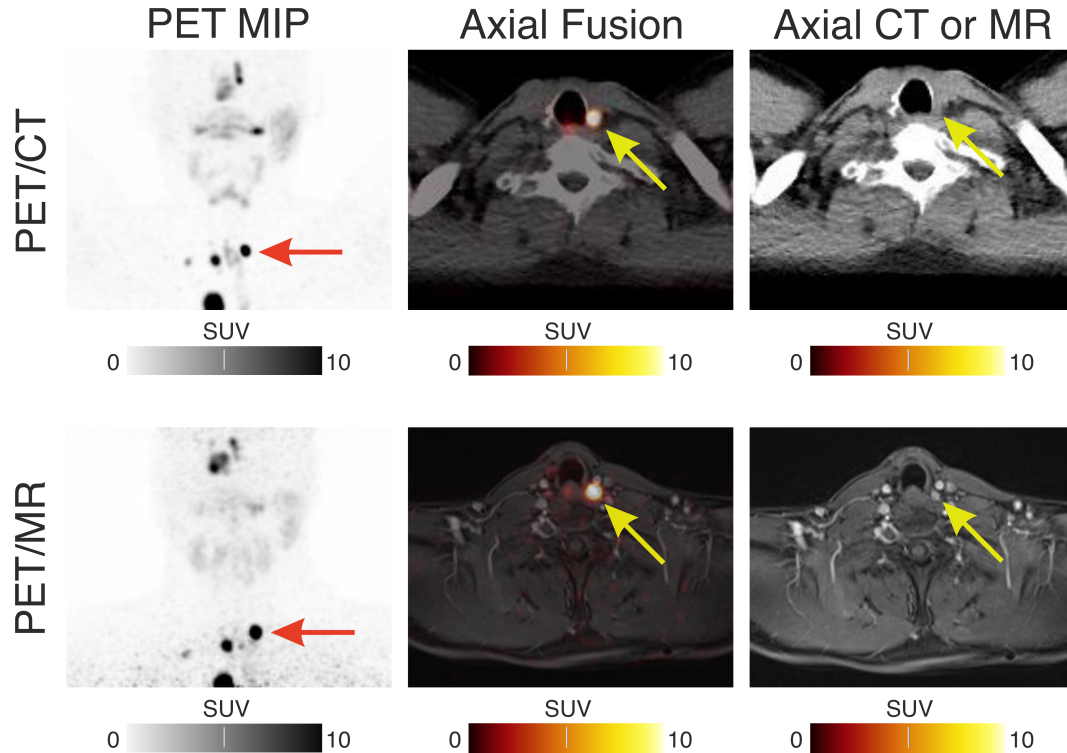The majority of clinical PET examinations is currently performed in PET/CT technique.

Figure 1.2: ^{124}I maximum intensity projection (MIP) PET images, axial fused PET/CT and PET/MR images as well as corresponding axial CT and MR images of a differentiated thyroid cancer patient showing a cervical lymph node metastasis with intense radioiodine uptake (arrows). The time interval between PET/CT and PET/MR was 5 h (image acquisition after single tracer administration). The MIP images show additional cervical lymph node metastases and pulmonary metastases.

Positron emission tomography - Magnetic resonance imaging

An alternative to PET/CT is hybrid imaging in PET/MR technique. On the one hand, PET/MR offers some advantages such as improved morphological assessment of soft tissue in MR images (which can improve lesion detectability) and reduces radiation exposure, as no CT scan is performed.

On the other hand, PET/MR is more expensive and requires more time compared to PET/CT. Moreover, attenuation correction of PET images is limited, as attenuation

coefficients cannot directly be measured by MR imaging [83]. Typically, like for the Biograph mMR PET/MR system used for the experiments in this thesis, segmentation-based approaches are applied [84]. In these techniques, MR data are used to assign each PET voxel a tissue type (for example, air, lung, fat tissue, or soft tissue). For each tissue type, a fixed attenuation coefficient is used [81]. This process is prone to inaccuracies, which can affect, for example, the quantification of the PET signal from bone lesions [85].

Because of its limitations and since it is only available in large centres, PET/MR imaging has gained clinical importance predominantly for specific indications like assessment of brain tumours [86]. Also for ^{124}I PET imaging of differentiated thyroid cancer patients, advantages for assessment of lesions in the neck region due to an improved soft tissue visualisation in MR images were described [87, 88]. Figure 1.2 shows image examples comparing ^{124}I PET/CT and PET/MR images of a differentiated thyroid cancer patient. The images indicate an improved morphological representation of soft issue in the MR images compared to the CT images which allows an exact delineation of a cervical lymph node metastasis and a volume estimate that can be used for dosimetry purposes.

1.2 PET detector technologies

PET systems are typically constructed of detector rings which contain multiple detector modules. Each module consists of detector blocks containing multiple scintillation crystals [1]. These are necessary to convert the 511-keV annihilation photons into short pulses of visible light (wavelength about 400 nm corresponding to a lower energy of about 3 eV), which can be sensed and processed by the downstream detection electronics [89]. Figure 1.3 A, B, and D show typical structures of PET detector elements, which consist of an array of multiple scintillation crystals that are coupled to a layer of photodetectors.

In current-generation PET systems, mainly lutetium orthosilicate (LSO)/lutetium-yttrium oxyorthosilicate (LYSO) or bismuth germanium oxide (BGO) scintillation crystals are used. These have favourable properties for PET imaging like a high stopping power (high material density), high light output, short decay time, high proportionality, and high energy resolution ($\frac{\Delta E}{E}$) [93]. Figure 1.3 C shows a photography of a scintillation crystal array.

Until the 2020s, for the detection of scintillation photons predominantly PMTs were used. However, these do not operate in the high magnetic fields of integrated PET/MR systems [94]. This led to the development of semiconductor-based detectors using avalanche photodiodes (APDs) or SiPMs. Since SiPMs exhibit improved properties compared to PMTs, in particular higher detector sensitivity and coincidence timing resolution, SiPMs have also found their way into current-generation PET/CT systems [30].

In the following, the detector types of the PET systems that are investigated in this thesis are introduced in more detail. All systems use LSO scintillation crystals which are coupled to PTMs (Biograph mCT PET/CT), APDs (Biograph mMR PET/MR), or SiPMs (Biograph Vision PET/CT). Large parts of the presentation of physical basics and history of PET detector technologies are described in reference to the review by Emilie Roncali and Simon R. Cherry [95], in which further details can be found.

1.2.1 Photomultiplier tubes

PMTs use photocathodes to generate electrons from incoming photons. The electrons are accelerated by several dynodes and, thus, exponentially multiplied. Finally, they reach the anode leading to detectable charge pulses. In block-detector
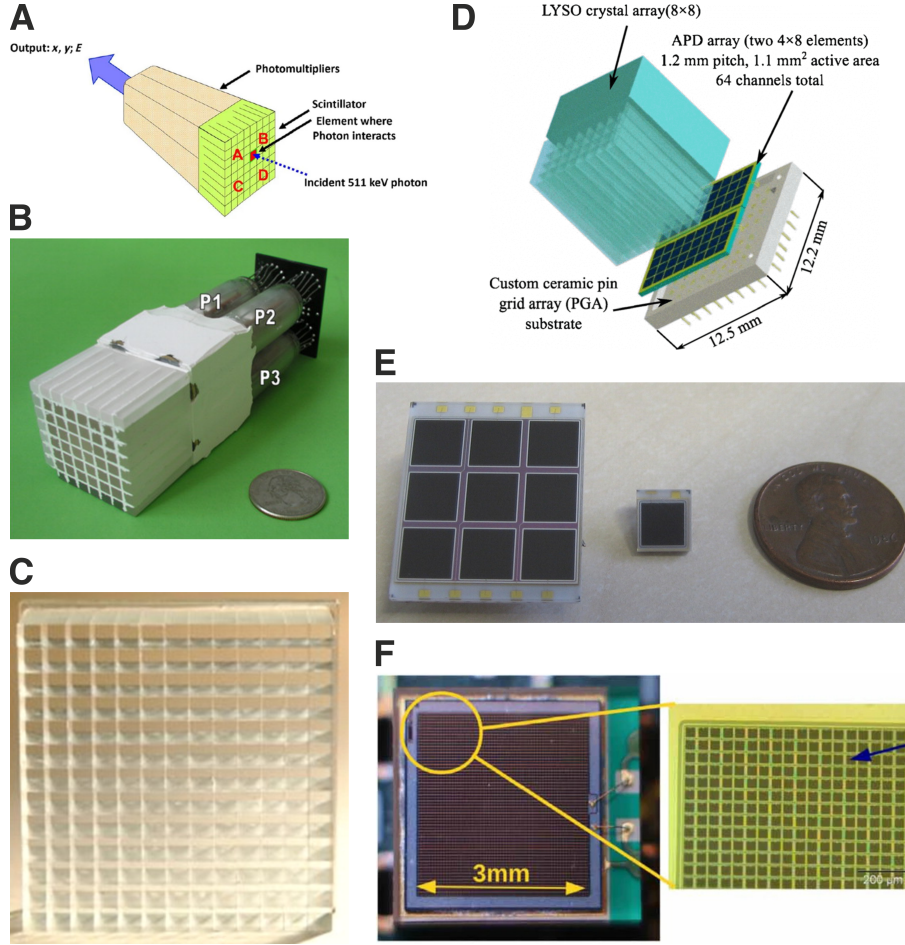
Figure 1.3: (A) Schematic representation and (B) image of a PMT-based PET block detector with 4 PMTs connected to the scintillator block. (C) LSO scintillation crystal array consisting of 13 x 13 crystals with an individual area of $4 \times 4\,\mathrm{mm}^2$. (D) Schematic representation of an APD-based PET block detector. (E) APD array consisting of 9 APDs, each with an active area of $5 \times 5\,\mathrm{mm}^2$. (F) SiPM with an active area of $3 \times 3\,\mathrm{mm}^2$ and magnification of single APD elements. A and F were reproduced from [90] under Creative Commons Attribution 4.0 International license (A: Image courtesy of D. Townsend). B, C, and E were originally published in *JNM* [91]. © (2008) SNMMI (E: Image courtesy of University of Tübingen). D was originally published in *IEEE Transactions on Nuclear Science* [92]. © (2014) IEEE.

designs, several rows of scintillation crystals (arrays) are connected to multiple PMTs [1] (a schematic representation and an image of a PMT are shown in Figure 1.3 A and B). The principle of signal readout to assign each charge pulse to a specific scintillator element is comparable to that of an Anger camera. In brief, an annihilation photon triggers a scintillation that generates specific amplitudes

in all PMTs connected to the respective crystal. These are used to discriminate the position of the initial scintillation event. PMTs exhibit a high signal gain (amplification by a factor of 10^6 to 10^7) and fast timing characteristics; main disadvantages include a limited quantum efficacy and the in-operability in strong magnetic fields [95].

1.2.2 Avalanche photodiodes

The development of PET/MR systems with the need for magnetic field-immune PET detectors led to the development of APDs (a schematic representation of an APD-based PET detector and a photography of an APD array are shown in Figure 1.3 D and E). APDs are photodiode detectors with p^+-i-p-n^+-doping that can be considered a semiconductor-based equivalent of a PMT. PET systems use silicon-based APDs that are operated in proportional mode slightly below their breakdown voltage. By application of the bias voltage, charges are generated in the i-zone (by absorbed scintillation photons) and drift into the multiplication zone, where the p-n^+ transition evokes a strong electric field. Consequently, they are accelerated and multiple additional electron-hole pairs are induced ("avalanche"). Thus, for a short time interval, the gain of the APD is strongly increased and a detectable electrical pulse is produced [95].

Compared to PMTs, APDs offer not only immunity against magnetic fields but also a higher quantum efficiency. However, disadvantages are lower gain (amplification by a factor of 10^2 to 10^3) and slow timing characteristics [60, 95]. Thus, they preclude PET imaging in TOF technique (see chapter 1.3 for details on TOF-based PET image reconstruction). Moreover, APDs are susceptible to changes in temperature and voltage, as their gain depends on these parameters, requiring complex regulation for stable operation with satisfactory signal-to-noise ratio [95]. APDs are applied in PET/MRI systems but, inter alia due to the mentioned limitations, have not been adopted to PET/CT systems, in which PMTs were continued to be used until SiPMs became available.

1.2.3 Silicon photomultipliers

SiPMs combine some of the advantages of PMTs and APDs like high gain, low operating voltage, and insensitivity to magnetic fields [95]. Moreover, they exhibit excellent timing characteristics which is beneficial for PET imaging in TOF

technique [26].

SiPMs consist of a two-dimensional array of APDs which are operated in Geiger mode slightly above their reverse breakdown voltage. They exhibit a p^+-n^+-junction with a thin depletion area leading to formation of a high electric field by application of a low bias voltage. This leads to acceleration of generated charges and induction of additional electron-hole-pairs (*avalanche*). Thus, every incoming photon causes a complete discharge of the micro-element. Figure 1.3 F shows a SiPM array with a magnification of the single Geiger-mode APD elements.

The high number of Geiger-mode APD microcells in every single SiPM makes the output signal become proportional to the number of incoming photons over a high dynamic range. For example, the Biograph Vision, which was applied for this thesis, uses SiPMs of an area of $3 \times 3\,\mathrm{mm}^2$. Assuming a typical microcell area of $50 \times 50\,\mathrm{\mu m}^2$ [96] and a typical fill factor of 0.8, each SiPM contains >3,000 microcells and a complete detector ring of 60,800 detector elements about 2×10^8 microcells. As the number of photons that are produced in the scintillation crystal is proportional to the energy of the annihilation photon, this energy can be resolved in the output signal [97]. After the Geiger discharge, the process is quenched, for example, via a quenching resistor, and recharged to reset the diode for detection of the next photon [60, 95].

1.3 Options in PET image reconstruction and post-processing

In addition to the hardware advances, also the software side of PET image reconstruction has been subject to continuous improvements. Initially, tomographic PET imaging employed direct inversion techniques, such as filtered back projection, to invert the Radon transform. Subsequently, the methodology evolved through Fourier rebinning towards the use of iterative methods, such as maximum-likelihood expectation maximisation [1]. Optimised versions of these algorithms are still implemented in today's PET systems. For example, the PET/CT and PET/MR scanners applied in this thesis use a three-dimensional ordinary Poisson ordered-subset expectation maximisation approach [30].

Continuous hardware improvements were the basis for implementing advanced features in the reconstruction algorithms to improve image noise, contrast recovery, and lesion detectability. Significant examples are TOF image reconstruction with narrow time kernels [26], point spread function (PSF) reconstruction to compensate for penetration effects in adjacent scintillator crystals [27, 98], or positron range correction to improve spatial resolution for radiotracers with high positron energy like ^{68}Ga or ^{124}I [28, 99]. In addition, PET imaging exhibits a higher image noise compared to MR or CT imaging. Therefore, smoothing filters are applied in image post-processing to reduce image noise and increase the signal-to-noise ratio; typically, Gaussian filters with a filter size (full width at half maximum) between 2 and 5 mm are used [100].

Time-of-flight-based PET imaging

TOF-based PET integrates the differential timing of two emitted annihilation photons detected on two opposite detector elements in the reconstruction process [61]. The timing difference can be translated into the distance from the middle of the line of response to the most probable point of annihilation. This information is considered in the iterative reconstruction algorithms to determine the point of annihilation more precisely [60]. The basic principle of TOF-based PET imaging is illustrated in Figure 1.4.

For high-quality TOF-based PET imaging, the coincidence timing resolution of the PET detectors is crucial. Therefore, this technique particularly benefits from SiPM-based detectors [90]. The major advantage of TOF-based PET is reduced

image noise, which results in a larger contrast-to-noise ratio for lesions [101, 102]. Hence, their detectability can be increased [103].

Both the SiPMs of the Biograph Vision and the PMTs of the Biograph mCT PET/CT allow TOF-based imaging, whereas the timing resolution of the APDs of the Biograph mMR PET/MR is not sufficient for this technique.
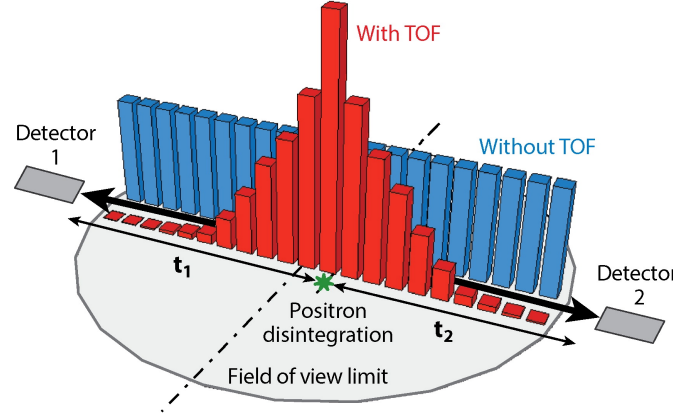

Figure 1.4: Principle of TOF-based PET. The time interval between the arrival of the 511-keV photons at two opposite detector elements on the detector ring is translated into the distance of the middle of the line-of-response to the most probable point of the annihilation event. This point is the center of the TOF-based probability density function (red), whereas for non-TOF PET imaging this function is uniform (blue). Figure reproduced from [61] with permission from Annual Reviews, Inc.

Point-spread-function modelling

The point spread function specifies how a point signal at each point of the PET scanner's field-of-view is processed. Several effects can interfere the imaging properties including positron range, photon non-colinearity, crystal distance, inter-crystal scattering, inter-crystal penetration, and depth-of-interaction effects [102, 104]. For points at the edge of the field-of-view, the probability is increased that annihilations photons pass scintillator crystals of the detector ring obliquely before being detected in neighbouring crystals (inter-crystal penetration and depth-of-interaction uncertainty) [104] (Figure 1.5 A). This leads to errors in the determination of the line-of-response reducing the PET resolution at the margins of the field of view (Figure 1.5 B). Image reconstruction with PSF-modelling option, which is implemented in current-generation PET systems, considers the scanner-specific PSF in the iterative reconstruction algorithms. The PSF can be determined in simulations, in analytical calculations, or experimentally using

17

positron-emitting point sources [105]. The integration of the effective PSF into the system matrix leads to an improved assignment of the lines-of-response to their true geometrical position (*sinogram deblurring*) [5]. The PSF-based reconstruction (also termed *resolution recovery*) can both improve and homogenise the PET resolution (particularly, at the edges of the field-of-view) [106]. Moreover, image noise can be reduced and the contrast-to-noise ratio can be increased [102].
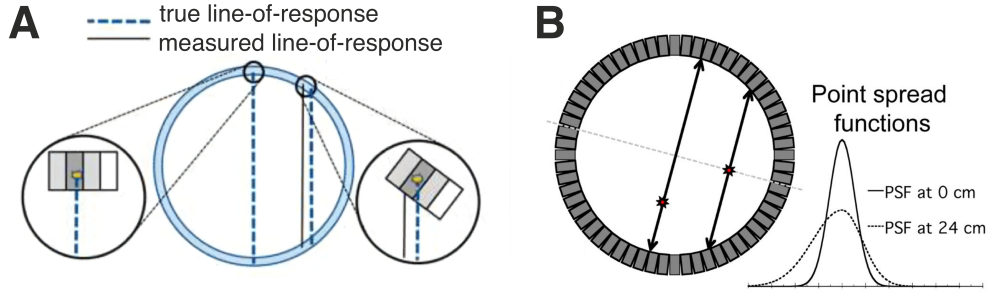

Figure 1.5: Principles of resolution degradation. (A) Representation of inter-crystal penetrations and depth of-interaction uncertainty leading to errors in the determination of the line-of-response. (B) At the edges of the field-of-view, inter-crystal penetration, depth-of-interaction, and other effects lead to a broad and asymmetric PSF which can be considered in PSF-based reconstruction algorithms. The left image in (B) additionally shows TOF effects. A (modified) was originally published in *IEEE Nuclear Science Symposium and Medical Imaging Conference (NSS/MIC)* [102]. © (2014) IEEE. B (modified) was originally published in *JNM* [103]. © (2009) SNMMI.

PSF-based PET image reconstruction can increase the detectability of small lesions [103]. However, in PSF-reconstructed images the accuracy of quantification can be limited for small lesions, as their signals can be artificially elevated [107]. A reason for this effect are Gibbs artefacts [108], which arise from overshoots at sharp intensity transitions (corresponding to edges of lesions) in the Fourier transformations performed in the reconstruction process [109, 110]. They can evoke overestimations in the radial activity profile at the edges of small lesions, interfering the quantification accuracy. Image examples of Gibbs artefacts are shown in Figure 1.6.

Prompt gamma coincidence correction

For radionuclides with a significant contribution of prompt gammas like ^{124}I or, to a lesser extent, ^{68}Ga, a prompt gamma coincidence correction is implemented in the PET scanner's reconstruction algorithms [112]. In this context, prompt
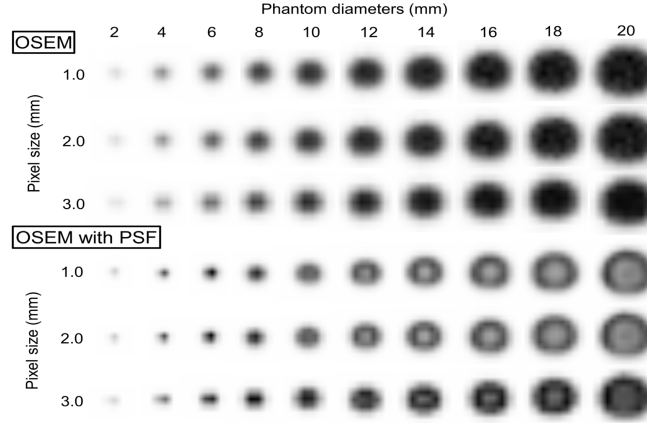
Figure 1.6: Comparison of phantom PET images that are reconstructed using OSEM without (upper row) or with PSF modelling option (lower row). The images show circular lesions of different diameters that are reconstructed using different pixel sizes. Only the PSF-reconstructed images show Gibbs artefacts, which are more prominent for larger spheres and smaller pixel sizes. The figure was reproduced from [111] under Creative Commons Attribution 3.0 International license.

gammas refer to gamma quanta that are emitted with the positrons and can, after scattering, fall into the coincidence time window of the PET detectors, thus, producing *spurious* coincidence events (*prompt gamma coincidence events*, exemplary illustration in Figure 1.7 A) [113]. As these can impair image quality and quantification accuracy, a prompt gamma coincidence correction is required for high quality PET imaging [5].

The prompt gamma coincidence correction approach which is applied in the reconstruction algorithms of the PET scanners in this thesis corrects the prompt gamma background in the PET sinograms (PET raw data). The prompt gamma coincidences evoke a flat elevation of the sinograms [5] which can be estimated at their radial edges (tails). The tails correspond to areas outside of an object where no activity source is present but the prompt gamma contribution can be evaluated [5, 114]. Figure 1.7 B shows exemplary sinogram profiles for different radionuclides indicating the background elevation for ^{124}I. In typically applied approaches, the prompt gamma background is estimated by polynomial fitting to the tails of the sinograms and substracted before iterative image reconstruction [5, 112]. In this process, correction for prompt gammas is separated from scatter correction which is also performed by tail-fitting and can, therefore, be impaired by prompt gamma coincidences [5]. Figure 1.7 C shows exemplary PET sinograms for ^{124}I and the

improved tail-fitting by a combination of scatter and prompt gamma coincidence correction.
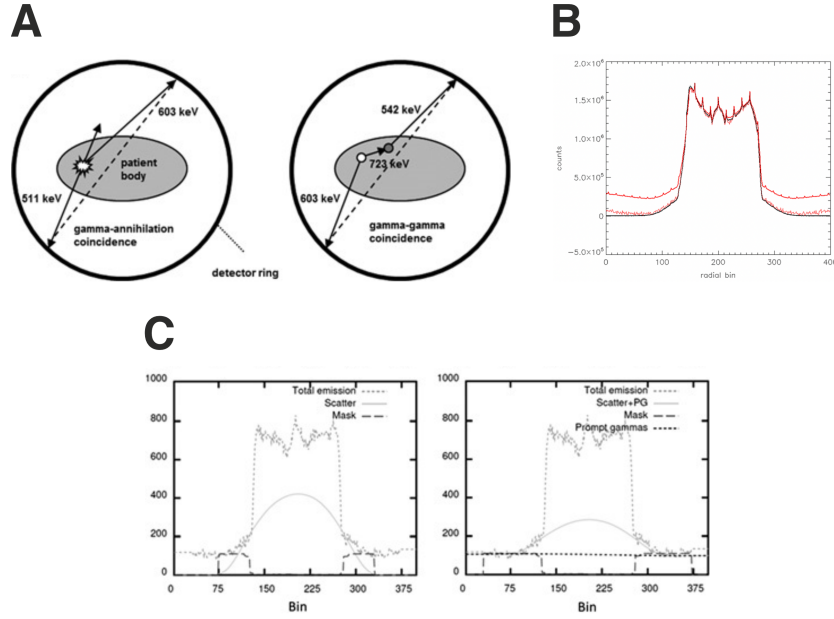
Figure 1.7: Prompt gamma coincidence effect and its correction. (A) Exemplary illustration of prompt gamma coincidence events for ^{124}I. Left: coincidence of a 511-keV photon with a prompt gamma photon, right: coincidence of two (scattered) prompt gamma photons. (B) Exemplary radial sinogram profiles for ^{124}I (thick red line), ^{90}Y (thin red line), ^{68}Ga (thick black line), and ^{18}F (black dotted line). (C) Exemplary ^{124}I sinogram profiles and improved tail-fitting by scatter + prompt gamma coincidence correction (right) compared to scatter correction (left). A and C were originally published in *Nuclear Medicine Communications* [112]. © (2018) Wolters Kluwer Health, Inc. B was reproduced from [114] under Creative Commons Attribution 4.0 International license.

1.4 PET tracer

Three different PET tracers (^{18}F-FDG, ^{68}Ga-PSMA, and ^{124}I) were investigated in this thesis. They differ both in their target structures and in the radionuclides used for PET imaging. The different radionuclides exhibit, inter alia, different half-lives, positron branching ratios, and proportions of potential prompt gammas quanta. Figure 1.8 shows simplified decay schemes for ^{18}F, ^{68}Ga, and ^{124}I. Further details are presented in the following subsections.
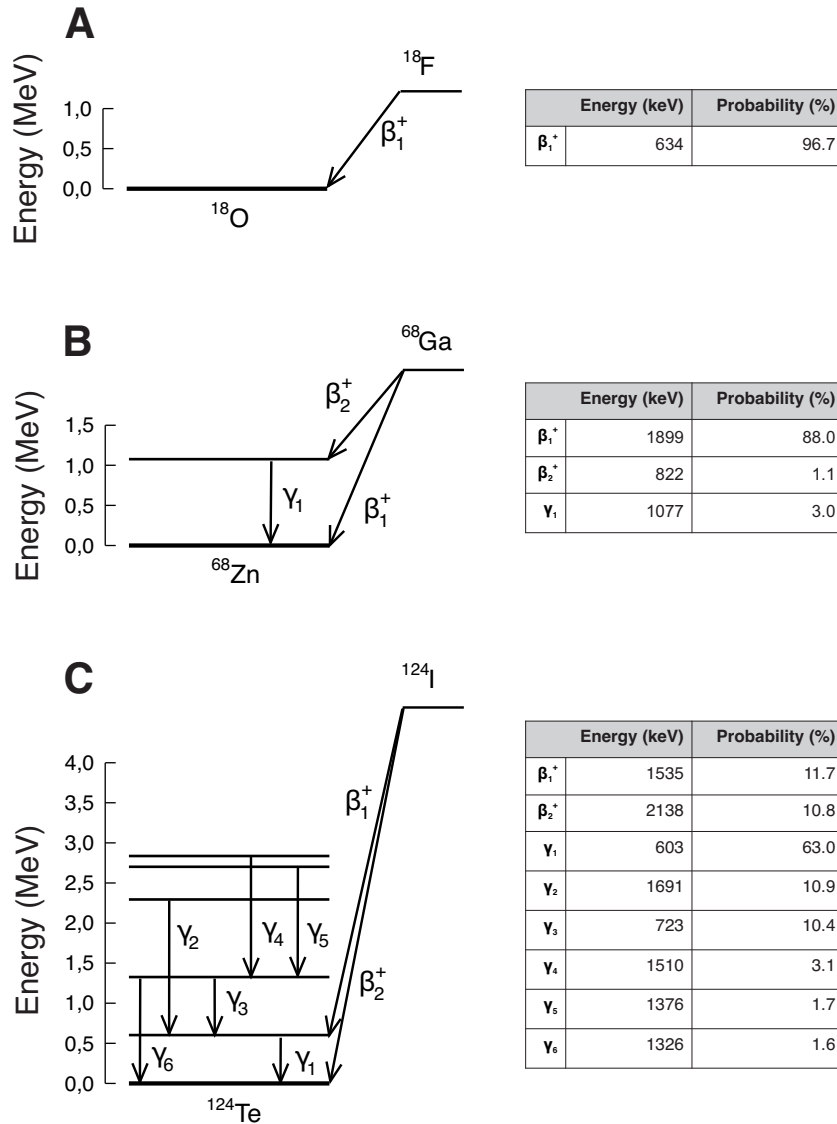

Figure 1.8: Simplified decay schemes of (A) ^{18}F, (B) ^{68}Ga, and (C) ^{124}I indicating decay types with a probability of >1% in accordance to [5]. The tables show maximum positron energies.

1.4.1 ^{18}F-FDG

^{18}F-FDG is the PET tracer that is most frequently applied in clinical routine [115]. It visualises cellular glucose uptake and is used to identify pathologies that exhibit increased glucose metabolism. In detail, the radioactively labelled glucose analogue ^{18}F-FDG is intravenously administered and intracellularly accumulated after cellular uptake via GLUT transporters and phosphorylation by hexokinase [54]. On the one hand, the majority of ^{18}F-FDG PET examinations in clinical routine are performed for tumour detection and whole-body staging in oncological patients [66]. For many tumour entities, cancer cells show an increased rate of glycolysis and can, therefore, be visualised by this imaging modality.

On the other hand, ^{18}F-FDG PET imaging can also be applied to other, non-malignant diseases like various types of inflammation [116] which also exhibit increased glucose metabolism. Inflammation ^{18}F-FDG PET imaging includes whole-body examinations to find the focus of an infection [117] but also partial-body examinations, for example, of the heart for diagnosis of endo-, myo-, or pericarditis [118,119]. Cardiac ^{18}F-FDG PET is not limited to imaging of inflammatory diseases but can also, after special patient preparation, be applied to assess myocardial viability [75]. Another partial-body examination using ^{18}F-FDG is cerebral PET for diagnosing Alzheimer's disease [73] or Parkinsonism [120], as these and other neurodegenerative disorders show characteristic cerebral uptake patterns.

The radionuclide ^{18}F has a half-life of 109.77 min. It exhibits some properties which are particularly favourable for high-quality PET imaging like a high positron branching ratio of 96.7 % and no relevant emission of potential prompt gammas (Figure 1.8 A). Moreover, the low maximum positron energy of 634 keV leads to a higher resolution compared to other radionuclides like ^{68}Ga [121].

A typical clinical indication for performing an ^{18}F-FDG PET is interim staging during and final staging after chemotherapy in lymphoma patients [122]. For example, detection of vital tumour burden in interim staging can lead to an intensification of chemotherapy in these patients. In this work, clinical ^{18}F-FDG PET images of lymphoma patients acquired on a SiPM-based Biograph Vision PET/CT system were analysed. Figure 1.9 A shows an exemplary ^{18}F-FDG PET image of a lymphoma patient.

1.4.2 ^{68}Ga-PSMA

PSMA PET is a clinically well established technique for specific imaging of prostate cancer. It uses radiotracers, mostly urea-based small-molecule inhibitors that bind to PSMA which is typically expressed by prostate cancer cells [123]. One of these tracers is ^{68}Ga-PSMA-11 [124] which was approved the FDA in 2020 for primary staging and re-staging of prostate cancer patients.

In addition, PSMA ligands can be used for radionuclide therapy in a theranostic approach. Typical therapeutic PSMA ligands, for example, ^{177}Lu-PSMA-617, are labelled with the β$^-$-emitter ^{177}Lu. Pre-therapeutic PSMA PET imaging is performed to validate sufficient PSMA expression for successful therapy [125]. The positive results of the phase III VISION trial [19], which demonstrated improved overall and progression-free survival for PSMA radionuclide therapy with ^{177}Lu-PSMA-617 in advanced metastatic prostate cancer under randomised controlled conditions, will probably lead to an increased demand for PSMA radionuclide therapy as well an increased interest in PSMA PET imaging. To meet the increasing demand for examinations many centres started to use ^{18}F-labelled PSMA PET tracers, which allow a higher examination volume due to improved production logistics [126]. However, ^{68}Ga-PSMA PET still offers clinical advantages and continues to be used as a complement. For example, ^{18}F-PSMA can show non-specific bone uptake [127], which can be problematic if it cannot clearly be distinguished from bone metastases.

The half-life of ^{68}Ga is 67.71 min. The radionuclide has a positron branching ratio of 89.1 % and maximum positron energies of 1899 keV (probability per decay: 88.0 %) and 822 keV (1.1 %), respectively. Compared to ^{18}F, this evokes a longer positron range in biological tissue and, therefore, a lower PET resolution [128]. ^{68}Ga emits gammas with a maximum energy of 1077 keV (3.0 %) which can potentially interfere as prompt gamma coincidences with true coincidence events after Compton scattering. Of note, the narrow energy windows of current-generation PET systems (for example, 435-585 keV for the Biograph Vision, 435-650 keV for the Biograph mCT, and 430-610 keV for the Biograph mMR) reduce the contribution of the prompt gamma effect, as their upper limit is below the maximum energy of the prompt gamma quanta. A simplified decay scheme for ^{68}Ga is given in Figure 1.8 B.

Typical clinical indications for whole-body PSMA PET include primary staging of high-risk prostate cancer patients or re-staging in biochemical recurrence (rising

tumour marker prostate-specific antigen, PSA) [129]. In primary staging, PSMA PET outperforms conventional CT and bone scan imaging in accuracy for identification of pelvic lymph node and distant (bone) metastases [130]. In biochemical recurrence, it likewise shows a high detection rate and high positive predictive value [131]. In this work, ^{68}Ga-PSMA-11 PET images of prostate cancer patients that were acquired on a SiPM-based Biograph Vision PET system were evaluated. Figure 1.9 B shows an exemplary ^{68}Ga-PSMA PET image of a prostate cancer patient.

1.4.3 ^{124}I

Radioiodine imaging and therapy in differentiated thyroid cancer patients exploit that thyrocytes and differentiated thyroid cancer cells express NIS. Therefore, they internalise radioiodide and accumulate it intracellularly [22, 132, 133]. Different iodine isotopes are regularly used in current clinical practice. For therapy, ^{131}I is applied, which emits high-energy β⁻-particles to induce apoptosis and necrosis in the target tissue [134]. Moreover, the β⁻-decay of ^{131}I includes emission of discrete γ-quanta enabling imaging in planar scintigraphy and SPECT techniques [135]. Therefore, ^{131}I can be considered an example of a classical theranostic agent [136]. Alternatives for radioiodine imaging are ^{123}I (planar scintigraphy and SPECT technique) and ^{124}I (PET technique), which exhibit improved imaging properties [137, 138] and can be combined with ^{131}I to form a *theranostic pair* [139]. In detail, ^{124}I PET imaging can be used for pre-therapeutic dosimetry of lesions and organs-at-risk which allows to determine the optimal amount of ^{131}I activity to be administered in an individualised theranostic concept [140]. Moreover, patients with insufficient radioiodine uptake, who would not benefit from radioiodine therapy, can be identified [141]. In contrast to ^{18}F-FDG and ^{68}Ga-PSMA, ^{124}I does not require binding to a ligand but directly interacts with its target structure.

^{124}I has a half-life of 4.2 d and a low positron branching ratio of 22.5 %. The maximum positron energies of 1535 keV (11.7 %) and 2138 keV (10.8 %) are in the same range like ^{68}Ga leading to a comparable positron range and PET resolution. ^{124}I emits a large fraction of gamma quanta of which particularly those with the lowest energies of 603 keV and 723 keV (probability per decay of 63.0 % and 10.4 %, respectively) can interfere as prompt gamma coincidences. As the fraction of gamma quanta is higher than for ^{68}Ga and their energies are closer to the energy windows of typical PET scanners, the prompt gamma coincidence effect is more

prominent for ^{124}I. Thus, in comparison to ^{18}F and ^{68}Ga, ^{124}I exhibits the most challenging properties for PET imaging. A simplified decay scheme for ^{124}I is given in Figure 1.8 C.

Typical clinical situations in which ^{124}I PET whole-body imaging is performed in differentiated thyroid cancer patients are (1) staging between primary surgery and first radioiodine therapy, (2) baseline/follow-up re-staging 6-18 months after first radioiodine therapy, or (3) re-staging, if recurrence or disease progression is suspected [142]. In these situations, ^{124}I PET allows risk stratification by identifying local lesions and distant metastases. In this work, clinical ^{124}I PET/CT and PET/MR scans of differentiated thyroid cancer patients acquired on different PET scanners were evaluated. Figure 1.9 C shows an exemplary ^{124}I PET image of a differentiated thyroid cancer patient. Moreover, a small tumour phantom (containing small ^{124}I-filled spheres at defined activity concentrations, lesion sizes, and signal-to-background ratio) was investigated.
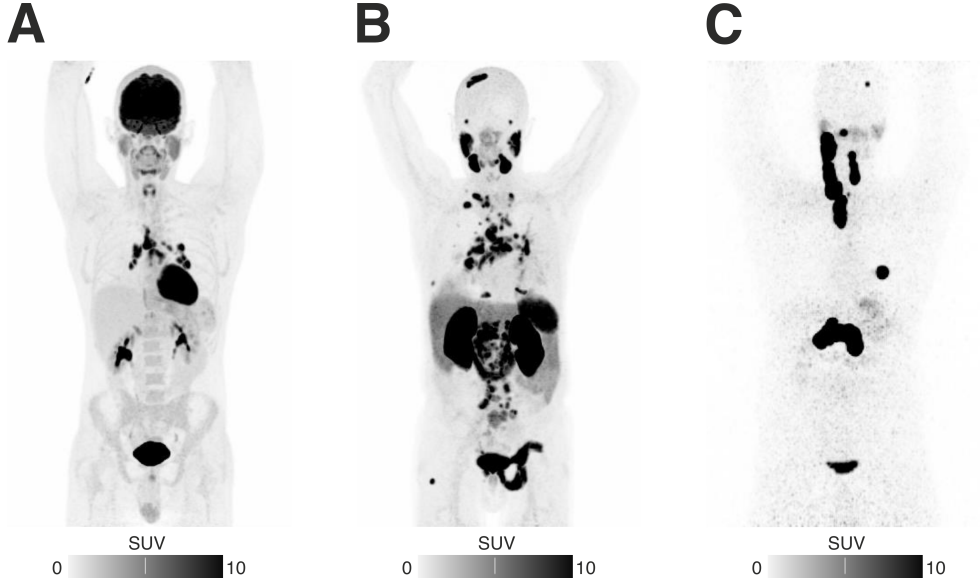
Figure 1.9: Maximum-intensity-projection images of (A) an ^{18}F-FDG PET of a lymphoma patient showing mediastinal and pulmonary manifestations, (B) a ^{68}Ga-PSMA PET of a prostate cancer patient showing local recurrence, regional, abdominal and thoracic lymph node metastases, disseminated bone metastases, and pulmonary metastases, (C) an ^{124}I PET of a differentiated thyroid cancer patient showing cervical, paratracheal, and mediastinal lymph node metastases as well as bone metastases.

1.5 Investigated types of malignancies

In this thesis, ^{18}F-FDG PET images of lymphoma patients, ^{68}Ga-PSMA PET images of prostate cancer patients, and [124]I PET images of differentiated thyroid cancer patients were investigated. In the following, these tumour entities will be introduced in detail with a special emphasis on clinical indications for PET imaging.

1.5.1 Lymphoma

Lymphomas are malignant tumours of the lymphatic system which are subdivided into two major groups, Hodgkin's lymphomas and non-Hodgkin's lymphomas. Hodgkin's lymphomas show a double-peaked age distribution (15-34 years and older than 55 years) [143]. Diagnosis is histopathologically confirmed by lymph node biopsy [144]. In Hodgkin's lymphoma patients, ^{18}F-FDG PET is a necessary part of diagnostic work-up for primary staging. If skeletal system and bone marrow do not show PET-positive foci, bone marrow aspiration is not mandatory as the negative predictive value of PET is 99% [145]. PET-positive foci which are stage-determining and, thus, relevant for selection of therapy regimens should undergo biopsy. The risk stratification of Hodgkin's lymphoma is based on the Ann-Arbor classification, with the distinction into limited (affecting one side of the diaphragm) and advanced disease (spread to both sides of the diaphragm) being the most important criterion [11]. Patients with low risk of recurrence are treated with short chemotherapy protocols in combination with radiotherapy, patients with high risk of recurrence with intensive chemotherapy. In addition to primary staging, ^{18}F-FDG PET is important in interim staging after 2 cycles of chemotherapy to decide on an intensification of the applied chemotherapy protocol [144]. In final staging, ^{18}F-FDG PET can be used to decide, if a consolidation radiotherapy of residual findings is necessary [144]. Nowadays, more than 80% of all patients can be cured by stage-adapted therapy [144].

In contrast to Hodgkin's lymphoma, the group of non-Hodgkin's lymphomas is not uniform and contains more than 50 sub-groups [146]. Low-malignant, indolent lymphomas show slow progression and respond well to therapies, although they cannot be cured [147]. Highly malignant, aggressive lymphomas (for example, diffuse large cell and Burkitt lymphomas) progress rapidly if left untreated, but can often be cured with intense treatment protocols. In aggressive lymphomas,

clinical indications for PET imaging are comparable to Hodgkin's lymphomas [148]. ^{18}F-FDG PET is likewise a standard diagnostic procedure in primary staging to determine nodal, extranodal, and bone marrow involvement as well as in re-staging to evaluate therapy response, monitor the course of disease, and decide for intensification of treatment [148].

1.5.2 Prostate cancer

Prostate cancer affects the glandular tissue of the prostate. It is the second most frequent cancer diagnosis in men and worldwide the fifth leading cause of death [149]. Screening can be performed by digital-rectal examination and transrectal sonography [150]. Standard diagnostic procedures are transrectal ultrasound guided or transperineal biopsy [151]. According to current guidelines, whole-body primary staging is performed by thoracoabdominal and pelvic CT as well as scintigraphic bone scan [152, 153]. In high-risk patients, these examinations can be replaced by PSMA PET which exhibits a higher accuracy for detection of lymph node and distant metastases [130].

For grading of prostate cancer patients the Gleason score is used which is derived from histological evaluation of tumour tissue samples retrieved from punch biopsy [154]. The grade of de-differentiation of the most de-differentiated and the most frequently occurring tumour type is evaluated on a scale from 1 to 5 and these numbers are added (leading to a Gleason score range from 2 to 10). If surgery has already been performed, the most frequent and the second most frequent Gleason grade in the entire prostate are added. Gleason score and TNM classification are important prognostic factors [155] and used to decide for further therapy. In locally limited disease and good patient constitution, radical (complete) prostatectomy is performed. Radiotherapy is used as consolidation therapy after surgery and in local recurrent and metastasised tumours [153].

After primary treatment, in metastasised tumours androgen deprivation therapy using gonadotropin-releasing hormone agonists or antiandrogen receptor antagonists is performed [156]. It is based on the typical dependence of prostate carcinoma cells on testosterone supply. Further patient follow-up is based on monitoring of serum levels of prostate-specific antigen (PSA). In case of rising PSA levels, PSMA PET can be performed to localise metastases [131].

In tumour recurrence and treatment failure of androgen deprivation therapy (castration-resistant prostate cancer), chemotherapy can be performed. Accord-

ing to current recommendations, the most promising chemotherapy regimen is a combination of cabazitaxel with one of the antiandrogens abiraterone or enzalutamide [153]. An alternative in metastasised castration-resistant prostate cancer is ^{177}Lu-PSMA therapy which shows benefits on both progression-free survival and overall survival [19] as well as, compared to chemotherapy, a more favourable safety profile [157]. Typically, PSMA PET is performed to verify sufficient PSMA uptake prior to ^{177}Lu-PSMA therapy.

1.5.3 Differentiated thyroid cancer

Thyroid cancer is the most common tumour of endocrine organs [158]. The incidence of thyroid cancer is about 10/100,000 with an average age at diagnosis of about 50-55 years [159]. Thyroid cancer is divided into different subgroups. Papillary thyroid cancers (60-80% of thyroid carcinomas) metastasise predominantly lymphogenically with a mortality of 0.5/100,000. Follicular thyroid cancers (10-30%) metastasise predominantly hematogenously leading to a higher rate of distant metastases and show a slightly less favourable prognosis [160]. Whereas papillary and follicular subtypes are classified as differentiated thyroid cancers, anaplastic thyroid cancers show an undifferentiated aggressive growth pattern and medullary thyroid cancers originate from parafollicular cells (C cells) [161]. The two latter ones do not express NIS and, therefore, are not susceptible to radioiodine imaging or therapy.

Ethological factors in the development of differentiated thyroid cancer are iodine deficiency and radiation exposure (for example, in patients who underwent radiotherapy for treatments of tumours when they were adolescents) [162]. Diagnostic work-up of suspected thyroid cancer includes cervical sonography, thyroid scintigraphy, and fine needle aspiration. The gold standard of therapy is thyroidectomy accompanied by cervical lymph node dissection [160]. Post-surgical radioiodine therapy is performed to remove residual thyroid and tumour tissue (ablation therapy). It is recommended in all differentiated thyroid cancers except for uni-focal papillary microcarcinomas without additional risk factors [133]. If one cycle of primary radioiodine therapy is not sufficient for complete ablation, a multi-stage approach with possibly higher applied activities can be performed. The therapeutic activity can be determined either through conventional, standardised protocols or through personalised ^{124}I PET-based dosimetry [133].

Follow-up monitoring is typically performed using the serum tumour marker thyroglobulin and neck ultrasound. In case of suspected recurrence, radioiodine

imaging, for example, [124]I PET, is performed. If iodine-avid local recurrence or metastases are detected, radioiodine therapy can be performed [22, 132, 133]. An alternative is surgical resection. In advanced radioiodine refractory stages (inoperable or metastatic), tyrosine kinase inhibitors (like lenvatinib or sorafenib) can be applied [163, 164]. An alternative in limited forms can be re-differentiation therapy to restore radiodione uptake and enable radioiodine therapy [165].

2 Experimental techniques

In this chapter, the experimental techniques that were applied in this thesis are presented. The chapter starts with a characterisation of the PET/CT and PET/MR scanners that were used. Next, the patient cohorts, the investigated small tumour phantom, and the acquisition protocols for ^{18}F-FDG, ^{68}Ga-PSMA, and ^{124}I PET are described. Finally, the image interpretation metrics are described, including those for patient images (such as visual lesion detectability, standardised PET image reporting metrics, lesion quantification, and image quality/noise) and those for phantom images (such as visual detectability in a human observer study, signal-to-noise ratio, minimum detectable activity, and the projection of phantom ^{124}I activity concentrations onto predicted lesion response in clinical radioiodine therapy).

2.1 PET scanners

To analyse the influence and advantages of SiPM-based PET detectors on clinical PET imaging, the PET data that were evaluated in this thesis were acquired on three different PET scanners: A Biograph Vision 600 PET/CT system, a Biograph mCT PET/CT system, and a Biograph mMR PET/MR system (all Siemens Healthineers, Erlangen, Germany). In brief, all scanners use LSO crystals that are coupled to SiPMs on the Vision, PMTs on the mCT, and APDs on the mMR. More detailed specifications are presented in Table 2.1.

Table 2.1: PET scanner specifications. LSO: Lutetium oxyorthosilicate. SiPM: Silicon photomultiplier. PMT: Photomultiplier tube. APD: Avalanche photodiode.

PET scanner	Vision	mCT	mMR
Detector material	LSO	LSO	LSO
Detector element dimension (mm^3)	3.2x3.2x20	4.0x4.0x20	4.0x4.0x20
Detector elements per block	16x16	13x13	8x8
Total number of detector elements	60,800	33,448	28,672
Signal readout	SiPM	PMT	APD
Axial FOV (cm)	26.3	21.8	25.8
Transaxial FOV (cm)	78	70	60
Plane spacing (mm)	1.65	2.00	2.00
Image planes	119	109	127
Coincidence time window (ns)	4.7	4.1	5.9
Energy window (keV)	435-585	435-650	430-610
Energy resolution (%)	9	11	14
System time resolution (ps)	210	540	-
NEMA sensitivity (kcps MBq^{-1})	16.4	9.7	15.0

Paper 1 [43] and paper 2 [44] analyse the influences of a reduced acquisition time on lesion detectability and quantification in clinical SiPM-based PET imaging for the standard radionuclides ^{18}F and [68]Ga. Therefore, in these papers only PET data acquired on the Biograph Vision are evaluated. In paper 3 [45], clinical PET scans using the non-standard radionuclide [124]I are compared across all three three PET scanners. In Paper 4 [46], for a quantitative evaluation the minimum detectable activity for small [124]I-filled spheres is compared between the SiPM-based Biograph Vision and the PMT-based Biograph mCT in a phantom study, and effects on radioiodine therapy planning are analysed.

2.2 Patient cohorts, PET data acquisition and image reconstruction

To evaluate the influences of SiPM-based PET/CT under realistic clinical conditions, for all patient investigations in this thesis the included patients were selected from routine practice. Typical clinical PET image acquisition and reconstruction protocols are defined in published guidelines of different nuclear medicine societies, most importantly, Deutsche Gesellschaft für Nuklearmedizin (DGN), European Association of Nuclear Medicine (EANM), and Society of Nuclear Medicine and Molecular Imaging (SNMMI). The PET data in this work were acquired in accordance with these guidelines. For all PET/CT scans, in addition to the PET data, full diagnostic or low-dose CT data were acquired and used for anatomic correlation, morphological evaluation of lesions, and attenuation correction. In the evaluation of ^{124}I PET/MR scans, MR data were used instead of CT data. Moreover, all PET data were corrected for scatter, randoms, dead time, decay, normalisation, and prompt gamma coincidence effects (for the prompt gamma-emitting radionuclides ^{68}Ga and ^{124}I [112, 166]).

2.2.1 ^{18}F-FDG PET and ^{68}Ga-PSMA PET

To investigate the influences of a reduced acquisition time on SiPM-based PET/CT using the standard radionuclides ^{18}F-FDG and ^{68}Ga-PSMA, 20 lymphoma patients (including Hodgkin lymphoma, Non-Hodgkin lymphoma, and suspected lymphoma) and 20 prostate cancer patients in primary staging and re-staging were randomly selected.

Reference whole-body PET/CT data resembling the clinical standard were acquired in accordance with the current EANM procedure guidelines for ^{18}F-FDG [4] and ^{68}Ga-PSMA [167] PET/CT imaging in tumour patients. The recommended PET acquisition times can be realised by fixed acquisition times per bed position in step-and-shoot mode or by continuous movement of the patient through the PET detector ring at a defined velocity in continuous-bed-motion mode. In our clinical routine acquisition protocols for the Biograph Vision, continuous-bed-motion mode is used. Moreover, regions with a high probability of tumour involvement (abdomen in ^{18}F-FDG and pelvis in ^{68}Ga-PSMA PET) are emphasised by prolonged PET acquisition which is realised by a selectively reduced continuous-bed-motion

table speed. Reduced-acquisition time whole-body PET data were acquired at continuous-bed-motion table speeds that were increased by a factor of 2.8 for ^{18}F-FDG and 3.7 for ^{68}Ga-PSMA. The choice for these factors was motivated by previously published data that suggest a threefold reduction in acquisition time to maintain accurate lesion quantification [168].

All images were reconstructed using OSEM-TOF or OSEM-TOF+PSF image reconstruction, each with 2 iterations (5 subsets) or 4 iterations (5 subsets); for all reconstructions, a 4-mm Gaussian filter was applied. Thus, for each radionuclide 4 different image reconstruction settings were compared. A more detailed description of patient cohorts, PET acquisition and image reconstruction protocols can be found in the Methods sections of paper 1 [43] and paper 2 [44].

2.2.2 ^{124}I PET

To investigate an improved detectability for the non-standard radionuclide ^{124}I by SiPM-based PET, data sets of 10 differentiated thyroid cancer patients who underwent imaging on all three PET systems were evaluated. All patients showed increasing serum levels of thyroglobulin or thyroglobulin antibody levels in the low measurable range after total thyroidectomy and adjuvant radioiodine therapies. Typically, patients of this group show tumour lesions that are small and of low radioiodine uptake. PET imaging of lesions that exhibit these characteristics is challenging which is why this patient group was selected to study the benefits of SiPM-based PET. ^{124}I PET images were acquired and reconstructed in accordance to a previously published and clinically established acquisition protocol [169]. PET/CT or PET/MR images were acquired on the three different scanners after single oral application of ^{124}I within an interval of 4.7(2.9) h which is small compared to the effective ^{124}I half-life of thyroid cancer lesions (range $59 - 116$ h [47–50]). Whole-body PET/CT imaging was performed in step-and-shoot mode using an acquisition time of 4 min per bed position. PET/MR imaging was performed only of the neck region (one single bed position) at an acquisition time of 20 min and used as reference scan. For comparison to the PET/CT scans, 4-min acquisition time PET/MR data were re-sampled from the full 20-min data. Images were reconstructed using OSEM, OSEM-TOF, and OSEM-TOF+PSF algorithms for the PET/CT scans. On the Biograph mMR PET/MR system, a TOF-option is not available because of the slower timing characteristics of the applied APD-based PET detectors. Reconstruction parameters for the different PET scanners are

presented in Table 2.2.

To investigate the detectability of lesions at defined activity concentrations, a phantom containing small ^{124}I-filled spheres was assessed. In the preparation of the phantom, the activity concentrations were determined using a calibrated dose calibrator. Phantom PET data were acquired on both PET/CT scanners for 30 min in list-mode format (one single bed position), shorter acquisition time data (4 min, 8 min, and 16 min) were re-sampled from the 30-min data set. PET acquisition and image reconstruction parameters were chosen in accordance with the patient study.

Table 2.2: Reconstruction parameters for ^{124}I PET

Iterative reconstruction	PET scanner	Iterations x subsets	Gaussian filter (mm)
OSEM	Biograph Vision	10 x 5	4
	Biograph mCT	3 x 24	3
	Biograph mMR	3 x 21	4
OSEM-TOF	Biograph Vision	4 x 5	4
	Biograph mCT	2 x 21	3
	Biograph mMR	-	-
OSEM-TOF+PSF	Biograph Vision	4 x 5	4
	Biograph mCT	2 x 21	3
	Biograph mMR	-	-

A more detailed description of patient cohorts, ^{124}I PET acquisition, and image reconstruction protocols can be found in the Methods sections of paper 3 [45] (clinical study) and paper 4 [46] (phantom study).

2.3 Analyses of patient PET images

2.3.1 Visual detectability

All patient PET images were visually interpreted by nuclear medicine physicians blinded to any clinical information and in random order. Detectable lesions were independently reported to compare the detectability in reduced- and full-acquisition time PET images or across different PET scanners. For ^{18}F-FDG and ^{68}Ga-PSMA PET, image evaluation was performed by a single reader, as these examinations show a high inter-observer agreement in lymphoma or prostate cancer patients, respectively [170, 171]. For the non-standard radionuclide ^{124}I, the images were interpreted in a consensus read by three nuclear medicine physicians.

Detected lesions were assigned to different anatomical regions (according to the investigated type of malignancy) to report per-region detection rates. For ^{18}F-FDG-avid lymphoma, these regions were supradiaphragmal nodal lesions, infradiaphragmal nodal lesions, and extranodal lesions (in accordance to the Ann-Arbor classification [11]). ^{68}Ga-PSMA-avid prostate cancer lesions were assigned to the established categories primary prostatic tumour, regional lymph node metastases, soft tissue metastases (including extrapelvic lymph node metastases), and bone metastases [172]. Thyroid cancer lesions with ^{124}I uptake were reported in the anatomical regions thyroid bed, cervical lymph node metastases, extra-cervical lymph node metastases, lung, and bone metastases.

In the ^{18}F-FDG and ^{68}Ga-PSMA PET studies, per-region detection rates were calculated for the reduced-acquisition time images using the full acquisition time images as reference standard. Moreover, structured clinical classification and scoring systems were used that are described in paragraph 2.3.2. In the ^{124}I PET study, patient-based and lesion-based detection rates were calculated in reference to the prolonged -acquisition time PET/MR scan; per-region detection rates were not calculated, as all lesions were located in the neck region.

2.3.2 Classifications and scoring systems

For the comparison between reduced- and standard-acquisition time ^{18}F-FDG and ^{68}Ga-PSMA PET images, clinical scoring systems and standardised PET image reporting scores were determined. These established scoring systems correlate with patient outcome and are used for clinical decision making. Thus, they allow to

asses, if an application of reduced-acquisition time PET imaging would influence patient and therapy management. For [124]I PET, no widely accepted standardised reporting systems have yet been established.

Ann Arbor Classification For staging of lymphoma patients by ^{18}F-FDG PET, a modified version of the Ann-Arbor cassification [11] was used. The Ann-Arbor classification stages lymphoma patients according to anatomical localisation(s) of tumour burden; details are given in Table 2.3.

Table 2.3: Modified Ann-Arbor classification. Table taken from [11].

Stage	Involvement	Extranodal Status
Limited		
I	One node or a group of adjacent nodes	Single extranodal lesions without nodal involvement
II	Two or more nodal groups on the same side of the diaphragm	Stage I or II by nodal extent with limited contiguous extranodal involvement
II bulky	II as above with „bulky"disease	Not applicable
Advanced		
III	Nodes on both sides of the diaphragm; nodes above the diaphragm with spleen involvement	Not applicable
IV	Additional noncontiguous extralymphatic involvement	Not applicable

Deauville Score Additionally, lymphoma patients were classified according to the Deauville criteria [173]. The Deauville criteria describe vitality of lymphomas on a 5-point scale according to their ^{18}F-FDG uptake in comparison to the reference tissues mediastinum and liver (details in Table 2.4).

miTNM score Staging of prostate cancer patients according to their ^{68}Ga-PSMA PET status was performed using the miTNM (molecular imaging TNM) classification [174]. The miTNM score is based on a standardised evaluation scheme for ^{68}Ga-PSMA PET images of prostate cancer patients. Focal PSMA-uptake is reported in 3 categories: Local tumour („T"), regional lymph node metastases („N"), and distant metastases („M"). For each category, tumour lesions can be

Table 2.4: Deauville 5-point scale according to [173].

Score	^{18}F-FDG uptake of lymphoma lesions
1	No uptake
2	Uptake $\leq$ mediastinum
3	Uptake $>$ mediastinum but $\leq$ liver
4	Uptake moderately higher than liver
5	Uptake markedly higher than liver and/or new lesions
X	New areas of uptake unlikely to be related to lymphoma

reported in different subcategories. Figure 2.1 shows a schematic overview of the different categories, subcategories and reporting options.
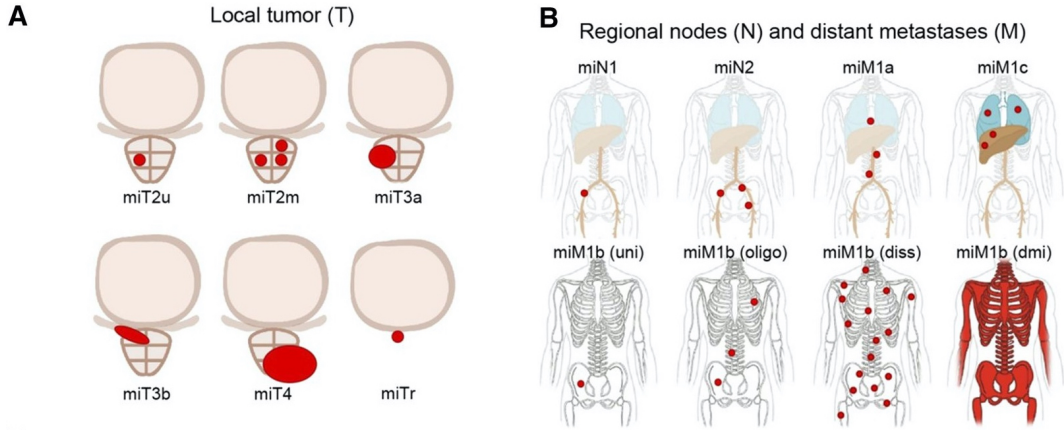

Figure 2.1: Schematic representation of miTNM reporting options. This figure (modified) was originally published in *JNM* [174]. © (2018) SNMMI.

2.3.3 Radionuclide uptake and lesion size

To characterise detected lesions, maximum and peak standardised uptake values (SUV_{max} and SUV_{peak}) were determined. SUVs are calculated as a normalised measure of radionuclide uptake to correct PET-derived quantification results for patient size and injected tracer activity [175, 176]. They are typically applied for oncological PET imaging and can particularly be beneficial for patient follow-up (including assessment of treatment response) [176]. SUVs are calculated from PET-

derived activity concentration measurements in an evaluated volume-of-interest using the following formula [176]:

$$SUV(t) = \frac{AC(t)}{(A'_0/m)},$$

with the activity concentration AC [kBq/ml], the administered activity A'_0 [kBq], and the patient weight m [g]. A decay correction of AC and A'_0 to the same time point is required. Assuming a body mass density of $\rho = 1\frac{g}{ml}$, SUV values become dimensionless quantities and a uniform distribution of administered activity corresponds to $SUV = 1$.

Image-derived activity concentrations (ACs) are evaluated in a defined volume-of-interest (resembling a tumour lesion) with AC_{mean}/SUV_{mean} referring to its mean value and AC_{max}/SUV_{max} referring its maximum value. SUV_{peak} was defined as mean SUV in a spherical volume-of-interest of 1-mL volume around the voxel with the maximum SUV (the voxel defining SUV_{max}) [177]. For small lesions, SUV_{max} can be more accurate and reproducible than SUV_{mean} which may be influenced by partial volume effects [176]. SUV_{peak} was proposed to be an even more robust measure than SUV_{max} [177, 178].

Lymphoma and prostate cancer lesions were classified according to their ^{18}F-FDG or ^{68}Ga-PSMA SUV_{max} as lesions with faint, moderate, or high radiotracer accumulation. To compare the quantification accuracy in reduced- and standard-acquisition time PET images, the ratio of SUV_{max} and SUV_{peak} in reduced to standard PET images was calculated. For ^{124}I-avid lesions, SUV_{max}, AC_{max}, and the local signal-to-background ratio (ratio of lesion SUV_{max} to background SUV_{bgr} measured in a representative volume-of-interest surrounding the lesion) were reported to characterise the lesions that were detected on the different PET systems.

For a characterisation of the lesion size, for nodal lesions the short-axis diameter and for non-nodal lesions the long-axis diameter was measured (for ^{18}F-FDG and ^{68}Ga-PSMA PET/CT imaging). For the non-standard radionuclide ^{124}I, for all lesions the long-axis diameter was reported. Diameters were measured using the corresponding CT or MR images; for lesions that were morphologically not clearly definable, an iterative volume segmentation approach [179] was applied to determine an upper size limit from the PET images.

2.3.4 Image quality and image noise

The image noise was determined in a tumour-independent physiological reference tissue and can be regarded as a measure of image quality. In ^{18}F-FDG and ^{68}Ga-PSMA PET images, the ratio of the standard deviation of the SUV to the mean SUV in a representative liver volume-of-interest [180, 181] was calculated. Liver tissue shows a tumour-independent physiological ^{18}F-FDG and ^{68}Ga-PSMA uptake and is therefore suitable for an assessment of image noise. For ^{124}I, however, physiological uptake in most organs is very low. Therefore, for this radionuclide the overall image quality was visually determined using an established 5-point Likert-like scale [182].

2.4 Analyses of phantom PET images

The investigation of the small tumour phantom was performed to evaluate the detectability of small spherical lesions of defined sizes and [124]I activity concentrations for the SiPM-based and the PMT-based PET/CT systems.

2.4.1 Small tumour phantom

The small tumour phantom consists of an abdominal torso NEMA phantom (Data Spectrum Corporation, Durham, USA) in which six refillable glass spheres were mounted. Figure 2.2 shows a schematic representation of the small tumour phantom. The diameters of the small spheres (from 3.7 mm to 9.7 mm) were selected to resemble the typical size range of normal cervical lymph nodes [183] and thyroid cancer lymph node metastases [50]. To simulate challenging detection conditions, different sphere activity concentrations ($0.25 \, \mathrm{kBq \, mL^{-1}}$ to $25 \, \mathrm{kBq \, mL^{-1}}$) and the signal-to-background ratio (20:1) were chosen to reflect the lower range of thyroid cancer patient lymph node metastases [50]. Initially, the small spheres where filled with [124]I-solution at the highest activity concentration. To realise lower sphere activity concentrations, 9 subsequent PET acquisitions were performed with an interval of about one [124]I half life between each acquisition.
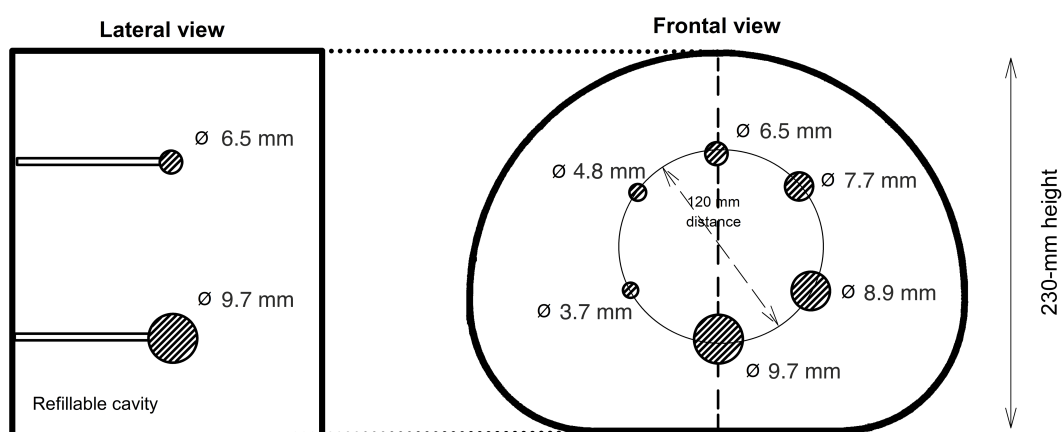

Figure 2.2: Schematic representation of the small tumour phantom.

2.4.2 Human observer study, signal-to-noise ratio, and minimum detectable activity

To quantify the improvements in detectability of the SiPM-based in comparison to the PMT-based PET/CT system, the minimum detectable activity for ^{124}I was determined. The minimum detectable activity is a lesion size-dependant measure which describes the minimum activity concentration of a lesion to be detectable by a human reader [36,184,185]. To determine the minimum detectable activity, first, the visual detectability of each small sphere was assessed in a human observer study by 5 readers. Next, the signal-to-noise ratio (SNR), a measure correlating with lesion detectability, was calculated [104]. The signal-to-noise ratio is the difference between the mean activity concentration of a small sphere $(\overline{AC_{sphere}})$ and the mean activity concentration of the phantom background $(\overline{AC_{background}})$ divided by the standard deviation of $AC_{background}$ $(\sigma_{background})$:

$$SNR = \frac{|\overline{AC_{sphere}} - \overline{AC_{background}}|}{\sigma_{background}}$$

Finally, SNR and visual detectability were correlated to determine the SNR threshold that indicates detectability for each reconstruction algorithm.

For each small sphere, the SNR was analysed as a function of the activity concentration and the minimum detectable activity was defined as the activity concentration at the SNR threshold value.

2.4.3 Projection of ^{124}I activity concentrations onto predicted response in radioiodine therapy

To evaluate the clinical significance of an improved detection of the investigated lesions, a correlation between lesion activity concentration and potential response to clinical radioiodine therapy was established [140]. The success of radioiodine therapy depends on the lesions' absorbed radiation dose.

Assuming (a) that the absorbed dose for small lesions arises from ^{131}I beta-particle self-irradiation, (b) that particle-range effects due to the limited beta-particle range can be neglected, as even for the smallest 3.7-mm sphere the percentage fraction of the deposited energy within the lesion is 90% [186], and (c) an instant ^{124}I activity concentration (AC_0^{I-124}) after administration of a diagnostic activity A_0^{I-124} and monoexponential clearance with an effective half-life T_{I-131}^{eff}, the average

self-absorbed dosage (D) after administration of a therapeutic ^{131}I activity A_0^{I-131} can be calculated using the following numerical value equation [187]:

$$(D/Gy) = 3.809 \cdot (AC_0^{I-124}/\text{kBq ml}^{-1}) \cdot (T_{I-131}^{eff}/d) \cdot \frac{(A_0^{I-131}/\text{GBq})}{(A_0^{I-124}/\text{MBq})}$$

The formula is based on the „Medical internal radiation dose (MIRD)" formalism for a spherical tumour model [187].

For absorbed doses <35 Gy a success of radioiodine therapy is unlikely, for doses ≥ 35 Gy and <85 Gy response rates are about 20%, and for doses ≥ 85 Gy they are $>98\%$ [188]. Thus, using the numerical value equation a low, a medium, and a high absorbed dose group corresponding to the likelihood of therapy success were defined. The groups indicate expected success of radioiodine therapy for a given activity concentration. For the calculation, clinical standard values for A_0^{I-124}, AC_0^{I-124}, A_0^{I-131} (resembling high-dose radioiodine therapy), and T_{I-131}^{eff} were used.

3 Publications

The papers resulting from this work are given in this chapter and include:

1. *Evaluation of ^{18}F-FDG PET/CT images acquired with a reduced scan time duration in lymphoma patients using the digital biograph vision*, M. Weber, W. Jentzen, R. Hofferber, K. Herrmann, W. P. Fendler, C. Rischpler, L. Umutlu, M. Conti, P. Fragoso Costa, M. Sraieb and D. Kersting, BMC Cancer **21**, 62 (2021)

2. *Evaluation of [^{68Ga}]Ga-PSMA PET/CT images acquired with a reduced scan time duration in prostate cancer patients using the digital biograph vision*, M. Weber, W. Jentzen, R. Hofferber, K. Herrmann, W. P. Fendler, M. Conti, A. Wetter, D. Kersting, C. Rischpler and P. Fragoso Costa, EJNMMI Research **11**, 21 (2021)

3. *Comparing lesion detection efficacy and image quality across different PET system generations to optimize the iodine-124 PET protocol for recurrent thyroid cancer*, D. Kersting, W. Jentzen, M. Sraieb, P. Fragoso Costa, M. Conti, L. Umutlu, G. Antoch, M. Nader, K. Herrmann, W. P. Fendler, C. Rischpler and M. Weber, EJNMMI Physics **8**, 14 (2021)

4. *Silicon-photomultiplier-based PET/CT reduces the minimum detectable activity of iodine-124*, D. Kersting, W. Jentzen, P. Fragoso Costa, M. Sraieb, P. Sandach, L. Umutlu, M. Conti, F. Zarrad, C. Rischpler, W. P. Fendler, K. Herrmann, and M. Weber, Scientific Reports **11**, 17477 (2021)

Evaluation of ^{18}F-FDG PET/CT images acquired with a reduced scan time duration in lymphoma patients using the digital biograph vision

Reference

Copyright statement

Contributions

I participated in planning of the study and data analysis and contributed to manuscript writing.

BMC Cancer

Evaluation of ^{18}F-FDG PET/CT images acquired with a reduced scan time duration in lymphoma patients using the digital biograph vision

Manuel Weber[1,2*], Walter Jentzen[1,2], Regina Hofferber[1,2], Ken Herrmann[1,2], Wolfgang Peter Fendler[1,2], Christoph Rischpler[1,2], Lale Umutlu[2,3], Maurizio Conti[4], Pedro Fragoso Costa[1,2], Miriam Sraieb[1,2] and David Kersting[1,2]

Abstract

Background: The superior accuracy and sensitivity of ^{18}F-FDG-PET/CT in comparison to morphological imaging alone leads to an upstaging in up to 30% of lymphoma patients. Novel digital PET/CT scanners might enable to reduce administered tracer activity or scan time duration while maintaining diagnostic performance; this might allow for a higher patient throughput or a reduced radiation exposure, respectively. In particular, the radiation exposure reduction is of interest due to the often young age and high remission rate of lymphoma patients.

Methods: Twenty patients with (suspected) lymphoma (6 for initial staging, 12 after systemic treatment, 2 in suspicion of recurrence) sequentially underwent ^{18}F-FDG-PET/CT examinations on a digital PET/CT (Siemens Biograph Vision) with a total scan time duration of 15 min (reference acquisition protocol) and 5 min (reduced acquisition protocol) using continuous-bed-motion. Both data sets were reconstructed using either standalone time of flight (TOF) or in combination with point spread function (PSF), each with 2 and 4 iterations. Lesion detectability by blinded assessment (separately for supra- and infradiaphragmal nodal lesions and for extranodal lesions), lesion image quantification, and image noise were used as metrics to assess diagnostic performance. Additionally, Deauville Score was compared for all patients after systemic treatment.

Results: All defined regions were correctly classified in the images acquired with reduced emission time, and therefore, no changes in staging were observed. Lesion quantification was acceptable, that is, mean absolute percentage deviation of maximum and peak standardized uptake values were 6.8 and 6.4% (derived from 30 lesions). A threefold reduction of scan time duration led to an increase in image noise from 7.1 to 11.0% (images reconstructed with 4 iterations) and from 4.7 to 7.2% (images reconstructed with 2 iterations). No deviations in Deauville Score were observed.

(Continued on next page)

* Correspondence: manuel.weber@uk-essen.de
[1]Department of Nuclear Medicine, University of Duisburg-Essen, University Hospital Essen, Hufelandstrasse 55, 45122 Essen, Germany
[2]University of Duisburg-Essen and German Cancer Consortium (DKTK)-University Hospital, Essen, Germany
Full list of author information is available at the end of the article

(Continued from previous page)

Conclusion: These results suggest that scan time duration or administered tracer activity can be reduced threefold without compromising diagnostic performance. Especially a reduction of administered activity might allow for a lower radiation exposure and better health economics. Larger trials are warranted to confirm our results.

Keywords: PET/CT, FDG, Image quality, Silicon photomultiplier, Lymphoma

Background

The 2014 Lugano Classification recommends performing ^{18}F-FDG-PET/CT in lymphoma patients for interim staging and after the completion of chemotherapy for the evaluation of treatment response. Accuracy in terms of sensitivity has been shown to be higher than in standalone morphological imaging, leading to an upstaging in up to 30% of patients, especially in a subcohort of frequently FDG-avid lymphoma subtypes [1]. Additionally, interim staging ^{18}F-FDG-PET/CT can predict survival in lymphoma patients after systemic treatment with combined chemo- and immunotherapy [2].

The two most relevant caveats in the imaging of lymphoma patients are (a) the high prevalence of brown adipose tissue bearing the risk of false-positive results [3, 4] and (b) the often small size of nodal lesions potentially leading to false-negative results [5]. These factors do not only place stringent requirements on the medical imaging specialists, but also on the imaging devices, image acquisition protocols, and image reconstruction algorithms. To ensure optimal image quality for tumor imaging, the EANM procedure guidelines on ^{18}F-FDG-PET/CT recommend starting the scan acquisition 60 min after the intravenous administration of ^{18}F-FDG and a patient-specific optimization of administered tracer activity. The necessary ^{18}F-FDG activity is calculated based on patient weight, scanning device, and emission time [6]. Typically, about 3 MBq/kg bodyweight of ^{18}F-FDG are administered when using an emission time of about 3 min per bed position [7].

With the advent of a new generation of silicon photomultiplier-based, so called digital PET/CT devices a reduction of the injected amount of ^{18}F-FDG appears feasible due to the higher detector sensitivity and improved coincidence timing resolution [7]: For example, phantom studies have shown that a reduction of acquisition time up to a factor of six is possible while maintaining a high diagnostic performance [8, 9]. Additionally, a threefold reduction in acquisition time duration (which is approximate to a reduction in administered activity by the same factor) only led to changes in tumor stage in a small fraction of oncological patients [10]. This finding has considerable implications:

The implementation of a low-activity acquisition protocol would lead to a reduction in radiation exposure for patients and medical staff. This low-activity regimen would be particularly beneficial for lymphoma patients, who are often young and have a high rate of long-term remission [11]. Additionally, lower activity requirements/scanning times would enable PET centers to perform more exams per day and optimize their cost efficiency.

We therefore aimed to evaluate the feasibility of a threefold reduction in scan time duration in lymphoma patients undergoing ^{18}F-FDG-PET/CT without compromising diagnostic performance. As a reduction of emission time correlates to a reduction in administered activity by the approximately the same factor [10, 12], our results would advocate for the use of a low-activity protocol.

Methods

Patient population and preparation

Twenty consecutively enrolled lymphoma patients (5 with Hodgkin lymphoma, 14 with Non-Hodgkin lymphoma, 1 with high clinical suspicion of lymphoma) undergoing ^{18}F-FDG PET examination (on clinical indication) were included. In 6 of these the examination was performed for initial staging, in 12 after systemic treatment and in the 2 remaining patients for suspicion of recurrence.

Detailed patient and imaging characteristics are provided in Supplemental Table S1. Mean patient age (range) was 50 (23–84) years and mean patient weight (range) was 81 (47–130) kg. Following joint EANM procedure guidelines for ^{18}F-FDG PET/CT in tumor imaging, a mean±standard deviation (SD) activity of 340± 72 MBq (corresponding to 4.2±0.4 MBq/kg bodyweight) ^{18}F-FDG was injected intravenously. PET/CT data were acquired after a mean±SD time interval of 73±11 min.

Image acquisition

All examinations were performed on a digital Biograph Vision PET/CT system (Siemens Healthcare; Erlangen, Germany), whose imaging properties have recently been assessed using ^{18}F [7]. The scan area comprised whole-body PET/CT from mid-thigh to skull base. Image acquisition started with a whole-body spiral CT in full-dose technique using automatic tube current and tube voltage adjustments (Care Dose 4D, quality reference 160 mAs, CARE kV, quality reference 120 kV). These data were used for attenuation correction and

Weber *et al. BMC Cancer*   (2021) 21:62

Page 3 of 8

anatomical correlation. Subsequently, two PET scans were applied in continuous-bed-motion mode.

The reference (or clinical standard) scan was acquired first and lasted approximately 15 min, the reduced scan was acquired subsequently with an emission time of about 5 min. We chose an approximate threefold reduction of emission time based on previously published in-vivo and phantom studies by other groups and an optimization study by our group performed on the same PET/CT system using an abdominal phantom under conditions observed in lymphoma imaging [10, 13, 14]. More precisely, in the phantom study our group has demonstrated that the optimized step-and-shoot emission time was approximately 60 s/bed (or 2.19 mm/s in continuous-bed-motion table speed) in association with appropriate image reconstruction algorithms (see below). Of note, the conversion from step-and-shoot emission time per bed (t_{bed}) to continuous-bed-motion table speed (v_{table}) was based on manufacturer recommended equivalence settings using an axial field of view (FOV) of 263 mm (or $v_{table} = 0.5$ FOV / t_{bed}).

More specifically, our clinical standard protocol comprised three regions: two non-abdomen regions (ranging from the skull-base to the upper abdomen and from the lower abdomen to mid-thigh) and an abdomen region. For the reference acquisition protocol, the continuous-bed-motion table speed (equivalent step-and-shoot emission time per bed position, approximate scan length of about 30 cm) for the non-abdomen regions and within abdomen region was 1.5 mm/s (88 s/bed) and 0.8 mm/s (164 s/bed), respectively. For the reduced acquisition protocol, the continuous-bed-motion table speeds were 2.2 mm/s (60 s/bed) and 4.1 mm/s (32 s/bed) within the abdomen and non-abdomen region, respectively. This translates to a reduction of the scan time duration exactly by a factor of 2.75 or approximately a threefold reduction in scan time duration.

Image reconstruction
The diagnostic CT images were reconstructed iteratively with a convolution kernel I30f (SAFIRE level of 3). The reconstructed CT slice thickness and the transversal voxel size was 3.0 mm and 1.5×1.5 mm^2, respectively. Based upon our previously conducted phantom-based optimization study images [13, 14] were reconstructed using the three-dimensional ordinary Poisson ordered-subset expectation maximization (OSEM) algorithm, either with standalone time of flight (TOF) approach or with combined TOF and point spread function (PSF). For both acquisition protocols, 4 image sets were reconstructed: TOF and TOF+PSF, each with 2 iterations (5 subsets) or 4 iterations (5 subsets). The reconstructed images had a voxel size of $3.3 \times 3.3 \times 3.0$ mm^3 and were smoothed

with an isotropic Gaussian post-reconstruction filter of 4 mm. The estimated reconstructed PET spatial resolution (expressed as the full-width-at-half maximum) was 5.4 mm and 4.9 mm for TOF- and TOF+ PSF-reconstructed images, respectively [13]. The resulting 4 images (reconstructed for each patient and each acquisition protocol) are referred to OSEM-TOF (2i), OSEM-TOF (4i), OSEM-TOF+PSF (2i), and OSEM-TOF+PSF (4i).

Image analyses
Pseudonymized PET/CT data were analyzed by a central reader blinded to any clinical information in random order on a per-region basis. Based on the Ann-Arbor Classification, three types of regions based on lesion location were defined [1], which are: supra-diaphragmal nodal lesions, infradiaphragmal nodal lesions, extranodal lesions. Subsequently, for each region, maximum and peak standardized uptake values (SUVmax and SUVpeak) were measured and its lesion size (short diameter for nodal lesions, long diameter for non-nodal lesion) were determined for the lesion with the highest tracer uptake. The resulting SUV ratios were further categorized in terms of SUVmax showing tumors with faint (SUVmax≤5), moderate (5<SUVmax< 10), and high uptake (SUVmax≥10). In addition, tumor stage according to the Ann-Arbor Classification and Deauville Score for patients after systemic treatment were assessed.

Metrics for diagnostic performance
Three metrics were used to evaluate the diagnostic performance. Primary endpoint was the accuracy of the per-region detectability in the images acquired with the reduced protocol. To this end, images reconstructed with the same image reconstruction algorithm, but acquired with standard emission time duration, were set as reference image. Subsequently, the fraction of correctly classified tumor regions and subsequent changes in Ann-Arbor stage were assessed.

Secondary endpoints were the precision in image quantification and image noise. The former was obtained by calculating the ratio between SUVmax (SUVpeak) of FDG-avid tumors in the reduced and reference acquisition protocol series for each of the respective image reconstruction algorithms. Image noise was assessed using the liver's activity distribution and is defined as the ratio of the standard deviation of SUV to the mean SUV in healthy liver tissue that were obtained by placing a spherical volume of interest with 3 cm in diameter in the lower right liver lobe [15, 16].

Results

Detectability

As assessed by the reference protocol, 9/20 patients (45%) were PET-positive. Of these, 1/20 patients was staged as Ann-Arbor I, 4/20 were staged as Ann-Arbor II, and 2/20 each as Ann-Arbor III and IV (the latter with adrenal and bone involvement). Using images acquired with the standard protocol as reference, 60/60 regions (100%) and 12/12 (100%) regions with at least one tumor lesion were correctly classified in the reduced protocol (Supplemental Tables S2 and S3). All defined regions were correctly classified in the images acquired with reduced scan time duration, and therefore, no changes in staging were observed. In addition, no differences regarding the lesion detectability were observed between the different reconstruction algorithms. Figure 1 shows images acquired with standard vs. reduced acquisition time of patients, using OSEM-TOF+PSF (4i) exemplary.

Image quantification

Figure 2 illustrates the ratio of SUVmax and SUVpeak, separately for lesions with faint, moderate, and high uptake. An absolute difference in SUVs of less than 20% was observed between images acquired with reduced vs. standard protocol. The error margin of ±20% was considered acceptable in this study, which is similar to the
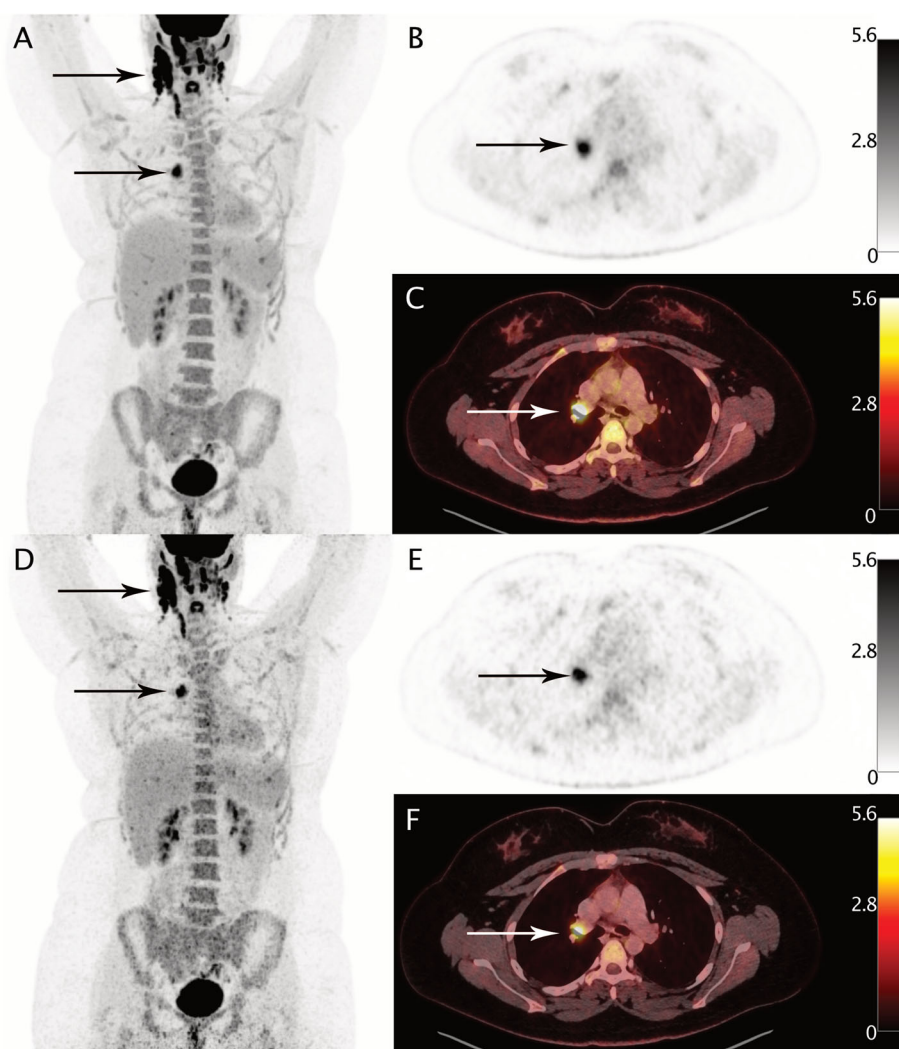
Fig. 1 A 25-year-old patient with biopsy-proven lymphoma undergoing ^{18}F-FDG-PET/CT before treatment. Panels **a**, **b**, and **c** show images acquired with the reference acquisition protocol, panels **c**, **d**, and **e** show image acquired with reduced emission time, all reconstructed with OSEM-PSF+TOF (4i). Axial slices (**b**, **c**, **c**, and **f**) and maximum intensity projections (**a** and **d**) reveal vital lymphoma manifestations in cervical and mediastinal lymph nodes. All lesions visible with standard acquisition protocol were also detectable after a threefold reduction of scan time duration. Values left to the color bares are in SUV units
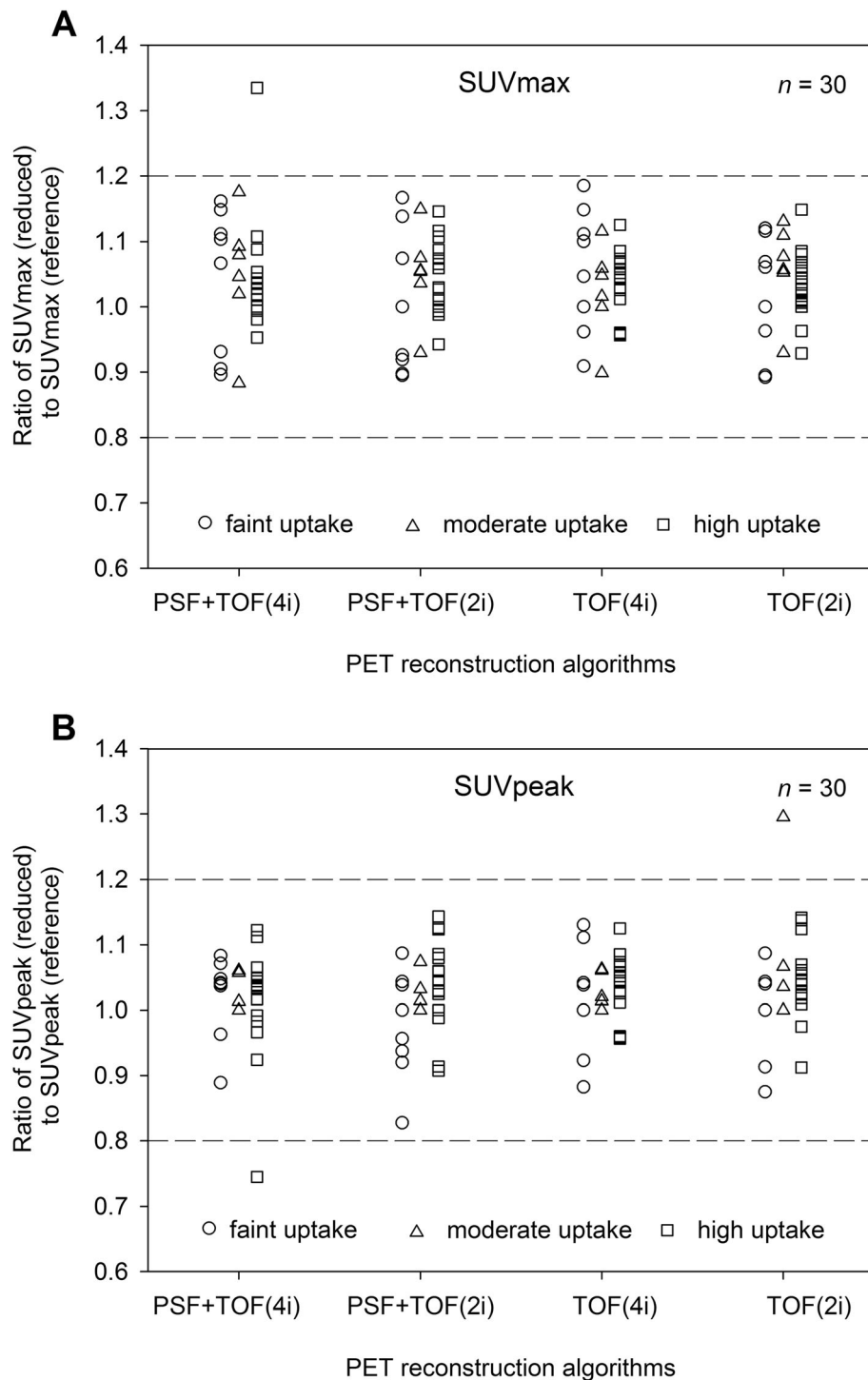
Fig. 2 Dot plots showing the ratio between lesion SUVmax (panel **a**) and SUVpeak (panel **b**) between images acquired with reference vs. reduced acquisition protocol. Quantitative assessment was performed separately for lesions with faint (circles, SUVmax≤5), moderate (triangles, 5< SUVmax< 10)), and high uptake (squares, SUVmax ≥ 10). Dashed lines indicate the maximum tolerated deviation of ±20%

mean percentage difference in lesion SUVmax for different scanners at different locations [17]. Across all measured lesions, the mean absolute percentage deviation for SUVmax (SUVpeak) was 7.5% (8.4%), 6.8% (5.7%), 6.5% (5.3%), and 6.2% (6.2%) for OSEM-TOF+PSF (4i), OSEM-TOF+PSF (2i), OSEM-TOF (4i), OSEM-TOF (2i), respectively. In the population after systemic treatment (*n*=12), Deauville Score was 1 in four patients,

2 in three patients, 4 in three patients and 5 in two patients. No deviations in Deauville Score were observed.

Image noise
Scan time reduction led to an increase in image noise and these differences were most pronounced in the images reconstructed with 4 iterations (Fig. 3). The mean image noise increased from 7.8 to 12.2% for OSEM-TOF (4i) and 5.2 to 8.1% for OSEM-TOF (2i). The same phenomenon was observed for OSEM-PSF+TOF reconstructed images, that is, image noise increased from 6.4 to 10.3% OSEM-TOF+PSF (4i), 4.3 to 6.5% for OSEM-TOF+PSF (2i)

Discussion
This study confirms that a digital PET/CT system enables a reduction of scan time duration or administered ^{18}F-FDG-PET/CT activity. In our cohort of 20 lymphoma patients all of our defined body regions (supradiaphragmal nodal, infradiaphragmal nodal, extranodal) were correctly classified and no down-staging was observed using images acquired with the reduced acquisition protocol. Hence, based on the images acquired with almost a threefold reduction in scan time duration, lesion detectability, image quantification, and image noise were highly reproducible across all reconstruction algorithms.

Similarly, van Sluis et al. [10] were able to show that a threefold reduction in scan time duration led to down-staging in a minor fraction of patients (1/30) of their patient cohort that encompassed different oncological entities. A prior study by our group showed comparable results for ^{68}Ga-PSMA PET in prostate cancer [18]. We observed down-staging in 1/20 patients due to missing small nodal lesions. The differences in findings to the previous study can be explained by the bigger size of nodal lesions in this study (mean short-axis diameter:
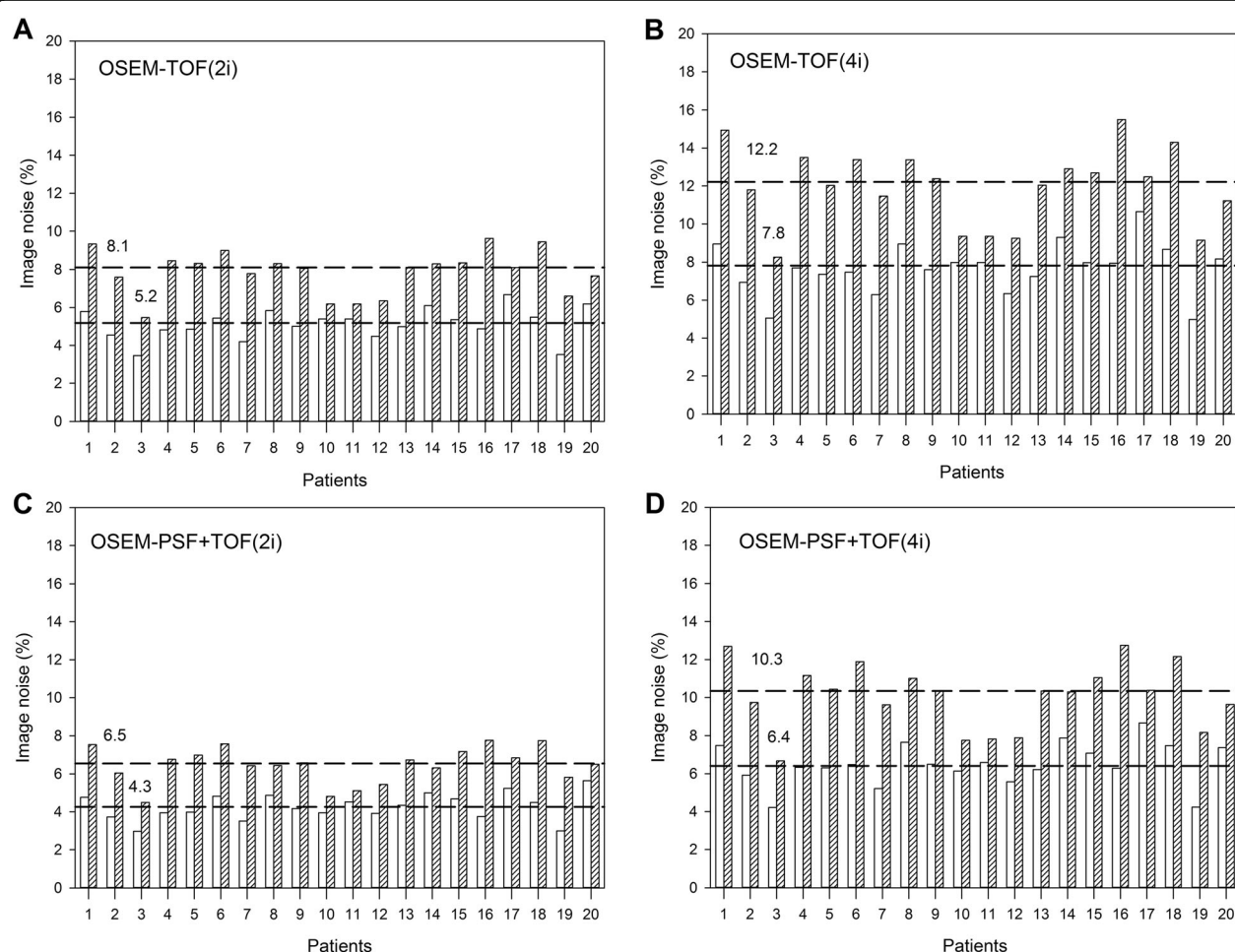

Fig. 3 Bar graph showing the image noise derived from the liver's activity distribution for images acquired with reference (white bars) vs. reduced acquisition time (hatched bars) across all reconstruction algorithms. Median values for each reconstruction algorithm are given and they are indicated with dashed lines

Weber *et al. BMC Cancer*   (2021) 21:62

Page 7 of 8

13.8 mm) as well as the different imaging properties of ^{18}F-FDG-based tracers [19]. However, at presentation, size of nodal lesions in lymphoma is often larger than 1 cm, so the lesion size in our patient cohort is likely to be representative [20]. Figure 1 shows an exemplary patient, who underwent ^{18}F-FDG-PET/CT using the reference acquisition and reduced acquisition protocol.

Image quantification acquired with the reduced scan time duration proved to be reliable across all reconstruction algorithms and the single absolute percentage deviation was considerably lower than < 20% (Fig. 2), which we previously defined as the acceptable margin of error. Of note, a recent study by Kurland et al. [17] demonstrated that lesion uptake (SUVmax) showed an average difference of 8% for the same scanner model within the same institution and 18% for different scanners from different institutions. No notable differences were observed between SUVmax and SUVpeak measurements and between low, moderate and high tracer uptake. In this study images acquired with the reduced acquisition protocol were acquired after the reference protocol. The occurrence of at least slight metabolic changes between the acquisitions of both scans is likely as prior studies employing dual time point ^{18}F-FDG-PET/CT have shown an increase of tumor specific ^{18}F-FDG-uptake on images acquired as late as 2 or 3 h after injection [21, 22]. This might partially explain the higher tumoral uptake on images acquired with reduced vs. reference emission time. A detailed depiction of quantitative assessment in all patients is provided in Fig. 2.

As expected, a reduction of emission time led to an increase in image noise, which is in line with prior studies by van Sluis et al. [10] and Sonni et al. [23]. An in-depth overview of image noise across all employed reconstruction algorithms is provided in Fig. 3.

Interestingly, a higher image noise was observed for images reconstructed with 2 iterations vs. 4 iterations, which is comparable with a previous study of our group on emission time reduction in ^{68}Ga-PSMA PET/CT [18].

Limitations of our study are the relatively small patient and lesion size and its retrospective nature. Additionally, in more than half of patients ^{18}F-FDG-PET/CT did not reveal any ^{18}F-FDG-avid lymphoma manifestations, which further restricts the reliability of our study results. For ethical reasons histopathological lesion validation was not performed. However, this was beyond the scope of this study as ^{18}F-FDG-PET/CT constitutes the current imaging gold standard [24].

Conclusion

This study shows that the advent of the new generation of digital PET/CT systems might enable a reduction of scan time duration (or administered activity) without sacrificing diagnostic performance. Especially a reduction in tracer activity might allow for higher patient throughput, better cost-efficiency, and a reduction in radiation exposure in the frequently young lymphoma patients. However, the results have to be validated in larger trials.

Supplementary Information

The online version contains supplementary material available at https://doi.org/10.1186/s12885-020-07723-2.

Additional file 1: Table S1. Patient and Imaging Characteristics (*n*=20).

Additional file 2: Table S2. Overview of the Lesion detectability using images reconstructed with OSEM-TOF+PSF 4i (served as reference) in comparison with the detectability using images reconstructed with OSEM-TOF 4i (short) and OSEM-TOF 2i (reduced).

Additional file 3: Table S3. Overview of the lesion detectability using images reconstructed with OSEM-TOF 4i (served as reference) in comparison with the detectability using images reconstructed with OSEM-TOF 4i (short) and OSEM-TOF 2i (reduced).

Author details
[1]Department of Nuclear Medicine, University of Duisburg-Essen, University Hospital Essen, Hufelandstrasse 55, 45122 Essen, Germany. [2]University of Duisburg-Essen and German Cancer Consortium (DKTK)-University Hospital, Essen, Germany. [3]Department of Department of Diagnostic and Interventional Radiology and Neuroradiology, University Hospital Essen, Essen, Germany. [4]Siemens Medical Solutions USA, INC, Erlangen, Germany.

References
1. Cheson BD, et al. Recommendations for initial evaluation, staging, and response assessment of Hodgkin and non-Hodgkin lymphoma: the Lugano classification. J Clin Oncol. 2014;32(27):3059–68.
2. Duhrsen U, et al. Positron emission tomography-guided therapy of aggressive non-Hodgkin lymphomas (PETAL): a multicenter, randomized phase III trial. J Clin Oncol. 2018;36(20):2024–34.
3. Gelfand MJ, et al. Pre-medication to block [(18) F] FDG uptake in the brown adipose tissue of pediatric and adolescent patients. Pediatr Radiol. 2005; 35(10):984–90.
4. Cohade C, et al. Uptake in supraclavicular area fat ("USA-Fat"): description on 18F-FDG PET/CT. J Nucl Med. 2003;44(2):170–6.
5. Barrington SF, Kluge R. FDG PET for therapy monitoring in Hodgkin and non-Hodgkin lymphomas. Eur J Nucl Med Mol Imaging. 2017;44(Suppl 1): 97–110.
6. Boellaard R, et al. FDG PET/CT: EANM procedure guidelines for tumour imaging: version 2.0. Eur J Nucl Med Mol Imaging. 2015;42(2):328–54.
7. van Sluis J, et al. Image quality and semi-quantitative measurements of the Siemens biograph vision PET/CT: initial experiences and comparison with Siemens biograph mCT PET/CT. J Nucl Med. 2020;61(1):129–135.
8. Gnesin S, et al. Phantom-based image quality assessment of clinical (18) F-FDG protocols in digital PET/CT and comparison to conventional PMT-based PET/CT. EJNMMI Phys. 2020;7(1):1.
9. Surti S, et al. Benefit of improved performance with state-of-the art digital PET/CT for lesion detection in oncology. J Nucl Med. 2020;61(11):1684–1690.
10. van Sluis J, et al. Image quality and activity optimization in oncological (18) F-FDG PET using the digital biograph vision PET/CT. J Nucl Med. 2019.
11. Shah DJ, Sachs RK, Wilson DJ. Radiation-induced cancer: a modern view. Br J Radiol. 2012;85(1020):e1166–73.
12. Rauscher I, et al. Can the injected dose be reduced in (68) Ga-PSMA-11 PET/ CT maintaining high image quality for lesion detection? J Nucl Med. 2020; 61(2):189–193.
13. Bramer, A., *Phantom study for optimization [18F] FDG imaging of lymphoma using Biograph Vision PET/CT.*, in *Department for Nuclear medicine.* 2019, University Duisburg-Essen.
14. Fragoso Costa P, et al. *Emission time reduction for 2-[18F] FDG examinations in lymphoma patients with a PET/CT with SiPM - a feasibility phantom study (EPS-093); European Association of Nuclear Medicine October 22–30,* 2020 *Virtual.* Eur J Nucl Med Mol Imaging. 2020;47(Suppl 1):257.
15. Nagaki A, Onoguchi M, Matsutomo N. Patient weight-based acquisition protocols to optimize (18) F-FDG PET/CT image quality. J Nucl Med Technol. 2011;39(2):72–6.
16. Viner M, et al. Liver SULmean at FDG PET/CT: interreader agreement and impact of placement of volume of interest. Radiology. 2013;267(2):596–601.
17. Kurland BF, et al. Test-retest reproducibility of (18) F-FDG PET/CT uptake in Cancer patients within a qualified and calibrated local network. J Nucl Med. 2019;60(5):608–14.
18. Weber, M., et al., Evaluation of 68Ga-PSMA PET/CT images acquired with a reduced scan time duration in prostate Cancer patients using the digital biograph vision. 2020.
19. Conti M, Eriksson L. Physics of pure and non-pure positron emitters for PET: a review and a discussion. EJNMMI Phys. 2016;3(1):8.
20. Haque W, et al. Radiation therapy is an effective modality in the treatment of mantle cell lymphoma, even in heavily pretreated patients. Clin Lymphoma Myeloma Leuk. 2014;14(6):474–9.
21. Kubota K, et al. Advantage of delayed whole-body FDG-PET imaging for tumour detection. Eur J Nucl Med. 2001;28(6):696–703.
22. Boerner AR, et al. Optimal scan time for fluorine-18 fluorodeoxyglucose positron emission tomography in breast cancer. Eur J Nucl Med. 1999;26(3): 226–30.
23. Sonni I, et al. Initial experience with a SiPM-based PET/CT scanner: influence of acquisition time on image quality. EJNMMI Phys. 2018;5(1):9.
24. Fueger BJ, et al. Comparison of CT, PET, and PET/CT for staging of patients with indolent non-Hodgkin's lymphoma. Mol Imaging Biol. 2009;11(4):269–74.

Publisher's Note

Springer Nature remains neutral with regard to jurisdictional claims in published maps and institutional affiliations.

Table S1. Patient and Imaging Characteristics (n=20)

Sex and age	Values for age
Mean (range) age (in years)	50.0 (23–84)
Mean (range) weight (in kg)	81 (47–130)
Men	8
Women	12

Lymphoma subtype	Number of patients
Hodgkin lymphoma	5
High clinical suspicion, NOS	1
NHL	14
- DLBCL	- 6
- Follicular lymphoma	- 2
- ALCL	- 1
- BCL NOS	- 3
- NHL NOS	- 2

Indication	Number of patients
Initial staging	6
Assessment of treatment response	12
Suspicion for recurrence	2

Imaging characteristics

Mean administered activity ±SD	340±72
Mean uptake time ± standard deviation	73±11

NOS: Non otherwise specified; NHL: Non-Hodgkin lymphoma; DLBCL: Diffuse B-Cell

Lymphoma; ALCL: anaplastic large-cell lymphoma; BCL: B-cell lymphoma, NHL: Non-

Hodgkin lymphoma

Table S2 Overview of the Lesion detectability using images reconstructed with OSEM-TOF+PSF 4i (served as reference) in comparison with the detectability using images reconstructed with OSEM-TOF 4i (short) and OSEM-TOF 2i (reduced).

Patient No.	OSEM-PSF+TOF 4i (reference)	OSEM-PSF+TOF 4i (reduced)	OSEM-PSF+TOF 2i (reduced)
5	1/0/0 (II)	1/0/0 (II)	1/0/0 (II)
9	0/0/0 (0)	0/0/0 (0)	0/0/0 (0)
10	0/0/1 (IV)	0/0/1 (IV)	0/0/1 (IV)
11	0/0/0 (0)	0/0/0 (0)	0/0/0 (0)
12	0/0/1 (I)	0/0/1 (I)	0/0/1 (I)
13	0/0/0 (0)	0/0/0 (0)	0/0/0 (0)
14	1/1/0 (III)	1/1/0 (III)	1/1/0 (III)
15	0/0/0 (0)	0/0/0 (0)	0/0/0 (0)
16	0/0/0 (0)	0/0/0 (0)	0/0/0 (0)
17	0/0/0 (0)	0/0/0 (0)	0/0/0 (0)
18	1/0/1 (IV)	1/0/1 (IV)	1/0/1 (IV)
19	0/0/0 (0)	0/0/0 (0)	0/0/0 (0)
20	1/1/0 (III)	1/1/0 (III)	1/1/0 (III)
21	1/0/0 (I)	1/0/0 (I)	1/0/0 (I)

22	0/0/0 (0)	0/0/0 (0)	0/0/0 (0)
23	0/0/0 (0)	0/0/0 (0)	0/0/0 (0)
24	0/1/0 (II)	0/1/0 (II)	0/1/0 (II)
25	1/0/0 (II)	1/0/0 (II)	1/0/0 (II)
26	0/0/0 (0)	0/0/0 (0)	0/0/0 (0)
27	0/0/0 (0)	0/0/0 (0)	0/0/0 (0)

Supradiaphragmal positive? / infradiaphragmal positive? / Extranodal positive? (Ann-Arbor-Stage); „1": yes, „0": no

Table S3 Overview of the lesion detectability using images reconstructed with OSEM-TOF 4i (served as reference) in comparison with the detectability using images reconstructed with OSEM-TOF 4i (short) and OSEM-TOF 2i (reduced).

Patient No.	OSEM-TOF 4i (reference)	OSEM-TOF 4i (reduced)	OSEM-TOF 2i (reduced)
5	1/0/0 (II)	1/0/0 (II)	1/0/0 (II)
9	0/0/0 (0)	0/0/0 (0)	0/0/0 (0)
10	0/0/1 (IV)	0/0/1 (IV)	0/0/1 (IV)
11	0/0/0 (0)	0/0/0 (0)	0/0/0 (0)
12	0/0/1 (I IS)	0/0/1 (IS)	0/0/1 (IS)
13	0/0/0 (0)	0/0/0 (0)	0/0/0 (0)
14	1/1/0 (III)	1/1/0 (III)	1/1/0 (III)
15	0/0/0 (0)	0/0/0 (0)	0/0/0 (0)
16	0/0/0 (0)	0/0/0 (0)	0/0/0 (0)
17	0/0/0 (0)	0/0/0 (0)	0/0/0 (0)
18	1/0/1 (IV)	1/0/1 (IV)	1/0/1 (IV)
19	0/0/0 (0)	0/0/0 (0)	0/0/0 (0)
20	1/1/0 (III)	1/1/0 (III)	1/1/0 (III)
21	1/0/0 (I)	1/0/0 (I)	1/0/0 (I)

22	0/0/0 (0)	0/0/0 (0)	0/0/0 (0)
23	0/0/0 (0)	0/0/0 (0)	0/0/0 (0)
24	0/1/0 (II)	0/1/0 (II)	0/1/0 (II)
25	1/0/0 (II)	1/0/0 (II)	1/0/0 (II)
26	0/0/0 (0)	0/0/0 (0)	0/0/0 (0)
27	0/0/0 (0)	0/0/0 (0)	0/0/0 (0)

Supradiaphragmal positive? / infradiaphragmal positive? / Extranodal positive? (Ann-Arbor-Stage); „1": yes, „0": no

Evaluation of [^{68Ga}]Ga-PSMA PET/CT images acquired with a reduced scan time duration in prostate cancer patients using the digital biograph vision

Reference

Copyright statement

Contributions

I participated in planning of the study and data analysis and contributed to manuscript writing.

ORIGINAL RESEARCH

Evaluation of [68Ga]Ga-PSMA PET/CT images acquired with a reduced scan time duration in prostate cancer patients using the digital biograph vision

Manuel Weber[1][*] , Walter Jentzen[1], Regina Hofferber[1], Ken Herrmann[1], Wolfgang Peter Fendler[1], Maurizio Conti[2], Axel Wetter[3], David Kersting[1], Christoph Rischpler[1] and Pedro Fragoso Costa[1]

Abstract

Aim: [68Ga]Ga-PSMA-11 PET/CT allows for a superior detection of prostate cancer tissue, especially in the context of a low tumor burden. Digital PET/CT bears the potential of reducing scan time duration/administered tracer activity due to, for instance, its higher sensitivity and improved time coincidence resolution. It might thereby expand [68Ga]Ga-PSMA-11 PET/CT that is currently limited by ^{68}Ge/^{68}Ga-generator yield. Our aim was to clinically evaluate the influence of a reduced scan time duration in combination with different image reconstruction algorithms on the diagnostic performance.

Methods: Twenty prostate cancer patients (11 for biochemical recurrence, 5 for initial staging, 4 for metastatic disease) sequentially underwent [68Ga]Ga-PSMA-11 PET/CT on a digital Siemens Biograph Vision. PET data were collected in continuous-bed-motion mode with a mean scan time duration of 16.7 min (reference acquisition protocol) and 4.6 min (reduced acquisition protocol). Four iterative reconstruction algorithms were applied using a time-of-flight (TOF) approach alone or combined with point-spread-function (PSF) correction, each with 2 or 4 iterations. To evaluate the diagnostic performance, the following metrics were chosen: (a) per-region detectability, (b) the tumor maximum and peak standardized uptake values (SUVmax and SUVpeak), and (c) image noise using the liver's activity distribution.

Results: Overall, 98% of regions (91% of affected regions) were correctly classified in the reduced acquisition protocol independent of the image reconstruction algorithm. Two nodal lesions (each ≤ 4 mm) were not identified (leading to downstaging in 1/20 cases). Mean absolute percentage deviation of SUVmax (SUVpeak) was approximately 9% (6%) for each reconstruction algorithm. The mean image noise increased from 13 to 21% (4 iterations) and from 10 to 15% (2 iterations) for PSF $+$ TOF and TOF images.

Conclusions: High agreement at 3.5-fold reduction of scan time in terms of per-region detection (98% of regions) and image quantification (mean deviation $\leq 10\%$) was demonstrated; however, small lesions can be missed in about 10% of patients leading to downstaging (T1N0M0 instead of T1N1M0) in 5% of patients. Our results suggest that a reduction of scan time duration or administered [68Ga]Ga-PSMA-11 activities can be considered in metastatic patients,

*Correspondence: manuel.weber@uk-essen.de
[1] Department of Nuclear Medicine, University of Duisburg-Essen and German Cancer Consortium (DKTK)-University Hospital Essen, Hufelandstrasse 55, 45122 Essen, Germany
Full list of author information is available at the end of the article

Weber *et al. EJNMMI Res*   (2021) 11:21

Page 2 of 12

where missing small lesions would not impact patient management. Limitations include the small and heterogeneous sample size and the lack of follow-up.

Keywords: PET/CT, PSMA, Image quality, Silicon photomultiplier

Introduction

The high sensitivity and specificity of [68]Ga -labeled prostate-specific membrane antigen-ligand positron-emission tomography ([^{68}Ga]Ga-PSMA-11 PET) for prostate cancer lesions has led to an increasing use over the past years [1]. Advantages over other modalities, such as computed tomography (CT) and magnetic resonance imaging as well as bone scan scintigraphy with regards to lesion detection, are particularly marked in patients with low tumor burden, influencing management in a substantial fraction of patients [2, 3].

To ensure optimal image quality the joint EANM/SNMMI procedure guidelines for ^{68}Ga-PSMA PET recommend intravenous administration of 1.8–2.2 MBq [^{68}Ga]Ga-PSMA-11 per kilogram body weight and an emission time of 2–4 min per bed position in step-and-shoot mode [4]. However, availability of [^{68}Ga]Ga-PSMA-11 PET is limited fundamentally by [68]Ge/^{68}Ga-generator yield and, to a lesser degree, positron-emission tomography (PET) scan duration time [5]. Current strategies to expand PSMA PET operation include distribution of ^{18}F-labeled probes with longer half-life.

Another approach will be optimization of acquisition techniques, i.e., reducing the administered activity without notable loss of diagnostic performance. Alternatively, a higher patient throughput could be achieved by reducing scan time duration, which would also decrease the risk for radioactive contamination and patient discomfort due to urinary incontinence [6].

A recent study has shown that the administration of a reduced [^{68}Ga]Ga-PSMA-11 activity was not feasible without sacrificing tumor detectability and image quality on a "conventional" Siemens Biograph mCT PET/CT system [5]. These limitations might potentially be overcome with the advent of a new generation of "digital" PET/CT systems using digital detector technology (of note, the frequently used term "digital" PET is in a way misleading and can be more aptly replaced by silicon photomultiplier-based PET; however, we adopt the term used in current literature). For example, the digital Biograph Vision PET/CT system allows for a higher detector sensitivity, a higher spatial resolution, and an improved coincidence timing resolution compared with its precedent model, the photomultiplier tube-based Biograph mCT [7, 8]. Phantom and patient studies using ^{18}F-labelled glucose have recently confirmed the superior imaging properties

of the new system [8]. This might allow for a better detectability of lesions with faint tracer accumulation.

A prior, still unpublished, phantom optimization study (simulating conditions observed for [^{68}Ga]Ga-PSMA-11 patients) by our group demonstrated that a three and a half-fold reduction of emission time per bed position did not result in any notable loss of lesion detectability and image quantification when using appropriate image reconstruction algorithms and reconstruction parameters [9]. These results can be projected to the use of low activity protocols, as a reduction of emission time roughly corresponds to a reduction of the administered activity by the same factor [5, 10].

Therefore, the aim of this study was to clinically evaluate the feasibility of a three and a half-fold reduced scan time duration on the digital Biograph Vision with regard to detectability, quantification precision, and image quality. In addition, the impact of different image reconstruction algorithms was evaluated.

Methods and materials

Patient population and preparation

Twenty randomly selected patients with prostate cancer undergoing [^{68}Ga]Ga-PSMA-11 PET examination (on clinical indication) were included. Mean patient age (range) was 68 (53–78) years, mean (range) prostate-specific antigen (PSA) levels were 26.1 (0.4–258) ng/mL. Additional file 1: Table S1 provides an in-depth overview of the patient characteristics. For [^{68}Ga]Ga-PSMA-11 PET performance, a mean $\pm$ standard deviation (SD) activity of 124 ± 23 MBq [^{68}Ga]Ga-PSMA-11 was injected intravenously. PET/CT data were acquired after a mean $\pm$ SD time interval of 58 ± 12 min.

Image acquisition

All patients were scanned using a digital Biograph Vision PET/CT system (Siemens Healthcare; Erlangen, Germany), which was recently characterized using [18]F [8]. The [^{68}Ga]Ga-PSMA-11 PET examinations included whole-body PET/CT scans from pelvic to the skull base. PET/CT started with a whole-body spiral CT in full-dose technique using automatic tube current and tube voltage adjustments (Care Dose 4D, quality reference 160 mAs; CARE kV, quality reference 120 kV). CT data were used for attenuation correction and anatomical localization. In the absence of contraindications iodinated contrast medium was administered intravenously. Subsequently,

Weber *et al. EJNMMI Res*   (2021) 11:21

Page 3 of 12

two PET scans—a reference acquisition and a reduced acquisition protocol—were applied in continuous-bed-mode. The reference (or clinical standard) scan was acquired first and lasted on average 16.7 min (standard deviation ± 0.6 min). After its completion, the reduced scan was acquired including the same region and lasted on average 4.6 min (standard deviation ± 0.2 min). The mean ± SD time interval between tracer injection and the first and second PET scan time point was 58 ± 12 min 74 ± 12 min, respectively. The three and a half-fold reduction of the scan time duration was based on a still unpublished optimization study performed on the same PET/CT system using an abdominal phantom simulating the prostate region under conditions observed in prostate cancer imaging [9]. The optimized step-and-shoot emission time in this phantom study was 60 s/bed (or 2.19 mm/s in continuous-bed-motion table speed) in association with appropriate image reconstruction algorithms (see below). The conversion from step-and-shoot emission time per bed (t_{bed}) to continuous-bed-motion table speed (v_{table}) was based on the manufacturer-recommended equivalence settings using an axial field of view (FOV) of 263 mm (or $v_{table} = 0.5$ FOV / t_{bed}) [11].

More specifically, our clinical standard protocol comprised two regions, a prostate and a non-prostate region. For the reference acquisition protocol, the continuous-bed-motion table speed (equivalent step-and-shoot emission time per bed position) was 0.6 mm/s (219 s/bed) within the prostate region (scan length of about 30 cm) and 1.2 mm/s (110 s/bed) from the lower abdomen to the skull base (scan length of about 60 cm). The acquisition time of the non-prostate region was slightly shorter than the EANM procedure guidelines recommend, based on the superior imaging properties of the Vision Biograph [7, 8].

For the reduced acquisition protocol, the table speeds for the respective regions were linearly scaled using the ratio of the optimized to standard step-and-shoot emission time for the prostate region (219 s/bed divided by 60 s/bed), that is, the continuous-bed-motion table speed was 2.2 mm/s (60 s/bed) for the prostate region and 4.4 mm/s (30 s/bed) for the non-prostate region, respectively.

Image reconstruction

The CT images were reconstructed iteratively with a convolution kernel I30f (SAFIRE level of 3). The reconstructed CT slice thickness and the transversal voxel size was 3 mm and 1.5×1.5 mm^2, respectively. In reference to the phantom optimization study, PET images were reconstructed using the three-dimensional ordinary Poisson ordered-subset expectation maximization (OSEM) algorithm with time-of-flight (TOF) approach

alone or combined with point-spread-function (PSF) correction [9]. All reconstructions included scatter and CT-based attenuation correction, decay correction, normalization, and correction for random coincidence. Scatter was corrected using the extended single-scatter simulation algorithm, which distinguished the scattered annihilation radiation according to its TOF [8]. In addition, a prompt gamma coincidence correction method is by default implemented in the PET reconstruction algorithm for radionuclides emitting prompt gammas such as ^{68}Ga (branching ratio of 89% and prompt gamma fraction of 1.2%) [12]. For both acquisition protocols, four image sets were reconstructed: TOF and TOF + PSF, each with 2 iterations (5 subsets) or 4 iterations (5 subsets). The reconstructed images had a voxel size of $3.3 \times 3.3 \times 3.0$ mm^3 and were smoothed with an isotropic Gaussian post reconstruction filter of 4 mm [9]. The measured reconstructed PET spatial resolution (expressed as the full-width-at-half maximum) was 6.2 mm and 5.6 mm for TOF- and TOF + PSF-reconstructed images, respectively [9]. The resulting 4 images (reconstructed for each patient and each acquisition protocol) are referred to OSEM-TOF(2i), OSEM-TOF(4i), OSEM-TOF + PSF (2i), and OSEM-TOF + PSF(4i).

Image analyses

PET data sets were pseudonymized and evaluated in random order by a blinded reader (with no image acquisition and reconstruction information as well as no clinical information). Focal PSMA-uptake higher than the surrounding background was classified as neoplastic if not associated with physiological organ uptake [13]. Pathological findings were then divided into four separate body regions (local tumor, regional lymph node metastases, and soft tissue metastases including extrapelvic lymph nodes and bone metastases) [14]. Maximum and peak standardized uptake values (SUVmax and SUVpeak) were measured for the tumor with the most intense tracer uptake in each body region. Additionally, in each patient, one lesion with faint tracer uptake (if available) was measured. Reading results were then compiled by a member not involved in the reading process. A joint consensus session by two physicians was performed for discordant reports between series of the same patient. Due to the published high inter-observer agreement for [^{68}Ga]Ga-PSMA-11 PET reporting by multiple blinded readers was not deemed necessary [15]. In addition, a spherical volume of interest with a diameter of 30 mm was drawn within the inferior right lob of the liver; the SD of the liver's tissue activity distribution and its mean was ascertained for image noise evaluation [16, 17].

Metrics for diagnostic performance

Three metrics were used to evaluate the diagnostic performance. Primary endpoint was the accuracy of the per-region detectability in the images acquired with the reduced protocol. To this end, images reconstructed with the same algorithm, but acquired with standard emission time duration, were set as reference image. The percentage fraction of correctly classified tumor regions in the images using the reduced acquisition was calculated and changes of miTNM stage were assessed. As secondary endpoint, the precision in image quantification was evaluated using SUVmax and SUVpeak. The ratio between SUVmax (SUVpeak) of PSMA-positive tumors in the reduced and reference acquisition protocol series was calculated among the respective image reconstruction algorithms. The resulting SUV ratios were further categorized in terms of SUVmax showing tumors with faint (SUVmax $\leq$ 5), moderate (5 < SUVmax < 30), and high uptake (SUVmax $\geq$ 30). The SUVmax (SUVpeak) among reference and reduced protocols were correlated by using Pearson product-moment correlation. For the same pairs, Bland–Altman analysis was used to determine the mean differences and 95% limits of agreement between the differences. Finally, the third metric evaluates the image noise and was the percentage ratio of the SD of the tissue activity distribution within the selected liver VOI to its mean value.

Results

Detectability

As assessed by the reference protocol 14/20 patients (70%) were PSMA PET-positive, 8/20 (40%) patients had local tumor, 3/20 (15%) pelvic lymph node metastases, 5/20 (25%) extrapelvic lymph node metastases, 7/20 (35%) bone metastases. None of the patients had visceral metastases. Additionally, focal [68Ga]Ga-PSMA uptake in a celiac ganglion, representing a common pitfall was visible across all acquisition and reconstruction protocols [18].

Using series acquired with the reference protocol, 78/80 regions (98%) and 21/23 (91%) regions with at least one tumour lesion were correctly classified in the reduced protocol (Additional file 1: Tables S2 and S3). Additional file 1: Table S4 gives an extensive overview of patient characteristics including miTNM stage [19] for both protocols. No differences regarding the region classification were observed between the different reconstruction algorithms.

In two patients, one small nodal lesion (each $\leq$ 4 mm short-axis diameter derived from CT images) was missed, each impacting miTNM stage (T1N0M0 instead of T1N1M0; T0N1M1b instead of T0N1M1aM1b). SUVmax (SUVpeak) of the missed mediastinal lymph node

(Fig. 1) was 5.7 (3.1), SUVmax (SUVpeak) of the missed pelvic lymph node (Fig. 2) was 3.8 (2.2). However, just one of these missed lesions led to clinically relevant downstaging.

Figures 1 and 2 show [68Ga]Ga-PSMA-11 PET/CT images of the patients, in whom the lesions were missed across all reconstruction algorithms.

Image quantification

In Fig. 3, dot plots of the ratio of SUVmax und SUVpeak for all 25 lesions are provided separately for lesions with faint, moderate and high uptake. SUVs between images acquired with reduced *vs.* standard protocol images reconstructed with the same algorithms differed by less than 20%, which we defined as an acceptable error margin. The mean absolute percentage deviation (including all 25 lesions) for SUVmax (SUVpeak) for the different image algorithms were 9.4% (6.1%), 8.1% (6.4%), 11.2% (6.2%), 8.3% (5.9%) for OSEM-TOF + PSF (4i), OSEM-TOF + PSF (2i), OSEM-TOF (4i), OSEM-TOF (2i), respectively. No notable differences ($\leq$ 20%) were observed when comparing lesions with different uptake intensities (faint, moderate, and high). Pearson's correlation coefficient between SUVmax of standard vs. reduced acquisition time was 0.996 (PSF + TOF 4i), 0.998 (PSF + TOF 2i), 0.997 (TOF 4i), 0.998 (TOF 2i), respectively. For SUVpeak Pearson's correlation coefficient was 1.000 (PSF + TOF 4i), 0.999 (PSF + TOF 2i), 0.999 (TOF 4i), 0.999 (TOF 2i), respectively. All Pearson coefficients were significantly correlated (p < 0.01). The Bland–Altman plot shows systematic overestimation of SUVmax and SUVpeak in the images acquired with reduced acquisition time (Figs. 4 and 5). This overestimation was more pronounced when using SUVmax. Outliers and scatter levels appear to be more pronounced in images reconstructed with 4 as opposed to 2 iterations.

Image noise

The mean image noise was higher for images acquired with the reduced protocol than for images acquired with the reference protocol (Fig. 6) and these differences were most pronounced in the images reconstructed with 4 iterations. The mean image noise increased from 12 to 20% for OSEM-TOF + PSF (4i), 9% to 13% for OSEM-TOF + PSF (2i), 14% to 22% for OSEM-TOF (4i) and 10% to 15% for OSEM-TOF (2i).

Discussion

This study indicates that a reduction of the scan time duration or administered [68Ga]Ga-PSMA-11 activity produces results comparable to the reference acquisition protocol on a digital Biograph Vision PET/CT system both for detectability (98% of regions correctly

Weber *et al. EJNMMI Res* (2021) 11:21

Page 5 of 12
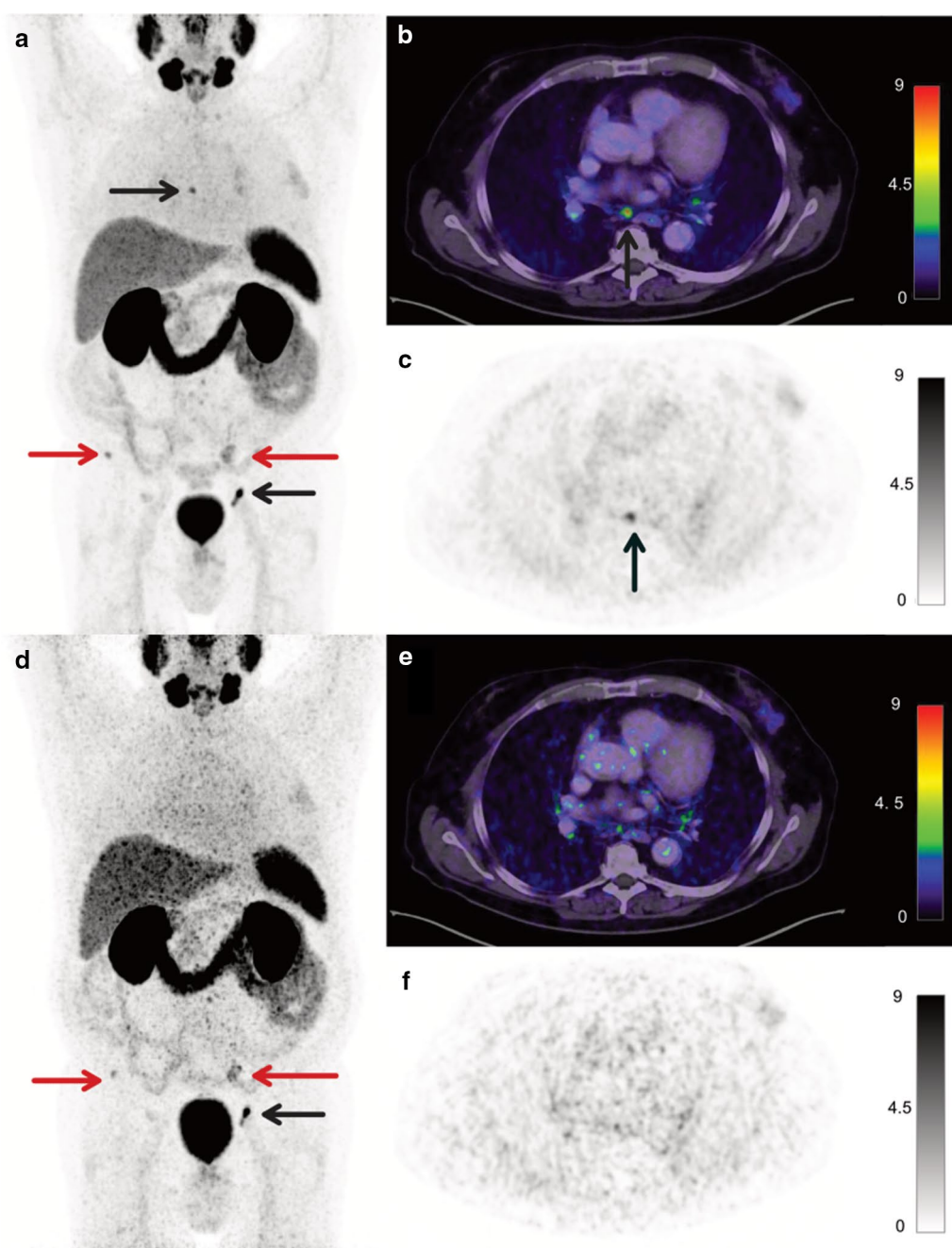
Fig. 1 A 65-years old patient (Pat. ID #7) with second biochemical recurrence after primary prostatectomy and salvage external beam radiation therapy. PSA was 0.6 ng/ml at the time of imaging. **a–c** show images acquired with the reference acquisition protocol; **d–f** show images acquired with the reduced acquisition protocol, all reconstructed with OSEM-PSF + TOF(4i). Pathological tracer uptake in a mediastinal lymph node visible on the images acquired with reference protocol (**c**, black arrow) was not reproducible with three and a half-fold reduction in scan time duration (**f**). Maximum intensity projection (**a**, **d**) and axial [⁶⁸Ga]Ga-PSMA-11 PET/CT slices (**b**, **c**, **e**, **f**) show pelvic and extrapelvic lymph node metastases (black arrows) and bone metastases (red arrows)

identified) and image quantification (mean absolute deviation ≤ 10%) for all reconstruction algorithms but OSEM-TOF (4i).

In our cohort of 20 prostate cancer patients across a variety of miTNM stages undergoing [⁶⁸Ga]Ga-PSMA-11 PET, only two small nodal lesions (short-axis diameter of ≤ 4 mm) were missed (Figs. 1 und 2) leading to
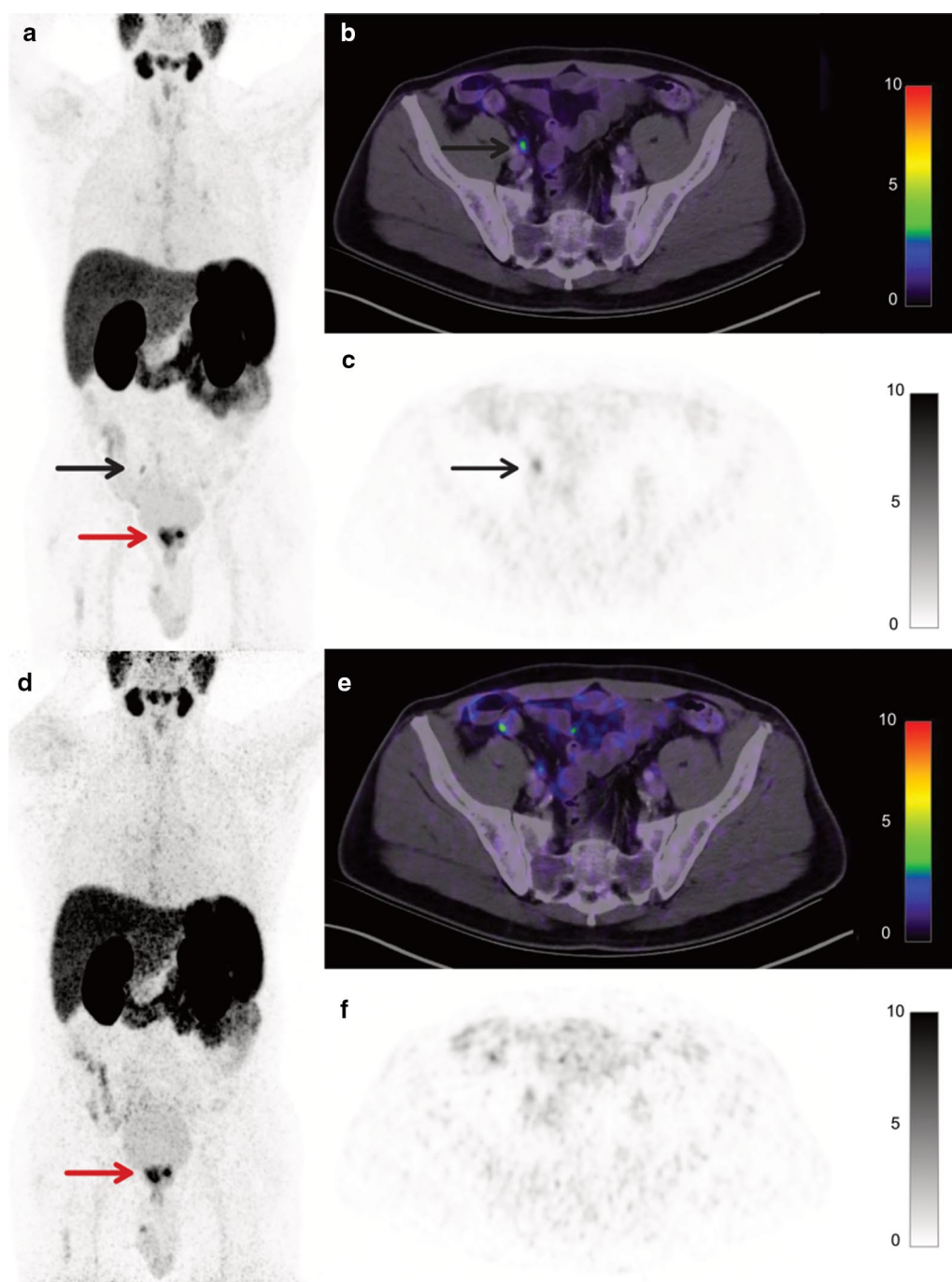
Fig. 2 A 61-year-old patient (Pat ID #13) with biopsy-proven prostate cancer undergoing [⁶⁸Ga]Ga-PSMA-11 PET/CT for initial tumor staging before treatment. Gleason Score was 9, PSA was 18.3 ng/ml at the time of imaging. **a**–**c** show images acquired with the reference acquisition protocol; **d**–**f** show images acquired with the reduced acquisition protocol all reconstructed with OSEM-PSF+TOF(4i). Maximum intensity projection (**a**, **d**) and axial [⁶⁸Ga]Ga-PSMA-11 PET/CT slices (**b**, **c**, **e**, **f**) show local tumor (red arrows). One right pelvic lymph node metastasis (black arrow) could not be unequivocally detected with a three and a half-fold scan time reduction (**c**, **f**). Until now the patient has not undergone surgery, a follow-up scan performed more than 6 months later confirmed the prostatic and lymph node lesions

Weber *et al. EJNMMI Res*   (2021) 11:21

Page 7 of 12

Fig. 3 Dot plots showing the ratio of SUVmax (**a**) and SUVpeak (**b**) between images acquired with reference and reduced scan duration, separately for lesions with faint (filled dots), moderate (white triangles) and intense tracer uptake (filled squares). Margins (± 20) are shown in dashed lines
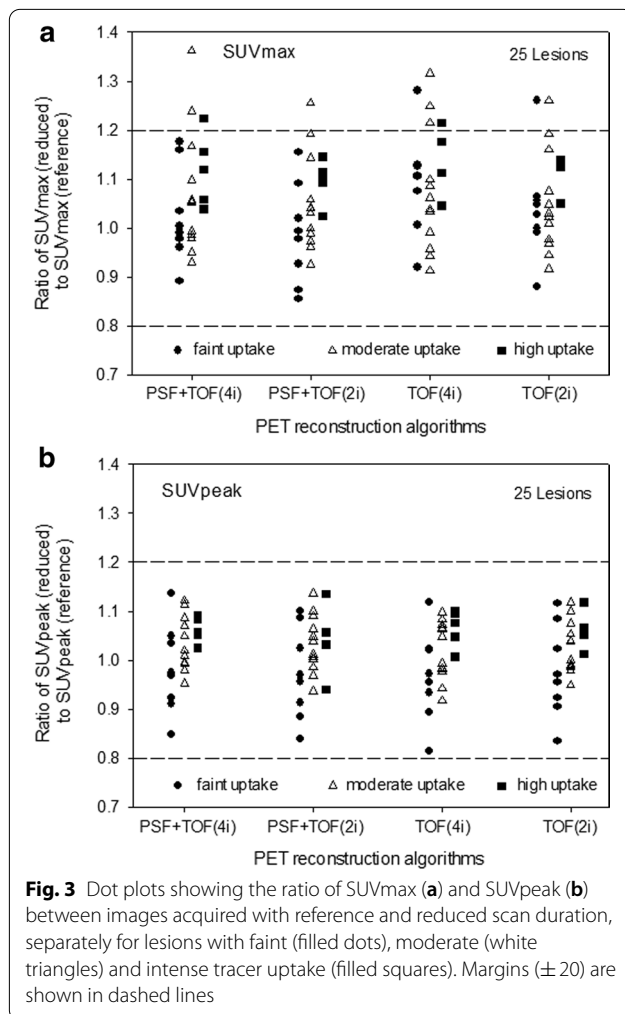
miTNM downstaging in one case. The first lesion was located close to the right common iliac artery, the second in the mediastinum. In one of these cases (lesion 1), this downstaging would have possibly impacted patient management negatively, in the other (lesion 2) the reduced emission time would have been unlikely to cause major changes in management as the patient also had bone metastases.

However, low sensitivities of PSMA PET performed with "conventional" PET/CT systems have previously been reported for the detection of small lesions (< 5 mm) due to partial volume effects [20]. Both of the missed lesions in our cohort showed moderate to faint tracer uptake (SUVmax 5.7 and SUVmax 3.8), which is also known to negatively affect detectability [21]. Additionally, high background due to unspecific small intestinal or mediastinal uptake considerably hampered lesion detection (Figs. 1 and 2). A further possible explanation would

be motion artifacts, among others caused by gastrointestinal peristaltic and arterial pulsation. Administered activities for these patients were above average (129 MBq, 135 MBq) and uptake time within one standard deviation of the mean (48 and 55 min); therefore, both factors are unlikely to be causal.

The main drawback of our reduced acquisition protocol is that small nodal lesions could be missed leading to false-negative [68Ga]Ga-PSMA-11 PET reports, especially in the non-prostate lesion, where the acquisition time is particularly short. This could be addressed by optimizing patient selection, and performing reduced activity protocols in patients, in whom missing small nodal lesions would not impact management. One example could be the imaging of patients with known remote metastases (although the appearance of small new lesions could be missed) and/or those before PSMA-directed radioligand therapy. On the other hand, patients with suspected low tumor burden and/or patients at initial diagnosis would not be ideal candidates.

Recently, two studies have been published that tried to optimize the administered activity and to reduce the emission time duration. First, our findings differ from a previous trial by Rauscher et al. [5], who showed unsatisfactory results for list-mode reconstructed images simulating the administration of one-third and two-third of the standard activity. In contrast to their methodology, whole-body PET list-mode reconstruction was not applicable in our study due to the use of continuous-bed-motion mode, which should preferably be used if available [22]. Additionally, patients enrolled in the trial by Rauscher et al. [5] underwent [68Ga]Ga-PSMA-11 PET on a Siemens Biograph mCT, so the discrepancy in findings might potentially be explained by the different imaging characteristics when compared to its successor, the Siemens Biograph Vision. Second, van Sluis et al. [10] showed an improvement in visually assessed image quality, tumor lesion demarcation, and overall image quality in oncological patients undergoing 2-[18F]FDG PET/CT [7]. In agreement with our short acquisition protocol the same group [10] also found that a threefold reduction of administered activity in oncological patients was feasible, with TNM down-staging only occurring in 1/30 patient cases.

No differences with regards to the detectability were observed for the different reconstruction algorithms. Of note, additional PSF reconstruction did not provide additional value in terms of detectability. This can be largely explained by the implementation of a 4-mm Gaussian filter, producing similar PET reconstructed spatial resolutions for TOF- and TOF + PSF-reconstructed images (6.2 mm vs. 5.6 mm) [9]. In addition, under reduced

Weber *et al. EJNMMI Res*   (2021) 11:21

Page 8 of 12

Fig. 4 Bland–Altman plots showing the agreement of SUVmax between images acquired with reduced vs. standard emission time reconstructed with PSF + TOF (4i, panel **a**) PSF + TOF (2i, panel **b**), TOF (4i, panel **c**), and TOF (2i, panel **d**). A systematic overestimation of high-uptake lesions was observed
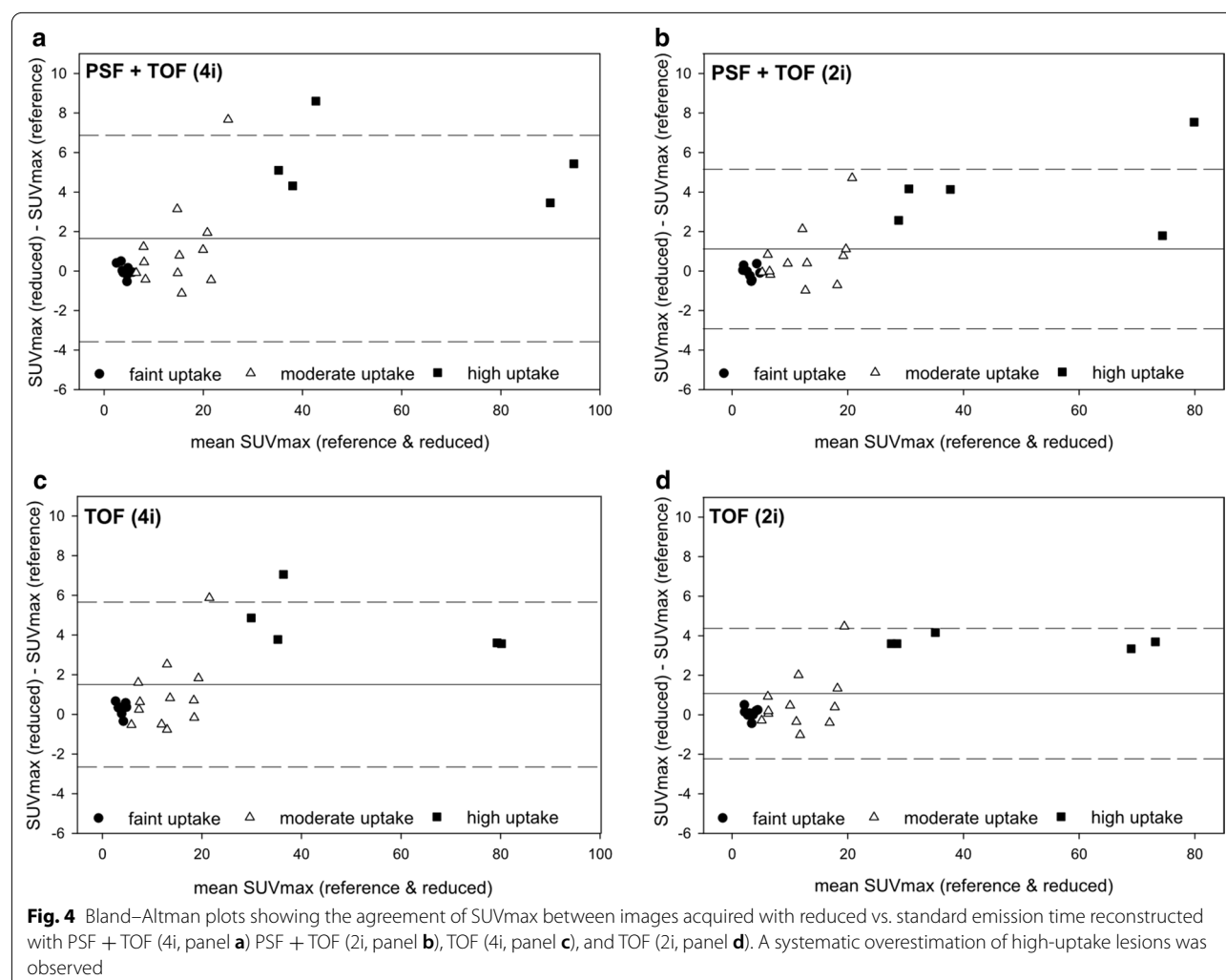
statistical conditions, PET images will inevitably display higher noise [23]. To compensate this loss in image quality, a careful adaptation of iteration number could be considered without compromising lesion detectability by insufficient iterative convergence. In fact, our data suggests that with TOF and TOF + PSF modelling, image noise in the liver can be reduced by applying 2 iterations instead of 4 (Fig. 6). This results confirm previous investigations, underlining the fast convergence capability of TOF [24]. Additionally, recent publications suggest that the implementation of machine learning approaches might enable the image reconstruction of standard activity images even when very low activities are used [25].

There are several limitations in this study. A limitation of our study is the relatively small and heterogeneous sample size, encompassing patients with a wide variety of miTNM stages. Additionally, the reduced acquisition protocol was applied after the reference acquisition protocol and uptake intervals were quite heterogeneous. On the one hand, by doing so the radionuclide decay occurring in the meantime as well as the better alignment with the CT scan favor the standard protocol. On the other hand, metabolic activity changes can occur between both scan acquisitions. As prior studies have observed an increase in tumoral PSMA uptake between images acquired 3 h after tracer administration versus 1 h

Fig. 5 Bland–Altman plots showing the agreement of SUVpeak between images acquired with reduced vs. standard emission time reconstructed with PSF + TOF (4i, panel **a**) PSF+TOF (2i, panel **b**), TOF (4i, panel **c**), and TOF (2i, panel **d**). A systematic overestimation of high-uptake lesions was observed
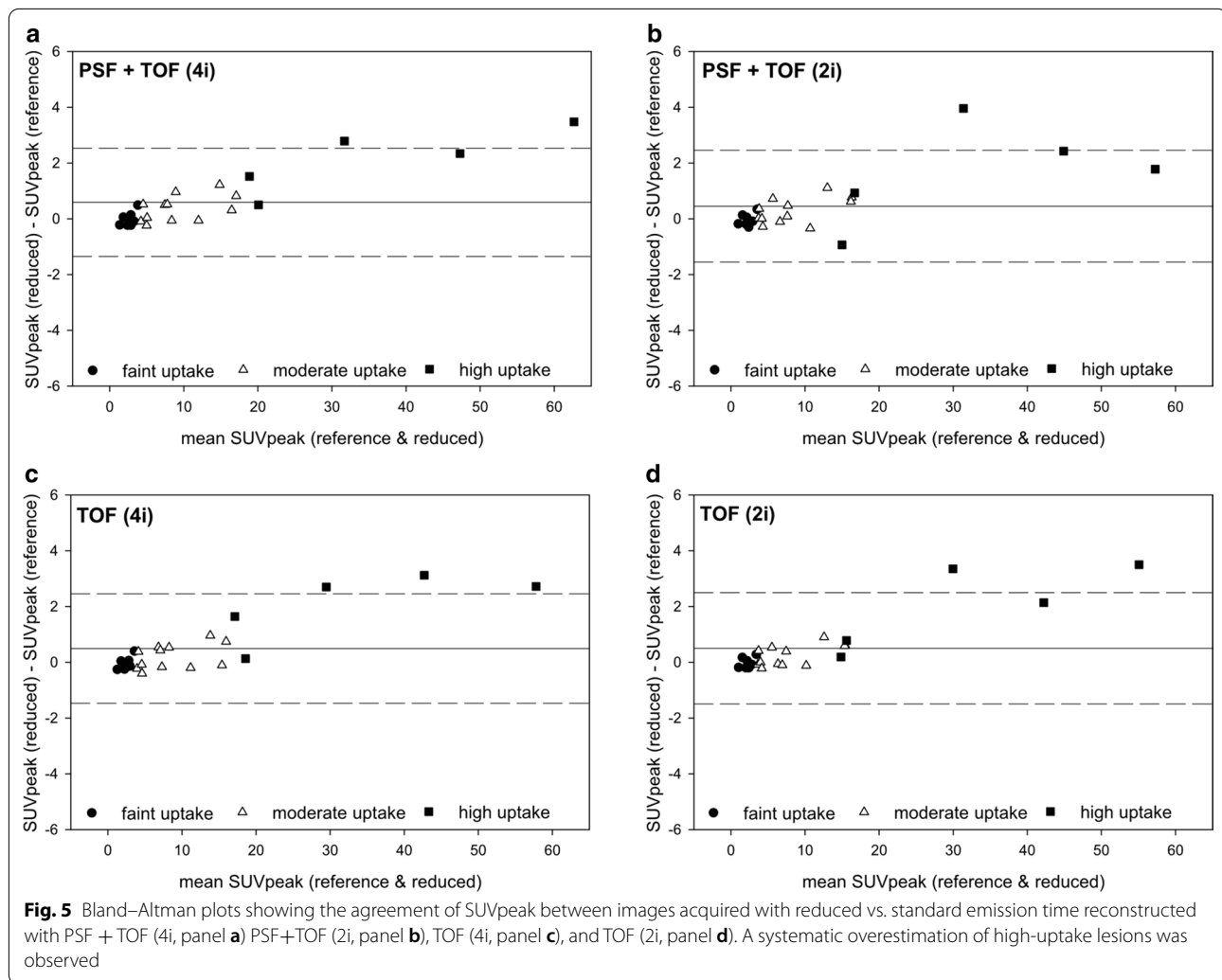
after tracer administration, this might have contributed to differences in image quantification (i.e., the observed overestimation for a few lesions) [26]. This leads to the alternative hypothesis that lesions inapparent on the images acquired (later) with the reduced acquisition protocol, might have been non-neoplastic lesions with decreasing PSMA-uptake over time. Therefore, the reason for missing them might rather be the later uptake interval than the reduced acquisition time.

Furthermore, detectability was performed on a per-region level instead of a per-lesion level. Since the per-region analysis does not account for the identification of additional lesions in the standard acquisition protocol in

a region that is already rated positive in both acquisition protocols, the per-lesion detectability is potentially lower. As the scan time duration of the non-prostate region in the clinical protocol was slightly below the 2–4 min recommended by the EANM guideline, patients might also have potentially been understaged by the clinical protocol. A further limitation of this study is that lesion validation was not performed. However, the current literature suggests a high positive predictive value of [68Ga]Ga-PSMA-11 PET making this a minor issue [3].

Fig. 6 Bar chart showing the image noise derived from the liver's activity distribution for images acquired with the reference (white bars) and reduced protocol (hatched bars) and reconstructed with different reconstruction algorithms (**a**–**d**). Medians are illustrated using dashed lines and the respective numbers are close to the lines
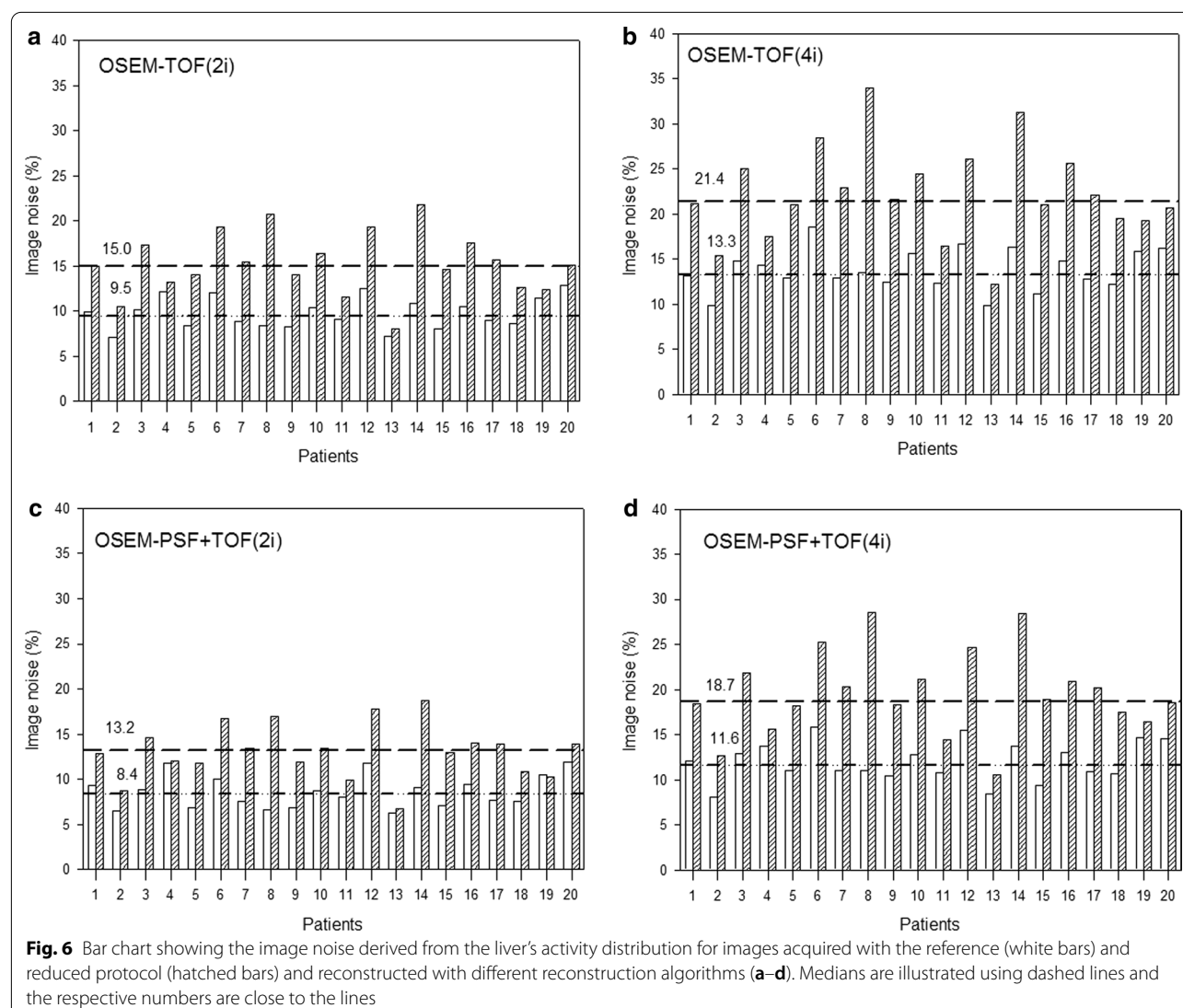
Conclusion

This study shows that the advent of a new generation of digital PET/CT systems bears the potential of reducing emission time (or administered activity) while maintaining an acceptable level of diagnostic performance, As small lesions can be missed, a potential application of a reduced activity/reduced emission time protocol is the imaging of metastatic patients in whom missing small nodal lesions would not impact patient management. As ^{68}Ge/^{68}Ga-generator yield is currently the main limiting factor in most imaging sites, an optimized protocol may subsequently considerably improve [^{68}Ga]Ga-PSMA-11 PET availability.

Supplementary Information

The online version contains supplementary material available at https://doi.org/10.1186/s13550-021-00765-y.

Additional file 1. Patient characteristics, details on lesion detection per region, and resulting stage migration.

Weber *et al. EJNMMI Res*   (2021) 11:21

Page 11 of 12

Author details

[1] Department of Nuclear Medicine, University of Duisburg-Essen and German Cancer Consortium (DKTK)-University Hospital Essen, Hufelandstrasse 55, 45122 Essen, Germany. [2] Siemens Medical Solutions USA, INC, Knoxville, TN, USA. [3] Institute of Diagnostic and Interventional Radiology and Neuroradiology, University of Duisburg-Essen, Essen, Germany.

References

1. Muller J, Ferraro DA, Muehlematter UJ, Garcia Schuler HI, Kedzia S, Eberli D, *et al*. Clinical impact of (68)Ga-PSMA-11 PET on patient management and outcome, including all patients referred for an increase in PSA level during the first year after its clinical introduction. Eur J Nucl Med Mol Imaging. 2019;46:889–900. https://doi.org/10.1007/s00259-018-4203-0.
2. Han S, Woo S, Kim YJ, Suh CH. Impact of (68)Ga-PSMA PET on the management of patients with prostate cancer: a systematic review and meta-analysis. Eur Urol. 2018;74:179–90. https://doi.org/10.1016/j.eururo.2018.03.030.
3. Hope TA, Goodman JZ, Allen IE, Calais J, Fendler WP, Carroll PR. Metaanalysis of (68)Ga-PSMA-11 PET accuracy for the detection of prostate cancer validated by histopathology. J Nucl Med. 2019;60:786–93. https://doi.org/10.2967/jnumed.118.219501.
4. Fendler WP, Eiber M, Beheshti M, Bomanji J, Ceci F, Cho S, *et al*. (68)Ga-PSMA PET/CT: Joint EANM and SNMMI procedure guideline for prostate cancer imaging: version 1.0. Eur J Nucl Med Mol Imaging. 2017;44:1014–24. https://doi.org/10.1007/s00259-017-3670-z.
5. Rauscher I, Fendler WP, Hope TA, Quon A, Nekolla SG, Calais J, *et al*. Can the injected dose be reduced in (68)Ga-PSMA-11 PET/CT while maintaining high image quality for lesion detection? J Nucl Med. 2020;61:189–93. https://doi.org/10.2967/jnumed.119.227207.
6. Freitag MT, Radtke JP, Afshar-Oromieh A, Roethke MC, Hadaschik BA, Gleave M, *et al*. Local recurrence of prostate cancer after radical prostatectomy is at risk to be missed in (68)Ga-PSMA-11-PET of PET/CT and PET/MRI: comparison with mpMRI integrated in simultaneous PET/MRI. Eur J Nucl Med Mol Imaging. 2017;44:776–87. https://doi.org/10.1007/s00259-016-3594-z.
7. van Sluis J, Boellaard R, Somasundaram A, van Snick PH, Borra RJH, Dierckx R, *et al*. Image quality and semiquantitative measurements on the biograph vision PET/CT system: initial experiences and comparison with the biograph mCT. J Nucl Med. 2020;61:129–35. https://doi.org/10.2967/jnumed.119.227801.
8. van Sluis J, de Jong J, Schaar J, Noordzij W, van Snick P, Dierckx R, *et al*. Performance characteristics of the digital biograph vision PET/CT system. J Nucl Med. 2019;60:1031–6. https://doi.org/10.2967/jnumed.118.215418.
9. Fragoso Costa P, Süßelbeck F, Bramer A, Conti M, Weber M, Kersting D, et al. Emission time optimisation for Ga-68-PSMA with a digital PET/CT – a phantom study [abstract]. https://www.nuklearmedizin.de/jahrestagungen/abstr_online2020/abstract_detail.php?navId=236&ald=107. Nuklearmedizin 2020 (submission accepted)
10. van Sluis J, Boellaard R, Dierckx R, Stormezand GN, Glaudemans A, Noordzij W. Image quality and activity optimization in oncologic (18) F-FDG PET using the digital biograph vision PET/CT system. J Nucl Med. 2020;61:764–71. https://doi.org/10.2967/jnumed.119.234351.
11. Siman W, Kappadath SC. Comparison of step-and-shoot and continuous-bed-motion PET modes of acquisition for limited-view organ scans. J Nucl Med Technol. 2017;45:290–6. https://doi.org/10.2967/jnmt.117.195438.
12. Wierts R, Conti M, Claessen AGG, Herrmann K, Kemerink GJ, Binse I, *et al*. Impact of prompt gamma coincidence correction on absorbed dose estimation in differentiated thyroid cancer using 124I PET/CT imaging. Nucl Med Commun. 2018;39:1156–64. https://doi.org/10.1097/MNM.0000000000000911.
13. Rauscher I, Maurer T, Fendler WP, Sommer WH, Schwaiger M, Eiber M. (68) Ga-PSMA ligand PET/CT in patients with prostate cancer: how we review and report. Cancer Imaging. 2016;16:14. https://doi.org/10.1186/s40644-016-0072-6.
14. Fendler WP, Weber M, Iravani A, Hofman MS, Calais J, Czernin J, *et al*. Prostate-specific membrane antigen ligand positron emission tomography in men with nonmetastatic castration-resistant prostate cancer. Clin Cancer Res. 2019;25:7448–54. https://doi.org/10.1158/1078-0432.CCR-19-1050.
15. Fendler WP, Calais J, Allen-Auerbach M, Bluemel C, Eberhardt N, Emmett L, *et al*. (68)Ga-PSMA-11 PET/CT interobserver agreement for prostate cancer assessments: an international multicenter prospective study. J Nucl Med. 2017;58:1617–23. https://doi.org/10.2967/jnumed.117.190827.
16. Boellaard R, O'Doherty MJ, Weber WA, Mottaghy FM, Lonsdale MN, Stroobants SG, *et al*. FDG PET and PET/CT: EANM procedure guidelines for tumour PET imaging: version 1.0. Eur J Nucl Med Mol Imaging. 2010;37:181–200. https://doi.org/10.1007/s00259-009-1297-4.
17. Wahl RL, Jacene H, Kasamon Y, Lodge MA. From RECIST to PERCIST: evolving considerations for PET response criteria in solid tumors. J Nucl Med. 2009;50(Suppl 1):122S-S150. https://doi.org/10.2967/jnumed.108.057307.
18. Rischpler C, Beck TI, Okamoto S, Schlitter AM, Knorr K, Schwaiger M, *et al*. (68)Ga-PSMA-HBED-CC uptake in cervical, celiac, and sacral ganglia as an important pitfall in prostate cancer PET imaging. J Nucl Med. 2018;59:1406–11. https://doi.org/10.2967/jnumed.117.204677.
19. Eiber M, Herrmann K, Calais J, Hadaschik B, Giesel FL, Hartenbach M, *et al*. Prostate cancer molecular imaging standardized evaluation (PROMISE): proposed miTNM classification for the interpretation of PSMA-ligand PET/CT. J Nucl Med. 2018;59:469–78. https://doi.org/10.2967/jnumed.117.198119.
20. van Leeuwen PJ, Emmett L, Ho B, Delprado W, Ting F, Nguyen Q, *et al*. Prospective evaluation of 68Gallium-prostate-specific membrane antigen positron emission tomography/computed tomography for preoperative lymph node staging in prostate cancer. BJU Int. 2017;119:209–15. https://doi.org/10.1111/bju.13540.
21. Fendler WP, Calais J, Eiber M, Flavell RR, Mishoe A, Feng FY, *et al*. Assessment of 68Ga-PSMA-11 PET accuracy in localizing recurrent prostate cancer: a prospective single-arm clinical trial. JAMA Oncol. 2019;5:856–63. https://doi.org/10.1001/jamaoncol.2019.0096.
22. Brasse D, Newport D, Carney J, Yap J, Reynolds C, Reed J, et al. Continuous bed motion acquisition on a whole body combined PET/CT system; 2002.
23. de Groot EH, Post N, Boellaard R, Wagenaar NR, Willemsen AT, van Dalen JA. Optimized dose regimen for whole-body FDG-PET imaging. EJNMMI Res. 2013;3:63. https://doi.org/10.1186/2191-219X-3-63.

Weber *et al. EJNMMI Res*   (2021) 11:21

Page 12 of 12

24. Conti M, Eriksson L, Westerwoudt V. Estimating image quality for future generations of TOF PET scanners. IEEE Trans Nucl Sci. 2013;60:87–94. https ://doi.org/10.1109/Tns.2012.2233214.

25. Ouyang J, Chen KT, Gong E, Pauly J, Zaharchuk G. Ultra-low-dose PET reconstruction using generative adversarial network with feature matching and task-specific perceptual loss. Med Phys. 2019;46:3555–64. https://doi.org/10.1002/mp.13626.

26. Afshar-Oromieh A, Malcher A, Eder M, Eisenhut M, Linhart HG, Hadaschik BA, *et al*. PET imaging with a [68Ga]gallium-labelled PSMA ligand for the diagnosis of prostate cancer: biodistribution in humans and first evaluation of tumour lesions. Eur J Nucl Med Mol Imaging. 2013;40:486–95. https://doi.org/10.1007/s00259-012-2298-2.

Publisher's Note

Springer Nature remains neutral with regard to jurisdictional claims in published maps and institutional affiliations.

Supplemental Table S1

Table S1.
Patient Characteristics (n=20)

Age and PSA	Values for age and PSA
Median (range) age (years)	68 (53–78)
Median (range) PSA (ng/mL)	3.2 (0.4–258)

Gleason score	Number of patients
6	4
7	5
8	3
9	3
NA	5

Initial treatment (number of patients)	Number of patients
None	5
Prostatectomy	11
Primary EBRT	3
Salvage EBRT	5
ADT	5
Enzalutamide/Abiraterone	4
Chemotherapy	3
Others	1

NA, not available; EBRT, external beam radiation therapy

Supplemental Table S2

Overview of the lesion detectability using images reconstructed with OSEM-TOF 4i (served as reference) in comparison with the detectability using images reconstructed with OSEM-TOF 4i (short) and OSEM-TOF 2i (reduced).

Pat. ID.	Lesion detection OSEM-TOF(4i) (reference)	Lesion detection OSEM-TOF(4i) (reduced)	Lesion detection OSEM-TOF(2i) (reduced)
1	1/0/1/1	1/0/1/1	1/0/1/1
2	0/0/1/0	0/0/1/0	0/0/1/0
3	0/0/0/0	0/0/0/0	0/0/0/0
4	0/0/0/0	0/0/0/0	0/0/0/0
5	1/0/0/0	1/0/0/0	1/0/0/0
6	0/0/1/0	0/0/1/0	0/0/1/0
7	0/1/1/1	0/1/**0**/1	0/1/**0**/1
8	1/0/0/0	1/0/0/0	1/0/0/0
9	0/0/0/1	0/0/0/1	0/0/0/1
10	0/0/0/1	0/0/0/1	0/0/0/1
11	0/0/0/0	0/0/0/0	0/0/0/0
12	0/0/0/0	0/0/0/0	0/0/0/0
13	1/1/0/0	1/**0**/0/0	1/**0**/0/0
14	1/1/1/1	1/1/1/1	1/1/1/1
15	1/0/0/0	1/0/0/0	1/0/0/0
16	0/0/0/1	0/0/0/1	0/0/0/1
17	1/0/0/0	1/0/0/0	1/0/0/0
18	1/0/0/1	1/0/0/1	1/0/0/1
19	0/0/0/0	0/0/0/0	0/0/0/0
20	0/0/0/0	0/0/0/0	0/0/0/0

*Classified tumor regions are local tumor/regional metastatic lymph nodes/extrapelvic soft-tissue tumors including lymph nodes/bone tumors. Symbol „1" marks the presence of at least one lesion, symbol „0" denotes the absence of lesions in this region. Mismatches in comparison with the reference are marked in red.

Supplemental Table S3

Table S3

Overview of the lesion detectability using images reconstructed with OSEM-TOF+PSF(4i) (served as as reference) in comparison with the detectability using images reconstructed with OSEM-TOF+PSF(4i) (reduced) and OSEM-TOF+PSF(2i) (reduced).

Pat. ID	Lesion detection OSEM-PSF+TOF(4i) (reference)	Lesion detection OSEM-PSF+TOF(4i) (reduced)	Lesion detection OSEM-PSF+TOF(2i) (reduced)
1	1/0/1/1	1/0/1/1	1/0/1/1
2	0/0/1/0	0/0/1/0	0/0/1/0
3	0/0/0/0	0/0/0/0	0/0/0/0
4	0/0/0/0	0/0/0/0	0/0/0/0
5	1/0/0/0	1/0/0/0	1/0/0/0
6	0/0/1/0	0/0/1/0	0/0/1/0
7	0/1/1/1	0/1/**0**/1	0/1/**0**/1
8	1/0/0/0	1/0/0/0	1/0/0/0
9	0/0/0/1	0/0/0/1	0/0/0/1
10	0/0/0/1	0/0/0/1	0/0/0/1
11	0/0/0/0	0/0/0/0	0/0/0/0
12	0/0/0/0	0/0/0/0	0/0/0/0
13	1/1/0/0	1/**0**/0/0	1/**0**/0/0
14	1/1/1/1	1/1/1/1	1/1/1/1
15	1/0/0/0	1/0/0/0	1/0/0/0
16	0/0/0/1	0/0/0/1	0/0/0/1
17	1/0/0/0	1/0/0/0	1/0/0/0
18	1/0/0/1	1/0/0/1	1/0/0/1
19	0/0/0/0	0/0/0/0	0/0/0/0
20	0/0/0/0	0/0/0/0	0/0/0/0

*Classified tumor regions are local tumor/regional metastatic lymph nodes/extrapelvic soft-tissue tumors including lymph nodes/bone tumors. Symbol „1" marks the presence of at least one lesion, symbol „0" denotes the absence of lesions in this region. Mismatches in comparison with the reference are marked in red.

Supplemental Table S4

Table S4.

Imaging Characteristics Including miTNM Stage as Assessed by the Reference and Reduced Protocol

Pat. ID	Activity (MBq)	Uptake period (min)	Weight (kg)	Reference protocol	Reduced protocol
1	124	45	75	T1N1M1aM1b	T1N1M1aM1b
2	155	63	94	T0N1M1a	T0N1M1a
3	86	32	79	T1N0	T1N0
4	94	57	83	T1N0	T1N0
5	134	48	94	T1N0	T1N0
6	119	65	76	T0N0M1a	T0N0M1a
7	129	48	75	T0N1M1aM1b	**T0N1M1b**
8	151	61	75	T1N0	T1N0
9	135	43	97	T1N0M1b	T1N0M1b
10	124	60	110	T0N0M1bM1c	T0N0M1bM1c
11	152	68	72	T1N0	T1N0
12	148	68	80	T1N0	T1N0
13	135	55	92	T1N1	**T1N0**
14	87	46	80	T1N1M1aM1b	T1N1M1aM1b
15	128	72	81	T1N0	T1N0
16	88	62	95	T0N0M1b	T0N0M1b
17	93	82	72	T1N0	T1N0
18	128	42	87	T1N0M1b	T1N0M1b
19	134	70	77	T0N1	T0N1
20	137	71	100	T0N0	T0N0

Pat. ID, patient identification; changes in miTNM stage are marked in red.

Comparing lesion detection efficacy and image quality across different PET system generations to optimize the iodine-124 PET protocol for recurrent thyroid cancer

Reference

Copyright statement

Contributions

I participated in study design, data acquisition and data analysis and mainly contributed to manuscript writing.

ORIGINAL RESEARCH   Open Access

Comparing lesion detection efficacy and image quality across different PET system generations to optimize the iodine-124 PET protocol for recurrent thyroid cancer

David Kersting[1,2,3*] , Walter Jentzen[1,2,3], Miriam Sraieb[1,2,3], Pedro Fragoso Costa[1,2,3], Maurizio Conti[4], Lale Umutlu[2,3,5], Gerald Antoch[3,6], Michael Nader[1,2,3], Ken Herrmann[1,2,3], Wolfgang Peter Fendler[1,2,3], Christoph Rischpler[1,2,3] and Manuel Weber[1,2,3]

* Correspondence: david.kersting@uni-due.de
[1]Department of Nuclear Medicine, University Hospital Essen, University of Duisburg-Essen, Hufelandstrasse 55, 45147 Essen, Germany
[2]West German Cancer Center (WTZ), Essen, Germany
Full list of author information is available at the end of the article

Abstract

Background: In recurrent differentiated thyroid cancer patients, detectability in ^{124}I PET is limited for lesions with low radioiodine uptake. We assess the improvements in lesion detectability and image quality between three generations of PET scanners with different detector technologies. The results are used to suggest an optimized protocol.

Methods: Datasets of 10 patients with low increasing thyroglobulin or thyroglobulin antibody levels after total thyroidectomy and radioiodine therapies were included. PET data were acquired and reconstructed on a Biograph mCT PET/CT (whole-body, 4-min acquisition time per bed position; OSEM, OSEM-TOF, OSEM-TOF+PSF), a non-TOF Biograph mMR PET/MR (neck region, 4 min and 20 min; OSEM), and a new generation Biograph Vision PET/CT (whole-body, 4 min; OSEM, OSEM-TOF, OSEM-TOF+PSF). The 20-min image on the mMR was used as reference to calculate the detection efficacy in the neck region. Image quality was rated on a 5-point scale.

Results: All detected lesions were in the neck region. Detection efficacy was 8/9 (Vision OSEM-TOF and OSEM-TOF+PSF), 4/9 (Vision OSEM), 3/9 (mMR OSEM and mCT OSEM-TOF+PSF), and 2/9 (mCT OSEM and OSEM-TOF). Median image quality was 4 (Vision OSEM-TOF and OSEM-TOF+PSF), 3 (Vision OSEM, mCT OSEM-TOF+PSF, and mMR OSEM 20-min), 2 (mCT OSEM-TOF), 1.5 (mCT OSEM), and 1 (mMR OSEM 4 min).

Conclusion: At a clinical standard acquisition time of 4 min per bed position, the new generation Biograph Vision using a TOF-based image reconstruction demonstrated the highest detectability and image quality and should, if available, be preferably used for imaging of low-uptake lesions. A prolonged acquisition time for the mostly affected neck region can be useful.

Keywords: Iodine-124 PET, Digital PET/CT, Biograph Vision, Detectability, Differentiated thyroid cancer

Background

Elevated thyroglobulin (Tg) levels in differentiated thyroid cancer (DTC) patients after total thyroidectomy and radioiodine therapies are associated with detectable recurrence [1] and poor outcome [2, 3]. According to the current American Thyroid Association (ATA) guideline [4], DTC patients with elevated Tg levels undergo a diagnostic iodine-131 (^{131}I) whole-body scan (~ 185 MBq). Radioiodine therapy (1.85–7.40 GBq) is performed if radioiodine-avid lesions are identified. However, diagnostic whole-body scans are limited, e.g., by a low diagnostic accuracy of 36% in biochemical recurrent intermediate- or high-risk DTC patients [5]. A suitable alternative is iodine-124 ([124]I) positron emission tomography (PET) imaging. For instance, studies demonstrated that 50% more foci of radioiodine-avid lesion compared to diagnostic whole-body scans were identified [6] and a high level of agreement (95%) between [124]I PET and intra-therapeutic ^{131}I single photon emission computed tomography/computed tomography (SPECT/CT) was found [7]. However, false negative results may arise for lesions with [124]I activities below the PET scanner's size-dependent minimum detectable activity [7–9]. The recently introduced "digital" silicon photomultiplier-based (SiPM-based) PET/CT systems show a higher coincidence time resolution and a higher spatial resolution [10] (compared to conventioanl PET/CT systems). These properties were associated with a higher image quality and a higher detectability of small lesions in phantom settings and clinical applications in different studies using 2-deoxy-2-[fluorine-18]-fluoro-D-glucose (^{18}F-FDG) [11–14] and, most recently, using [gallium-68]gallium-prostate-specific membrane antigen-11 [15].

In DTC patients with low but increasing Tg levels, the recurring lesions are often small and exhibit low [124]I uptake values. Moreover, [124]I possesses a low positron branching ratio (23%) and [124]I PET emission data are contaminated by a high prompt gamma fraction (about one-third of total coincidences) requiring advanced image correction prior to image reconstruction [16]. In combination with typically low administered [124]I activities, these properties result in low count statistics and noisy images — one reason why [124]I PET especially benefits from time-of-flight (TOF) image reconstructions [17]. Therefore, the improved TOF performance and sensitivity of SiPM-based PET/CT systems might have a particularly pronounced effect for [124]I in this patient cohort. In addition, a combination of TOF and point spread function modeling (PSF) image reconstruction bears potential for further quality improvement [18]. In a comparison using ^{18}F-FDG on a digital PET/CT system, OSEM-TOF+PSF reached improvements to OSEM-TOF image reconstruction in image quality, image sharpness, and lesion conspicuity [19].

We hypothesize that the use of SiPM-based PET systems will lead to relevant improvements in thyroid cancer detectability and image quality. In this study, datasets of 10 DTC patients were evaluated, who received [124]I imaging on three PET systems with different detector technologies. We aim to assess the influence of SiPM-based PET on detection efficacy for lesions in the neck region, and on visual image quality. Furthermore, the data are used to suggest an [124]I PET protocol for recurrent thyroid cancer considering, inter alia, the acquisition time duration, and the amount of applied [124]I activity.

Methods

PET scanners

All patients were scanned on two PET/CT systems, a SiPM-based Biograph Vision 600 and a photomultiplier tube (PMT)-based Biograph mCT, and one PET/MR (magnetic

resonance imaging) system, an avalanche photodiode (APD)-based Biograph mMR (all from Siemens Healthineers, Erlangen, Germany). A short description of the scanner specifications is shown as Supplemental Material.

Patient characteristics

The local institutional ethics committee (University of Duisburg-Essen) approved the study (Ethics protocol number 20-9203-BO). In the following, all scaled variables are presented as mean ± standard deviation (SD), and ordinal data are presented as median (interquartile range = IQR).

We routinely perform whole-body ^{124}I PET/CT on the analog Biograph mCT as well as a prolonged scan duration PET/MR of the neck region using the Biograph mMR in DTC patients with low increasing Tg and/or Tg antibody levels after total thyroid ablation. Since its introduction at our center, patients of this rare group [20] were additionally examined on the digital Biograph Vision PET/CT system, resulting in 10 DTC patients examined on three PET systems until April 2020. These patients were retrospectively evaluated in this study. Specifically, datasets of these 5 males and 5 females after total thyroidectomy and adjuvant radioiodine therapies were included (7 with papillary and 3 with follicular thyroid cancer, mean ± SD age 52 ± 18 years). In 9 patients, Tg levels were elevated in the low measurable range (mean unstimulated Tg value of 1.8 ± 1.8 ng/mL, range 0.1–5.5 ng/mL), in one patient Tg antibody levels were elevated (273 IU/mL) with non-measurable Tg. Serum thyroid stimulating hormone level stimulation (≥ 30 mU/L) was achieved by levothyroxine withdrawal or intramuscular recombinant human thyroid stimulating hormone injection prior to ^{124}I application. Detailed patient characteristics are given in the Supplemental Material.

Acquisition and image reconstruction

The initial PET scans were acquired 17.1 ± 1.0 h after oral application of 38.3 ± 2.1 MBq of ^{124}I; acquisitions on all three scanners were performed within an interval of 4.7 ± 2.9 h (details in Supplemental Material). For the Vision and mCT, the examinations included whole-body PET/CT scans from head to thigh using 5–8 bed positions; the acquisition time duration was 4 min per bed position. For the mMR, a neck scan (a single bed position) was acquired at 20-min acquisition time in list-mode (allowing for resampling of 4-min acquisition time data). PET/CT scans started with a whole-body spiral CT in low-dose technique (tube voltage of 120 kVp, tube current time product of 15 mAs, beam pitch of 1.0, and slice width of 5 mm) without application of contrast agent. Subsequently, the PET scan was acquired. On the PET/MR, simultaneous with PET, T1-weighted MR images were acquired using a VIBE sequence after application of gadolinium-based contrast agent.

All scanners allow for iterative image reconstruction algorithms. Image reconstructions were performed using (three-dimensional) ordinary Poisson ordered-subsets expectation maximization (OSEM), with TOF reconstruction alone (OSEM-TOF), or with both TOF and PSF (OSEM-TOF+PSF). On the mMR, the slow timing characteristics of avalanche photodiodes preclude the TOF reconstruction. All PET data were reconstructed using our clinically standard reconstruction protocols that were optimized for quantitative ^{124}I imaging [21] and are listed in Table 1. They were corrected for scatter,

Table 1 Standard clinical reconstruction parameters for the different PET scanners

Iterative reconstruction	Scanner type	Iterations × subsets	Gauss filter (mm)	Voxel size (mm^3)
OSEM	Vision	10 × 5	4	1.7 × 1.7 × 2.0
	mCT	3 × 24	3	2.0 × 2.0 × 2.0
	mMR	3 × 21	4	2.1 × 2.1 × 2.0
OSEM-TOF	Vision	4 × 5	4	1.7 × 1.7 × 2.0
	mCT	2 × 21	3	2.0 × 2.0 × 2.0
	mMR	–	–	–
OSEM-TOF+PSF	Vision	4 × 5	4	1.7 × 1.7 × 2.0
	mCT	2 × 21	3	2.0 × 2.0 × 2.0
	mMR	–	–	–

randoms, attenuation, dead time, decay, and normalization. For PET/MR images, attenuation correction was based on an attenuation map (μ-map) derived from a 3-dimensional Dixon-VIBE MR sequence. In addition, for all PET systems, the same prompt gamma coincidence correction method is by default implemented in the PET reconstruction algorithm for radionuclides emitting prompt gammas such as [124]I [22, 23].

Image analysis

Detection efficacy and visual image quality

All PET datasets were assigned a random number as identifier. The images were anonymized and interpreted in random order in a consensus read by three nuclear medicine residents. The readers were blinded to clinical information, PET scanner type, and acquisition protocol to exclude prior knowledge from previously evaluated studies about the localizations of lesions. Focal [124]I uptake was reported in five separate anatomical regions: local thyroid bed, cervical lymph nodes, extra-cervical lymph nodes (only PET/CT), lungs (only PET/CT), and bones. For each lesion, the maximum standardized uptake value (SUV_{max}), the maximum activity concentration (AC_{max}), and the local signal-to-background ratio (ratio of lesion SUV_{max} to background SUV_{bgr} derived from a region of interest surrounding the lesion) were determined. The long-axis diameters of the lesions were measured on the MR images; for morphologically not clearly definable lesions, an upper size limit was estimated from the PET data using an iterative volume segmentation approach [24]. These functional and morphological properties were assessed to correlate their values with differences in detectability. Moreover, the image quality was visually assessed in transversal slices of the PET images on an established 5-point Likert-like scale from 1 (poor) to 5 (excellent) [25].

Lesion- and patient-based analysis

For the lesion-based analysis, the total number of [124]I-positive lesions in the neck region were counted across all PET systems, acquisition time durations, and image reconstruction algorithms. A total of nine lesions were detected in the neck region; the 20-min acquisition time reference scan on the mMR was the only acquisition in which all lesions were detectable, no additional lesions were reported on the whole-body PET/CT images. The detectability in PET images is dependent on the acquisition time [26].

We therefore used PET data acquired for a clinical standard acquisition time of 4 min per bed position to compare the detectability across the different generations of PET systems. Detection efficacy was defined as the number of lesions identified divided by nine lesions (in the reference image). For the patient-based analysis, the total number of radioiodine-positive patients was counted, and the distinct levels of agreement were determined.

Statistical analysis

Statistical analyses were performed using OriginPro 2020b (OriginLab, Northampton, USA). For assessing changes in visual image quality (ordinal data) a Mann-Whitney test was used. A p value < 0.05 was considered statistically significant.

Results

Lesion-based and patient-based detection efficacy analysis

Detection efficacy results are summarized in Fig. 1a, b and Table 2, detailed lesion characteristics are presented in Table 3. If not otherwise stated, the individual values presented in the subsequent paragraphs were taken from images acquired on the Vision and reconstructed using OSEM-TOF.

Detection efficacy was 8/9 on the Vision in both OSEM-TOF and OSEM-TOF+PSF images. The only lesion (#4, about 7 mm in diameter), which was not detected (Fig. 2b), had the lowest AC_{max} of 0.8 kBq/mL and SUV_{max} of 2.3 (all values for this specific lesion were measured on the mMR images at 20-min acquisition time). A detection efficacy of 4/9 (lesions #1, #2, #6, #8) was reached on the Vision using OSEM. The four lesions that were only detected in OSEM-TOF and OSEM-TOF+PSF images were small (≤ 9 mm) and of very low AC_{max} (≤ 1.2 kBq/mL) and SUV_{max} (≤ 3.4) (e.g., lesion #5 in Fig. 2a).

Detection efficacy was 3/9 (lesions #1, #6, #8) on the mMR at 4-min acquisition time. The six lesions that were not detected at 4-min acquisition time comprised the five lesions that were not detected using OSEM on the Vision and one cervical lymph node (#2, 17 mm, AC_{max} 3.5 kBq/mL, SUV_{max} 9.9) that was probably not detected, as it was hardly distinguishable from a different lymph node localized directly next to it.

Detection efficacy was 3/9 on the mCT using OSEM-TOF+PSF (lesions #1, #2, #6) and 2/9 (lesions #1, #6) using OSEM or OSEM-TOF. The six lesions that were not detected on the mCT were of small size (≤ 9 mm), low AC_{max} of ≤ 2.8 kBq/mL, and SUV_{max} of ≤ 5.1 (examples in Fig. 2a–c). Figure 2c illustrates the only lesion (#8, < 6 mm, AC_{max} 2.8 kBq/mL, SUV_{max} 5.1) that was detectable on the Vision using OSEM but not on the mCT. The lymph node that was hardly distinguishable (#2, detailed description above) was only detected using OSEM-TOF+PSF. However, OSEM-TOF+PSF induced two additional foci (hilar lymph node and bone, not shown) with probably artificially elevated uptake. These lesions were not discernible in the images from the scanners with higher sensitivity and a critical re-evaluation revealed that the reported uptakes were of the same magnitude as other spots in the background noise of the evaluated images; the hilar lymph node was not included in the scan area of the PET/MR.

As illustrated in Fig. 1b, the patient-based detection efficacy revealed that 5 of the 10 included patients were radioiodine-positive (in the 20-min acquisition time reference scan on the mMR). On the Vision, 4/5 patients were identified using OSEM-TOF or
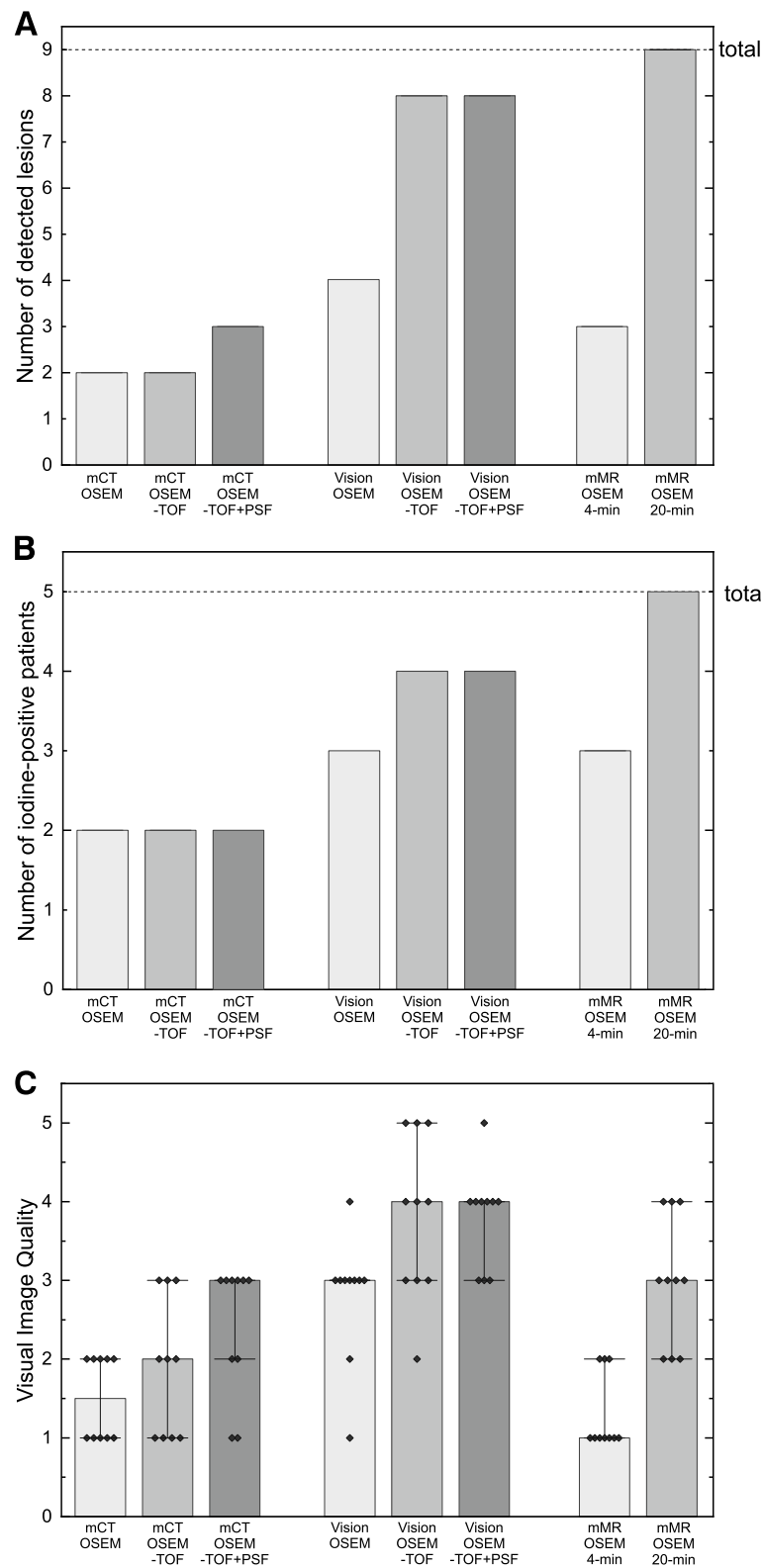
Fig. 1 Bar charts of **a** lesion-based detection efficacy, **b** patient-based detection efficacy, and **c** visual image quality (diamonds: data points, bar: median, whiskers: quartiles). The detection efficacy was evaluated using as reference the five-fold prolonged scan duration image acquired on the PET/MR system

Table 2 Lesion-based detection efficacy analysis

Lesion ID	Patient ID	mCT OSEM	mCT OSEM-TOF	mCT OSEM-TOF+PSF	Vision OSEM	Vision OSEM-TOF	Vision OSEM-TOF+PSF	mMR 4-min	mMR 20-min
1	1	1	1	1	1	1	1	1	1
2	1	0	0	1	1	1	1	0	1
3	1	0	0	0	0	1	1	0	1
4	2	0	0	0	0	0	0	0	1
5	3	0	0	0	0	1	1	0	1
6	5	1	1	1	1	1	1	1	1
7	5	0	0	0	0	1	1	0	1
8	9	0	0	0	1	1	1	1	1
9	9	0	0	0	0	1	1	0	1

Detection is indicated by "1", while missed detection is indicated by "0"

OSEM-TOF+PSF and 3/5 using OSEM. On the mMR, 3/5 patients were identified at 4-min acquisition time. On the mCT, 2/5 patients were identified independent of the image reconstruction algorithm.

Visual image quality

For the PET/CT systems, the median (IQR) visual image quality showed statistically significant increases from the mCT to the Vision from 1.5 (2–1) to 3 (3–2.75) for OSEM ($p < 0.005$), from 2 (3–1) to 4 (5–3) for OSEM-TOF ($p < 0.005$), and from 3 (3–1.75) to 4 (4–3) for OSEM-TOF+PSF images ($p < 0.005$), respectively (Fig. 1c). For the Vision, the changes from OSEM to OSEM-TOF images ($p < 0.05$) and from OSEM to OSEM-TOF+PSF images ($p < 0.01$) were statistically significant, whereas for the mCT, only the change from OSEM to OSEM-TOF+PSF images was statistically significant ($p < 0.05$).

The non-TOF mMR reached a visual image quality of 1 (2–1) at 4-min acquisition time duration. It was not significantly different from the mCT except for OSEM-TOF+PSF images ($p < 0.01$), but significantly lower than all image reconstructions on the

Table 3 Lesion characteristics

Lesion ID	AR	Size (mm)	SUV_{max} mMR 20-min	SUV_{max} Vision OSEM-TOF	AC_{max} mMR 20-min (kBq/mL)	AC_{max} Vision OSEM-TOF (kBq/mL)	SBR mMR 20-min
1	CLN	13	15.2	14.0	4,6	4.2	42.6
2	CLN	17	8.8	9.9	2.6	3.5	25.7
3	CLN	9	3.1	3.4	0.9	1.0	10.7
4	CLN	7	2.3	–	0.8	–	12.6
5	Bone	< 6	8.4[a]	3.1	3.2[a]	1.2	14.4
6	TB	16	10.2	9.9	4.7	4.6	29.6
7	CLN	6	3.0	2.2	1.4	1.0	8.4
8	TB	<6	5.6	5.1	2.4	2.8	7.1
9	CLN	4	3.0	1.8	1.3	0.9	6.5

AR Anatomical region, *CLN* Cervical lymph node, *TB* Thyroid bed, *SBR* Signal-to-background ratio (only reported for the 20-min acquisition on the mMR, in which all lesions were detectable)
[a]Potentially artificially elevated activity concentration in PET/MR attenuation correction, as the bone lesion was osteolytic

Kersting *et al. EJNMMI Physics*   (2021) 8:14

Page 8 of 14

Fig. 2 PET(/CT) images of **a** an osteolytic lesion in cervical vertebra 7 (lesion #5), of **b** a cervical lymph node (lesion #4), and of **c** a thyroid bed lesion (lesion #8). Detected lesions are indicated by arrows. In **a** and **c** oesophageal tracer uptake is not visible on all images due to different imaging times
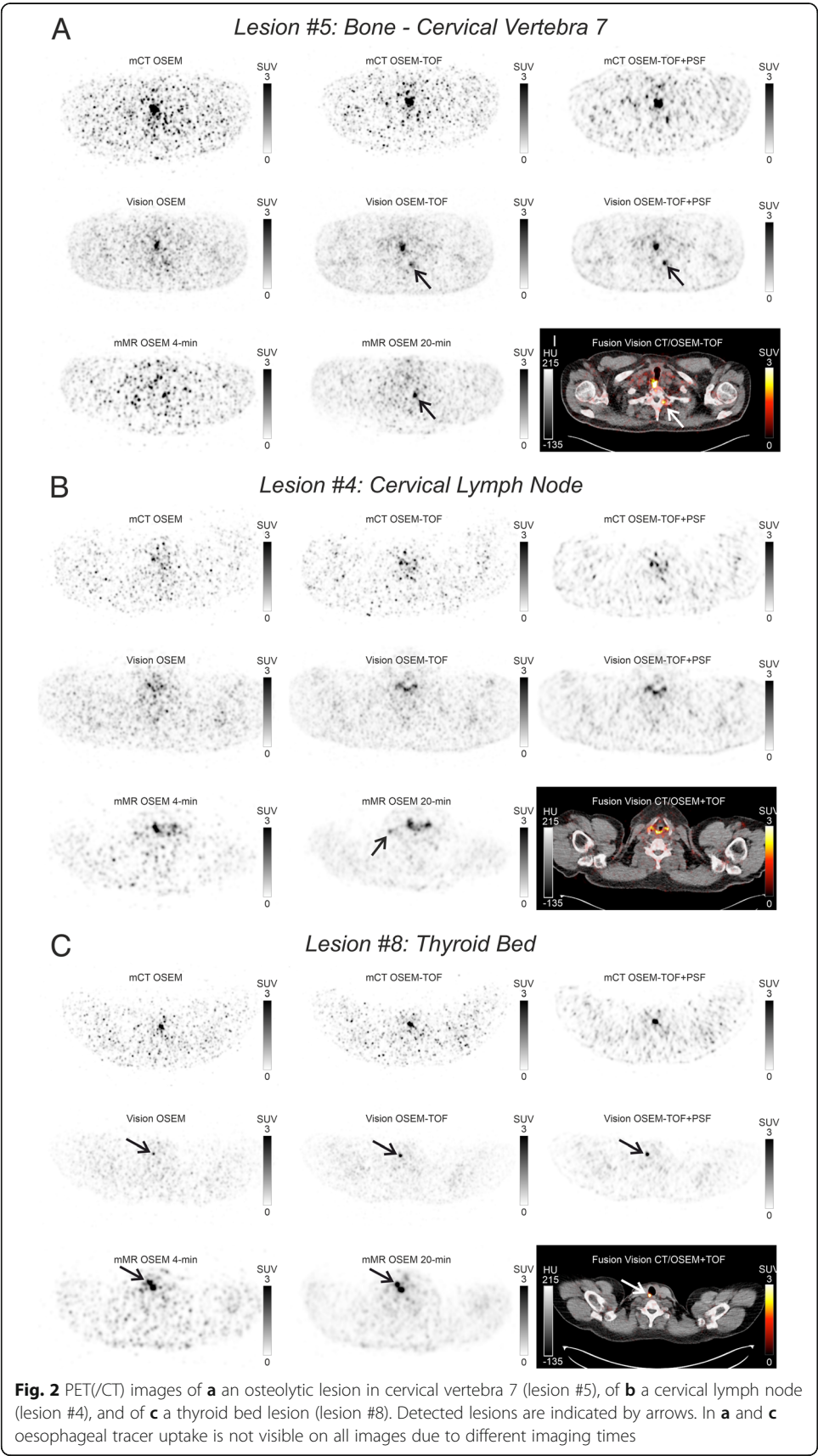
Vision (all $p < 0.001$). When prolonging the acquisition time duration to 20 min, the visual image quality increased to 3 (4–2), a value significantly larger than OSEM ($p < 0.001$) and OSEM-TOF images ($p < 0.05$) on the mCT. Of note, the difference to OSEM-TOF and OSEM-TOF+PSF reconstructions on the Vision did not reach statistical significance.

Discussion

A radioiodine-avid DTC lesion is detectable in [124]I PET/CT if its accumulated activity is above the PET scanner's size-dependent minimum detectable activity. Several influencing factors in lesion detection shown in Fig. 3 will be discussed to achieve an optimized scan protocol with regards to detection of recurrent DTC lesions.

The minimum detectable activity is largely determined by technical aspects such as scanner's sensitivity, PET spatial resolution, and image reconstruction algorithms [26]. Sensitivity, time and spatial resolutions are improved in the new generation of SiPM-based PET scanners, leading to an increased detectability [12, 27] and image quality [28]. Recent studies demonstrate that an increased detectability of SiPM-based systems can allow for shorter acquisition time durations in ^{18}F-FDG PET without impairing the diagnostic accuracy [29–31]. In this study, we evaluated the effects on [124]I PET imaging.

At standard acquisition time duration, the Vision outperformed both the mCT and the mMR in detection efficacy and visual image quality; these results were almost independent of the image reconstruction algorithms (Fig. 1 and Table 2). Of note, the image quality on the mMR was relatively low compared to its detection efficacy. An explanation may be associated with non-TOF modeling on this PET system leading to an increase in image noise that impairs visual image quality [32]. In OSEM-TOF and OSEM-PSF+TOF images, the Vision reached, in standard acquisitions, comparable results to those in five-fold prolonged acquisitions on the mMR, which we used as reference. As expected, the missed lesions on the old generation systems were small and of low radioiodine uptake (Table 3). We therefore propose, if available, image acquisition on a new generation SiPM-based PET system for recurrent DTC patients with increasing Tg or Tg antibody levels in the low measurable range. The observed differences in
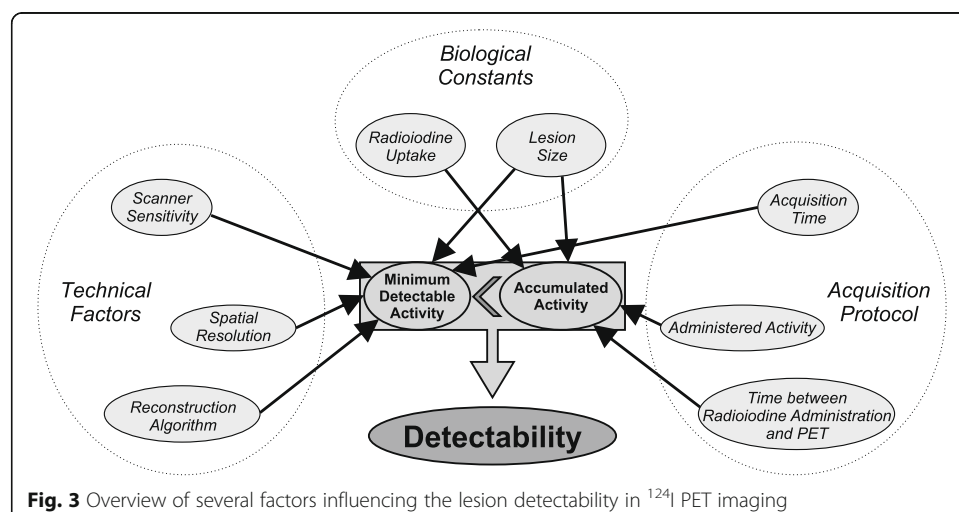
Fig. 3 Overview of several factors influencing the lesion detectability in [124]I PET imaging

detectability across the PET scanners might not hold for patients with only large and/or high radioiodine uptake lesions that might be detectable on each PET scanner.

Regarding the choice of image reconstruction algorithm, on the Vision the refinements obtained by OSEM-TOF were not further enhanced by OSEM-TOF+PSF, while OSEM-TOF+PSF was necessary on the mCT for improvements in both detection efficacy and image quality. On the mCT, OSEM-TOF+PSF induced probably artificial elevated uptake in two patients rated as a cervical lymph node and a bone pseudo-lesion (these lesions were not discernible in the images from the scanners with higher sensitivity and a critical re-evaluation revealed that the reported uptakes were of the same magnitude as other spots in the background noise of the evaluated images). Moreover, quantification artifacts in small lesions by PSF modeling are a known phenomenon [33] and have yet to be investigated in phantom studies for the new generation SiPM-based ^{124}I PET. On the Vision, part of the contrast enhancement results from the better intrinsic spatial resolution due to the smaller crystal size. Therefore, we currently propose the usage of OSEM-TOF or OSEM-TOF+PSF reconstruction for ^{124}I PET on the Vision.

Apart from improving the minimum detectable activity, the detectability for small structures can be increased by prolonged acquisition time durations [26, 34]. Comparing the neck PET/MR at standard and five-fold prolonged acquisition time durations, the lesion-based detection efficacy was increased by a factor of 3 (Fig. 1a). Only one lesion detectable on the prolonged PET/MR acquisitions was missed on the SiPM-based PET/CT (Fig. 2b). Still, emphasis on scan duration of critical anatomical regions might be beneficial. As DTC lymph node metastases are typically — like every detected lesion in this study — localized in the neck region [4], we propose a selectively prolonged acquisition time duration for the neck region. Especially, PET acquisition in continuous bed motion mode, which can itself lead to an improved detectability compared to the stop-and-shoot acquisition mode due to a more uniform axial sensitivity [35], allows for easy emphasis of particular body regions. The table speed velocity could be decreased for the neck region. Of the evaluated PET systems, only the Vision is capable of scanning in continuous bed motion mode. An analysis of the effects on detectability and image quality would require an additional study.

A further possibility for improving the detectability is to increase the accumulated ^{124}I activity in the lesion by higher administered activities. In a previous phantom study [8], an ^{124}I activity of 74 MBq was calculated to yield a detectability for small lesions similar to intra-therapeutic SPECT imaging after application of 7.4 GBq of ^{131}I. The administration of larger amounts of ^{124}I may be limited by thyroid stunning (i.e., missing/reduced uptake of radioiodine-avid lesions in intra-therapeutic ^{131}I whole-body scans compared to pre-therapeutic radioiodine imaging). Thyroid stunning is controversially discussed [36] and not sufficiently investigated for ^{124}I [37]. In the literature, applications of up to 74 MBq [6] are described. We therefore believe that an activity of 74 MBq of ^{124}I can safely be administered without risking thyroid stunning. The administration of higher activities could be possible but should be validated in an experimental setting.

Additionally, the time interval between ^{124}I administration and PET scan can influence the detectability. Studies of the lesion kinetics revealed an optimal temporal distance of approximately 8 h [38]. At our department, the realization of this interval is

logistically not possible, explaining the choice for our protocol with a PET start of 15–19 hours after radioiodine application. However, if possible, a shorter temporal distance could be beneficial to improve the detectability.

Of importance, one lesion that was additionally detected on the Vision and on the prolonged neck PET/MR scan (lesion #5, osteolytic lesion in cervical vertebra 7, see Fig. 2a) caused a change in patient management, that is, the patient received a radioiodine therapy with an amount of 6.1 GBq of ^{131}I. Regarding the other additionally detected lesions, treatment by radioiodine therapy was already determined by other lesions in the same patient or watchful waiting was performed (due to other radioiodine-negative metastases in the same patient or equivocal dignity in case of low uptake in the thyroid bed).

The different types of co-registered morphological images (i.e., CT or MR) might influence clinical patient management [39]. On the one hand, neck PET/MR was described as superior to PET/CT in identifying morphological correlates to focal ^{124}I uptake, particularly for small lymph nodes and can increase the diagnostic certainty [39]. On the other hand, PET quantification can be challenging, as attenuation correction by MR data is limited and the neck region comprises different tissue types in close proximity. However, it was reported that ^{124}I PET quantification from PET/MR data is reliable and can be used for dosimetry planning prior to radioiodine therapy [40]. We therefore propose to perform an additional PET/MR of the neck region, if available and if tolerated by the patient. Alternatively, an additional MR scan could be performed and co-registered with the PET/CT scan. The influence on the detectability should be evaluated in a clinical study.

There are four main limitations in this study. First, the number of patients and ^{124}I-positive lesions is low possibly resulting in a low statistical power. A low power can lead to an overestimation of small effects [41]. Additional phantom measurements could be beneficial to verify the results of this study. Thus, it is not possible to estimate from this study whether the improved detectability and image quality have a relevant impact on patient outcome. However, the number of detected lesions is typically low in this selected patient group and the number of patients with these characteristics is generally small [20]. Second, the temporal distances between application of ^{124}I and PET start among the evaluated PET systems differed. However, we do not expect a pronounced effect as all scans were performed within a mean time interval of 4.7 ± 2.9 h (maximum 8.7 h) that is relatively small compared to the effective ^{124}I half-lives of the lesions (previously reported in the range of 59–116 h) [42–45]. Third, a PET start at an optimal time of 8 h after ^{124}I administration could lead to higher accumulated activities and higher signal-to-background ratios and, thus, reduce the observed benefits of a high-sensitivity PET scanner. Fourth, on the PET/MR system only one bed position was used while on the PET/CT systems PET data were acquired in step and shoot acquisition mode with overlapping bed positions. Thus, on the PET/MR, lesions on the end slices of the reconstructed images might be impaired by a non-uniform axial sensitivity profile.

Conclusion

In the evaluated case series of 10 DTC patients at clinical standard acquisition time of 4 min per bed position, the use of the new generation SiPM-based PET/CT (Biograph

Vision) and OSEM-TOF or OSEM-TOF+PSF image reconstruction resulted in the highest lesion detection efficacy and visual image quality. The Biograph Vision should, if available, be preferred over the PMT-based Biograph mCT and the APD-based Biograph mMR for standard acquisition time PET of DTC patients with potential low-uptake lesions. As the detectability was dependent on the acquisition time, a selectively prolonged scan duration should be implemented for the neck region.

Supplementary Information

The online version contains supplementary material available at https://doi.org/10.1186/s40658-021-00361-y.

Additional file 1: Supplemental Table S1. PET Scanner Specifications. **Supplemental Table S2.** Detailed patient characteristics and PET time intervals. **Supplemental Table S3.** Detailed PET time intervals.

Author details
[1]Department of Nuclear Medicine, University Hospital Essen, University of Duisburg-Essen, Hufelandstrasse 55, 45147 Essen, Germany. [2]West German Cancer Center (WTZ), Essen, Germany. [3]German Cancer Consortium (DKTK), Essen and Dusseldorf, Germany. [4]Siemens Medical Solutions USA, Inc., Knoxville, TN, USA. [5]Department of Diagnostic and Interventional Radiology and Neuroradiology, University Hospital Essen, 45147 Essen, Germany. [6]Medical Faculty, Department of Diagnostic and Interventional Radiology, University Dusseldorf, 40225 Dusseldorf, Germany.

References
1. Ahn J, Song E, Kim WG, Kim TY, Kim WB, Shong YK, et al. Long-term clinical outcomes of papillary thyroid carcinoma patients with biochemical incomplete response. Endocrine. 2019. https://doi.org/10.1007/s12020-019-02142-1.
2. Castagna MG, Maino F, Cipri C, Belardini V, Theodoropoulou A, Cevenini G, et al. Delayed risk stratification, to include the response to initial treatment (surgery and radioiodine ablation), has better outcome predictivity in differentiated thyroid cancer patients. Eur J Endocrinol. 2011;165(3):441–6. https://doi.org/10.1530/EJE-11-0466.
3. Ito Y, Miyauchi A, Kobayashi K, Kihara M, Miya A. Static and dynamic prognostic factors of papillary thyroid carcinoma. Endocr J. 2014;61(12):1145–51. https://doi.org/10.1507/endocrj.EJ14-0303.

Kersting *et al. EJNMMI Physics*   (2021) 8:14

Page 13 of 14

4.   Haugen BR, Alexander EK, Bible KC, Doherty GM, Mandel SJ, Nikiforov YE, et al. 2015 American Thyroid Association management guidelines for adult patients with thyroid nodules and differentiated thyroid cancer: the American Thyroid Association guidelines task force on thyroid nodules and differentiated thyroid cancer. Thyroid. 2016;26(1):1–133. https://doi.org/10.1089/thy.2015.0020.

5.   Carrillo JF, Vazquez-Romo R, Ramirez-Ortega MC, Carrillo LC, Gomez-Argumosa E, Onate-Ocana LF. Prognostic impact of direct (131)I therapy after detection of biochemical recurrence in intermediate or high-risk differentiated thyroid cancer: a retrospective cohort study. Front Endocrinol (Lausanne). 2019;10:737. https://doi.org/10.3389/fendo.2019.00737.

6.   Van Nostrand D, Moreau S, Bandaru VV, Atkins F, Chennupati S, Mete M, et al. (124)I positron emission tomography versus (131)I planar imaging in the identification of residual thyroid tissue and/or metastasis in patients who have well-differentiated thyroid cancer. Thyroid. 2010;20(8):879–83. https://doi.org/10.1089/thy.2009.0430.

7.   Ruhlmann M, Jentzen W, Ruhlmann V, Pettinato C, Rossi G, Binse I, et al. High level of agreement between pretherapeutic 124I PET and intratherapeutic 131I imaging in detecting iodine-positive thyroid cancer metastases. J Nucl Med. 2016;57(9):1339–42. https://doi.org/10.2967/jnumed.115.169649.

8.   Beijst C, Kist JW, Elschot M, Viergever MA, Hoekstra OS, de Keizer B, et al. Quantitative comparison of 124I PET/CT and 131I SPECT/CT detectability. J Nucl Med. 2016;57(1):103–8. https://doi.org/10.2967/jnumed.115.162750.

9.   Kist JW, de Keizer B, van der Vlies M, Brouwers AH, Huysmans DA, van der Zant FM, et al. 124I PET/CT to predict the outcome of blind 131I treatment in patients with biochemical recurrence of differentiated thyroid cancer: results of a multicenter diagnostic cohort study (THYROPET). J Nucl Med. 2016;57(5):701–7. https://doi.org/10.2967/jnumed.115.168138.

10. van Sluis J, de Jong J, Schaar J, Noordzij W, van Snick P, Dierckx R, et al. Performance characteristics of the digital biograph vision PET/CT system. J Nucl Med. 2019;60(7):1031–6. https://doi.org/10.2967/jnumed.118.215418.

11. Meyer M, Allenbach G, Nicod Lalonde M, Schaefer N, Prior JO, Gnesin S. Increased (18)F-FDG signal recovery from small physiological structures in digital PET/CT and application to the pituitary gland. Sci Rep. 2020;10(1):368. https://doi.org/10.1038/s41598-019-57313-x.

12. Koopman D, van Dalen JA, Stevens H, Slump CH, Knollema S, Jager PL. Performance of digital PET compared to high-resolution conventional PET in patients with cancer. J Nucl Med. 2020. https://doi.org/10.2967/jnumed.119.238105.

13. Lopez-Mora DA, Flotats A, Fuentes-Ocampo F, Camacho V, Fernandez A, Ruiz A, et al. Comparison of image quality and lesion detection between digital and analog PET/CT. Eur J Nucl Med Mol Imaging. 2019;46(6):1383–90. https://doi.org/10.1007/s00259-019-4260-z.

14. Fuentes-Ocampo F, Lopez-Mora DA, Flotats A, Camacho V, Sizova M, Abouzian S, et al. Digital versus analog PET/CT in patients with known or suspected liver metastases. Nucl Med Commun. 2020. https://doi.org/10.1097/MNM.0000000000001341.

15. Alberts I, Prenosil G, Sachpekidis C, Weitzel T, Shi K, Rominger A, et al. Digital versus analogue PET in [(68)Ga]Ga-PSMA-11 PET/CT for recurrent prostate cancer: a matched-pair comparison. Eur J Nucl Med Mol Imaging. 2020;47(3):614–23. https://doi.org/10.1007/s00259-019-04630-y.

16. Conti M, Eriksson L. Physics of pure and non-pure positron emitters for PET: a review and a discussion. EJNMMI Phys. 2016;3(1):8. https://doi.org/10.1186/s40658-016-0144-5.

17. Conti M, Bendriem B. The new opportunities for high time resolution clinical TOF PET. Clin Transl Imaging. 2019;7(2):139–47. https://doi.org/10.1007/s40336-019-00316-5.

18. Akamatsu G, Ishikawa K, Mitsumoto K, Taniguchi T, Ohya N, Baba S, et al. Improvement in PET/CT image quality with a combination of point-spread function and time-of-flight in relation to reconstruction parameters. J Nucl Med. 2012;53(11):1716–22. https://doi.org/10.2967/jnumed.112.103861.

19. Messerli M, Stolzmann P, Egger-Sigg M, Trinckauf J, D'Aguanno S, Burger IA, et al. Impact of a Bayesian penalized likelihood reconstruction algorithm on image quality in novel digital PET/CT: clinical implications for the assessment of lung tumors. EJNMMI Phys. 2018;5(1):27. https://doi.org/10.1186/s40658-018-0223-x.

20. Khorjekar GR, Van Nostrand D, Garcia C, O'Neil J, Moreau S, Atkins FB, et al. Do negative 124I pretherapy positron emission tomography scans in patients with elevated serum thyroglobulin levels predict negative 131I posttherapy scans? Thyroid. 2014;24(9):1394–9. https://doi.org/10.1089/thy.2013.0713.

21. Jentzen W. Experimental investigation of factors affecting the absolute recovery coefficients in iodine-124 PET lesion imaging. Phys Med Biol. 2010;55(8):2365–98. https://doi.org/10.1088/0031-9155/55/8/016.

22. Wierts R, Jentzen W, Quick HH, Wisselink HJ, Pooters INA, Wildberger JE, et al. Quantitative performance evaluation of (124)I PET/MRI lesion dosimetry in differentiated thyroid cancer. Phys Med Biol. 2017;63(1):015014. https://doi.org/10.1088/1361-6560/aa990b.

23. Hayden CH Jr, Casey ME, Watson CC. Prompt gamma correction for non-standard isotopes in a PET scanner. US Patent. 2011:7894652. https://patents.google.com/patent/US20080283758.

24. Jentzen W. An improved iterative thresholding method to delineate PET volumes using the delineation-averaged signal instead of the enclosed maximum signal. J Nucl Med Technol. 2015;43(1):28–35. https://doi.org/10.2967/jnmt.114.152678.

25. van Sluis J, Boellaard R, Somasundaram A, van Snick PH, Borra RJH, Dierckx R, et al. Image quality and semiquantitative measurements on the biograph vision PET/CT system: initial experiences and comparison with the biograph mCT. J Nucl Med. 2020;61(1):129–35. https://doi.org/10.2967/jnumed.119.227801.

26. Adler S, Seidel J, Choyke P, Knopp MV, Binzel K, Zhang J, et al. Minimum lesion detectability as a measure of PET system performance. EJNMMI Phys. 2017;4(1):13. https://doi.org/10.1186/s40658-017-0179-2.

27. Surti S, Viswanath V, Daube-Witherspoom ME, Conti M, Casey ME, Karp JS. Benefit of improved performance with state-of-the art digital PET/CT for lesion detection in oncology. J Nucl Med. 2020. https://doi.org/10.2967/jnumed.120.242305.

28. Gnesin S, Kieffer C, Zeimpekis K, Papazyan JP, Guignard R, Prior JO, et al. Phantom-based image quality assessment of clinical (18)F-FDG protocols in digital PET/CT and comparison to conventional PMT-based PET/CT. EJNMMI Phys. 2020;7(1):1. https://doi.org/10.1186/s40658-019-0269-4.

29. Lasnon C, Coudrais N, Houdu B, Nganoa C, Salomon T, Enilorac B, et al. How fast can we scan patients with modern (digital) PET/CT systems? Eur J Radiol. 2020;129:109144. https://doi.org/10.1016/j.ejrad.2020.109144.

30. Hatami S, Frye S, McMunn A, Botkin C, Muzaffar R, Christopher K, et al. Added value of digital over analog PET/CT: more significant as image field of view and body mass index increase. J Nucl Med Technol. 2020;48(4):354–60. https://doi.org/10.2967/jnmt.120.244160.

31. Weber M, Jentzen W, Hofferber R, Herrmann K, Fendler WP, Rischpler C, et al. Evaluation of (18)F-FDG PET/CT images acquired with a reduced scan time duration in lymphoma patients using the digital biograph vision. BMC Cancer. 2021; 21(1):62. https://doi.org/10.1186/s12885-020-07723-2.

32. Maebatake A, Akamatsu G, Miwa K, Tsutsui Y, Himuro K, Baba S, et al. Relationship between the image quality and noise-equivalent count in time-of-flight positron emission tomography. Ann Nucl Med. 2016;30(1):68–74. https://doi.org/10.1007/s12149-015-1032-0.

33. Munk OL, Tolbod LP, Hansen SB, Bogsrud TV. Point-spread function reconstructed PET images of sub-centimeter lesions are not quantitative. EJNMMI Phys. 2017;4(1):5. https://doi.org/10.1186/s40658-016-0169-9.

34. Kadrmas DJ, Oktay MB, Casey ME, Hamill JJ. Effect of scan time on oncologic lesion detection in whole-body PET. IEEE Trans Nucl Sci. 2012;59(5):1940–7. https://doi.org/10.1109/TNS.2012.2197414.

35. Brasse D, Newport D, Carney JP, Yap JT, Reynolds C, Reed J et al., editors. Continuous bed motion acquisition on a whole body combined PET/CT system. 2002 IEEE nuclear science symposium conference record; 2002 10-16 Nov. 2002.

36. McDougall IR, Iagaru A. Thyroid stunning: fact or fiction? Semin Nucl Med. 2011;41(2):105–12. https://doi.org/10.1053/j.semnuclmed.2010.10.004.

37. Walrand S, Hesse M, Jamar F. Statistical and radiobiological analysis of the so-called thyroid stunning. EJNMMI Res. 2015; 5(1):67. https://doi.org/10.1186/s13550-015-0144-9.

38. Jentzen W, Freudenberg L, Eising EG, Sonnenschein W, Knust J, Bockisch A. Optimized 124I PET dosimetry protocol for radioiodine therapy of differentiated thyroid cancer. J Nucl Med. 2008;49(6):1017–23. https://doi.org/10.2967/jnumed.107.047159.

39. Nagarajah J, Jentzen W, Hartung V, Rosenbaum-Krumme S, Mikat C, Heusner TA, et al. Diagnosis and dosimetry in differentiated thyroid carcinoma using 124I PET: comparison of PET/MRI vs PET/CT of the neck. Eur J Nucl Med Mol Imaging. 2011;38(10):1862–8. https://doi.org/10.1007/s00259-011-1866-1.

40. Jentzen W, Phaosricharoen J, Gomez B, Hetkamp P, Stebner V, Binse I, et al. Quantitative performance of (124)I PET/MR of neck lesions in thyroid cancer patients using (124)I PET/CT as reference. EJNMMI Phys. 2018;5(1):13. https://doi.org/10.1186/s40658-018-0214-y.

41. Button KS, Ioannidis JP, Mokrysz C, Nosek BA, Flint J, Robinson ES, et al. Power failure: why small sample size undermines the reliability of neuroscience. Nat Rev Neurosci. 2013;14(5):365–76. https://doi.org/10.1038/nrn3475.

42. Rosenbaum-Krumme S, Nagarajah J, Ruhlmann M, Bockisch A, Jentzen W. 124I-PET/CT images of differentiated thyroid cancer patients. Distinguishing lymph node metastases from thyroid remnants using kinetic quantities. Nuklearmedizin. 2012;51(6):213–6. https://doi.org/10.3413/Nukmed-0481-12-02.

43. Jentzen W, Verschure F, van Zon A, van de Kolk R, Wierts R, Schmitz J, et al. 124I PET assessment of response of bone metastases to initial radioiodine treatment of differentiated thyroid cancer. J Nucl Med. 2016;57(10):1499–504. https://doi.org/10.2967/jnumed.115.170571.

44. Jentzen W, Moldovan AS, Ruhlmann M, Gorges R, Bockisch A, Rosenbaum-Krumme S. Lowest effective 131I activity for thyroid remnant ablation of differentiated thyroid cancer patients. Dosimetry-based model for estimation. Nuklearmedizin. 2015;54(3):137–43. https://doi.org/10.3413/Nukmed-0711-14-12.

45. Jentzen W, Hoppenbrouwers J, van Leeuwen P, van der Velden D, van de Kolk R, Poeppel TD, et al. Assessment of lesion response in the initial radioiodine treatment of differentiated thyroid cancer using 124I PET imaging. J Nucl Med. 2014;55(11):1759–65. https://doi.org/10.2967/jnumed.114.144089.

Publisher's Note

Springer Nature remains neutral with regard to jurisdictional claims in published maps and institutional affiliations.

Supplemental Material to "Comparing Lesion Detection Efficacy and Image Quality across Different PET System Generations to Optimize the Iodine-124 PET Protocol for Recurrent Thyroid Cancer"

SUPPLEMENTAL TABLE S1 PET Scanner Specifications

	Biograph mCT	Biograph Vision	Biograph mMR
Detector material	LSO	LSO	LSO
Detector element dimension (mm^3)	4x4x20	3.2x3.2x20	4x4x20
Detector elements per block	13x13	16x16	8x8
Total number of detector elements	33,448	60,800	28,672
Signal readout	PMTs (2x2 per block)	SiPM (2x2 per block)	APDs (3x3 per block)
Axial FOV (cm)	21.8	26.3	25.8
Transaxial FOV (cm)	70	78	59
Plane spacing (mm)	2	1.65	2
Image planes	109	119	127
Coincidence time window (ns)	4.1	4.7	5.9
Energy window (keV)	435-650	435-585	430-610
Energy resolution (%)	11	9	14
System time resolution (ps)	540	210	-
NEMA sensitivity (kcps/MBq)	9.7	16.4	15

Supplemental Table S1: Technical specifications for the Biograph mCT, the Biograph Vision and the Biograph mMR. LSO = Lutetium Oxyorthosilicate.

SUPPLEMENTAL TABLE S2: Detailed patient characteristics and PET time intervals

Patient ID	Sex	Age (yrs)	Histology	TNM	Tg (ng/mL)	Tg anti-bodies (IU/mL)	No. of RAIT	Cumulated activity of ^{131}I (GBq)	Applied activity of ^{124}I (MBq)	Time of first PET scan after ^{124}I application (h)	Time interval between 1st and 3rd PET scan (h)	Further patient management
1	m	68	PTC	T3N1M1	NM	273	1	3.7	37.9	18.1	2.1	W&W
2	m	59	PTC	T2N1M0	0.12	NM	2	11.3	44.1	16.9	2.4	W&W
3	m	72	FTC	T3N0M1	5.50	NM	1	3.2	38.4	15.1	2.8	RAIT
4	m	32	FTC	T3N0M0	0.41	NM	2	7.4	37.3	17.4	3.3	W&W
5	f	50	PTC	T1bN0M0	1.21	NM	1	6.3	37.3	16.8	3.3	RAIT
6	f	66	PTC	T1N1M0	0.72	NM	1	2.9	36.6	16.4	8.1	W&W
7	m	19	FTC	T3N0M1	2.60	NM	2	9.4	38.5	18.4	7.0	W&W
8	f	57	PTC	T1N1M0	3.50	NM	2	9.0	38.0	18.2	1.9	W&W
9	f	33	PTC	T3N1M0	0.76	NM	1	3.0	37.6	17.0	8.1	RAIT
10	f	63	PTC	T1bN0M0	1.57	NM	1	4.0	36.9	16.8	8.7	W&W

Supplemental Table S2: Tg = Unstimulated Tg. RAIT = Radioiodine therapy. NM = Not measurable. W&W: Watch and wait.

SUPPLEMENTAL TABLE S3: Detailed PET time intervals

Patient ID	Time of PET scan after [124]I application on the mCT (h)	Time of PET scan after [124]I application on the Vision (h)	Time of PET scan after [124]I application on the mMR (h)
1	18.1	19.1	20.2
2	17.9	16.9	19.3
3	15.2	15.9	17.9
4	17.4	18.6	20.7
5	16.8	17.9	20.1
6	16.4	24.5	17.5
7	18.4	25.5	19.7
8	18.2	19.1	20.1
9	17.9	25.2	17.1
10	16.8	25.4	18.2

Silicon-photomultiplier-based PET/CT reduces the minimum detectable activity of iodine-124

Reference

Copyright statement

Contributions

I participated in study design, data acquisition and data analysis and mainly contributed to manuscript writing.

scientific reports

OPEN

Silicon-photomultiplier-based PET/CT reduces the minimum detectable activity of iodine-124

D. Kersting[1,4]✉, W. Jentzen[1,4], P. Fragoso Costa[1,4], M. Sraieb[1,4], P. Sandach[1,4], L. Umutlu[2,4], M. Conti[3], F. Zarrad[1,4], C. Rischpler[1,4], W. P. Fendler[1,4], K. Herrmann[1,4] & M. Weber[1,4]

The radioiodine isotope pair ¹²⁴I/¹³¹I is used in a theranostic approach for patient-specific treatment of differentiated thyroid cancer. Lesion detectability is notably higher for ¹²⁴I PET (positron emission tomography) than for ¹³¹I gamma camera imaging but can be limited for small and low uptake lesions. The recently introduced silicon-photomultiplier-based (SiPM-based) PET/CT (computed tomography) systems outperform previous-generation systems in detector sensitivity, coincidence time resolution, and spatial resolution. Hence, SiPM-based PET/CT shows an improved detectability, particularly for small lesions. In this study, we compare the size-dependant minimum detectable ¹²⁴I activity (MDA) between the SiPM-based Biograph Vision and the previous-generation Biograph mCT PET/CT systems and we attempt to predict the response to ¹³¹I radioiodine therapy of lesions additionally identified on the SiPM-based system. A tumour phantom mimicking challenging conditions (derived from published patient data) was used; i.e., 6 small spheres (diameter of 3.7–9.7 mm), 9 low activity concentrations (0.25–25 kBq/mL), and a very low signal-to-background ratio (20:1). List-mode emission data (single-bed position) were divided into frames of 4, 8, 16, and 30 min. Images were reconstructed with ordinary Poisson ordered-subsets expectation maximization (OSEM), additional time-of-flight (OSEM-TOF) or TOF and point spread function modelling (OSEM-TOF+PSF). The signal-to-noise ratio and the MDA were determined. Absorbed dose estimations were performed to assess possible treatment response to high-activity ¹³¹I radioiodine therapy. The signal-to-noise ratio and the MDA were improved from the mCT to the Vision, from OSEM to OSEM-TOF and from OSEM-TOF to OSEM-TOF+PSF reconstructed images, and from shorter to longer emission times. The overall mean MDA ratio of the Vision to the mCT was 0.52 ± 0.18. The absorbed dose estimations indicate that lesions ≥ 6.5 mm with expected response to radioiodine therapy would be detectable on both systems at 4-min emission time. Additional smaller lesions of therapeutic relevance could be detected when using a SiPM-based PET system at clinically reasonable emission times. This study demonstrates that additional lesions with predicted response to ¹³¹I radioiodine therapy can be detected. Further clinical evaluation is warranted to evaluate if negative ¹²⁴I PET scans on a SiPM-based system can be sufficient to preclude patients from blind radioiodine therapy.

Radioiodine therapy has been a cornerstone of treatment of differentiated thyroid cancer (DTC) patients for decades. In both current American Thyroid Association (ATA)[1] and European Association of Nuclear Medicine (EANM)[2] guidelines for the management of DTC patients, the radioiodine therapy is not only recommended after initial thyroidectomy but also in case of recurring unresectable radioiodine-avid tumour lesions. Typically, radioiodine uptake is verified by planar or tomographic gamma camera imaging using low ¹³¹I activities in the range of 74–185 MBq[1]. However, in cases of rising thyroglobulin levels and negative radioiodine scans, therapy management becomes challenging. In these instances, "blind" radioiodine therapy is a controversially discussed option[1]. In a 2014 published survey among ATA members, 15% to 52% would perform radioiodine therapy, even if diagnostic ¹²³I whole body scans are negative[3]. On the one hand, more than half of DTC patients show pathologic radioiodine uptake after blind therapy[3,4], on the other hand, radioiodine therapy is not free of

¹Department of Nuclear Medicine, University Hospital Essen, University of Duisburg-Essen, Hufelandstrasse 55, 45147 Essen, Germany. ²Department of Diagnostic and Interventional Radiology and Neuroradiology, University Hospital Essen, University of Duisburg-Essen, Essen, Germany. ³Siemens Medical Solutions USA, Inc., Knoxville, TN, USA. ⁴German Cancer Consortium (DKTK, Partner Site Essen), Essen, Germany. ✉email: david.kersting@uni-due.de

adverse effects, e.g., gastrointestinal symptoms, sialadenitis, secondary cancers, or bone marrow suppression[5]. These aspects show the demand for improved diagnostic approaches to identify patients, who might benefit from radioiodine therapy.

Whole-body [124]I positron emission tomography ([124]I PET) after application of typical activities in the range of 25 to 74 MBq can be alternatively performed and its detectability was described as superior to diagnostic[6–8] and comparable[9] or superior[10] to intra-therapeutic ^{131}I gamma camera imaging. Moreover, this imaging modality allows for pre-therapeutic dosimetry as a theranostic approach[11,12] to optimize the individual therapeutic activity.

However, reports of undetected lesions in [124]I PET raised concern about the applicability of [124]I PET to preclude patients from blind radioiodine treatment[13,14]. Undetected lesions may be explained by technical factors, e.g., a limited sensitivity of the PET/CT scanner[15,16]. Recently, technical improvements have become available in the field of PET detector technologies. New-generation silicon-photomultiplier (SiPM)-based "digital" PET systems outperform photomultiplier tube (PMT)-based "analog" PET systems in detector sensitivity and show improvements in detectability for various tracers, especially with regards to small and low-uptake lesions[17–21].

The hardware technical improvements have enabled key reconstruction software advances, for example the highly improved, noise suppressing, TOF reconstruction with very narrow time kernels, which offers new opportunities for clinical PET[22]. Moreover, other advanced reconstruction methods have progressed in parallel, improving noise level, contrast recovery, detectability. In particular, it is worth mentioning: resolution recovery or point spread function (PSF) reconstruction, which recovers spatial resolution compensating for penetration effects in the scintillator crystals[23,24]; positron range correction, which improves spatial resolution and therefore detectability for tracers with high energy positrons[25–27]; maximum-a-posteriori (MAP) reconstruction, which allows to increase convergence and to contain the noise at the same time[28,29].

We hypothesise that additional lesions (possibly not detectable in previous-generation PMT-based systems) that are treatable by radioiodine therapy can be identified in [124]I PET by usage of a SiPM-based PET/CT system. Hence, we performed phantom measurements under challenging, but clinically realistic conditions, on both a SiPM- and a PMT-based system using a small tumour phantom with spherical inserts covering the typical size of small lymph node metastases and low activity concentrations.

Thus, the primary aim of this phantom study was to compare the size-dependant minimum detectable [124]I activity (MDA) between the SiPM-based and the PMT-based PET/CT systems for different emission times and image reconstruction algorithms. In addition, we attempt to predict the response to radioiodine therapy of those lesions that are additionally identified on the SiPM-based system (at standard and at longer emission time durations).

Methods

PET/CT systems.
Measurements were performed using two PET/CT scanners (Siemens Healthineers, Erlangen, Germany) with time-of-flight (TOF) modelling option: a new-generation Biograph Vision 600 and a previous-generation Biograph mCT, which are called Vision and mCT systems in this study, respectively. A short description of the scanner specifications is shown as Supplemental Material (Supplemental Table S1). In short, the Vision is equipped with SiPM detectors, a crystal size of 3.2 mm, time coincidence resolution of 214 ps, field of view of 26.3 cm, energy window of 435–585 keV, and NEMA sensitivity of 16.4 cps/kBq. In comparison, the mCT is equipped with PMT detectors, a crystal size of 4.0 mm, time coincidence resolution of 540 ps, field of view of 21.8 cm, energy window of 435–650 keV, and NEMA sensitivity of 9.7 cps/kBq.

Small tumour phantom and its preparation.
Small tumour phantom. The small tumour phantom consists of an abdominal torso NEMA phantom (Data Spectrum Corporation, Durham, USA) to simulate the patient body and of six refillable glass spheres to simulate small tumours (manufactured in our institution). Both a schematic representation of the small tumour phantom and pictures of the phantom and the small spherical inserts are shown in Fig. 1. The small spheres were mounted on a lid in a circle with a 6-cm radius. The centre of each sphere was positioned centrally within the phantom (approximately 10 cm from the lid). The inner diameters (inner volumes) were 3.7 mm (27 µl), 4.8 mm (58 µl), 6.5 mm (144 µl), 7.7 mm (239 µl), 8.9 mm (369 µl), and 9.7 mm (478 µl) and the inner cavity volume (with mounted spheres) was 9748 mL. The glass thickness of the spheres was 0.7 ± 0.2 mm.

Of note, the selected sphere diameters overlap well with the basic diameter range of 2–15 mm for normal lymph nodes in the head–neck region[30]. In addition, our group[31] demonstrated that three quarters of the lymph nodes metastases observed in thyroid cancer patients were smaller than 11.5 mm (also in well agreement with findings in the basic literature, that is, that approximately 75% of normal lymph nodes in the head–neck region are smaller than 10 mm).

Phantom preparation. The spheres and the cavity of the phantom contained radioactive solution of [124]I. The non-standard positron-emitter [124]I was delivered by DSD pharma GmbH (Purkersdorf, Austria). The activity calibration measurements using a dose calibrator CRC-15R (Capintec Inc., Ramsey, NJ, USA) have been published elsewhere[32]. The [124]I solution for the spheres was taken from a stock solution, whereas the radioactivity for the cavity (background activity) was directly added to the water-filled phantom. Both the cavity and the stock solutions contained non-radioactive iodine to prevent adsorption on the phantom walls.

The initial activity concentration (AC) in the spheres and the background was derived from published thyroid cancer patient data[31]. (To avoid confusion, the ACs given in the text are all prepared ACs, that is, the AC derived from dose calibrator measurements.) Using the ACs from a total of 89 lymph node metastases and scaling the ACs to a commonly used administered [124]I activity of 37 MBq, the statistics—expressed in mean (median) ± standard deviation (minimum–maximum)—of the actual ACs (after partial-volume-effect correction of the imaged

2
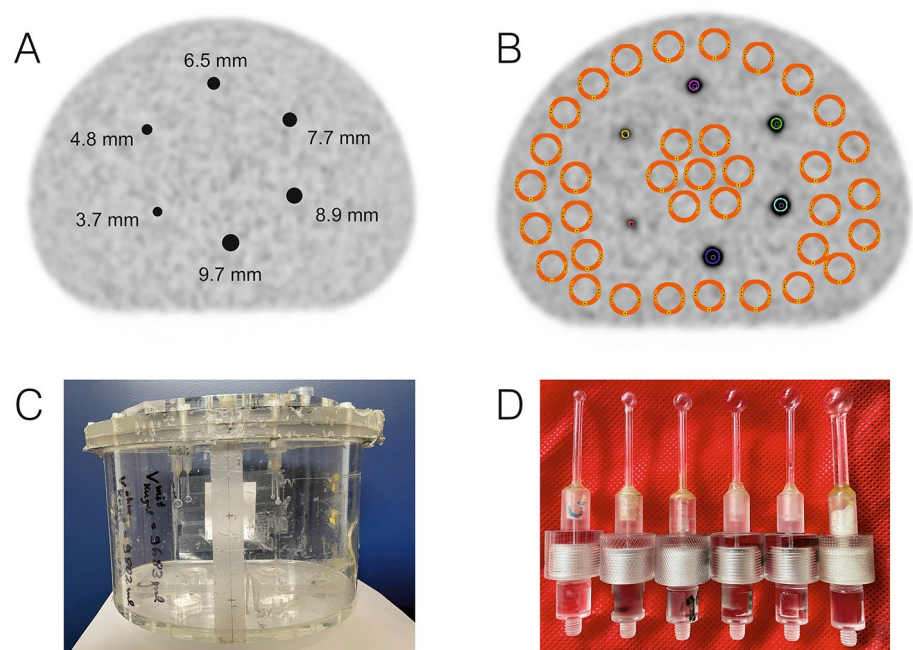
Figure 1. (A) Schematic representation of the small tumour phantom with small spherical inserts (sphere diameters are indicated). (B) Positions of the background ROIs (orange) and sphere VOIs (multiple colours). (C) Pictures of the small tumour phantom and (D) pictures of the spherical inserts.

Number of measurement	Biograph Vision PET/CT system			Biograph mCT PET/CT system		
	Temporal distance to measurement 1 (h)	Sphere activity concentration (kBq/ml)	Background activity concentration (kBq/ml)	Temporal distance to measurement 1 (h)	Sphere activity concentration (kBq/ml)	Background activity concentration (kBq/ml)
1	0	24.99	1.24	0	24.85	1.23
2	67.0	15.72	0.78	67.0	15.63	0.78
3	161.6	8.17	0.41	161.7	8.13	0.40
4	233.8	4.83	0.24	237.7	4.93	0.24
5	331.4	2.53	0.13	331.0	2.51	0.12
6	402.5	1.37	0.07	420.1	1.54	0.08
7	498.4	0.80	0.04	497.1	0.79	0.04
8	571.1	0.43	0.02	588.4	0.48	0.02
9	666.6	0.26	0.01	659.9	0.25	0.01

Table 1. Calculated sphere and background activity concentrations for both PET systems.

ACs) was 155 kBq/mL (72 kBq/mL) ± 186 kBq/mL (1.6–691 kBq/mL). The AC ratio of lesion to background (signal-to-background) was 1075 (346) ± 2069 (17–15,538), respectively. Corresponding numerical values for lung metastases and bone metastases are presented in the Supplemental Material (Supplemental Table S2). To simulate tumours under increasing challenging conditions, the initial (prepared) sphere AC was 25 kBq/mL and a signal-to-background ratio of 20:1 was used (values close to the minimum ranges of the evaluated DTC metastases). Lower sphere ACs were realised by 9 sequential PET acquisitions (temporal distance between each acquisition about one ^{124}I half-life) and ranged from 25 kBq/ml down to 0.25 kBq/mL. The individual sphere and background ACs for both scanners at different starting times of PET image acquisition are shown in Table 1.

Phantom PET acquisition and its image reconstruction. *PET acquisition.* The phantom measurements were all one-bed scans with the phantom placed centrally within the scanner's field of view. The acquisition started with a CT scan (tube voltage of 120 kVp, tube current time product of 15 mAs). Thereafter, PET emission data were acquired for 30 min in list mode format. The total phantom measurements lasted 28 days, resulting in lower and more challenging sphere ACs.

Iterative reconstruction	Scanner type	Iterations × subsets	Gauss filter (mm)	Matrix size	Voxel size (mm³)
OSEM	Vision	10 × 5	2	440 × 440	1.65 × 1.65 × 2.00
	mCT	3 × 24	2	400 × 400	2.04 × 2.04 × 2.00
OSEM-TOF	Vision	4 × 5	2	440 × 440	1.65 × 1.65 × 2.00
	mCT	2 × 21	2	400 × 400	2.04 × 2.04 × 2.00
OSEM-TOF+PSF	Vision	4 × 5	2	440 × 440	1.65 × 1.65 × 2.00
	mCT	2 × 21	2	400 × 400	2.04 × 2.04 × 2.00

Table 2. Overview of the image reconstruction parameters for both PET systems.

Image reconstruction. Both scanners allow for iterative image reconstruction algorithms. Image reconstructions were performed using (three-dimensional) ordinary Poisson ordered-subsets expectation maximization (OSEM), with TOF reconstruction alone (OSEM-TOF), or with both TOF and point spread function (PSF) modelling (OSEM-TOF+PSF). All PET data were reconstructed using our clinically standard reconstruction protocols that were optimized for quantitative ^{124}I imaging[21,33] and are listed in Table 2. All data were corrected for scatter, randoms, attenuation, dead time, decay, and normalization. In addition, for all PET systems, a prompt gamma coincidence correction method is by default implemented in the PET reconstruction algorithm for radionuclides emitting prompt gammas such as ^{124}I.

Phantom data analysis. To quantify the detectability improvements by the SiPM-based system, the size-dependant MDA was used as metric[34]. To estimate the MDA, three steps were performed. First, all PET images were evaluated in a human observer study to assess the visual detectability of the small spheres. Second, the signal-to-noise ratio (SNR) of all spheres was estimated. Third, visual detectability and SNR were correlated to define the threshold SNR that indicates visual detectability (separately for OSEM, OSEM-TOF, and OSEM-TOF+PSF reconstructed images). The MDA was defined as the AC at the threshold SNR. In the following, the three steps are outlined in detail.

Human observer study. All data were interpreted by five nuclear medicine physicians (DK, MS, PS, CR, MW). The (lesion) detectability of each sphere was scored on an established 3-point scale differentiating between 0 = "not observed", 1 = "observed but comparable to noise" or 2 = "observed"[34,35]. As an adaption of the previously published method by Øen et al.[35], a sphere was rated as detected, if its sum score was ≥ 5.

Signal-to-noise ratio. The SNR of each sphere was determined for all evaluated data set (PET scanner, emission time and image reconstruction algorithm) using the following definition:

$$SNR = \frac{\left| \overline{AC_{sphere}} - \overline{AC_{background}} \right|}{\sigma_{background}},$$

with $\overline{AC_{sphere}}$ defined as mean sphere AC, $\overline{AC_{background}}$ as mean background AC, and $\sigma_{background}$ as standard deviation of $AC_{background}$.

Sphere ACs were evaluated in spherical volumes-of-interests (VOIs) of diameters that matched the real diameters of the small spheres (Fig. 1A). For positioning, the co-registered CT data were used; VOI positions were locally optimised in the 30-min emission time OSEM-TOF+PSF images with respect to a maximal mean sphere AC. The background AC was measured in 35 circular regions of interests of 20-mm diameter (representing twice the diameter of the largest sphere), which were positioned in the same transversal plane as the centres of the spherical VOIs (Fig. 1B).

Minimum detectable activity. The SNR distributions of detected and undetected spheres were visually analysed in a histogram plot to determine a threshold SNR indicating visibility[34,35]; the evaluation was separately performed for the different reconstruction algorithms. For each sphere, the SNR was analysed as a function of the AC. To reduce the influence of image noise, a cubic spline regression analysis was performed as previously described[36]. The MDA value was calculated as the AC at the threshold SNR.

Activity concentration thresholds reflecting response levels to radioiodine therapy. Under certain assumptions, the actual ^{124}I AC in the lesions can be used to predict the level of response to radioiodine therapy[11]. The key quantity is the absorbed (radiation) dose to the lesion. In the radioiodine treatment of lymph node metastases, a target dose of > 85 Gy reaches a high response of 98%, a target dose between 35 and 85 Gy a medium response of about 20%, whereas for a value below 35 Gy a therapeutic effect is unlikely[37]. Thus, the lesions can be categorized in a low, a medium, and a high absorbed dose group, according to the likelihood of success of radioiodine therapy. For small lesion sizes, the absorbed dose (D) mainly arises from beta-particle irradiation form ^{131}I. Using the "medical internal radiation dose" (MIRD) formalism and spherical tumour model, the (average) self-absorbed (D) after administration of a therapeutic activity ($A_0^{I\text{-}131}$) can be written in the following numerical value equation[38]:

$$\left(D/\mathrm{Gy}\right) = 3.809 \cdot \left(C_0^{\mathrm{I\text{-}124}}/\mathrm{kBq\ mL^{-1}}\right) \cdot \left(T_{\mathrm{I\text{-}131}}^{\mathrm{eff}}/\mathrm{d}\right) \cdot \frac{\left(A_0^{\mathrm{I\text{-}131}}/\mathrm{GBq}\right)}{\left(A_0^{\mathrm{I\text{-}124}}/\mathrm{MBq}\right)}$$

Its derivation depends on several assumptions: (a) In the case of small lesions ranging from 3.7 to 10 mm, the absorbed dose essentially arises from self-irradiation by the beta particles of ^{131}I. (b) In addition, particle-range effects due to the limited mean beta-particle range of ^{131}I, even for the smallest sphere of 3.7 mm, can be neglected, as the percentage fraction of energy deposited within this lesion is still 90%[39]. (c) After administration of diagnostic activity ($A_0^{\mathrm{I\text{-}124}}$), an instant ^{124}I AC ($C_0^{\mathrm{I\text{-}124}}$) and a monoexponential clearance with an effective half-life ($T_{\mathrm{I\text{-}131}}^{\mathrm{eff}}$) are assumed. Of note, the instant ^{124}I AC equals the prepared sphere AC in our phantom setup. The equation given above was used to calculate the AC thresholds for the different absorbed lesion groups.

Patient investigations. PET images of two thyroid cancer patients are presented to visualise the effects of the application of SiPM-based ^{124}I PET. The detailed patient characteristics are: Patient #1: papillary thyroid cancer, male, 68 years, TNM: T3N1M1, unstimulated Tg: not measurable, Tg antibodies: 273 IU/mL, 1 previous radioiodine therapy, cumulative activity of ^{131}I: 3.7 GBq. Patient #2: poorly differentiated thyroid cancer, male, 58 years, TNM: T3N0M1, unstimulated Tg: 1765 ng/ml, Tg antibodies: not measurable, 4 previous radioiodine therapies, cumulative activity of ^{131}I: 21.5 GBq. Patient #1 underwent PET/CT acquisition on the mCT 18.1 h after oral application of 37.9 MBq of ^{124}I, the PET/CT scan of patient #2 was started 17.4 h after application of 37.5 MBq of ^{124}I on the mCT. Approximately 1 h after the acquisition on the mCT, PET/CT data were acquired on the Vision. Whole-body PET/CT data were acquired from head to thigh using 5–8 bed positions. Serum thyroid stimulating hormone level stimulation (≥ 30 mU/L) was achieved by levothyroxine withdrawal. The same PET protocol as described above for the phantom PET acquisition was used; the emission time was 4 min per bed position for each scanner type. PET/CT scans started with a whole-body spiral CT in low-dose technique without application of contrast agent (tube voltage of 120 kVp, tube current time product of 15 mAs, beam pitch of 1.0, and slice width of 5 mm). The patients gave written informed consent. The presentation of the patient examples was performed in accordance with the Declaration of Helsinki and approved by the institutional ethics committee (University of Duisburg-Essen, medical faculty, ethics protocol number 20-9203-BO).

Software. PET data analysis was performed using PMOD 4.2 (PMOD Technologies LLC, Zurich, Switzerland). OriginPro 2019b (OriginLab, Northampton, Massachusetts, USA) and MATLAB R2019b (MathWorks, Natick, Massachusetts, USA) were used for data handling. Cubic spline regression analyses were performed using MATLAB R2019b.

Results

In the phantom study, a total of 216 images (for each scanner type 9 ACs, 4 emission time durations for a single bed position, and 3 reconstruction algorithms) were analysed. As each image contains six spheres, a total of 1296 data points were evaluable. For reasons of clarity, only selected data are presented in the following section. The complete evaluated data are shown as Supplemental Material. In the following, all indicated emission times refer to a single bed position.

Human observer study. Table 3 summarises the results of the human observer study; for each reconstruction algorithm, AC and reconstruction algorithm, the diameter of the smallest detected sphere is indicated. The data show a shift towards a smaller size of the smallest detected sphere from the mCT to the Vision, from OSEM to OSEM-TOF and from OSEM-TOF to OSEM-TOF+PSF image reconstruction, and from shorter to longer emission times (Table 3).

For example, the smallest sphere (3.7-mm diameter) was, at the highest AC, solely detectable on the Vision, using long emission times of ≥ 16 min, and using OSEM-TOF or OSEM-TOF+PSF image reconstruction. The second smallest sphere (4.8-mm diameter) was, at the highest AC and using OSEM-TOF or OSEM-TOF+PSF image reconstruction, detectable on the Vision at an emission time of ≥ 4 min, whereas on the mCT an emission time of ≥ 8 min was necessary (Fig. 2 and Table 3).

Signal-to-noise ratio. The SNR shifted to higher values from the mCT to the Vision, from OSEM to OSEM-TOF and from OSEM-TOF to OSEM-TOF+PSF reconstructed images, from shorter to longer emission times, and from smaller to larger sphere sizes. For an acquisition comparable to our clinical standard PET protocol (4-min emission time, OSEM-TOF image reconstruction), the SNR is presented as a function of the AC for all sphere sizes in Fig. 3. Similar curves for all other imaging modalities are shown in the Supplemental Material.

Histograms of the SNR of all detected and undetected spheres are shown in Fig. 4. For OSEM and OSEM-TOF reconstructions, a threshold value to indicate detectability of SNR ≥ 5, for OSEM-TOF+PSF, a value of SNR ≥ 8 was derived. These SNR threshold values were consistent with the commonly applied Rose criterion (originally derived from a theoretical contemplation of quantum effects in the visual process) that assumes a threshold SNR of 5 to define a detectable object[40]. The slightly higher threshold for the OSEM-TOF+PSF reconstructed images may be explained by a lower image noise that is a known phenomenon for PSF-reconstructed PET images[41]. In our data, the mean standard deviation of the background AC was lower in the OSEM-TOF+PSF reconstructed images. For example, for the 30-min emission time at the highest AC the ratios of the mean standard deviation of the background AC for OSEM-TOF+PSF to OSEM-TOF were 0.49 (mCT) and 0.61 (Vision). The respective ratios for OSEM-TOF+PSF to OSEM were 0.40 (mCT) and 0.44 (Vision).

Sphere activity concentration (kBq/ml)	Scanner	OSEM				OSEM-TOF				OSEM-TOF+PSF			
		30 min	16 min	8 min	4 min	30 min	16 min	8 min	4 min	30 min	16 min	8 min	4 min
24.99	Vision	4.8	4.8	6.5	6.5	3.7	3.7	4.8	4.8	3.7	3.7	4.8	4.8
24.85	mCT	4.8	4.8	6.5	7.7	4.8	4.8	6.5	6.5	4.8	4.8	4.8	6.5
15.72	Vision	4.8	6.5	6.5	6.5	3.7	4.8	4.8	4.8	3.7	4.8	4.8	4.8
15.63	mCT	6.5	6.5	6.5	7.7	4.8	6.5	6.5	7.7	4.8	4.8	6.5	6.5
8.17	Vision	6.5	6.5	6.5	7.7	4.8	6.5	6.5	6.5	4.8	4.8	4.8	4.8
8.13	mCT	6.5	7.7	9.7	9.7	6.5	6.5	7.7	7.7	4.8	4.8	6.5	7.7
4.83	Vision	4.8	6.5	7.7	8.9	3.7	4.8	6.5	7.7	3.7	4.8	6.5	6.5
4.93	mCT	6.5	7.7	–	–	6.5	6.5	8.9	–	6.5	6.5	6.5	8.9
2.53	Vision	6.5	7.7	8.9	–	6.5	6.5	6.5	7.7	4.8	6.5	6.5	6.5
2.51	mCT	7.7	–	–	–	7.7	8.9	–	–	6.5	6.5	7.7	–
1.37	Vision	8.9	9.7	–	–	6.5	6.5	7.7	–	4.8	6.5	7.7	7.7
1.54	mCT	–	–	–	–	8.9	–	–	–	6.5	6.5	–	–
0.80	Vision	8.9	9.7	–	–	6.5	6.5	7.7	–	6.5	6.5	6.5	–
0.79	mCT	–	–	–	–	7.7	–	–	–	6.5	7.7	–	–
0.43	Vision	–	–	–	–	7.7	8.9	–	–	6.5	7.7	–	–
0.48	mCT	–	–	–	–	–	–	–	–	8.9	–	–	–
0.26	Vision	–	–	–	–	8.9	8.9	–	–	8.9	8.9	–	–
0.25	mCT	–	–	–	–	–	–	–	–	–	–	–	–

Table 3. Human observer study results—smallest detected sphere size (in mm) for each scanner type, reconstruction algorithm and emission time.

Minimum detectable activity. For each sphere, reconstruction algorithm and PET scanner, the minimum detectable activity was separately calculated using the SNR threshold values derived from Fig. 4 (see above). Considering, for instance, the largest sphere (9.7 mm), the MDA is 1.8 kBq/ml on the Vision and 3.7 kBq/ml on the mCT at 4-min emission time and using OSEM-TOF+PSF reconstructed images (see Fig. 5, numbers are given in Supplemental Table S3 in the Supplemental Material). For the smallest sphere (3.7 mm), the MDA is 17.0 kBq/ml on the Vision at 16-min emission time and using OSEM-TOF+PSF reconstructed images; this sphere was not detected on the mCT.

In the relative comparison, the MDA decreased from the mCT to the Vision, from OSEM to OSEM-TOF and from OSEM-TOF to OSEM-TOF+PSF image reconstruction, with increasing emission time, and with increasing sphere size (Fig. 5). Across all evaluated emission times and reconstruction algorithms, the (overall) mean MDA ratio of Vision to mCT is 0.52 ± 0.18. Comparing the different image reconstruction algorithms, the mean MDA ratio is 0.61 ± 0.17 (OSEM), 0.41 ± 0.17 (OSEM-TOF), and 0.53 ± 0.15 (OSEM-TOF+PSF), respectively. No dependency of the mean MDA ratio on the emission time (0.47 ± 0.25 for 30-min, 0.59 ± 0.23 for 16-min, 0.59 ± 0.16 for 8-min, and 0.53 ± 0.12 for 4-min emission time, respectively) or on the sphere size is observed (Table 4). The MDA for all evaluated data points and the MDA ratio separately for each combination of emission time and image reconstruction algorithm is shown as Supplemental Material.

Correlation between minimum detectable activity and emission time. For validation, we determined the MDA ratio of shorter to longer emission time for all spheres for which exact MDA values for two emission times that differed by a factor of two were available (n = 41). The mean ± standard deviation ratio of shorter to longer emission time was 0.48 ± 0.15. This confirms that, in a first approximation, the MDA correlates linearly with the emission time.

Activity concentration thresholds for the absorbed lesion groups. In the calculation, a mean effective ^{131}I half-life of approximately 3.5 days was used, a value that was derived from 52 lymph node metastases[42]. Moreover, an applied [124]I activity of 37 MBq (based on our clinically established dosimetry protocol) and a maximum single ^{131}I therapeutic activity of 15 GBq applied at our department[11,43] were selected. A threshold AC of 7 kBq/ml was calculated to achieve a lesion dose of 35 Gy and a threshold AC of 16 kBq/ml is required to achieve a lesion dose of 85 Gy. Thus, the three lesion groups exhibit AC ranges of AC < 7 kBq/ml for the low absorbed dose group, $7 \leq AC \leq 16$ kBq/ml for the medium absorbed dose group, and AC > 16 kBq/ml for the high absorbed dose group. These three groups are separated by horizontal lines in Fig. 5.

Of note, transferring above model calculations to clinical lesion dosimetry, several contributions limiting the accuracy of absorbed doses are to be considered. The largest uncertainties in small lesion absorbed dose estimates, as investigated in this phantom study, remain the volume determinations. Assuming an uncertainty in diameter of ± 1 mm in each dimension, the maximum error uncertainties, for the smallest (3.7 mm) and for the largest (9.7 mm) investigated spheres are approximately 80% and 30%, respectively. Other error contributions are, for instance, related to parameterisation of the time-activity curves and activity concentration measurements.
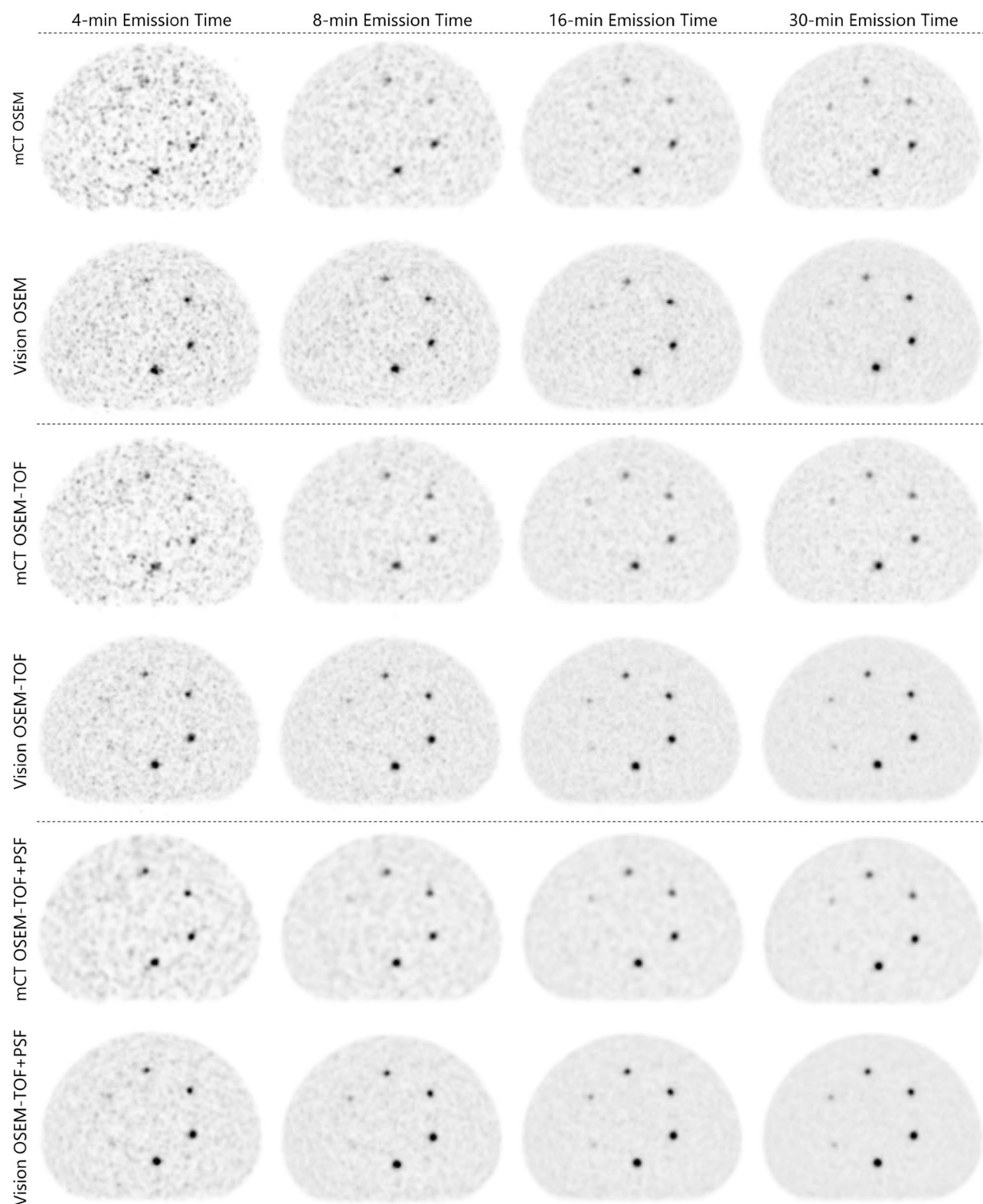
Figure 2. Evaluated PET images at the first imaging time point (sphere activity concentration ~ 25 kBq/ml). The position of the small spheres inside the phantom is presented in Fig. 1). Sphere diameters are depicted in Fig. 1A.

Patient examples. In patient 1, an additional [124]I-avid cervical lymph node metastasis was detected (Fig. 6). In this patient three other lymph node metastases were detected also on the mCT and therapy management
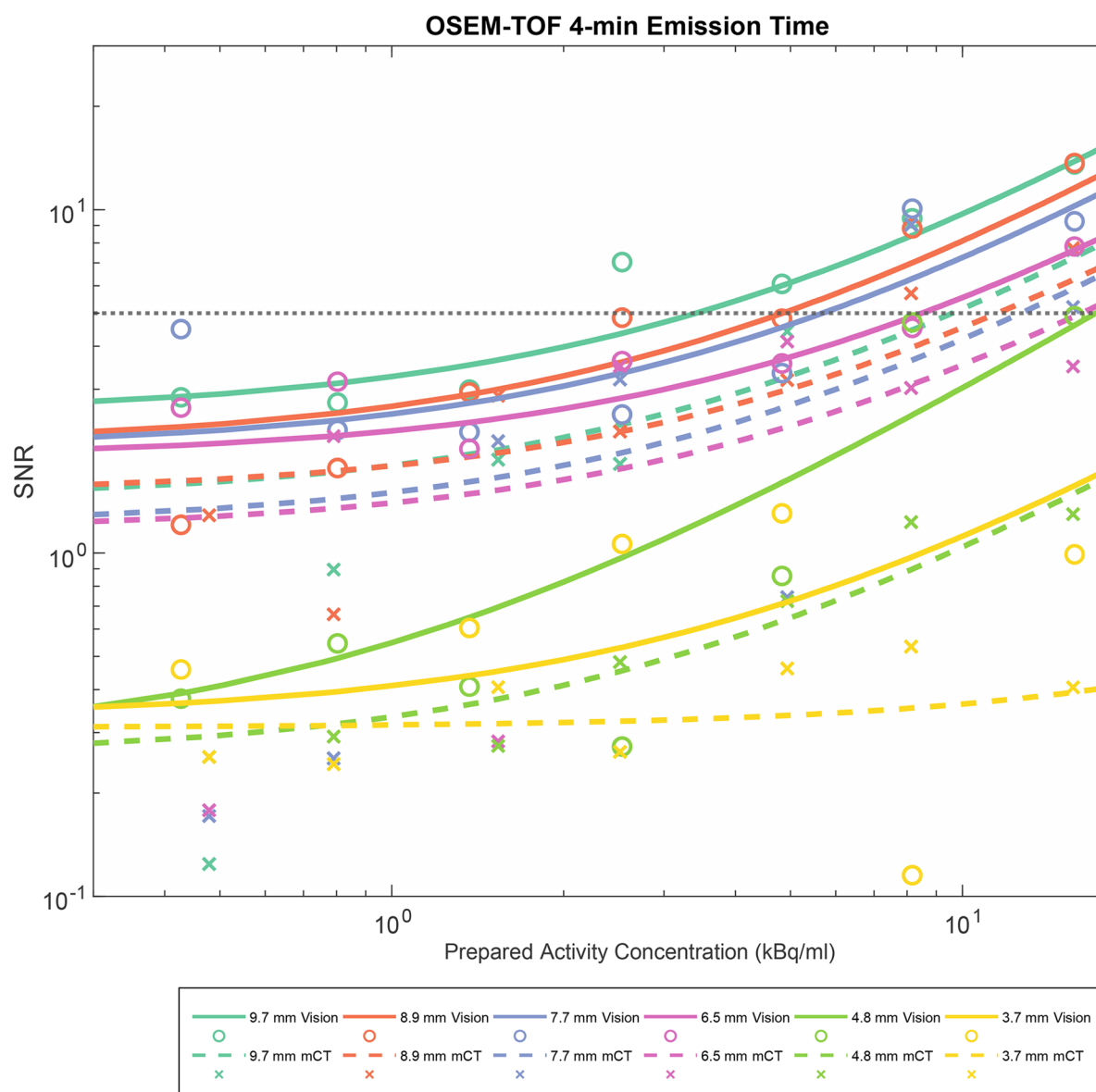
Figure 3. SNR as a function of the AC for all evaluated spheres for a clinical standard emission protocol (OSEM-TOF, 4-min emission time). A horizontal line at SNR = 5 indicates the threshold for visual detectability in OSEM-TOF reconstructed images.

(watchful waiting) was not altered. As shown in Fig. 7, multiple additional [124]I-avid pulmonary metastases are observed in patient 2. In this patient, therapy management was chosen to watchful waiting due to the presence of other radioiodine-negative metastases. Visually, image quality and detectability increase, and image noise decreases from the mCT to the Vision, and from OSEM to OSEM-TOF and OSEM-TOF to OSEM-TOF+PSF reconstructed images.

Discussion

In the comparison between the SiPM- and PMT-based systems, a qualitative and a quantitative detectability analysis were performed. In the qualitative human observer study, the detectability was higher on the Vision (Table 3, Figs. 3 and 4). The clinical PET image exemplified the benefits of the SiPM-based PET system (Fig. 6 & Fig. 7). In the quantitative comparison of the MDA (which is a scanner-specific metric under fixed acquisition conditions), the Vision outperformed the mCT in all examined imaging conditions (Table 4); the overall mean MDA ratio (Vision to mCT) was 0.52 ± 0.18. Both an improved detectability[21,44] and an increased SNR[45] for small spheres were previously observed for SiPM-based PET/CT systems in studies using ^{18}F-FDG.

In agreement with a previous study by Beijst et al.[36] who evaluated slightly larger spheres (≥ 10 mm) and only used the mCT, the MDA decreased from OSEM to OSEM-TOF and from OSEM-TOF to OSEM-TOF+PSF image reconstruction and with increasing sphere size (Fig. 5). Of note, the MDA ratio did not correlate with the emission time or the sphere size (Table 4). The MDA ratio was slightly improved for OSEM-TOF and
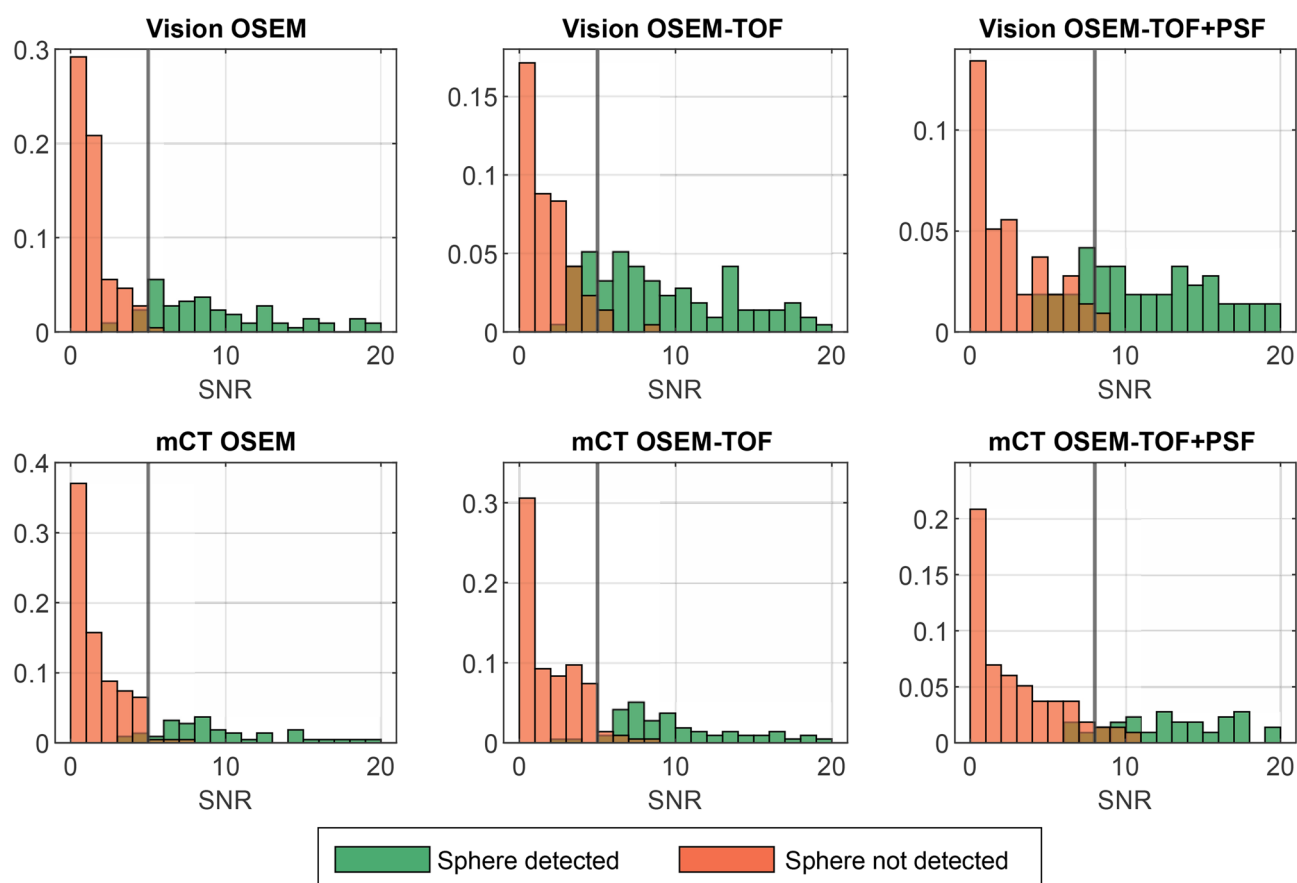
Figure 4. Normalised histograms of the SNR of detected and undetected spheres in the human observer study. Vertical lines at SNR = 5 for OSEM and OSEM-TOF image reconstruction, and SNR = 8 for OSEM-TOF+PSF image reconstruction, respectively, indicate the threshold that was derived to define a lesion as detectable in the mathematical model. For clarity purposes, SNR values > 20 are not displayed. The mixed organge-brown color arises from superposition of orange and green.

OSEM-TOF+PSF image reconstructions (Table 4), a possible explanation may be the improved timing resolution of the Vision (214 ps for the Vision versus 540 ps for the mCT). The improved timing resolution is particularly beneficial for the typically noisy ^{124}I PET images[22] that are limited by a low positron branching ratio and low administered activities.

Based on these phantom data, we attempt to predict the response to radioiodine therapy of those lesions that are only identified on the Vision (Fig. 5). The following considerations refer to the image reconstruction with the best detectability, i.e., OSEM-TOF or OSEM-TOF+PSF on the Vision and OSEM-TOF+PSF on the mCT, respectively. Moreover, lesions are assigned to three groups by their AC (low, medium, and high absorbed dose groups) that correlate with a possible success of radioiodine therapy. The respective AC thresholds were based on patient data, who underwent imaging after application of 37 MBq of ^{124}I (according to our standard clinical PET protocol), an observed mean effective ^{131}I half-life of 3.5 days for lymph node metastases, and maximum single ^{131}I therapeutic activity of 15 GBq. Also, the selected sphere sizes reflect the typical size range for cervical lymph nodes[30,31].

A striking feature is that the AC thresholds indicating treatment response to radioiodine therapy fall within the MDA range of the PET/CT devices under clinical acquisition conditions. Thus, the detectability of a treatable lesion can depend on the emission time and a separate evaluation of different-sized lesions is mandatory. One major consequence of the detailed analysis is that for spheres ≥ 6.5 mm in diameter, lesions from each group could be identified on both PET/CT systems using a standard clinical emission time of 4-min per bed position. Regarding the second smallest sphere (4.8-mm diameter) at 4-min emission time per bed position, only lesions belonging to the high absorbed dose group would be detectable on the Vision. To identify lesions belonging to all absorbed dose groups, an increased emission time of 16 min per bed position would be necessary. On the mCT, a 16-min emission time per bed position would be necessary to detect lesions from the high absorbed dose group, lesions from the low and medium groups would not be detectable even at an emission time of 30 min per bed position. For the smallest sphere (3.7-mm diameter), lesions from the high absorbed dose group would be detectable on the Vision at 16-min and from all groups at 30-min emission time per bed position. Of note, the smallest sphere was not detectable on the mCT under any examined condition.

The examined conditions also cover the typical activity ranges of clinically detected lung and bone lesions (Supplemental Table S2 in the Supplemental Material). In the evaluated pulmonary metastasised DTC patient
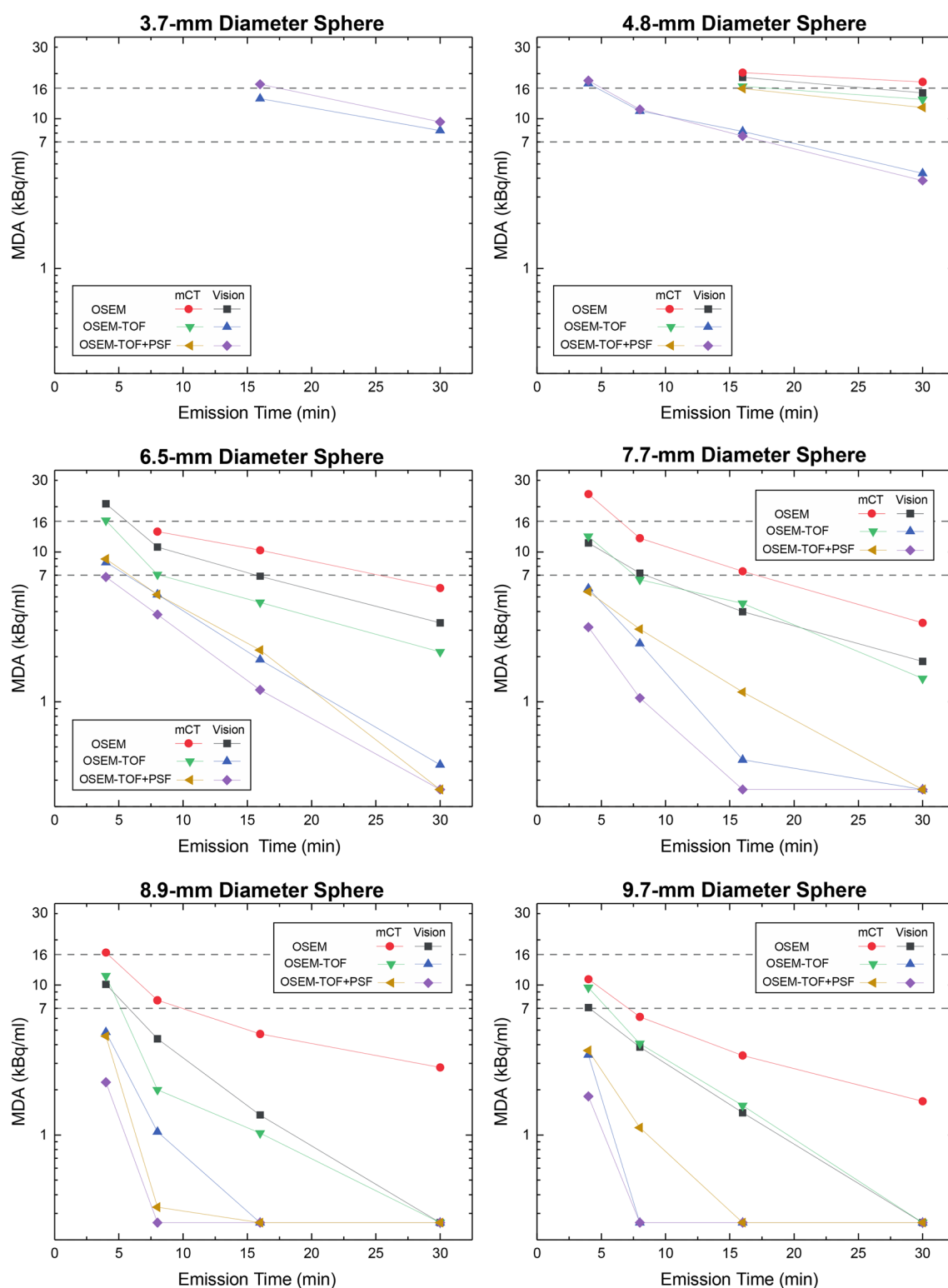
Figure 5. Semi-logarithmic representation of the MDA for both PET/CT systems as a function of the emission time for all spheres and image reconstructions. Horizontal lines at a MDA of 7 kBq/mL and at MDA of 16 kBq/mL are the dividing lines for the low, medium, and high absorbed dose lesion groups. Data points of a MDA < 0.26 kBq/ml were set to 0.26 kBq/ml meaning that the respective sphere was detected at every AC in this study.

(patient 2), the size range of lung metastases (4–24 mm in diameter) indicates that the size range of small

Sphere diameter (mm)	OSEM				OSEM-TOF				OSEM-TOF+PSF				All reconstructions
	30-min	16-min	8-min	4-min	30-min	16-min	8-min	4-min	30-min	16-min	8-min	4-min	All emission times (mean ± SD)
3.7	–	–	–	–	–	–	–	–	–	–	–	–	–
4.8	0.84	0.93	–	–	0.32	0.50	–	–	0.33	0.48	–	–	0.56 ± 0.26
6.5	0.59	0.67	0.79	–	0.18	0.42	0.74	0.53	–	0.54	0.74	0.76	0.60 ± 0.19
7.7	0.56	0.54	0.59	0.47	–	0.09	0.38	0.45	–	–	0.35	0.58	0.45 ± 0.16
8.9	–	0.29	0.55	0.61	–	–	0.53	0.42	–	–	–	0.49	0.48 ± 0.12
9.7	–	0.42	0.63	0.65	–	–	–	0.36	–	–	–	0.49	0.51 ± 0.13
All spheres (mean ± SD)	0.66 ± 0.16	0.57 ± 0.25	0.65 ± 0.11	0.58 ± 0.10	0.25 ± 0.11	0.34 ± 0.22	0.55 ± 0.19	0.44 ± 0.08	0.33 ± 0	0.51 ± 0.05	0.54 ± 0.28	0.58 ± 0.13	0.52 ± 0.18

Table 4. MDA-Ratios between the Vision and the mCT for each sphere size, reconstruction algorithm, and emission time. No values are indicated, if the MDA was outside the range that can be evaluated within this investigation (< 0.26 kBq/ml or > 25 kBq/ml) for one or both examined PET/CT systems.
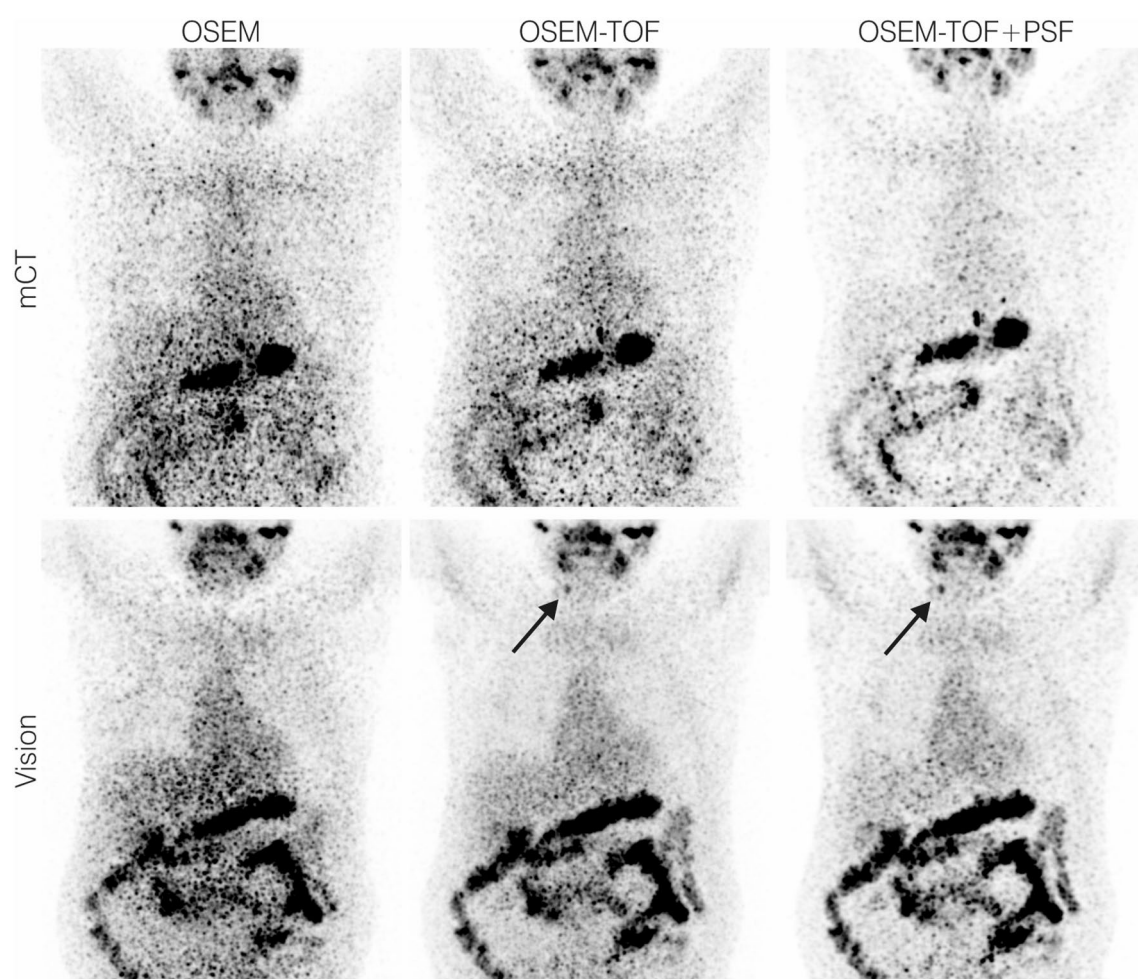
Figure 6. Maximum intensity projection PET images of exemplary patient data set 1 acquired using our clinical PET protocol (4-min emission time per bed position, image acquisition approximately 1 day after application of 37.9 MBq of ^{124}I). The black arrow indicates an additional cervical lymph node metastasis detected on the SiPM-based system.
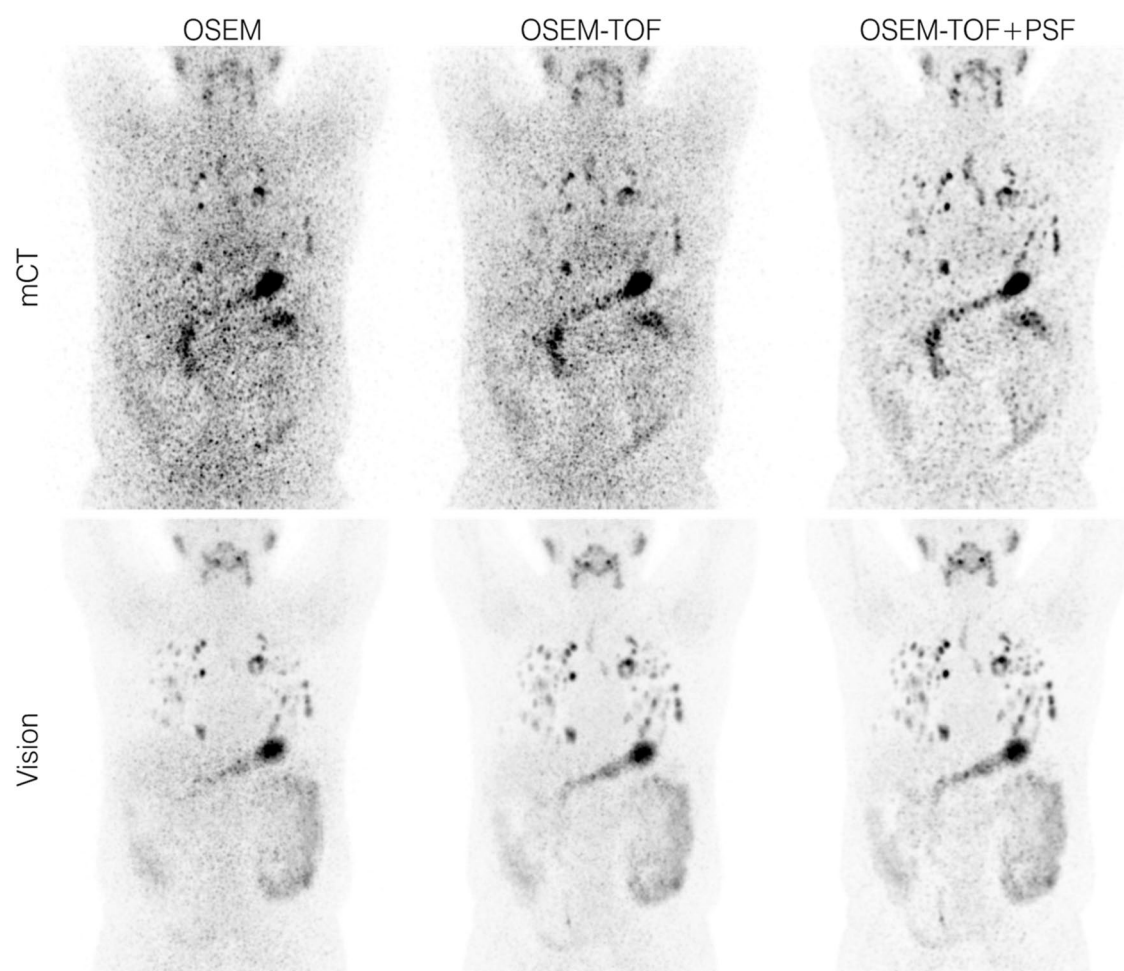
Figure 7. Maximum intensity projection PET images of exemplary patient data set 2 acquired using our clinical PET protocol (4-min emission time per bed position, image acquisition approximately 1 day after application of 37.5 MBq of ^{124}I). The size range of the detected lung lesions was 4–24 mm in diameter.

detectable pulmonary metastases is also represented in this study. We therefore suppose that the results can be projected to small lung metastases. Patients with even smaller disseminated pulmonary metastases (i.e., miliary pulmonary metastases that are detected in intratherapeutic ^{131}I scintigraphy) can be challenging[46], even for SiPM-based ^{124}I PET/CT. A published method that may help to detect these lesions and can also be applied for SiPM-based systems is the quantitative analysis of the ^{124}I activity concentration ratio of the lung to the background (L/B ratio)[46]. A detailed analysis of patient data may be warranted to evaluate the clinical benefit of the L/B ratio for SiPM based PET/CT systems.

Further consequences are related to "blind" radioiodine therapies and the results published by the THYROPET study[14]. The improved detectability using the Vision might allow for the additional identification of small lesions that could respond to radioiodine therapy. Hence, the number of patients subjected to "blind" radioiodine therapy might be reduced, thus reducing the risk of adverse effects in a scenario, in which a clinical benefit is unlikely. The data also suggest that a limited PET scanner sensitivity of previous-generation scanners can contribute to explain the discrepancies between ^{124}I PET and intratherapeutic ^{131}I imaging that were reported in previous studies including the prospective THYROPET study[13,14]. Specifically, the Biograph mCT that was used as example for a previous-generation PET/CT system in the present study was a high-end scanner at the time of the published results that reported false negative ^{124}I PET findings[13,14]. In the previous studies, not only the mCT but also less sophisticated PET/CT systems, some without TOF modelling, were used[13,14]. Following our data, on the mCT without TOF modelling, for the 6.5-mm and 7.7-mm spheres, lesions belonging to the low and medium absorbed dose groups would not be identified.

The clinical benefit of additionally detected lesions may be limited by the presence of other metastases that are also visualised by older devices. In the two patients presented (Figs. 6 and 7), the additional lesions had no impact on therapy management. We recently performed a clinical evaluation of SiPM-based ^{124}I PET/CT in patients with thyroglobulin levels in the low measurable range[21]. Additional lesions were detected in 2 of 10 patients; however, only in one patient the therapeutic concept was changed (begin of radioiodine therapy)[21].

The results can also be used to discuss a clinical acquisition protocol that allows for the detection of therapeutically relevant lesions. Using a SiPM-based PET/CT system, OSEM-TOF or OSEM-TOF+PSF reconstructed

images and an emission time of 8 min (per bed position), all spheres except the smallest 3.7-mm diameter sphere were detectable, a sphere size being at the lower end of typical lymph node metastases in the neck region[30]. For smaller lesions, an increased emission time could be necessary. However, the maximum emission time of a clinical scan is limited by patient condition and the availability of PET scanning time. A particularly increased emission time for single regions, e.g., the neck region that is mostly affected by DTC lymph node metastases[1], appears to be feasible. Our results suggest a linear correlation between emission time and MDA. Alternatively, the applied amount of ^{124}I could be increased to improve the detectability. According to published literature, up to 74 MBq of ^{124}I are applied in clinical protocols[7]. The application of higher amounts of ^{124}I may be critical due to thyroid stunning (i.e., diminished uptake of ^{131}I after diagnostic scans), which has not been conclusively clarified yet for ^{124}I[47].

Besides the usage of SiPM-based PET/CT systems, the implantation of improved image reconstruction algorithms may increase the detectability of small lesions. Since SIPM-based systems will not probably be available in all centres within the next years, software improvements are particularly important because they can also be applied to existing PET/CT systems.

The study faces four limitations. First, the discussed clinical consequences are limited by the assumption of the administration of 37 MBq of ^{124}I. However, this is a commonly applied activity in clinical protocols[21]. Second, in contrast to the phantom setting, real metastases can be inhomogeneous, of non-spherical geometry, their signal-to-background ratio can be variable, and their PET signal can be influenced by motions. Moreover, an abdominal phantom was used that could affect a projection of the results to the neck region. However, these limitations affect both examined PET systems. Third, the spheres are located at fixed positions; therefore, the human observer analysis is biased by prior knowledge. Fourth, the choice of reconstruction parameters was guided by the manufacturer's recommendation; further MDA improvements could be achieved by an optimisation study (e.g., regarding number of iterations).

Conclusion

The overall mean MDA for ^{124}I was improved by a factor of 0.52 ± 0.18 for the Biograph Vision in comparison to the Biograph mCT. Under challenging conditions, all lesions with expected response to radioiodine therapy of ≥ 6.5 mm in diameter could be identified on both PET/CT systems using a standard clinical protocol. Lesions of smaller size—still with predicted response to radioiodine therapy—could be detected when applying a SiPM-based PET system at reasonable scan duration times. Further clinical studies are warranted to evaluate if negative ^{124}I PET scans on a SiPM-based system can be sufficient to preclude patients from blind radioiodine therapy. In the future, the clinical application of total body PET systems can further reduce the MDA.

References

1. Haugen, B. R. *et al.* 2015 American Thyroid Association Management Guidelines for Adult Patients with Thyroid Nodules and Differentiated Thyroid Cancer: The American Thyroid Association Guidelines Task Force on Thyroid Nodules and Differentiated Thyroid Cancer. *Thyroid* **26**, 1–133. https://doi.org/10.1089/thy.2015.0020 (2016).
2. Luster, M. *et al.* Guidelines for radioiodine therapy of differentiated thyroid cancer. *Eur. J. Nucl. Med. Mol. Imaging* **35**, 1941–1959. https://doi.org/10.1007/s00259-008-0883-1 (2008).
3. Smallridge, R. C., Diehl, N. & Bernet, V. Practice trends in patients with persistent detectable thyroglobulin and negative diagnostic radioiodine whole body scans: A survey of American Thyroid Association members. *Thyroid* **24**, 1501–1507. https://doi.org/10.1089/thy.2014.0043 (2014).
4. Ma, C., Xie, J. & Kuang, A. Is empiric 131I therapy justified for patients with positive thyroglobulin and negative 131I whole-body scanning results?. *J. Nucl. Med.* **46**, 1164–1170 (2005).
5. Fard-Esfahani, A. *et al.* Adverse effects of radioactive iodine-131 treatment for differentiated thyroid carcinoma. *Nucl. Med. Commun.* **35**, 808–817. https://doi.org/10.1097/MNM.0000000000000132 (2014).
6. Phan, H. T. *et al.* The diagnostic value of 124I-PET in patients with differentiated thyroid cancer. *Eur. J. Nucl. Med. Mol. Imaging* **35**, 958–965. https://doi.org/10.1007/s00259-007-0660-6 (2008).
7. Van Nostrand, D. *et al.* (124)I positron emission tomography versus (131)I planar imaging in the identification of residual thyroid tissue and/or metastasis in patients who have well-differentiated thyroid cancer. *Thyroid* **20**, 879–883. https://doi.org/10.1089/thy.2009.0430 (2010).
8. Ruhlmann, M. *et al.* High level of agreement between pretherapeutic 124I PET and intratherapeutic 131I imaging in detecting iodine-positive thyroid cancer metastases. *J. Nucl. Med.* **57**, 1339–1342. https://doi.org/10.2967/jnumed.115.169649 (2016).
9. Pettinato, C. *et al.* Usefulness of 124I PET/CT imaging to predict absorbed doses in patients affected by metastatic thyroid cancer and treated with 131I. *Q. J. Nucl. Med. Mol. Imaging* **56**, 509–514 (2012).
10. de Pont, C., Halders, S., Bucerius, J., Mottaghy, F. & Brans, B. (1)(2)(4)I PET/CT in the pretherapeutic staging of differentiated thyroid carcinoma: Comparison with posttherapy (1)(3)(1)I SPECT/CT. *Eur. J. Nucl. Med. Mol. Imaging* **40**, 693–700. https://doi.org/10.1007/s00259-012-2331-5 (2013).
11. Jentzen, W. *et al.* Optimized 124I PET dosimetry protocol for radioiodine therapy of differentiated thyroid cancer. *J. Nucl. Med.* **49**, 1017–1023. https://doi.org/10.2967/jnumed.107.047159 (2008).
12. Pettinato, C. *et al.* Pretherapeutic dosimetry in patients affected by metastatic thyroid cancer using 124I PET/CT sequential scans for 131I treatment planning. *Clin. Nucl. Med.* **39**, e367-374. https://doi.org/10.1097/RLU.0000000000000490 (2014).
13. Khorjekar, G. R. *et al.* Do negative 124I pretherapy positron emission tomography scans in patients with elevated serum thyroglobulin levels predict negative 131I posttherapy scans?. *Thyroid* **24**, 1394–1399. https://doi.org/10.1089/thy.2013.0713 (2014).
14. Kist, J. W. *et al.* 124I PET/CT to predict the outcome of blind 131I treatment in patients with biochemical recurrence of differentiated thyroid cancer: Results of a multicenter diagnostic cohort study (THYROPET). *J. Nucl. Med.* **57**, 701–707. https://doi.org/10.2967/jnumed.115.168138 (2016).
15. Pattison, D. A. & Hicks, R. J. THYROPET study: Is it biology or technology that is the issue?. *J. Nucl. Med.* **58**, 354. https://doi.org/10.2967/jnumed.116.181420 (2017).

16. Kist, J. W., de Keizer, B., Hoekstra, O. S. & Vogel, W. V. Reply: THYROPET study: Is it biology or technology that is the issue?. *J. Nucl. Med.* **58**, 354–355. https://doi.org/10.2967/jnumed.116.181685 (2017).
17. Lopez-Mora, D. A. *et al.* Superior performance of 18F-fluorocholine digital PET/CT in the detection of parathyroid adenomas. *Eur. J. Nucl. Med. Mol. Imaging* **47**, 572–578. https://doi.org/10.1007/s00259-020-04680-7 (2020).
18. Miwa, K. *et al.* Detection of sub-centimeter lesions using digital TOF-PET/CT system combined with Bayesian penalized likelihood reconstruction algorithm. *Ann. Nucl. Med.* https://doi.org/10.1007/s12149-020-01500-8 (2020).
19. Surti, S. *et al.* Benefit of improved performance with state-of-the art digital PET/CT for lesion detection in oncology. *J. Nucl. Med.* https://doi.org/10.2967/jnumed.120.242305 (2020).
20. Weber, M. *et al.* Evaluation of (18)F-FDG PET/CT images acquired with a reduced scan time duration in lymphoma patients using the digital biograph vision. *BMC Cancer* **21**, 62. https://doi.org/10.1186/s12885-020-07723-2 (2021).
21. Kersting, D. *et al.* Comparing lesion detection efficacy and image quality across different PET system generations to optimize the iodine-124 PET protocol for recurrent thyroid cancer. *EJNMMI Phys.* **8**, 14. https://doi.org/10.1186/s40658-021-00361-y (2021).
22. Conti, M. & Bendriem, B. The new opportunities for high time resolution clinical TOF PET. *Clin. Transl. Imaging* **7**, 139–147. https://doi.org/10.1007/s40336-019-00316-5 (2019).
23. Alessio, A. M., Kinahan, P. E. & Lewellen, T. K. Modeling and incorporation of system response functions in 3-D whole body PET. *IEEE Trans. Med. Imaging* **25**, 828–837. https://doi.org/10.1109/tmi.2006.873222 (2006).
24. Panin, V. Y., Kehren, F., Michel, C. & Casey, M. Fully 3-D PET reconstruction with system matrix derived from point source measurements. *IEEE Trans. Med. Imaging* **25**, 907–921. https://doi.org/10.1109/tmi.2006.876171 (2006).
25. Rahmim, A. *et al.* Resolution modeled PET image reconstruction incorporating space-variance of positron range: Rubidium-82. in *2008 IEEE Nuclear Science Symposium Conference Record, NSS/MIC 2008*, 3643–3650.https://doi.org/10.1109/NSSMIC.2008.4774108 (2008).
26. Cal-Gonzalez, J. *et al.* Tissue-dependent and spatially-variant positron range correction in 3D PET. *IEEE Trans. Med. Imaging* **34**, 2394–2403. https://doi.org/10.1109/TMI.2015.2436711 (2015).
27. Bertolli, O. *et al.* PET iterative reconstruction incorporating an efficient positron range correction method. *Phys. Med.* **32**, 323–330. https://doi.org/10.1016/j.ejmp.2015.11.005 (2016).
28. Qi, J. & Leahy, R. M. Resolution and noise properties of MAP reconstruction for fully 3-D PET. *IEEE Trans. Med. Imaging* **19**, 493–506. https://doi.org/10.1109/42.870259 (2000).
29. Mehranian, A. *et al.* PET image reconstruction using multi-parametric anato-functional priors. *Phys. Med. Biol.* **62**, 5975–6007. https://doi.org/10.1088/1361-6560/aa7670 (2017).
30. Richter, E., Bohndorf, W. & Feyerabend, T. *Normal Lymph Node Topography: CT Atlas* (Springer, 2004).
31. Jentzen, W. *et al.* Assessment of lesion response in the initial radioiodine treatment of differentiated thyroid cancer using 124I PET imaging. *J. Nucl. Med.* **55**, 1759–1765. https://doi.org/10.2967/jnumed.114.144089 (2014).
32. Jentzen, W. *et al.* Iodine-124 PET dosimetry in differentiated thyroid cancer: Recovery coefficient in 2D and 3D modes for PET(/CT) systems. *Eur. J. Nucl. Med. Mol. Imaging* **35**, 611–623. https://doi.org/10.1007/s00259-007-0554-7 (2008).
33. Jentzen, W. Experimental investigation of factors affecting the absolute recovery coefficients in iodine-124 PET lesion imaging. *Phys. Med. Biol.* **55**, 2365–2398. https://doi.org/10.1088/0031-9155/55/8/016 (2010).
34. Adler, S. *et al.* Minimum lesion detectability as a measure of PET system performance. *EJNMMI Phys.* **4**, 13. https://doi.org/10.1186/s40658-017-0179-2 (2017).
35. Oen, S. K., Aasheim, L. B., Eikenes, L. & Karlberg, A. M. Image quality and detectability in Siemens biograph PET/MRI and PET/CT systems—A phantom study. *EJNMMI Phys.* **6**, 16. https://doi.org/10.1186/s40658-019-0251-1 (2019).
36. Beijst, C. *et al.* Quantitative comparison of 124I PET/CT and 131I SPECT/CT detectability. *J. Nucl. Med.* **57**, 103–108. https://doi.org/10.2967/jnumed.115.162750 (2016).
37. Maxon, H. R. *et al.* Relation between effective radiation dose and outcome of radioiodine therapy for thyroid cancer. *N. Engl. J. Med.* **309**, 937–941. https://doi.org/10.1056/NEJM198310203091601 (1983).
38. Jentzen, W. *et al.* Pre-therapeutic (124)I PET(/CT) dosimetry confirms low average absorbed doses per administered (131)I activity to the salivary glands in radioiodine therapy of differentiated thyroid cancer. *Eur. J. Nucl. Med. Mol. Imaging* **37**, 884–895. https://doi.org/10.1007/s00259-009-1351-2 (2010).
39. Li, W. B. *et al.* Track structures and dose distributions from decays of (131)I and (125)I in and around water spheres simulating micrometastases of differentiated thyroid cancer. *Radiat. Res.* **156**, 419–429. https://doi.org/10.1667/0033-7587(2001)156[0419:tsaddf]2.0.co;2 (2001).
40. Rose, A. *Vision: Human and Electronic* (Plenum Press, 1973).
41. Tong, S., Alessio, A. M. & Kinahan, P. E. Evaluation of noise properties in PSF-based PET image reconstruction. *IEEE Nucl. Sci. Symp. Conf. Rec.* **1997**(2009), 3042–3047. https://doi.org/10.1109/nssmic.2009.5401574 (2009).
42. Rosenbaum-Krumme, S., Nagarajah, J., Ruhlmann, M., Bockisch, A. & Jentzen, W. 124I-PET/CT images of differentiated thyroid cancer patients. Distinguishing lymph node metastases from thyroid remnants using kinetic quantities. *Nuklearmedizin* **51**, 213–216. https://doi.org/10.3413/Nukmed-0481-12-02 (2012).
43. Tuttle, R. M. *et al.* Empiric radioactive iodine dosing regimens frequently exceed maximum tolerated activity levels in elderly patients with thyroid cancer. *J. Nucl. Med.* **47**, 1587–1591 (2006).
44. Meyer, M. *et al.* Increased (18)F-FDG signal recovery from small physiological structures in digital PET/CT and application to the pituitary gland. *Sci. Rep.* **10**, 368. https://doi.org/10.1038/s41598-019-57313-x (2020).
45. Salvadori, J. *et al.* Head-to-head comparison between digital and analog PET of human and phantom images when optimized for maximizing the signal-to-noise ratio from small lesions. *EJNMMI Phys.* **7**, 11. https://doi.org/10.1186/s40658-020-0281-8 (2020).
46. Freudenberg, L. S., Jentzen, W., Muller, S. P. & Bockisch, A. Disseminated iodine-avid lung metastases in differentiated thyroid cancer: A challenge to 124I PET. *Eur. J. Nucl. Med. Mol. Imaging* **35**, 502–508. https://doi.org/10.1007/s00259-007-0601-4 (2008).
47. Walrand, S., Hesse, M. & Jamar, F. Statistical and radiobiological analysis of the so-called thyroid stunning. *EJNMMI Res.* **5**, 67. https://doi.org/10.1186/s13550-015-0144-9 (2015).

Author contributions

Funding

Competing interests

Walter Jentzen received research funding from Siemens Healthineers. Lale Umutlu is a Speaker / Advisory Board Member for Bayer Healthcare and Siemens Healthcare and received research grants from Siemens Healthcare,

Additional information

Supplementary Information The online version contains supplementary material available at https://doi.org/10.1038/s41598-021-95719-8.

Correspondence and requests for materials should be addressed to D.K.

Reprints and permissions information is available at www.nature.com/reprints.

Publisher's note Springer Nature remains neutral with regard to jurisdictional claims in published maps and institutional affiliations.

Supplementary Material to:

Silicon-Photomultiplier-Based PET/CT Reduces the Minimum Detectable Activity of Iodine-124

D. Kersting* [1,4], W. Jentzen[1,4], P. Fragoso Costa[1,4], M. Sraieb[1,4], P. Sandach[1,4], L. Umutlu[2,4], M. Conti[3], F. Zarrad[1,4], C. Rischpler[1,4], W. P. Fendler[1,4], K. Herrmann[1,4], and M. Weber[1,4]

[1] Department of Nuclear Medicine, University Hospital Essen, University of Duisburg-Essen, Essen, Germany

[2] Department of Diagnostic and Interventional Radiology and Neuroradiology, University Hospital Essen, University of Duisburg-Essen, Essen, Germany

[3] Siemens Medical Solutions USA, Inc., Knoxville, TN, United States

[4] German Cancer Consortium (DKTK, partner site Essen), Essen, Germany
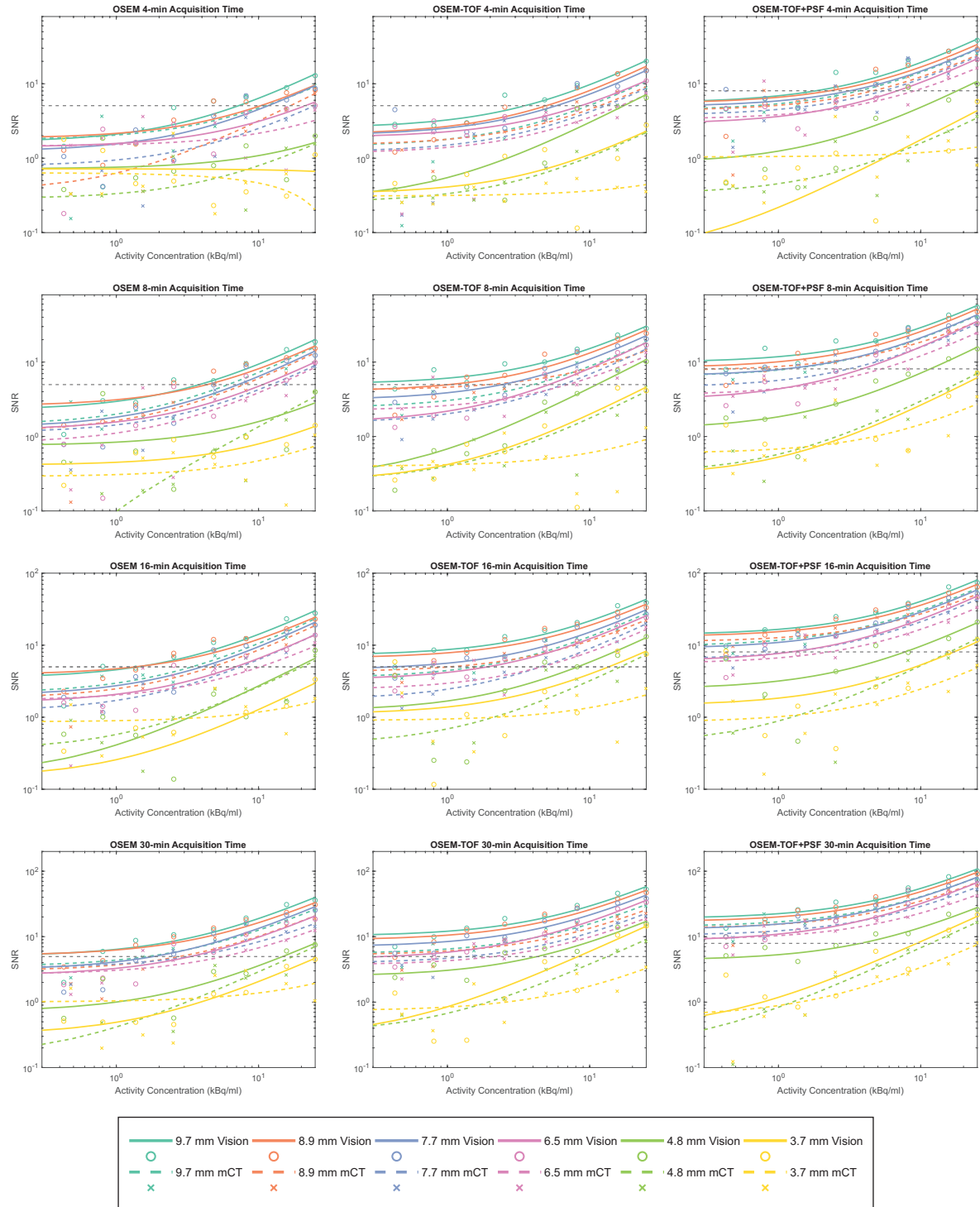
Figure 1: SNR as a function of the AC for all evaluated spheres, separately for all evaluated reconstruction algorithms and emission times. A horizontal line at SNR = 5 (OSEM and OSEM-TOF) or SNR = 8 (OSEM-TOF+PSF), respectively, indicates the threshold for visual detectability.

Supplemental Table S1: Scanner Specifications

Technical specifications for the Biograph mCT and the Biograph Vision. LSO = Lutetium Oxyorthosilicate.

	Biograph mCT	Biograph Vision
Detector material	LSO	LSO
Detector element dimension (mm^3)	4x4x20	3.2x3.2x20
Detector elements per block	13x13	16x16
Total number of detector elements	33,448	60,800
Signal readout	PMTs (2x2 per block)	SiPM (2x2 per block)
Axial FOV (cm)	21.8	26.3
Transaxial FOV (cm)	70	78
Plane spacing (mm)	2	1.65
Image planes	109	119
Coincidence time window (ns)	4.1	4.7
Energy window (keV)	435-650	435-585
Energy resolution (%)	11	9
System time resolution (ps)	540	210
NEMA sensitivity (kcps/MBq)	9.7	16.4

Supplemental Table S2: Activity Concentration Characterization for Different Metastases

Activity Concentrations (AC) and AC to background AC for different types of differentiated thyroid cancer metastases.

	Lymph node metastases	Lung metastases	Bone metastases
Number of evaluated metastases	89	34	61
AC (kBq/ml)			
mean	155	22	104
median	72	16	60
standard deviation	186	16	124
minimum-maximum	1.6–691	3.5-72	5.4-684
Ratio AC to the background AC			
mean	1075	91	659
median	346	38	232
standard deviation	2069	199	976
minimum-maximum	17–15538	11-1186	21-5167

Supplemental Table S3: MDA for each evaluated sphere size, PET/CT system, reconstruction algorithm and emission time.

Sphere Diameter (mm)	Scanner	OSEM				OSEM+TOF				OSEM+TOF+PSF			
		30-min	16-min	8-min	4-min	30-min	16-min	8-min	4-min	30-min	16-min	8-min	4-min
3.7	Vision	>25	>25	>25	>25	8.33	13.59	>25	>25	9.51	16.96	>25	>25
	mCT	>25	>25	>25	>25	>25	>25	>25	>25	>25	>25	>25	>25
4.8	Vision	14.86	18.87	>25	>25	4.32	8.22	11.26	17.16	3.87	7.67	11.52	17.96
	mCT	17.59	20.29	>25	>25	13.41	16.43	>25	>25	11.86	15.87	>25	>25
6.5	Vision	3.36	6.88	10.76	20.93	0.38	1.91	5.20	8.50	<0.26	1.20	3.82	6.80
	mCT	5.74	10.25	13.66	>25	2.15	4.60	7.05	16.19	<0.26	2.21	5.19	8.98
7.7	Vision	1.86	3.99	7.22	11.47	<0.26	0.41	2.45	5.70	<0.26	<0.26	1.06	3.15
	mCT	3.36	7.42	12.34	24.33	1.43	4.53	6.52	12.68	<0.26	1.16	3.05	5.43
8.9	Vision	<0.26	1.36	4.38	10.12	<0.26	<0.26	1.05	4.85	<0.26	<0.26	<0.26	2.25
	mCT	2.82	4.72	7.92	16.50	<0.26	1.03	2.00	11.53	<0.26	<0.26	0.33	4.57
9.7	Vision	<0.26	1.41	3.86	7.08	<0.26	<0.26	<0.26	3.42	<0.26	<0.26	<0.26	1.81
	mCT	1.68	3.39	6.14	10.95	<0.26	1.57	4.07	9.61	<0.26	<0.26	1.12	3.66
Ratio Vision/mCT Mean±SD		0.66 ± 0.16	0.57 ± 0.25	0.65 ± 0.11	0.58 ± 0.10	0.25 ± 0.11	0.34 ± 0.22	0.55 ± 0.19	0.44 ± 0.08	0.33 ± 0	0.51 ± 0.05	0.54 ± 0.28	0.58 ± 0.13
Number of evaluated spheres		3	5	4	3	2	3	3	4	1	2	2	4

Presented values in units of kBq/ml. MDA <0.26 kBq/ml: No MDA could be calculated, as the SNR was > cut-off value for visual detection for all ACs (meaning detection for every examined AC). MDA >25 kBq/ml: No MDA could be calculated, as the SNR was < cut-off value for all ACs (meaning no detection for any examined AC).

Supplemental Table S4: Human observer study results for the 3.7-mm sphere.

The human observer study results are separately presented for the examined PET/CT scanners, reconstruction algorithms and emission times. 1 = detected.

0 = undetected.

Sphere Activity Concentration (kBq/ml)	Scanner	OSEM				OSEM+TOF				OSEM+TOF+PSF			
		30 min	16 min	8 min	4 min	30 min	16 min	8 min	4 min	30 min	16 min	8 min	4 min
24.99	Vision	0	0	0	0	1	1	0	0	1	1	0	0
24.85	mCT	0	0	0	0	0	0	0	0	0	0	0	0
15.72	Vision	0	0	0	0	1	0	0	0	1	0	0	0
15.63	mCT	0	0	0	0	0	0	0	0	0	0	0	0
8.17	Vision	0	0	0	0	0	0	0	0	0	0	0	0
8.13	mCT	0	0	0	0	0	0	0	0	0	0	0	0
4.83	Vision	0	0	0	0	1	0	0	0	1	0	0	0
4.93	mCT	0	0	0	0	0	0	0	0	0	0	0	0
2.53	Vision	0	0	0	0	0	0	0	0	0	0	0	0
2.51	mCT	0	0	0	0	0	0	0	0	0	0	0	0
1.37	Vision	0	0	0	0	0	0	0	0	0	0	0	0
1.54	mCT	0	0	0	0	0	0	0	0	0	0	0	0
0.80	Vision	0	0	0	0	0	0	0	0	0	0	0	0
0.79	mCT	0	0	0	0	0	0	0	0	0	0	0	0
0.43	Vision	0	0	0	0	0	0	0	0	0	0	0	0
0.48	mCT	0	0	0	0	0	0	0	0	0	0	0	0
0.26	Vision	0	0	0	0	0	0	0	0	0	0	0	0
0.25	mCT	0	0	0	0	0	0	0	0	0	0	0	0

Supplemental Table S5: Human observer study results for the 4.8-mm sphere.

The human observer study results are separately presented for the examined PET/CT scanners, reconstruction algorithms and emission times. 1 = detected.

0 = undetected.

Sphere Activity Concentration (kBq/ml)	Scanner	OSEM				OSEM+TOF				OSEM+TOF+PSF			
		30 min	16 min	8 min	4 min	30 min	16 min	8 min	4 min	30 min	16 min	8 min	4 min
24.99	Vision	1	1	0	0	1	1	1	1	1	1	1	1
24.85	mCT	1	1	0	0	1	1	0	0	1	1	1	0
15.72	Vision	1	0	0	0	1	1	1	1	1	1	1	1
15.63	mCT	0	0	0	0	1	0	0	0	1	1	0	0
8.17	Vision	0	0	0	0	1	0	0	0	1	1	1	1
8.13	mCT	0	0	0	0	0	0	0	0	1	1	0	0
4.83	Vision	1	0	0	0	1	1	0	0	1	1	0	0
4.93	mCT	0	0	0	0	0	0	0	0	0	0	0	0
2.53	Vision	0	0	0	0	0	0	0	0	1	0	0	0
2.51	mCT	0	0	0	0	0	0	0	0	0	0	0	0
1.37	Vision	0	0	0	0	0	0	0	0	1	0	0	0
1.54	mCT	0	0	0	0	0	0	0	0	0	0	0	0
0.80	Vision	0	0	0	0	0	0	0	0	0	0	0	0
0.79	mCT	0	0	0	0	0	0	0	0	0	0	0	0
0.43	Vision	0	0	0	0	0	0	0	0	0	0	0	0
0.48	mCT	0	0	0	0	0	0	0	0	0	0	0	0
0.26	Vision	0	0	0	0	0	0	0	0	0	0	0	0
0.25	mCT	0	0	0	0	0	0	0	0	0	0	0	0

Supplemental Table S6: Human observer study results for the 6.5-mm sphere.

The human observer study results are separately presented for the examined PET/CT scanners, reconstruction algorithms and emission times. 1 = detected.

0 = undetected.

Sphere Activity Concentration (kBq/ml)	Scanner	OSEM				OSEM+TOF				OSEM+TOF+PSF			
		30 min	16 min	8 min	4 min	30 min	16 min	8 min	4 min	30 min	16 min	8 min	4 min
24.99	Vision	1	1	1	1	1	1	1	1	1	1	1	1
24.85	mCT	1	1	1	0	1	1	1	1	1	1	1	1
15.72	Vision	1	1	1	1	1	1	1	1	1	1	1	1
15.63	mCT	1	1	1	0	1	1	1	0	1	1	1	1
8.17	Vision	1	1	1	0	1	1	1	1	1	1	1	1
8.13	mCT	1	0	0	0	1	1	0	0	1	1	1	0
4.83	Vision	1	1	0	0	1	1	1	0	1	1	1	1
4.93	mCT	1	0	0	0	1	1	0	0	1	1	1	0
2.53	Vision	1	0	0	0	1	1	1	0	1	1	1	1
2.51	mCT	0	0	0	0	0	0	0	0	1	1	0	0
1.37	Vision	0	0	0	0	1	1	0	0	1	1	0	0
1.54	mCT	0	0	0	0	0	0	0	0	1	1	0	0
0.80	Vision	0	0	0	0	1	1	0	0	1	1	1	0
0.79	mCT	0	0	0	0	0	0	0	0	1	0	0	0
0.43	Vision	0	0	0	0	0	0	0	0	1	0	0	0
0.48	mCT	0	0	0	0	0	0	0	0	0	0	0	0
0.26	Vision	0	0	0	0	0	0	0	0	0	0	0	0
0.25	mCT	0	0	0	0	0	0	0	0	0	0	0	0

Supplemental Table S7: Human observer study results for the 7.7-mm sphere.

The human observer study results are separately presented for the examined PET/CT scanners, reconstruction algorithms and emission times. 1 = detected.

0 = undetected.

Sphere Activity Concentration (kBq/ml)	Scanner	OSEM				OSEM+TOF				OSEM+TOF+PSF			
		30 min	16 min	8 min	4 min	30 min	16 min	8 min	4 min	30 min	16 min	8 min	4 min
24.99	Vision	1	1	1	1	1	1	1	1	1	1	1	1
24.85	mCT	1	1	1	1	1	1	1	1	1	1	1	1
15.72	Vision	1	1	1	1	1	1	1	1	1	1	1	1
15.63	mCT	1	1	1	1	1	1	1	1	1	1	1	1
8.17	Vision	1	1	1	1	1	1	1	1	1	1	1	1
8.13	mCT	1	1	0	0	1	1	1	1	1	1	1	1
4.83	Vision	1	1	1	0	1	1	1	1	1	1	1	1
4.93	mCT	1	1	0	0	1	1	0	0	1	1	1	0
2.53	Vision	1	1	0	0	1	1	1	1	1	1	1	1
2.51	mCT	1	0	0	0	1	0	0	0	1	1	1	0
1.37	Vision	0	0	0	0	1	1	1	0	1	1	1	1
1.54	mCT	0	0	0	0	0	0	0	0	1	1	0	0
0.80	Vision	0	0	0	0	1	1	1	0	1	1	1	0
0.79	mCT	0	0	0	0	1	0	0	0	1	1	0	0
0.43	Vision	0	0	0	0	1	0	0	0	1	1	0	0
0.48	mCT	0	0	0	0	0	0	0	0	0	0	0	0
0.26	Vision	0	0	0	0	0	0	0	0	0	0	0	0
0.25	mCT	0	0	0	0	0	0	0	0	0	0	0	0

Supplemental Table S8: Human observer study results for the 8.9-mm sphere.

The human observer study results are separately presented for the examined PET/CT scanners, reconstruction algorithms and emission times. 1 = detected.

0 = undetected.

Sphere Activity Concentration (kBq/ml)	Scanner	OSEM				OSEM+TOF				OSEM+TOF+PSF			
		30 min	16 min	8 min	4 min	30 min	16 min	8 min	4 min	30 min	16 min	8 min	4 min
24.99	Vision	1	1	1	1	1	1	1	1	1	1	1	1
24.85	mCT	1	1	1	1	1	1	1	1	1	1	1	1
15.72	Vision	1	1	1	1	1	1	1	1	1	1	1	1
15.63	mCT	1	1	1	0	1	1	1	1	1	1	1	1
8.17	Vision	1	1	1	1	1	1	1	1	1	1	1	1
8.13	mCT	1	1	0	0	1	1	1	1	1	1	1	1
4.83	Vision	1	1	1	1	1	1	1	1	1	1	1	1
4.93	mCT	1	1	0	0	1	1	1	0	1	1	1	1
2.53	Vision	1	1	1	0	1	1	1	1	1	1	1	1
2.51	mCT	1	0	0	0	1	1	0	0	1	1	1	0
1.37	Vision	1	0	0	0	1	1	1	0	1	1	1	1
1.54	mCT	0	0	0	0	1	0	0	0	1	0	0	0
0.80	Vision	1	0	0	0	1	1	1	0	1	1	1	0
0.79	mCT	0	0	0	0	1	0	0	0	1	0	0	0
0.43	Vision	0	0	0	0	1	1	0	0	1	1	0	0
0.48	mCT	0	0	0	0	1	0	0	0	1	0	0	0
0.26	Vision	0	0	0	0	1	1	0	0	1	1	0	0
0.25	mCT	0	0	0	0	0	0	0	0	0	0	0	0

Supplemental Table S9: Human observer study results for the 9.7-mm sphere.

The human observer study results are separately presented for the examined PET/CT scanners, reconstruction algorithms and emission times. 1 = detected.

0 = undetected.

Sphere Activity Concentration (kBq/ml)	Scanner	OSEM				OSEM+TOF				OSEM+TOF+PSF			
		30 min	16 min	8 min	4 min	30 min	16 min	8 min	4 min	30 min	16 min	8 min	4 min
24.99	Vision	1	1	1	1	1	1	1	1	1	1	1	1
24.85	mCT	1	1	1	1	1	1	1	1	1	1	1	1
15.72	Vision	1	1	1	1	1	1	1	1	1	1	1	1
15.63	mCT	1	1	1	1	1	1	1	1	1	1	1	1
8.17	Vision	1	1	1	1	1	1	1	1	1	1	1	1
8.13	mCT	1	1	1	1	1	1	1	1	1	1	1	1
4.83	Vision	1	1	1	1	1	1	1	1	1	1	1	1
4.93	mCT	1	1	0	0	1	1	1	0	1	1	1	1
2.53	Vision	1	1	1	0	1	1	1	1	1	1	1	1
2.51	mCT	1	0	0	0	1	1	0	0	1	1	1	0
1.37	Vision	1	1	0	0	1	1	1	0	1	1	1	1
1.54	mCT	0	0	0	0	1	0	0	0	1	0	0	0
0.80	Vision	1	1	0	0	1	1	1	0	1	1	1	0
0.79	mCT	0	0	0	0	1	0	0	0	1	0	0	0
0.43	Vision	0	0	0	0	1	1	0	0	1	1	0	0
0.48	mCT	0	0	0	0	0	0	0	0	1	0	0	0
0.26	Vision	0	0	0	0	1	1	0	0	1	1	0	0
0.25	mCT	0	0	0	0	0	0	0	0	0	0	0	0

Supplemental Table S10: SNR for the 3.7-mm sphere.

The SNR values are separately presented for the examined PET/CT scanners, reconstruction algorithms and emission times.

Sphere Activity Concentration (kBq/ml)	Scanner	OSEM				OSEM+TOF				OSEM+TOF+PSF			
		30 min	16 min	8 min	4 min	30 min	16 min	8 min	4 min	30 min	16 min	8 min	4 min
24.99	Vision	4.51	3.35	1.41	1.11	14.55	7.53	4.11	2.78	21.68	11.90	7.07	5.77
24.85	mCT	1.05	1.82	1.04	0.00	3.42	2.50	1.31	0.36	8.05	5.25	3.42	0.81
15.72	Vision	3.51	1.42	0.78	0.31	10.56	8.25	4.48	0.99	12.56	7.81	3.49	1.25
15.63	mCT	1.91	0.59	0.12	0.62	1.47	0.45	0.18	0.41	3.85	2.28	1.02	1.71
8.17	Vision	1.40	1.18	0.99	0.35	1.51	1.15	0.11	0.12	3.18	2.52	0.65	0.08
8.13	mCT	3.03	1.40	0.26	0.47	2.73	2.01	0.17	0.53	2.66	2.98	0.65	1.93
4.83	Vision	1.33	0.07	0.53	0.23	4.15	2.26	1.39	1.30	5.98	2.64	0.92	0.14
4.93	mCT	2.56	2.53	0.42	0.18	1.37	1.40	0.54	0.46	2.44	1.50	0.41	0.56
2.53	Vision	0.46	0.62	0.90	0.49	1.12	0.56	0.62	1.06	1.25	0.37	0.83	1.17
2.51	mCT	0.24	0.57	0.61	2.16	0.49	1.07	1.11	0.26	2.85	2.10	3.09	3.63
1.37	Vision	0.49	0.71	0.60	0.46	0.26	1.09	0.79	0.61	0.84	1.42	0.65	0.74
1.54	mCT	0.32	0.53	0.51	0.42	1.90	0.33	0.36	0.41	0.64	0.60	0.48	0.51
0.80	Vision	0.50	0.03	0.08	1.27	0.25	0.12	0.27	0.09	1.20	0.56	0.79	0.55
0.79	mCT	0.20	0.29	0.08	0.33	0.37	0.46	0.46	0.24	0.60	0.16	0.55	0.25
0.43	Vision	0.51	0.34	0.22	1.79	1.37	5.87	0.26	0.46	2.59	8.32	1.43	0.48
0.48	mCT	1.63	1.49	0.32	0.33	0.66	2.18	0.40	0.25	0.12	1.67	0.32	0.43
0.26	Vision	0.47	0.29	0.45	0.33	2.23	0.03	0.49	0.24	1.53	0.36	0.71	0.42
0.25	mCT	0.34	0.42	0.31	0.20	0.27	0.40	0.27	0.18	0.65	0.64	0.47	0.39

Supplemental Table S11: SNR for the 4.8-mm sphere.

The SNR values are separately presented for the examined PET/CT scanners, reconstruction algorithms and emission times.

Sphere Activity Concentration (kBq/ml)	Scanner	OSEM				OSEM+TOF				OSEM+TOF+PSF			
		30 min	16 min	8 min	4 min	30 min	16 min	8 min	4 min	30 min	16 min	8 min	4 min
24.99	Vision	7.48	8.47	3.97	1.99	15.75	13.13	10.15	6.49	25.92	20.97	15.04	9.95
24.85	mCT	7.85	7.17	3.98	1.56	8.43	7.75	4.59	2.21	16.49	12.51	7.34	3.64
15.72	Vision	6.06	1.65	0.67	0.51	13.93	7.23	7.76	4.90	22.02	12.37	11.06	6.06
15.63	mCT	2.60	1.73	1.67	1.36	6.18	3.15	1.93	1.30	10.09	6.64	4.21	2.30
8.17	Vision	2.73	1.02	0.98	1.46	5.96	5.00	3.78	4.70	11.13	7.94	6.89	8.95
8.13	mCT	2.33	2.49	0.25	0.20	3.66	3.36	0.30	1.23	6.31	6.14	1.70	0.92
4.83	Vision	2.93	2.10	0.62	0.79	6.58	5.81	2.89	0.86	11.02	9.87	5.57	3.43
4.93	mCT	3.63	2.45	0.67	0.08	3.15	4.52	2.12	0.72	3.69	3.48	2.21	0.31
2.53	Vision	0.57	0.14	0.20	0.67	5.71	2.32	0.75	0.27	7.31	4.32	2.73	0.73
2.51	mCT	0.36	0.99	0.23	1.06	1.11	0.09	0.40	0.48	2.44	0.24	0.03	1.68
1.37	Vision	0.04	0.56	0.64	0.54	2.15	0.24	0.59	0.41	4.18	0.47	0.53	0.40
1.54	mCT	0.07	0.18	0.19	0.36	0.01	0.44	0.91	0.27	0.63	0.09	1.83	0.41
0.80	Vision	2.26	1.01	3.77	1.85	3.70	0.25	0.65	0.55	6.81	2.07	1.71	0.71
0.79	mCT	0.48	0.44	0.17	0.31	0.05	0.43	0.27	0.29	0.78	1.84	0.25	0.35
0.43	Vision	0.56	0.58	0.45	0.38	2.38	3.74	0.19	0.38	5.11	6.45	1.77	0.46
0.48	mCT	0.03	0.91	0.44	0.33	0.63	0.06	0.37	0.25	0.11	0.60	0.64	0.42
0.26	Vision	0.84	1.05	0.43	0.42	0.69	0.44	0.46	0.19	1.29	0.37	0.60	0.47
0.25	mCT	0.24	0.32	0.27	0.30	0.32	0.37	0.27	0.18	0.02	0.41	0.43	0.38

Supplemental Table S12: SNR for the 6.5-mm sphere.

The SNR values are separately presented for the examined PET/CT scanners, reconstruction algorithms and emission times.

Sphere Activity Concentration (kBq/ml)	Scanner	OSEM				OSEM+TOF				OSEM+TOF+PSF			
		30 min	16 min	8 min	4 min	30 min	16 min	8 min	4 min	30 min	16 min	8 min	4 min
24.99	Vision	18.50	13.77	9.88	5.09	33.48	24.13	16.91	10.94	64.28	46.36	33.15	21.23
24.85	mCT	12.36	10.82	9.62	4.44	18.34	17.71	13.35	7.49	41.96	33.44	24.34	16.22
15.72	Vision	16.17	8.68	5.72	4.60	26.64	18.96	13.43	7.81	47.61	34.23	25.47	15.33
15.63	mCT	8.79	4.01	3.54	0.69	13.59	8.31	6.09	3.50	32.49	20.73	17.31	12.26
8.17	Vision	10.79	7.13	6.48	4.05	17.20	11.26	7.36	4.53	32.06	20.41	14.54	9.18
8.13	mCT	6.23	4.54	3.02	1.01	9.23	7.18	4.96	3.02	19.83	14.21	8.01	5.22
4.83	Vision	5.76	4.14	1.87	1.14	11.09	8.90	6.89	3.56	19.56	15.23	12.49	6.39
4.93	mCT	6.45	4.75	3.16	2.99	8.32	7.94	5.84	4.13	17.47	15.41	13.66	6.72
2.53	Vision	7.79	5.26	4.68	2.83	8.76	6.40	3.23	3.62	17.39	13.28	7.52	5.75
2.51	mCT	4.34	3.81	0.28	0.89	4.60	2.04	1.86	3.50	12.13	6.69	4.36	6.02
1.37	Vision	1.89	1.25	1.41	1.63	5.84	3.61	1.76	2.01	12.41	7.56	2.74	2.49
1.54	mCT	6.16	4.81	4.51	3.63	7.80	6.15	2.33	0.28	17.36	13.87	4.47	2.04
0.80	Vision	2.34	1.41	0.15	2.45	4.83	5.62	1.93	3.16	8.94	10.29	5.45	4.92
0.79	mCT	1.96	1.20	0.76	1.86	4.50	3.48	6.26	2.19	14.50	6.92	6.50	10.86
0.43	Vision	1.85	1.60	0.79	0.18	3.44	2.31	1.33	2.65	7.06	3.55	2.60	4.67
0.48	mCT	1.31	0.21	0.19	1.49	2.26	1.93	2.36	0.18	5.24	3.86	3.47	1.20
0.26	Vision	0.91	0.37	0.75	0.83	3.61	1.29	0.41	0.37	6.54	2.62	0.05	0.47
0.25	mCT	0.44	0.22	0.31	0.30	0.99	0.25	0.21	0.18	2.06	0.26	0.45	0.14

Supplemental Table S13: SNR for the 7.7-mm sphere.

The SNR values are separately presented for the examined PET/CT scanners, reconstruction algorithms and emission times.

Sphere Activity Concentration (kBq/ml)	Scanner	OSEM				OSEM+TOF				OSEM+TOF+PSF			
		30 min	16 min	8 min	4 min	30 min	16 min	8 min	4 min	30 min	16 min	8 min	4 min
24.99	Vision	25.43	19.01	12.31	8.64	38.14	26.98	20.44	14.83	73.41	52.04	39.71	28.17
24.85	mCT	14.30	14.00	8.75	4.90	20.57	19.89	15.39	7.61	52.52	42.25	31.57	21.23
15.72	Vision	21.55	15.35	10.40	6.07	32.60	24.73	16.43	9.25	59.13	45.52	30.70	18.73
15.63	mCT	11.90	7.90	5.06	3.26	16.36	11.17	7.59	5.20	42.05	28.19	19.62	13.59
8.17	Vision	15.85	9.78	8.68	6.89	26.90	17.88	13.87	10.07	50.75	34.56	28.15	21.09
8.13	mCT	8.81	6.65	5.41	3.52	12.95	9.53	8.63	9.03	29.63	21.13	21.15	22.27
4.83	Vision	11.20	8.61	4.93	3.69	17.34	11.77	8.25	3.34	30.14	20.29	13.96	9.75
4.93	mCT	8.51	5.28	4.21	1.05	10.34	6.71	3.67	0.74	24.95	16.42	10.53	4.14
2.53	Vision	5.41	2.23	1.51	0.93	9.68	6.96	3.61	2.53	17.39	13.57	7.53	4.69
2.51	mCT	6.10	2.65	1.79	1.98	8.32	4.22	4.77	3.20	20.04	13.07	12.46	9.34
1.37	Vision	4.37	3.65	2.44	2.39	10.34	6.63	4.67	2.25	20.63	14.04	8.79	4.68
1.54	mCT	4.01	2.92	0.65	0.23	5.03	3.32	2.27	2.12	14.54	9.42	4.91	4.49
0.80	Vision	1.54	1.16	0.72	0.42	5.56	4.10	3.86	2.28	10.64	8.85	8.55	6.36
0.79	mCT	4.01	1.46	2.19	0.68	2.38	2.09	1.72	0.25	9.34	8.30	3.99	3.19
0.43	Vision	1.42	1.89	0.78	1.05	5.56	3.49	2.88	4.49	10.00	6.70	6.99	8.38
0.48	mCT	1.86	0.05	0.36	0.08	3.68	1.33	0.91	0.17	9.70	4.83	2.13	1.40
0.26	Vision	1.77	0.81	0.24	0.40	2.03	1.10	0.02	0.06	4.80	2.44	0.82	0.42
0.25	mCT	0.06	0.16	0.24	1.52	0.15	0.01	0.26	0.18	1.17	0.68	1.50	0.37

Supplemental Table S14: SNR for the 8.9-mm sphere.

The SNR values are separately presented for the examined PET/CT scanners, reconstruction algorithms and emission times.

Sphere Activity Concentration (kBq/ml)	Scanner	OSEM				OSEM+TOF				OSEM+TOF+PSF			
		30 min	16 min	8 min	4 min	30 min	16 min	8 min	4 min	30 min	16 min	8 min	4 min
24.99	Vision	30.79	22.99	15.21	8.24	46.98	33.30	24.28	15.21	90.52	64.11	47.26	29.45
24.85	mCT	18.91	19.37	14.27	7.34	22.61	22.06	14.53	7.51	60.25	47.50	32.39	21.05
15.72	Vision	23.50	16.86	11.45	7.59	37.91	28.83	20.59	13.67	68.51	53.23	38.48	27.20
15.63	mCT	14.72	10.11	7.13	4.39	20.09	14.99	10.44	7.73	51.34	38.67	26.72	20.80
8.17	Vision	18.01	12.33	9.34	5.70	27.41	19.46	13.35	8.81	51.32	36.81	26.45	17.66
8.13	mCT	10.97	6.66	4.16	2.30	15.52	10.85	6.90	5.70	40.46	26.66	17.73	12.43
4.83	Vision	13.56	12.00	7.56	5.88	22.08	17.11	12.77	4.81	40.70	30.86	23.52	15.68
4.93	mCT	9.67	8.53	4.97	3.83	11.94	9.83	6.43	3.19	30.22	24.21	16.97	9.54
2.53	Vision	9.94	7.73	5.28	3.25	15.47	11.98	6.63	4.85	28.16	23.03	13.70	8.92
2.51	mCT	8.28	7.06	2.87	0.93	9.05	7.67	4.39	2.26	23.18	17.29	9.83	5.47
1.37	Vision	7.41	4.53	2.65	1.55	12.66	7.89	6.29	2.94	25.10	15.88	13.11	5.64
1.54	mCT	3.19	2.50	2.05	0.36	6.81	4.81	3.89	2.87	17.91	12.72	10.78	6.22
0.80	Vision	4.31	3.45	1.57	0.80	8.35	6.09	3.41	1.77	16.44	13.85	7.84	5.37
0.79	mCT	1.12	1.19	0.02	0.02	3.49	4.11	4.88	0.66	11.50	11.20	5.78	8.10
0.43	Vision	3.45	2.28	1.41	1.28	4.82	3.81	1.93	1.21	9.95	7.34	4.85	1.96
0.48	mCT	1.92	0.73	0.13	0.33	3.08	3.04	1.69	1.29	7.35	9.61	5.25	0.59
0.26	Vision	1.50	1.38	1.49	0.76	3.95	3.13	1.37	1.07	8.78	7.58	2.45	4.01
0.25	mCT	0.37	0.13	3.48	0.30	2.97	3.91	8.43	0.18	6.12	6.95	7.76	2.17

Supplemental Table S15: SNR for the 9.7-mm sphere.

The SNR values are separately presented for the examined PET/CT scanners, reconstruction algorithms and emission times.

Sphere Activity Concentration (kBq/ml)	Scanner	OSEM				OSEM+TOF				OSEM+TOF+PSF			
		30 min	16 min	8 min	4 min	30 min	16 min	8 min	4 min	30 min	16 min	8 min	4 min
24.99	Vision	35.92	27.78	18.72	12.85	52.81	39.00	28.32	20.09	100.62	73.80	54.52	38.37
24.85	mCT	24.68	23.51	16.51	9.46	29.40	27.76	18.37	8.81	76.88	59.12	40.52	25.62
15.72	Vision	30.92	23.23	14.71	8.88	45.98	35.37	23.09	13.55	82.33	64.45	42.74	27.43
15.63	mCT	17.20	12.84	8.14	4.70	21.15	16.44	10.65	7.62	55.17	40.88	26.68	20.00
8.17	Vision	19.23	12.32	9.47	6.59	29.94	20.62	14.88	9.43	55.49	38.19	29.11	18.84
8.13	mCT	15.61	12.56	9.82	6.97	16.52	12.55	9.79	9.07	43.27	31.56	24.75	21.41
4.83	Vision	12.69	10.93	5.62	5.84	20.67	16.03	10.02	6.08	36.80	28.49	19.25	14.19
4.93	mCT	8.62	7.14	3.77	2.68	13.54	11.73	6.75	4.42	34.29	27.84	19.04	10.01
2.53	Vision	10.70	6.88	5.76	4.77	18.91	13.14	9.48	7.03	33.68	24.96	19.21	14.21
2.51	mCT	6.59	3.06	1.74	1.25	9.24	6.78	4.44	1.82	22.64	14.24	10.19	6.90
1.37	Vision	8.75	4.81	2.86	1.60	13.48	8.52	5.31	2.99	25.75	16.48	9.57	4.84
1.54	mCT	4.93	3.86	1.79	2.47	6.10	4.13	3.15	1.87	15.94	10.30	7.29	7.77
0.80	Vision	5.95	5.08	3.03	0.41	9.95	8.56	7.88	2.74	18.43	16.39	15.31	6.28
0.79	mCT	4.19	3.70	1.26	3.66	7.79	5.38	4.02	0.90	22.25	16.09	8.38	4.15
0.43	Vision	2.00	1.43	1.06	1.44	7.02	4.96	4.35	2.84	13.47	9.73	7.95	4.56
0.48	mCT	2.36	1.79	2.92	0.15	3.37	3.48	1.91	0.12	8.45	7.66	5.82	1.70
0.26	Vision	1.15	2.01	1.16	0.40	6.31	4.42	1.96	0.56	14.34	10.51	4.57	2.27
0.25	mCT	0.86	0.70	1.31	1.94	2.21	0.25	0.26	0.18	5.89	1.97	0.04	0.21

4 Conclusions and Outlook

In this thesis, we investigated implications of SiPM-based PET on clinical oncological imaging with a focus on reductions in emission time and detectability. In the following, the major results will be summarised and an outlook on possible future clinical applications and research projects will be given.

First, we evaluated the feasibility of reducing the acquisition time in clinical SiPM-based PET examinations using standard radionuclides. ^{18}F-FDG PET images of 20 lymphoma and ^{68}Ga-PSMA PET images of 20 prostate cancer patients were analysed. For ^{18}F-FDG, a reduction in acquisition time by a factor of 2.8 did not negatively affect the diagnostic performance. The reduced-acquisition time images showed the same results in region-based detectability and in imaging-derived clinical scores as the full-acquisition time images. For ^{68}Ga-PSMA, however, a slightly higher reduction in acquisition time by a factor of 3.7 resulted in missed detection of two small lymph node metastases with low tracer uptake. This led to under-diagnosis in two patients affecting region-based detectability and miTNM score. In one patient this would probably have influenced further therapy management. For both ^{18}F-FDG and ^{68}Ga-PSMA, the increase in image noise from full- to reduced-acquisition time images - as an indicator of image quality - was acceptable and image-based lesion quantification was comparable.

In summary, the maximum reduction in acquisition time in SiPM-based PET to maintain diagnostic performance is by a factor of about 3. Further reductions could negatively influence lesion detectability particularly regarding small and low-uptake lesions. A clinical use case of reduced-acquisition time PET imaging is more likely to re-stage patients with high tumour burden, in whom missed detection of single metastases would not influence clinical management. In patients with low tumour load, in whom evaluation of single lesions or searching for primary tumour is important, a standard protocol should be used. If possible, a reduced acquisition time could help to meet an increasing demand for clinical PET examinations. Moreover, it can be beneficial to reduce motion artefacts [189] which can occur, as typical PET acquisition times are large in comparison, for example, to CT imaging. Instead of reducing the acquisition time, the administered activity could be lowered, as the correlation between these measures is, in a first approximation, linear [37].

Reductions in administered activity can have major implications on radiation protection for both patients and medical staff. In case of ^{68}Ga-based PET tracers usage of lower activities could also help to overcome the shortcomings of limited ^{68}Ge/^{68}Ga-generator yield.

Because of the short half-lives of ^{18}F and ^{68}Ga, for these radionuclides a direct comparison between different PET scanners requiring subsequent PET scans of the same patient after single tracer administration would be biased by decay, tracer kinetics, and biological metabolism. We extended the patient analysis to ^{124}I PET imaging of differentiated thyroid cancer patients. The longer physical (4.2 d) half-life of ^{124}I and its long effective half-life (59-116 h [47–50]) allow a direct comparison of different PET systems. Data sets of 10 patients who underwent subsequent PET imaging on three different PET scanners after single administration of ^{124}I were investigated. These PET scanners were equipped with PET detectors from three generations (SiPMs, APDs, and PMTs). In this analysis, SiPM-based PET outperformed APD- and PMT-based PET in visual image quality and detectability with particular benefits for small lesions with low-tracer uptake. In detail, SiPM-based PET almost reached the detectability of a scan with fivefold-prolonged acquisition time on the APD-based system which was used as reference.

To quantify these effects, we performed a phantom analysis using defined conditions (fixed ^{124}I activity concentrations, lesion sizes, and signal-to-background ratio - all resembling clinical lymph node metastases) to compare the minimum detectable activity of the SiPM-based and the PMT-based PET/CT systems. Overall, the minimum detectable activity was reduced by a factor of 0.5 for the SiPM-based system and the increase in detectability was emphasised for small and low-uptake lesions. Moreover, the minimum detectable activity correlated, in a first approximation, linearly with the acquisition time. We, therefore, recommend SiPM-based PET and an emphasis of selected body regions with high pre-test probability for metastases by a prolonged acquisition time in thyroid cancer patients with suspected tumour recurrence.

Furthermore, we evaluated the impact of SiPM-based ^{124}I PET on ^{131}I radioiodine therapy planning in a dosimetry model. We were able to show that, for a typical clinical PET acquisition time, lesions of ≥ 4.5 mm in diameter with predicted response to radioiodine therapy would be detectable on both a SiPM- and a PMT-based system. Smaller lesions, yet with predicted response to therapy, would only be detected using the SiPM-based system. This underlines the potential of

SiPM-based PET to improve clinical therapy management. Further prospective studies are warranted to validate these effects in larger patient cohorts.

An improvement on the hardware-side which can, in future, further increase the detectability and reduce the acquisition time is the introduction of large field-of-view PET systems which cover greater parts of the patient body (≥ 1 m field-of-view compared to 21.8-26.3 cm for the scanners applied in this thesis). Large field-of-view systems not only exhibit an increased sensitivity but also allow to examine the complete trunk of a patient simultaneously, thus reducing the acquisition time of a whole-body scan. On the software-side, image post-processing under application of artificial intelligence-based methods bears the potential to further reduce the acquisition time or administered activity. Several approaches have been introduced by various research groups and one software product has been FDA-approved and is commercially distributed. For this tool, possible reductions by a factor of four were described [189]. Large field-of-view PET scanners and artificial intelligence-based image post-reconstruction are examples for many software and hardware developments with the potential to substantially improve future characteristics of PET imaging.

Clinical applications which can benefit from both SiPM-based PET and future improvements are, for example, pre- and intra-therapeutic dosimetry in radionuclide therapy planning and application. The improved sensitivity of SiPM-based PET can enable imaging for radionuclides with very challenging properties like ^{90}Y, which is used for radionuclide therapies. ^{90}Y shows a very low rate of positron emission by internal positron-electron pair conversion occurring in only 0.00326% per decay [190]. For typically accumulated activities in systemic radionuclide therapies this results in a very weak PET signal. First studies show that, in this context, PET-based dosimetry is feasible by SiPM-based ^{90}Y-PET [191]. Moreover, the improved timing characteristics of SiPM-based PET enable time-resolved dynamic imaging and tracer kinetic modelling to derive additional imaging features like kinetic constants for a more detailed description of tracer uptake and binding characteristics [192]. Multiparametric PET can deliver extended information on the investigated tumour but is, hitherto, rather used in research than in clinical routine applications.

In conclusion, future hardware and software improvements bear a tremendous potential for relevant further enhancements of clinical and research-driven PET imaging. These can be the starting point for advanced image analysis and derivation

of molecular imaging biomarkers. Consequently, a more precise *in vivo* description of biological characteristics offers potential benefits for diagnosis and therapy planing in various oncological diseases.

Bibliography

[1] T. Jones and D. Townsend, Journal of Medical Imaging **4**, 011013 (2017).

[2] F. de Galiza Barbosa, G. Delso, E. ter Voert, M. Huellner, K. Herrmann, and P. Veit-Haibach, Clinical Radiology **71**, 660 (2016).

[3] A. Almuhaideb, N. Papathanasiou, and J. Bomanji, Annals of Saudi Medicine **31**, 3 (2011).

[4] R. Boellaard, R. Delgado-Bolton, W. J. G. Oyen, F. Giammarile, K. Tatsch, W. Eschner, F. J. Verzijlbergen, S. F. Barrington, L. C. Pike, W. A. Weber, S. Stroobants, D. Delbeke, K. J. Donohoe, S. Holbrook, M. M. Graham, G. Testanera, O. S. Hoekstra, J. Zijlstra, E. Visser, C. J. Hoekstra, J. Pruim, A. Willemsen, B. Arends, J. Kotzerke, A. Bockisch, T. Beyer, A. Chiti, and B. J. Krause, European Journal of Nuclear Medicine and Molecular Imaging **42**, 328 (2014).

[5] V. Stebner, P. Hetkamp, I. Binse, and W. Jentzen, Der Nuklearmediziner **41**, 37 (2018).

[6] F. Jamar, J. Buscombe, A. Chiti, P. E. Christian, D. Delbeke, K. J. Donohoe, O. Israel, J. Martin-Comin, and A. Signore, Journal of Nuclear Medicine **54**, 647 (2013).

[7] V. Dilsizian, S. L. Bacharach, R. S. Beanlands, S. R. Bergmann, D. Delbeke, S. Dorbala, R. J. Gropler, J. Knuuti, H. R. Schelbert, and M. I. Travin, Journal of Nuclear Cardiology **23**, 1187 (2016).

[8] E. Guedj, A. Varrone, R. Boellaard, N. L. Albert, H. Barthel, B. van Berckel, M. Brendel, D. Cecchin, O. Ekmekcioglu, V. Garibotto, A. A. Lammertsma, I. Law, I. Peñuelas, F. Semah, T. Traub-Weidinger, E. van de Giessen, D. V. Weehaeghe, and S. Morbelli, European Journal of Nuclear Medicine and Molecular Imaging **49**, 632 (2021).

[9] S. Basu, S. Hess, P.-E. N. Braad, B. B. Olsen, S. Inglev, and P. F. Høilund-Carlsen, PET Clinics **9**, 355 (2014).

[10] H. A. Ziessman, J. P. O'Malley, and J. H. Thrall, in *Nuclear Medicine (Fourth Edition)*, W.B. Saunders, Philadelphia, 2014, pp. 227–264.

[11] B. D. Cheson, R. I. Fisher, S. F. Barrington, F. Cavalli, L. H. Schwartz, E. Zucca, and T. A. Lister, Journal of Clinical Oncology **32**, 3059 (2014).

[12] Y. L. Kasamon and R. L. Wahl, Current Opinion in Oncology **20**, 206 (2008).

[13] U. Dührsen, S. Müller, B. Hertenstein, H. Thomssen, J. Kotzerke, R. Mesters, W. E. Berdel, C. Franzius, F. Kroschinsky, M. Weckesser, D. Kofahl-Krause, F. M. Bengel, J. Dürig, J. Matschke, C. Schmitz, T. Pöppel, C. Ose, M. Brinkmann, P. L. Rosée, M. Freesmeyer, A. Hertel, H.-G. Höffkes, D. Behringer, G. Prange-Krex, S. Wilop, T. Krohn, J. Holzinger, M. Griesshammer, A. Giagounidis, A. Raghavachar, G. Maschmeyer, I. Brink, H. Bernhard, U. Haberkorn, T. Gaska, L. Kurch, D. M. van Assema, W. Klapper, D. Hoelzer, L. Geworski, K.-H. Jöckel, A. Scherag, A. Bockisch, J. Rekowski, and A. Hüttmann, Journal of Clinical Oncology **36**, 2024 (2018).

[14] B. Hochhegger, G. R. T. Alves, K. L. Irion, C. C. Fritscher, L. G. Fritscher, N. H. Concatto, and E. Marchiori, Jornal Brasileiro de Pneumologia **41**, 264 (2015).

[15] S. A. Deppen, E. Liu, J. D. Blume, J. Clanton, C. Shi, L. B. Jones-Jackson, V. Lakhani, R. P. Baum, J. Berlin, G. T. Smith, M. Graham, M. P. Sandler, D. Delbeke, and R. C. Walker, Journal of Nuclear Medicine **57**, 708 (2016).

[16] M. S. Hofman, R. J. Hicks, T. Maurer, and M. Eiber, RadioGraphics **38**, 200 (2018).

[17] L. S. Freudenberg, W. Jentzen, A. Stahl, A. Bockisch, and S. J. Rosenbaum-Krumme, European Journal of Nuclear Medicine and Molecular Imaging **38**, 48 (2011).

[18] J. R. Strosberg, M. E. Caplin, P. L. Kunz, P. B. Ruszniewski, L. Bodei, A. Hendifar, E. Mittra, E. M. Wolin, J. C. Yao, M. E. Pavel, E. Grande, E. V. Cutsem, E. Seregni, H. Duarte, G. Gericke, A. Bartalotta, M. F. Mariani,

A. Demange, S. Mutevelic, and E. P. Krenning, The Lancet Oncology **22**, 1752 (2021).

[19] O. Sartor, J. de Bono, K. N. Chi, K. Fizazi, K. Herrmann, K. Rahbar, S. T. Tagawa, L. T. Nordquist, N. Vaishampayan, G. El-Haddad, C. H. Park, T. M. Beer, A. Armour, W. J. Pérez-Contreras, M. DeSilvio, E. Kpamegan, G. Gericke, R. A. Messmann, M. J. Morris, and B. J. Krause, New England Journal of Medicine **385**, 1091 (2021).

[20] C. Kratochwil, W. P. Fendler, M. Eiber, R. Baum, M. F. Bozkurt, J. Czernin, R. C. D. Bolton, S. Ezziddin, F. Forrer, R. J. Hicks, T. A. Hope, L. Kabasakal, M. Konijnenberg, K. Kopka, M. Lassmann, F. M. Mottaghy, W. Oyen, K. Rahbar, H. Schöder, I. Virgolini, H.-J. Wester, L. Bodei, S. Fanti, U. Haberkorn, and K. Herrmann, European Journal of Nuclear Medicine and Molecular Imaging **46**, 2536 (2019).

[21] J. J. Zaknun, L. Bodei, J. Mueller-Brand, M. E. Pavel, R. P. Baum, D. Hörsch, M. S. O'Dorisio, T. M. O'Dorisiol, J. R. Howe, M. Cremonesi, and D. J. Kwekkeboom, European Journal of Nuclear Medicine and Molecular Imaging **40**, 800 (2013).

[22] B. R. Haugen, E. K. Alexander, K. C. Bible, G. M. Doherty, S. J. Mandel, Y. E. Nikiforov, F. Pacini, G. W. Randolph, A. M. Sawka, M. Schlumberger, K. G. Schuff, S. I. Sherman, J. A. Sosa, D. L. Steward, R. M. Tuttle, and L. Wartofsky, Thyroid **26**, 1 (2016).

[23] G. Sgouros, R. F. Hobbs, F. B. Atkins, D. V. Nostrand, P. W. Ladenson, and R. L. Wahl, European Journal of Nuclear Medicine and Molecular Imaging **38**, 41 (2011).

[24] E. Berg and S. R. Cherry, Seminars in Nuclear Medicine **48**, 311 (2018), Instrumentation.

[25] T. K. Lewellen, Physics in Medicine and Biology **53**, R287 (2008).

[26] M. Conti and B. Bendriem, Clinical and Translational Imaging **7**, 139 (2019).

[27] A. Alessio, P. Kinahan, and T. Lewellen, IEEE Transactions on Medical Imaging **25**, 828 (2006).

[28] J. Cal-Gonzalez, M. Perez-Liva, J. L. Herraiz, J. J. Vaquero, M. Desco, and J. M. Udias, IEEE Transactions on Medical Imaging **34**, 2394 (2015).

[29] A. Mehranian, M. A. Belzunce, F. Niccolini, M. Politis, C. Prieto, F. Turkheimer, A. Hammers, and A. J. Reader, Physics in Medicine and Biology **62**, 5975 (2017).

[30] J. van Sluis, J. de Jong, J. Schaar, W. Noordzij, P. van Snick, R. Dierckx, R. Borra, A. Willemsen, and R. Boellaard, Journal of Nuclear Medicine **60**, 1031 (2019).

[31] I. Rausch, A. Ruiz, I. Valverde-Pascual, J. Cal-González, T. Beyer, and I. Carrio, Journal of Nuclear Medicine **60**, 561 (2018).

[32] D. F. Hsu, E. Ilan, W. T. Peterson, J. Uribe, M. Lubberink, and C. S. Levin, Journal of Nuclear Medicine **58**, 1511 (2017).

[33] D. A. López-Mora, M. Sizova, M. Estorch, A. Flotats, V. Camacho, A. Fernández, S. Abouzian, F. Fuentes-Ocampo, J. I. P. Garcia, A. I. C. Ballesteros, J. Duch, A. Domènech, A. M. Duarte, and I. Carrió, European Journal of Nuclear Medicine and Molecular Imaging **47**, 572 (2020).

[34] K. Miwa, K. Wagatsuma, R. Nemoto, M. Masubuchi, Y. Kamitaka, T. Yamao, S. Hiratsuka, M. Yamaguchi, T. Yoshii, R. Kobayashi, N. Miyaji, and K. Ishii, Annals of Nuclear Medicine **34**, 762 (2020).

[35] S. Surti, V. Viswanath, M. Daube-Witherspoon, M. Conti, M. Casey, and J. Karp, Journal of Nuclear Medicine **61**, 1684 (2020).

[36] S. Adler, J. Seidel, P. Choyke, M. V. Knopp, K. Binzel, J. Zhang, C. Barker, S. Conant, and R. Maass-Moreno, EJNMMI Physics **4** (2017).

[37] J. Schaefferkoetter, Y.-H. Nai, A. Reilhac, D. W. Townsend, L. Eriksson, and M. Conti, Medical Physics **46**, 2638 (2019).

[38] I. Rauscher, W. P. Fendler, T. A. Hope, A. Quon, S. G. Nekolla, J. Calais, A. Richter, B. Haller, K. Herrmann, W. A. Weber, J. Czernin, and M. Eiber, Journal of Nuclear Medicine **61**, 189 (2019).

[39] R. C. Smallridge, N. Diehl, and V. Bernet, Thyroid **24**, 1501 (2014).

[40] J. W. Kist, B. de Keizer, M. van der Vlies, A. H. Brouwers, D. A. Huysmans, F. M. van der Zant, R. Hermsen, M. P. Stokkel, O. S. Hoekstra, and W. V. Vogel, Journal of Nuclear Medicine **57**, 701 (2015).

[41] D. Pattison and R. Hicks, Journal of Nuclear Medicine **58**, 354 (2017).

[42] J. W. Kist, B. de Keizer, O. S. Hoekstra, and W. V. Vogel, Journal of Nuclear Medicine **58**, 354.2 (2016).

[43] M. Weber, W. Jentzen, R. Hofferber, K. Herrmann, W. P. Fendler, C. Rischpler, L. Umutlu, M. Conti, P. F. Costa, M. Sraieb, and D. Kersting, BMC Cancer **21** (2021).

[44] M. Weber, W. Jentzen, R. Hofferber, K. Herrmann, W. P. Fendler, M. Conti, A. Wetter, D. Kersting, C. Rischpler, and P. Fragoso Costa, EJNMMI Research **11** (2021).

[45] D. Kersting, W. Jentzen, M. Sraieb, P. F. Costa, M. Conti, L. Umutlu, G. Antoch, M. Nader, K. Herrmann, W. P. Fendler, C. Rischpler, and M. Weber, EJNMMI Physics **8** (2021).

[46] D. Kersting, W. Jentzen, P. F. Costa, M. Sraieb, P. Sandach, L. Umutlu, M. Conti, F. Zarrad, C. Rischpler, W. P. Fendler, K. Herrmann, and M. Weber, Scientific Reports **11** (2021).

[47] S. Rosenbaum-Krumme, J. Nagarajah, M. Ruhlmann, A. Bockisch, and W. Jentzen, Nuklearmedizin **51**, 213 (2012).

[48] W. Jentzen, F. Verschure, A. van Zon, R. van de Kolk, R. Wierts, J. Schmitz, A. Bockisch, and I. Binse, Journal of Nuclear Medicine **57**, 1499 (2016).

[49] W. Jentzen, A.-S. Moldovan, M. Ruhlmann, R. Görges, A. Bockisch, and S. Rosenbaum-Krumme, Nuklearmedizin **54**, 137 (2015).

[50] W. Jentzen, J. Hoppenbrouwers, P. van Leeuwen, D. van der Velden, R. van de Kolk, T. D. Poeppel, J. Nagarajah, W. Brandau, A. Bockisch, and S. Rosenbaum-Krumme, Journal of Nuclear Medicine **55**, 1759 (2014).

[51] V. Valotassiou, J. Malamitsi, J. Papatriantafyllou, E. Dardiotis, I. Tsougos, D. Psimadas, S. Alexiou, G. Hadjigeorgiou, and P. Georgoulias, Annals of Nuclear Medicine **32**, 583 (2018).

[52] J. M. Tarkin, A. Ćorović, C. Wall, D. Gopalan, and J. H. Rudd, Heart **106**, 1712 (2020).

[53] A. Berger, BMJ **326**, 1449 (2003).

[54] W. Wadsak and M. Mitterhauser, European Journal of Radiology **73**, 461 (2010).

[55] T. J. Ruth, Reports on Progress in Physics **72**, 016701 (2008).

[56] J. Conway, Advanced Drug Delivery Reviews **64**, 357 (2012).

[57] S. Banerjee, M. R. A. Pillai, and N. Ramamoorthy, Seminars in Nuclear Medicine **31**, 260 (2001).

[58] A. K. Buck, S. Nekolla, S. Ziegler, A. Beer, B. J. Krause, K. Herrmann, K. Scheidhauer, H.-J. Wester, E. J. Rummeny, M. Schwaiger, and A. Drzezga, Journal of Nuclear Medicine **49**, 1305 (2008).

[59] J. Czernin, O. Israel, K. Herrmann, M. Barrio, D. Nathanson, and M. Allen-Auerbach, in *Physics of PET and SPECT Imaging*, CRC Press, 2017, pp. 461–494.

[60] Jiang, Chalich, and Deen, Sensors **19**, 5019 (2019).

[61] J. J. Vaquero and P. Kinahan, Annual Review of Biomedical Engineering **17**, 385 (2015), PMID: 26643024.

[62] W. H. Sweet, New England Journal of Medicine **245**, 875 (1951).

[63] G. L. Brownell and W. H. Sweet, Acta Radiologica **os-46**, 425 (1956).

[64] M. M. Ter-Pogossian, M. E. Phelps, E. J. Hoffman, and N. A. Mullani, Radiology **114**, 89 (1975).

[65] D. Brasse, D. Newport, J. Carney, J. Yap, C. Reynolds, J. Reed, J. Bao, P. Luk, C. Michel, and D. Townsend, in *2002 IEEE Nuclear Science Symposium Conference Record*, 2002, volume 2, pp. 951–955.

[66] M. D. Farwell, D. A. Pryma, and D. A. Mankoff, Cancer **120**, 3433 (2014).

[67] H. T. T. Phan, P. L. Jager, A. M. J. Paans, J. T. M. Plukker, M. G. G. Sturkenboom, W. J. Sluiter, B. H. R. Wolffenbuttel, R. A. J. O. Dierckx, and T. P. Links, European Journal of Nuclear Medicine and Molecular Imaging **35**, 958 (2008).

[68] C. Boy, T. A. Heusner, T. D. Poeppel, A. Redmann-Bischofs, N. Unger, W. Jentzen, W. Brandau, K. Mann, G. Antoch, A. Bockisch, and S. Petersenn, European Journal of Nuclear Medicine and Molecular Imaging **38**, 1224 (2011).

[69] T. Maurer, M. Eiber, M. Schwaiger, and J. E. Gschwend, Nature Reviews Urology **13**, 226 (2016).

[70] G. Sgouros, L. Bodei, M. R. McDevitt, and J. R. Nedrow, Nature Reviews Drug Discovery **19**, 589 (2020).

[71] L. Specht and A. K. Berthelsen, Seminars in Nuclear Medicine **48**, 67 (2018).

[72] K. Kubota, M. Ogawa, B. Ji, T. Watabe, M.-R. Zhang, H. Suzuki, M. Sawada, K. Nishi, and T. Kudo, in *PET/CT for Inflammatory Diseases*, Springer Singapore, 2019, pp. 1–42.

[73] G. Chételat, J. Arbizu, H. Barthel, V. Garibotto, I. Law, S. Morbelli, E. van de Giessen, F. Agosta, F. Barkhof, D. J. Brooks, M. C. Carrillo, B. Dubois, A. M. Fjell, G. B. Frisoni, O. Hansson, K. Herholz, B. F. Hutton, C. R. Jack, A. A. Lammertsma, S. M. Landau, S. Minoshima, F. Nobili, A. Nordberg, R. Ossenkoppele, W. J. G. Oyen, D. Perani, G. D. Rabinovici, P. Scheltens, V. L. Villemagne, H. Zetterberg, and A. Drzezga, The Lancet Neurology **19**, 951 (2020).

[74] J. Iking, M. Staniszewska, L. Kessler, J. M. Klose, K. Lückerath, W. P. Fendler, K. Herrmann, and C. Rischpler, Biomedicines **9**, 212 (2021).

[75] N. Ghosh, O. E. Rimoldi, R. S. Beanlands, and P. G. Camici, European Heart Journal **31**, 2984 (2010).

[76] C. Kratochwil, P. Flechsig, T. Lindner, L. Abderrahim, A. Altmann, W. Mier, S. Adeberg, H. Rathke, M. Röhrich, H. Winter, P. K. Plinkert, F. Marme, M. Lang, H.-U. Kauczor, D. Jäger, J. Debus, U. Haberkorn, and F. L. Giesel, Journal of Nuclear Medicine **60**, 801 (2019).

[77] F. L. Giesel, C. Kratochwil, T. Lindner, M. M. Marschalek, A. Loktev, W. Lehnert, J. Debus, D. Jäger, P. Flechsig, A. Altmann, W. Mier, and U. Haberkorn, Journal of Nuclear Medicine **60**, 386 (2018).

[78] W. Wei, Z. T. Rosenkrans, J. Liu, G. Huang, Q.-Y. Luo, and W. Cai, Chemical Reviews **120**, 3787 (2020).

[79] C. L. Wright, J. Zhang, M. F. Tweedle, M. V. Knopp, and N. C. Hall, BioMed Research International **2015**, 1 (2015).

[80] A. Kjaer, Cancer Imaging **14** (2014).

[81] T. C. Lee, A. M. Alessio, R. M. Miyaoka, and P. E. Kinahan, The Quarterly Journal of Nuclear Medicine and Molecular Imaging **60**, 25 (2016).

[82] C. Burger, G. Goerres, S. Schoenes, A. Buck, A. Lonn, and G. von Schulthess, European Journal of Nuclear Medicine and Molecular Imaging **29**, 922 (2002).

[83] A. Martinez-Möller and S. G. Nekolla, Zeitschrift für Medizinische Physik **22**, 299 (2012), Schwerpunkt: Multimodale Bildgebung und Therapie.

[84] M. Hofmann, B. Pichler, B. Schölkopf, and T. Beyer, European Journal of Nuclear Medicine and Molecular Imaging **36**, 93 (2008).

[85] A. Samarin, C. Burger, S. D. Wollenweber, D. W. Crook, I. A. Burger, D. T. Schmid, G. K. von Schulthess, and F. P. Kuhn, European Journal of Nuclear Medicine and Molecular Imaging **39**, 1154 (2012).

[86] S. Song, Y. Cheng, J. Ma, L. Wang, C. Dong, Y. Wei, G. Xu, Y. An, Z. Qi, Q. Lin, and J. Lu, European Journal of Nuclear Medicine and Molecular Imaging **47**, 1458 (2020).

[87] J. Nagarajah, W. Jentzen, V. Hartung, S. Rosenbaum-Krumme, C. Mikat, T. A. Heusner, G. Antoch, A. Bockisch, and A. Stahl, European Journal of Nuclear Medicine and Molecular Imaging **38**, 1862 (2011).

[88] I. Binse, T. D. Poeppel, M. Ruhlmann, B. Gomez, L. Umutlu, A. Bockisch, and S. J. Rosenbaum-Krumme, European Journal of Nuclear Medicine and Molecular Imaging **43**, 1011 (2015).

[89] C. Melcher, Journal of Nuclear Medicine **41**, 1051 (2000).

[90] P. Lecoq and S. Gundacker, The European Physical Journal Plus **136** (2021).

[91] B. Pichler, H. Wehrl, and M. Judenhofer, Journal of Nuclear Medicine **49**, 5S (2008).

[92] M. Bergeron, C. Thibaudeau, J. Cadorette, M.-A. Tétrault, C. M. Pepin, J. Clerk-Lamalice, F. Loignon-Houle, M. Davies, H. Dautet, P. Deschamps, R. Fontaine, and R. Lecomte, IEEE Transactions on Nuclear Science **62**, 756 (2015).

[93] C. Pepin, P. Berard, A.-L. Perrot, C. Pepin, D. Houde, R. Lecomte, C. Melcher, and H. Dautet, IEEE Transactions on Nuclear Science **51**, 789 (2004).

[94] C. S. Levin, S. H. Maramraju, M. M. Khalighi, T. W. Deller, G. Delso, and F. Jansen, IEEE Transactions on Medical Imaging **35**, 1907 (2016).

[95] E. Roncali and S. R. Cherry, Annals of Biomedical Engineering **39**, 1358 (2011).

[96] S. Gundacker and A. Heering, Physics in Medicine and Biology **65**, 17TR01 (2020).

[97] S. Surti and J. S. Karp, Physica Medica **80**, 251 (2020).

[98] V. Panin, F. Kehren, C. Michel, and M. Casey, IEEE Transactions on Medical Imaging **25**, 907 (2006).

[99] O. Bertolli, A. Eleftheriou, M. Cecchetti, N. Camarlinghi, N. Belcari, and C. Tsoumpas, Physica Medica **32**, 323 (2016).

[100] Y. Tsutsui, S. Awamoto, K. Himuro, Y. Umezu, S. Baba, and M. Sasaki, Asia Oceania Journal of Nuclear Medicine and Biology **6**, 15 (2018).

[101] G. Muehllehner and J. S. Karp, Physics in Medicine and Biology **51**, R117 (2006).

[102] N. A. Karakatsanis, M. A. Lodge, A. Rahmim, and H. Zaidi, in *2014 IEEE Nuclear Science Symposium and Medical Imaging Conference (NSS/MIC)*, 2014, pp. 1–6.

[103] D. Kadrmas, M. Casey, M. Conti, B. Jakoby, C. Lois, and D. Townsend, Journal of Nuclear Medicine **50**, 1315 (2009).

[104] C. S. van der Vos, D. Koopman, S. Rijnsdorp, A. J. Arends, R. Boellaard, J. A. van Dalen, M. Lubberink, A. T. M. Willemsen, and E. P. Visser, European Journal of Nuclear Medicine and Molecular Imaging **44**, 4 (2017).

[105] B. Aklan, M. Oehmigen, K. Beiderwellen, M. Ruhlmann, D. H. Paulus, B. W. Jakoby, P. Ritt, and H. H. Quick, Journal of Nuclear Medicine **57**, 78 (2015).

[106] Y. S. Lee, J. S. Kim, K. M. Kim, J. H. Kang, S. M. Lim, and H.-J. Kim, Annals of Nuclear Medicine **28**, 340 (2014).

[107] O. L. Munk, L. P. Tolbod, S. B. Hansen, and T. V. Bogsrud, EJNMMI Physics **4** (2017).

[108] A. Nakamura, Y. Tanizaki, M. Takeuchi, S. Ito, Y. Sano, M. Sato, T. Kanno, H. Okada, T. Torizuka, and S. Nishizawa, Japanese Journal of Radiological Technology **70**, 542 (2014).

[109] S. Tong, A. Alessio, K. Thielemans, C. Stearns, S. Ross, and P. Kinahan, Journal of Nuclear Medicine **52**, 106 (2011).

[110] J. Devriese, L. Beels, A. Maes, C. V. de Wiele, and H. Pottel, EJNMMI Physics **5** (2018).

[111] Y. Tsutsui, S. Awamoto, K. Himuro, Y. Umezu, S. Baba, and M. Sasaki, Asia Oceania Journal of Nuclear Medicine and Biology (2017).

[112] R. Wierts, M. Conti, A. G. Claessen, K. Herrmann, G. J. Kemerink, I. Binse, J. E. Wildberger, F. M. Mottaghy, W. H. Backes, and W. Jentzen, Nuclear Medicine Communications **39**, 1156 (2018).

[113] W. Jentzen, L. Freudenberg, and A. Bockisch, The Quarterly Journal of Nuclear Medicine and Molecular Imaging **55**, 21 (2011).

[114] M. Conti and L. Eriksson, EJNMMI Physics **3** (2016).

[115] M. S. Hofman and R. J. Hicks, Cancer Imaging **16** (2016).

[116] S. Vaidyanathan, C. Patel, A. Scarsbrook, and F. Chowdhury, Clinical Radiology **70**, 787 (2015).

[117] C. Love, M. B. Tomas, G. G. Tronco, and C. J. Palestro, RadioGraphics **25**, 1357 (2005).

[118] M. Mahmood, A. T. Kendi, S. Ajmal, S. Farid, J. C. O'Horo, P. Chareonthaitawee, L. M. Baddour, and M. R. Sohail, Journal of Nuclear Cardiology **26**, 922 (2017).

[119] F. Nensa, J. Kloth, E. Tezgah, T. D. Poeppel, P. Heusch, J. Goebel, K. Nassenstein, and T. Schlosser, Journal of Nuclear Cardiology **25**, 785 (2016).

[120] P. T. Meyer, L. Frings, G. Rücker, and S. Hellwig, Journal of Nuclear Medicine **58**, 1888 (2017).

[121] A. Sanchez-Crespo, Applied Radiation and Isotopes **76**, 55 (2013), Ga-68 Special Issue.

[122] T. C. El-Galaly, D. Villa, L. C. Gormsen, J. Baech, A. Lo, and C. Y. Cheah, Journal of Internal Medicine **284**, 358 (2018).

[123] U. Hennrich and M. Eder, Pharmaceuticals **14**, 713 (2021).

[124] A. Afshar-Oromieh, U. Haberkorn, M. Eder, M. Eisenhut, and C. Zechmann, European Journal of Nuclear Medicine and Molecular Imaging **39**, 1085 (2012).

[125] J. Calais and J. Czernin, Journal of Nuclear Medicine **62**, 1489 (2021).

[126] C. Kesch, C. Kratochwil, W. Mier, K. Kopka, and F. Giesel, Journal of Nuclear Medicine **58**, 687 (2017).

[127] H. Grünig, A. Maurer, Y. Thali, Z. Kovacs, K. Strobel, I. A. Burger, and J. Müller, European Journal of Nuclear Medicine and Molecular Imaging **48**, 4483 (2021).

[128] L. M. Carter, A. L. Kesner, E. C. Pratt, V. A. Sanders, A. V. F. Massicano, C. S. Cutler, S. E. Lapi, and J. S. Lewis, Molecular Imaging and Biology **22**, 73 (2019).

[129] A. Farolfi, L. Calderoni, F. Mattana, R. Mei, S. Telo, S. Fanti, and P. Castellucci, Journal of Nuclear Medicine **62**, 596 (2021).

[130] M. S. Hofman, N. Lawrentschuk, R. J. Francis, C. Tang, I. Vela, P. Thomas, N. Rutherford, J. M. Martin, M. Frydenberg, R. Shakher, L.-M. Wong, K. Taubman, S. T. Lee, E. Hsiao, P. Roach, M. Nottage, I. Kirkwood, D. Hayne, E. Link, P. Marusic, A. Matera, A. Herschtal, A. Iravani, R. J. Hicks, S. Williams, and D. G. Murphy, The Lancet **395**, 1208 (2020).

[131] W. P. Fendler, J. Calais, M. Eiber, R. R. Flavell, A. Mishoe, F. Y. Feng, H. G. Nguyen, R. E. Reiter, M. B. Rettig, S. Okamoto, L. Emmett, H. D. Zacho, H. Ilhan, A. Wetter, C. Rischpler, H. Schoder, I. A. Burger, J. Gartmann, R. Smith, E. J. Small, R. Slavik, P. R. Carroll, K. Herrmann, J. Czernin, and T. A. Hope, JAMA Oncology **5**, 856 (2019).

[132] M. Luster, S. E. Clarke, M. Dietlein, M. Lassmann, P. Lind, W. J. G. Oyen, J. Tennvall, and E. Bombardieri, European Journal of Nuclear Medicine and Molecular Imaging **35**, 1941 (2008).

[133] M. Dietlein, W. Eschner, F. Grünwald, M. Lassmann, F. A. Verburg, and M. Luster, Nuklearmedizin **55**, 77 (2016).

[134] K. Marx, D. Moka, K. Schomäcker, T. Fischer, B. Gabruk-Szostak, C. Kobe, M. Dietlein, and H. Schicha, Nuclear Medicine Communications **27**, 353 (2006).

[135] A. Wyszomirska, Nuclear Medicine Review **15**, 120 (2012).

[136] E. B. Silberstein, Seminars in Nuclear Medicine **42**, 164 (2012).

[137] H.-M. Park, Journal of Nuclear Medicine **43**, 77 (2002).

[138] D. V. Nostrand, S. Moreau, V. V. Bandaru, F. Atkins, S. Chennupati, M. Mete, K. Burman, and L. Wartofsky, Thyroid **20**, 879 (2010).

[139] J. Nagarajah, M. Janssen, P. Hetkamp, and W. Jentzen, Journal of Nuclear Medicine **58**, 34S (2017).

[140] W. Jentzen, L. Freudenberg, E. G. Eising, W. Sonnenschein, J. Knust, and A. Bockisch, Journal of Nuclear Medicine **49**, 1017 (2008).

[141] M. Weber, I. Binse, J. Nagarajah, A. Bockisch, K. Herrmann, and W. Jentzen, The Quarterly Journal of Nuclear Medicine and Molecular Imaging **63** (2019).

[142] D. V. Nostrand, Thyroid **29**, 901 (2019).

[143] L. J. Medeiros and T. C. Greiner, Cancer **75**, 357 (1995).

[144] Leitlinienprogramm-Onkologie: Diagnostik, Therapie und Nachsorge des Hodgkin Lymphoms bei erwachsenen Patienten, Version 3.1 - März 2022, https://www.leitlinienprogramm-onkologie.de/leitlinien/hodgkin-lymphom/ (received: 13.08.2022).

[145] H. Adams, T. Kwee, B. de Keizer, R. Fijnheer, J. de Klerk, A. Littooij, and R. Nievelstein, Annals of Oncology **25**, 921 (2014).

[146] T. N.-H. L. C. Project, Blood **89**, 3909 (1997).

[147] S. H. Jeong, Blood Research **57**, S120 (2022).

[148] Leitlinienprogramm-Onkologie: S3-Leitlinie Diagnostik, Therapie und Nachsorge für erwachsene Patient*innen mit einem diffusen großzelligen B- Zell-Lymphom und verwandten Entitäten, Version 1.01 - Juni 2022, https://www.leitlinienprogramm-onkologie.de/leitlinien/dlbcl/ (received: 15.09.2022).

[149] P. Rawla, World Journal of Oncology **10**, 63 (2019).

[150] M. Palken, O. E. Cobb, C. E. Simons, B. H. Warren, and H. C. Aldape, Journal of Urology **145**, 86 (1991).

[151] A. Moe and D. Hayne, Translational Andrology and Urology **9**, 3018 (2020).

[152] A. Carneiro, D. Racy, C. E. Bacchi, K. R. M. Leite, R. Z. Filippi, I. A. F. Martins, J. V. Salvajoli, R. de Morais Hanriot, R. H. Baroni, A. S. Sarkis, A. C. L. Pompeo, B. S. Benigno, G. C. Guimarães, S. Aldousari, A. C. Nardi, A. S. F. L. Pompeo, A. Nowier, A. N. Jr, A. A. Jr, C. H. de Freitas Jr, D. C. Chade, D. A. C. Otero, D. C. V. da Silva Neto, E. F. Carvalhal, F. Korkes, and R. Ferrigno, JCO Global Oncology , 516 (2021).

[153] Leitlinienprogramm-Onkologie: S3-Leitlinie Prostatakarzinom, Version 6.2 – Oktober 2021, https://www.leitlinienprogramm-onkologie.de/leitlinien/prostatakarzinom/ (received: 05.10.2022).

[154] B. Delahunt, R. J. Miller, J. R. Srigley, A. J. Evans, and H. Samaratunga, Histopathology **60**, 75 (2011).

[155] A. M. Hoogland, C. F. Kweldam, and G. J. L. H. van Leenders, BioMed Research International **2014**, 1 (2014).

[156] M. A. Perlmutter and H. Lepor, Rev Urol **9**, S3 (2007).

[157] M. S. Hofman, L. Emmett, S. Sandhu, A. Iravani, A. M. Joshua, J. C. Goh, D. A. Pattison, T. H. Tan, I. D. Kirkwood, S. Ng, R. J. Francis, C. Gedye, N. K. Rutherford, A. Weickhardt, A. M. Scott, S.-T. Lee, E. M. Kwan, A. A. Azad, S. Ramdave, A. D. Redfern, W. Macdonald, A. Guminski, E. Hsiao, W. Chua, P. Lin, A. Y. Zhang, M. M. McJannett, M. R. Stockler, J. A. Violet, S. G. Williams, A. J. Martin, I. D. Davis, A. A. Azad, W. Chua, I. D. Davis, N. Dhiantravan, L. Emmett, K. Ford, M. S. Hofman, R. J. Francis, C. Gedye, J. C. Goh, A. Guminski, E. Hsiao, A. Iravani, A. M. Joshua, I. D. Kirkwood, A. Langford, N. Lawrence, S.-T. Lee, P. Lin, A. J. Martin, W. McDonald, M. M. McJannett, S. Ng, D. A. Pattison, S. Ramdave, N. Rana, A. D. Redfern, N. K. Rutherford, S. Sandhu, A. M. Scott, M. R. Stockler, S. Subramaniam, T. H. Tan, J. A. Violet, A. Weickhardt, S. G. Williams, S. Yip, and A. Y. Zhang, The Lancet **397**, 797 (2021).

[158] Q. T. Nguyen, E. J. Lee, M. G. Huang, Y. I. Park, A. Khullar, and R. A. Plodkowski, Am Health Drug Benefits **8**, 30 (2015).

[159] Robert Koch Institut: Krebs in Deutschland für 2017/2018, https://www.krebsdaten.de/Krebs/DE/Content/Publikationen/ Krebs_in_Deutschland/kid_2021/krebs_in_deutschland_2021.pdf (received: 01.10.2022).

[160] C. Reiners, *Diagnostik, Therapie und Nachsorge des Schilddrüsenkarzinoms*, UNI-MED Science, UNI-MED, Bremen, Germany, 2 edition, 2006.

[161] E. Olson, G. Wintheiser, K. M. Wolfe, J. Droessler, and P. T. Silberstein, Cureus **11** (2019).

[162] K. Fruth, TumorDiagnostik & Therapie **31**, 12 (2010).

[163] M. Schlumberger, M. Tahara, L. J. Wirth, B. Robinson, M. S. Brose, R. Elisei, M. A. Habra, K. Newbold, M. H. Shah, A. O. Hoff, A. G. Gianoukakis,

N. Kiyota, M. H. Taylor, S.-B. Kim, M. K. Krzyzanowska, C. E. Dutcus, B. de las Heras, J. Zhu, and S. I. Sherman, New England Journal of Medicine **372**, 621 (2015).

[164] M. S. Brose, C. M. Nutting, B. Jarzab, R. Elisei, S. Siena, L. Bastholt, C. de la Fouchardiere, F. Pacini, R. Paschke, Y. K. Shong, S. I. Sherman, J. W. A. Smit, J. Chung, C. Kappeler, C. Peña, I. Molnár, and M. J. Schlumberger, The Lancet **384**, 319 (2014).

[165] M. Weber, D. Kersting, B. Riemann, T. Brandenburg, D. Führer-Sakel, F. Grünwald, M. C. Kreissl, H. Dralle, F. Weber, K. W. Schmid, K. Herrmann, W. Jentzen, H. Grafe, C. Rischpler, S. Theurer, A. Bockisch, J. Nagarajah, and W. P. Fendler, Clinical Cancer Research **28**, 4194 (2022).

[166] R. Wierts, W. Jentzen, H. H. Quick, H. J. Wisselink, I. N. A. Pooters, J. E. Wildberger, K. Herrmann, G. J. Kemerink, W. H. Backes, and F. M. Mottaghy, Physics in Medicine and Biology **63**, 015014 (2017).

[167] W. P. Fendler, M. Eiber, M. Beheshti, J. Bomanji, F. Ceci, S. Cho, F. Giesel, U. Haberkorn, T. A. Hope, K. Kopka, B. J. Krause, F. M. Mottaghy, H. Schöder, J. Sunderland, S. Wan, H.-J. Wester, S. Fanti, and K. Herrmann, European Journal of Nuclear Medicine and Molecular Imaging **44**, 1014 (2017).

[168] J. van Sluis, R. Boellaard, R. Dierckx, G. Stormezand, A. Glaudemans, and W. Noordzij, Journal of Nuclear Medicine **61**, 764 (2020).

[169] W. Jentzen, Physics in Medicine and Biology **55**, 2365 (2010).

[170] M. Hofman, N. Smeeton, S. Rankin, T. Nunan, and M. O'Doherty, Journal of Nuclear Medicine **50**, 1594 (2009).

[171] W. Fendler, J. Calais, M. Allen-Auerbach, C. Bluemel, N. Eberhardt, L. Emmett, P. Gupta, M. Hartenbach, T. Hope, S. Okamoto, C. Pfob, T. Pöppel, C. Rischpler, S. Schwarzenböck, V. Stebner, M. Unterrainer, H. Zacho, T. Maurer, C. Gratzke, A. Crispin, J. Czernin, K. Herrmann, and M. Eiber, Journal of Nuclear Medicine **58**, 1617 (2017).

[172] W. Fendler, M. Weber, A. Iravani, M. Hofman, J. Calais, J. Czernin, H. Ilhan, F. Saad, E. Small, M. Smith, P. Perez, T. Hope, I. Rauscher,

A. Londhe, A. Lopez-Gitlitz, S. Cheng, T. Maurer, K. Herrmann, M. Eiber, and B. Hadaschik, Clin Cancer Res; Clinical Cancer Research **25**, 7448 (2019).

[173] S. F. Barrington, N. G. Mikhaeel, L. Kostakoglu, M. Meignan, M. Hutchings, S. P. Müeller, L. H. Schwartz, E. Zucca, R. I. Fisher, J. Trotman, O. S. Hoekstra, R. J. Hicks, M. J. O'Doherty, R. Hustinx, A. Biggi, and B. D. Cheson, Journal of Clinical Oncology **32**, 3048 (2014).

[174] M. Eiber, K. Herrmann, J. Calais, B. Hadaschik, F. Giesel, M. Hartenbach, T. Hope, R. Reiter, T. Maurer, W. Weber, and W. Fendler, Journal of Nuclear Medicine **59**, 469 (2018).

[175] J. Thie, Journal of Nuclear Medicine **45**, 1431 (2004).

[176] P. E. Kinahan and J. W. Fletcher, Seminars in Ultrasound, CT and MRI **31**, 496 (2010).

[177] A. Sher, F. Lacoeuille, P. Fosse, L. Vervueren, A. Cahouet-Vannier, D. Dabli, F. Bouchet, and O. Couturier, EJNMMI Research **6** (2016).

[178] P. J. Julyan, J. H. Taylor, D. L. Hastings, H. A. Williams, and J. Zweit, Nuclear Medicine Communications **25** (2004).

[179] W. Jentzen, Journal of Nuclear Medicine Technology **43**, 28 (2015).

[180] M. Viner, G. Mercier, F. Hao, A. Malladi, and R. M. Subramaniam, Radiology **267**, 596 (2013).

[181] A. Nagaki, M. Onoguchi, and N. Matsutomo, Journal of Nuclear Medicine Technology **39**, 72 (2011).

[182] J. van Sluis, R. Boellaard, A. Somasundaram, P. van Snick, R. Borra, R. Dierckx, G. Stormezand, A. Glaudemans, and W. Noordzij, Journal of Nuclear Medicine **61**, 129 (2020).

[183] E. Richter, T. Feyerabend, and E. Richter, *Normal lymph node topography*, Springer, 2004.

[184] S. K. Øen, L. B. Aasheim, L. Eikenes, and A. M. Karlberg, EJNMMI Physics **6** (2019).

[185] C. Beijst, J. W. Kist, M. Elschot, M. A. Viergever, O. S. Hoekstra, B. de Keizer, and H. W. de Jong, Journal of Nuclear Medicine **57**, 103 (2015).

[186] W. B. Li, W. Friedland, E. Pomplun, P. Jacob, H. G. Paretzke, M. Lassmann, and C. Reiners, Radiation Research **156**, 419 (2001).

[187] W. Jentzen, R. F. Hobbs, A. Stahl, J. Knust, G. Sgouros, and A. Bockisch, European Journal of Nuclear Medicine and Molecular Imaging **37**, 884 (2010).

[188] H. R. Maxon, S. R. Thomas, V. S. Hertzberg, J. G. Kereiakes, I.-W. Chen, M. I. Sperling, and E. L. Saenger, New England Journal of Medicine **309**, 937 (1983).

[189] A. S. Chaudhari, E. Mittra, G. A. Davidzon, P. Gulaka, H. Gandhi, A. Brown, T. Zhang, S. Srinivas, E. Gong, G. Zaharchuk, and H. Jadvar, npj Digital Medicine **4** (2021).

[190] A. S. Pasciak, A. C. Bourgeois, J. M. McKinney, T. T. Chang, D. R. Osborne, S. N. Acuff, and Y. C. Bradley, Frontiers in Oncology **4** (2014).

[191] D. Kersting, W. Jentzen, D. Jeronim, I.-A. Mavroeidi, M. Conti, F. Büther, K. Herrmann, C. Rischpler, R. Hamacher, W. P. Fendler, R. Seifert, and P. F. Costa, Journal of Nuclear Medicine (2022).

[192] A. Dimitrakopoulou-Strauss, L. Pan, and C. Sachpekidis, European Journal of Nuclear Medicine and Molecular Imaging **48**, 21 (2020).

Danksagung

Allen voran danke ich Herrn Prof. Dr. Dr. Walter Jentzen ganz besonders für seine ausgezeichnete Betreuung und fachliche Beratung, sein immer offenes Ohr sowie seine ständige Bereitschaft für die Diskussion aufkommender Fragen. Unsere Gespräche und Diskussionen waren mir immer eine große Freude.

Mein ganz besonderer Dank gilt ebenso dem Zweitgutachter dieser Arbeit, Herrn Prof. Dr. Thomas Heinzel, für die sofortige Bereitschaft, diese Arbeit zu betreuen. Unsere hervorragende Zusammenarbeit war schon in meiner gesamten Studienzeit mitsamt meiner Bacherlorarbeit und Masterarbeit an Ihrem Institut stets eine große Bereicherung.

Zudem danke ich Herrn Prof. Dr. Ken Herrmann ganz besonders für die hervorragende und angenehme Zusammenarbeit, seine ständige Unterstützung und die Möglichkeit, diese Arbeit in seiner Klinik anzufertigen.

Mein ganz besonderer Dank geht ebenso an Herrn Prof. Dr. Christoph Rischpler für seine große Unterstützung, viele Gespräche, die angenehme Zusammenarbeit und die Beratung bei fachlichen Fragen.

Zudem danke ich der gesamten Klinik für Nuklearmedizin für das stets angenehme Arbeitsumfeld.

Zuletzt danke ich meinen Eltern und meiner Freundin für ihre immer während Unterstützung.